

**Joint Polar Satellite System (JPSS)  
Visible Infrared Imaging Radiometer  
Suite (VIIRS) Sensor Data Records (SDR)  
Algorithm Theoretical Basis Document  
(ATBD)**

**For Public Release**

The information provided herein does not contain technical data as defined in the International Traffic in Arms Regulations (ITAR) 22 CFC 120.10.  
This document has been approved For Public Release.



National Oceanic and  
Atmospheric  
Administration

**Center for Satellite Applications and Research  
College Park, Maryland**

This page intentionally left blank.

**Joint Polar Satellite System (JPSS)  
Visible Infrared Imaging Radiometer Suite (VIIRS)  
Sensor Data Records (SDR) Radiometric  
Calibration Algorithm Theoretical Basis  
Document (ATBD)**

**JPSS Electronic Signature Page**

**Prepared By:**

NOAA/STAR VIIRS SDR Team and the science team members  
(Electronic Approvals available online at <http://www.star.nesdis.noaa.gov/jpss/ATBD.php#S978737>)  
Point of Contact/Custodian: Changyong Cao ([Changyong.Cao@noaa.gov](mailto:Changyong.Cao@noaa.gov))

**Approved By:**

Eric Gottshall ([eric.gottshall@noaa.gov](mailto:eric.gottshall@noaa.gov) )  
DPA IPT Lead/Algorithm Engineering Review Board (AERB) Chair  
JPSS Ground Project

Lihang Zhou ([lihang.zhou@noaa.gov](mailto:lihang.zhou@noaa.gov))  
DPA IPT Deputy-Science/Algorithm Engineering Review Board (AERB) Co-Chair  
NOAA/NESDIS/STAR

Arron L. Layns ([arron.layns@noaa.gov](mailto:arron.layns@noaa.gov) )  
DPA IPT Deputy-Integration  
NOAA/NESDIS/NJO

**Center for Satellite Applications and Research  
College Park, Maryland**

Check the STAR JPSS web site at <http://www.star.nesdis.noaa.gov/jpss> to verify that this is the correct version prior to use

This page intentionally left blank.

## Change History Log

Center for Satellite Applications and Research National Center for Weather and Climate Prediction College Park, Maryland		 	
<b>Revision/Change Record</b>		<b>For Document No. E/RA-00003</b>	
Revision	Document Date	Revision/Change Description (Reference the CCR & CCB/ERB Approve Date)	Pages Affected
E/RA-00003 Rev. C	11/18/2013	<b>474-CCR-11-0362:</b> Section 3.4.10 on DNB straylight correction has been updated. Appendix D on Description of Theoretical Basis for Reflective Solar Band (RSB) Automated Calibration (RSBAutoCal) Algorithm is added. Corrections have been made to all sections and references have been updated to include recent publications.	All
E/RA-00003 Rev. B	04/11/2012	<b>474-CCR-11-0362:</b> This CCR is for an update to the VIIRS SDR CAL code and LUT format to provide scan-by-scan Reflective Solar Band (RSB) correction. This correction permits F-factor calculations for each scan using current scan time and functional form coefficients drawn from LUTs, providing effectively continuous correction of calibration as bands degrade faster than expected due the abnormal mirror coating anomaly. This CCR was approved by the JPSS Algorithm ERB on April 11, 2012.	All
E/RA-00003 Rev. A	02/15/2012	<b>474-CCR-11-0202:</b> DR 4342 updates to rev F, pages Section 3.3.3.2 - see document Solar Diffuser Geometry Equations for change pages. (a) Remove the sentence in the ATBD about the flipping of the coordinate system. It may have been relating to the change in sign in the y-axis, without considering that the 180 deg flip would also change the sign in z. (b) Atan2 is now consistently defined. (c) The sun_inst angles were removed from Eq. 103, since they are no longer used. This CCR was approved by the JPSS Algorithm ERB on November 2, 2011. <b>474-CCR-11-0316:</b> For M13, table 18 is specifically called out and the need to capture the on board calibrator readings for both the high and low gain states as well as the space view readings. (b) Clarification that scan N is the true scan line number and not the row number in the processing. Special handling had to be designed in by Raytheon to support cross granule access to calibration readings. (c) Aggregation methodology to support DR 4563 so that the M13 aggregation is done in radiance space in the same manner that it is performed on board for M14-M16 to support sea surface temperature retrieval accuracy. This CCR was approved by the JPSS Algorithm ERB on February 15, 2012.	All

E/RA-00003	04/22/2011	<p><b>474-CCR-11-0042:</b> This version baselines D43777, VIIRS Radiometric Calibration Algorithm Theoretical Basis Document ATBD (ref Y3261), Rev E dated 03/31/2010 as a JPSS document, version Rev -. This is the version that was approved for NPP launch. Per NPOESS CDFCB - External, Volume V – Metadata, doc number D34862-05, this has been approved for Public Release into CLASS. This CCR was approved by the JPSS Algorithm ERB on April 22, 2011.</p>	All

**TABLE OF CONTENTS**

	<u>Page</u>
TABLE OF CONTENTS .....	IV
LIST OF FIGURES.....	VIII
LIST OF TABLES.....	X
GLOSSARY OF ACRONYMS.....	XI
GLOSSARY OF SYMBOLS .....	XIV
ABSTRACT .....	XXVI
1. INTRODUCTION .....	1
1.1 HISTORICAL PERSPECTIVE .....	1
1.2 PURPOSE OF DOCUMENT .....	2
1.3 SCOPE OF DOCUMENT .....	2
1.4 REVISIONS.....	3
2. OVERVIEW .....	5
2.1 OBJECTIVES OF RADIOMETRIC CALIBRATION .....	5
2.1.1 Requirements Summary .....	5
2.1.2 Data Products.....	9
2.1.2.1 Sensor Data Records.....	9
2.1.2.2 Intermediate Products .....	11
2.2 INSTRUMENT OVERVIEW.....	12
2.2.1 Spectral Bands .....	12
2.2.2 Opto-Mechanical Module .....	16
2.2.2.1 Rotating Telescope Assembly .....	21
2.2.2.2 Half Angle Mirror .....	21
2.2.2.3 'M' and 'I' Band Focal Plane Assemblies.....	23
2.2.2.3.1 Vis/NIR FPA.....	24
2.2.2.3.2 S/MWIR FPA.....	24
2.2.2.3.3 LWIR FPA.....	25
2.2.2.3.4 Gain Switching .....	25
2.2.2.4 Day-Night Band FPA and Interface Electronics .....	25
2.2.3 Electronics Module .....	30
2.2.3.1 Analog to Digital Conversion .....	32
2.2.3.2 Digital Pre-processing .....	32
2.2.3.3 DC Restore .....	34
2.2.4 On-board Calibrators .....	36
2.2.4.1 Solar Diffuser (SD).....	37

2.2.4.2	Solar Diffuser Stability Monitor (SDSM).....	37
2.2.4.3	On-Board Calibrator (OBC) Blackbody.....	37
2.2.5	Operation Modes.....	38
2.2.6	Instrument Data Output.....	38
2.2.7	Along-scan Aggregation.....	38
2.3	GENERAL RADIOMETRIC EQUATIONS.....	39
2.3.1	Combining Detector and Electronics Subsystem Response.....	43
2.3.2	Response and Thermal Dependence.....	49
2.3.3	General Equations for Emissive Bands.....	49
2.4	RADIOMETRIC CALIBRATION TIMELINE.....	52
2.4.1	Pre-Launch.....	53
2.4.1.1	Subsystem Tests.....	54
2.4.1.2	System Tests.....	55
2.4.1.2.1	System Level Calibration from Pre-Launch Testing..	57
2.4.1.2.2	Reflective Band RVS.....	63
2.4.1.2.3	Pre-Launch Calibration Coefficients from the BCS ...	63
2.4.1.2.4	Emissive Band RVS.....	66
2.4.1.3	Creating Calibration Tables.....	66
2.4.2	Early Orbit Activation and Evaluation.....	68
2.4.3	Operations Phase.....	69
3.	ALGORITHM DESCRIPTION.....	73
3.1	PROCESSING OUTLINE.....	73
3.1.1	Near Real-time Processing.....	74
3.1.2	Offline Processing.....	75
3.2	ALGORITHM INPUTS.....	76
3.2.1	VIIRS Data.....	76
3.2.2	Non-VIIRS Data.....	77
3.2.3	LUTs and Input Parameters.....	77
3.3	THEORETICAL DESCRIPTION.....	81
3.3.1	Zero Offset Determination.....	81
3.3.1.1	'M' and 'I' Band Zero Offsets.....	82
3.3.1.2	Day-Night Band Zero Offsets.....	83
3.3.2	Determination of Instrument Temperatures.....	83
3.3.3	Reflective 'M' and 'I' Band Calibration.....	83
3.3.3.1	Solar Diffuser Stability Monitor Equations.....	88
3.3.3.2	Solar Diffuser Geometry.....	94
3.3.4	Emissive 'M' and 'I' Band Calibration.....	96
3.3.4.1	Earth View Emissive Band Radiometric Calibration.....	96
3.3.4.1.1	M13 Low Gain.....	99
3.3.4.1.2	M13 Band Aggregation.....	101
3.3.5	Day-Night Band Calibration.....	101
3.3.5.1	Overview.....	101
3.3.5.2	Offset Determination On Orbit.....	103
3.3.5.3	On-Orbit Determination of Gain for LGS.....	104

3.3.5.4	On-Orbit Gain Transfer for MGS & HGS.....	106
3.3.5.5	Conversion From DN To Radiometric Units.....	107
3.4	PRACTICAL CONSIDERATIONS .....	109
3.4.1	Numerical Computation Considerations.....	109
3.4.2	Programming and Procedural Considerations.....	110
3.4.2.1	Quality Control .....	110
3.4.2.2	Exception Handling .....	110
3.4.3	Initialization.....	111
3.4.4	Validation.....	112
3.4.4.1	Pre-Launch Verification .....	112
3.4.4.2	On Orbit Validation .....	112
3.4.4.3	Long Term Monitoring .....	113
3.4.5	Striping and Mitigation Strategies .....	113
3.4.6	Sub-frame Offset for Imagery Bands .....	115
3.4.6.1	Hardware Case and Test Observations.....	115
3.4.6.2	Algorithm Overview .....	117
3.4.6.2.1	Calculating the Space View Offset.....	117
3.4.6.2.2	Calculating the Black Body Offset.....	117
3.4.6.2.3	Swapping the First/second Sub-frame Averages, Robust Substitution .....	117
3.4.6.2.4	Calibrating the Reflective Bands (I1, I2, I3).....	117
3.4.6.2.5	Calibrating the Emissive Bands (I4, I5) .....	118
3.4.6.2.6	Aggregation of IMG band samples.....	118
3.4.7	SDR Robust Algorithm Processes .....	119
3.4.7.1	Deviations from Optimal Calibration Conditions.....	119
3.4.7.2	Alternate data sources .....	121
3.4.8	Bright Pixel Identification.....	123
3.4.8.1	Estimating % Scattered Light .....	124
3.4.8.2	as an estimate of $\mathcal{E}_{true}$ .....	126
3.4.8.3	“Calculation Unreliable” Flag .....	126
3.4.8.4	Creation of Non-Saturated Scene.....	127
3.4.8.4.1	Saturated radiance.....	127
3.4.8.4.2	In-scan angular resolution and Aggregation.....	127
3.4.8.4.3	Bowtie and Edge of scan effects.....	127
3.4.8.4.4	Missing radiance .....	128
3.4.8.4.5	Scan & Granule limits .....	128
3.4.8.4.6	Scene edges .....	128
3.4.9	Dual Gain Anomaly Flagging .....	128
3.4.10	DNB Stray Light Flagging .....	129
3.4.11	Spike Noise Filter for Thermistor Data .....	134
4.	ASSUMPTIONS AND LIMITATIONS.....	136
4.1	ONBOARD PROCESSING .....	136
4.2	INPUT DATA .....	136
4.3	PRE-LAUNCH CALIBRATION .....	136

5. REFERENCES .....	138
5.1 VIIRS DOCUMENTS .....	138
5.2 NON-VIIRS DOCUMENTS .....	139
APPENDIX A: DESCRIPTION OF VIIRS OBC BB THERMISTOR TEMPERATURE PROCESSING .....	143
APPENDIX B: SOLAR DIFFUSER CALIBRATION MULTI-ORBIT AGGREGATION .	145
APPENDIX C: DESCRIPTION OF REFLECTIVE SOLAR BAND (RSB) CALIBRATION PROCESS IMPLEMENTED TO COMPENSATE FOR ANOMALOUS ON-ORBIT THROUGHPUT DEGRADATION.....	152
APPENDIX D: DESCRIPTION OF THEORETICAL BASIS FOR REFLECTIVE SOLAR BAND (RSB) AUTOMATED CALIBRATION (RSBAUTOCAL) ALGORITHM .....	154

## LIST OF FIGURES

	<u>Page</u>
Figure 1: VIIRS Spectral Bands; Visible and Near Infrared .....	14
Figure 2: VIIRS Spectral Bands; Shortwave Infrared .....	14
Figure 3: VIIRS Spectral Bands; Midwave Infrared .....	15
Figure 4: VIIRS Spectral Bands, Long-wave Infrared.....	15
Figure 5: Cut-out View of the VIIRS Opto-Mechanical Module.....	16
Figure 6: Diagram of VIIRS Scan Pattern. Parameters shown in this figure are from early design specs. The as-built values for Suomi-NPP VIIRS can be found in Cao et al., 2013b. ....	18
Figure 7: Timeline of Typical VIIRS Scan.....	18
Figure 8: VIIRS Optical Path .....	19
Figure 9: VIIRS RTA-HAM Synchronization throughout Scan.....	22
Figure 10: VIIRS Vis/NIR Detector Lay-out .....	23
Figure 11: VIIRS S/MWIR & LWIR Detector Layout.....	24
Figure 12: VIIRS Dual Gain ‘M’ Band Gain Switching .....	26
Figure 13: Simplified VIIRS DNB Block Diagram .....	27
Figure 14: VIIRS DNB CCD Layout.....	28
Figure 15: VIIRS Electronics Module Block Diagram .....	30
Figure 16: VIIRS Electronics Module Orientation .....	31
Figure 17: VIIRS ‘M’ and ‘I’ Band Data Representation.....	33
Figure 18: VIIRS DNB Gain Selection .....	34
Figure 19: Architecture of the VIIRS Radiometric Calibration Component .....	74
Figure 20: VIIRS Granule-by-Granule Near Real-Time Processing .....	75
Figure 21: Timing of SDSM collect.....	93
Figure 22: Changes to MODIS Terra SD reflectance trended over 1000 days.....	94
Figure 23: $dn$ as a function of EBBT for band M13 in the low gain mode .....	100
Figure 24: Simulated raw counts for 16 scans of dark earthview data for LGS, MGS and HGS .....	
Figure 25: Simulated DNB earth view scene. Data modeled from EVEREST. by 3000 km region crossing the terminator. ....	
Figure 26: Corresponding gain stages selected by DNB during normal operation. ....	
Figure 27: Transition region used to determine MGS/LGS & HGS/MGS gain ratio.....	106
Figure 28: Near Real-time DNB Processing.....	109
Figure 29: Response seen for dual gain anomaly. ....	128
Figure 30: Northern Hemisphere Stray Light Contamination.....	130
Figure 31: Southern Hemisphere Stray Light Contamination .....	130
Figure 32: a) Fitting of Earth view data to create stray light offset. Data are shown as dots and fits are shown as solid lines. Only data for detectors 1-6 are shown in the figure. b) Radiances corrected for stray light. ....	131
Figure 33: Flowchart of Stray Light Correction .....	132
Figure 34: Northern Hemisphere Stray Light Corrected Radiances .....	133
Figure 35: Southern Hemisphere Stray Light Corrected Radiances.....	134
Figure 36: Noise and spike filtering applied to a simulated thermistor measurement with 3 spikes. ....	135
Figure 37: VIIRS simplified generic passive analog telemetry circuit .....	144

Figure 38: Flow diagram of SD Multi-orbit history and aggregation..... 146

## LIST OF TABLES

	<u>Page</u>
Table 1: Dynamic Range for Reflective Bands .....	6
Table 2: Dynamic Range for Emissive Bands .....	6
Table 3: SNR for Reflective Bands.....	7
Table 4: Noise Requirements for Emissive Bands .....	8
Table 5: Absolute Radiometric Calibration Uncertainty of Spectral Radiance for Moderate Resolution Emissive Bands.....	8
Table 6: Radiometric Calibration Uncertainty for Imaging Emissive Bands.....	9
Table 7: Radiometric Calibration Uncertainty for Day-Night Band.....	9
Table 8: VIIRS Spectral Bands as Compared to Other Vis/IR Instruments .....	13
Table 9: Optical Train Components.....	20
Table 10: Key DNB Performance Requirements .....	27
Table 11: Fourth Order Calibration Coefficients .....	46
Table 12: Second Order & 3 <sup>rd</sup> Order Calibration Coefficients.....	48
Table 13: Alternative Second Order & 3 <sup>rd</sup> Order Calibration Coefficients.....	48
Table 14: Summary of TV Testing.....	57
Table 15: Relative change in Response per K observed in RC3.....	58
Table 16: Bands Included in the Three Primary VIIRS SDR's.....	71
Table 17: LUT Limits and Increments.....	79
Table 18: Space View Selection for Dual Gain Bands .....	82
Table 19: Conditions triggering quality flags and fill value.....	111
Table 20: Original Calibration Pixel Matching, Current Matching with Even Detectors Swapped.....	116
Table 21: Aggregation from Samples to Pixels .....	118
Table 22: Number of thermistors assigned to given temperature readings .....	120
Table 23: Parameters reported in the History File .....	147

## GLOSSARY OF ACRONYMS

ADC	Analog to Digital Converter
AOI	Angle of Incidence
ARR	Application Related Requirement
ASP	Analog Signal Processor
ATBD	Algorithm Theoretical Basis Document
ATLAS	Atmospheric Laboratory for Applications and Science
AVHRR	Advanced Very High Resolution Radiometer
BB	Blackbody
BCS	Blackbody Calibration Source
BIT	Built-In Test
BMI	Border Match Index
BRDF	Bi-directional Reflectance Distribution Function
BRF	Bi-directional Reflectance Function
Cal/Val	Calibration and Validation
CCA	Circuit Card Assembly
CDR	Critical Design Review
CCD	Charge Coupled Device
CCSDS	Consultative Committee for Space Data Systems
DC	Digital Count
DCR	DC Restore
DMSP	Defense Meteorological Satellite Program
<i>DN</i>	Digital Number (raw)
<i>dn</i>	Digital Number (raw less background)
DNB	Day-Night Band
DoD	Department of Defense
DPA	Data Processing Architecture
DPP	Digital Pre-Processor
DWSS	Defense Weather Satellite System
EBBT	Effective Blackbody Temperature
EDR	Environmental Data Record
EDU	Engineering Data Unit
EDD	Engineering Data Description
EOL	End Of Life
EOS	Earth Observing System
ETM+	Enhanced Thematic Mapper Plus
EV	Earth View
FPA	Focal Plane Assembly
FPIE	Focal Plane Interface Electronics
GCP	Ground Control Point
GIFOV	Ground Instantaneous Field of View
GVSLE	Gain Value Versus Scene Lunar Elevation
GVSSE	Gain Value Versus Scene Solar Elevation
HAM	Half Angle Mirror
HGA	High Gain Stage – A (for DNB)
HGB	High Gain Stage – B (for DNB)
HGS	High Gain Stage (for DNB)
HRD	High Rate Data

HSI	Horizontal Sampling Interval
HSR	Horizontal Spatial Resolution
IDPS	Interface Data Processing Segment
IP	Intermediate Product
IPO	Integrated Program Office
IR&D	Internal Research and Development
ITSS	Information Technology and Scientific Services
JPSS	Joint Polar Satellite System
LABB	Laboratory Ambient Blackbody
LGS	Low-Gain Stage (for DNB)
LLLS	Low Level Light Sensor
LUT	Lookup Table
LWIR	Long-Wave Infrared
MIB	Modulated Instrument Background
MGS	Mid-Gain Stage (for DNB)
mks	meter-kilogram-second
MODIS	Moderate Resolution Imaging Spectroradiometer
NASA	National Aeronautics and Space Administration
NEdT	Noise Equivalent Differential Temperature
NGST	Northrop Grumman Space Technology
NIST	National Institute of Standards and Technology
NOAA	National Oceanic and Atmospheric Administration
NPOESS	National Polar-orbiting Operational Environmental Satellite System
NPP	NPOESS Preparatory Project
NRT	Near Real-Time
OBC	Onboard Calibrator
OBCBB	Onboard Calibrator Blackbody
OLS	Operational Linescan System
PDR	Preliminary Design Review
POES	Polar Operational Environmental Satellite
PS	Performance Specification
QF	Quality Flag
RAM	Random Access Memory
RCI	Radiometric Correlation Index
RDR	Raw Data Record
RMS	Root Mean Square
ROIC	Read-Out Integrated Circuit
RSB	Reflective Solar Band
RSR	Relative Spectral Response
RTA	Rotating Telescope Assembly
RVS	Response Versus Scan
SBRS	Santa Barbara Remote Sensing
SBC	Single Board Computer
SCA	Sensor Chip Assembly
SCMA	Scattering Measurement Assembly
SD	Solar Diffuser
SDR	Sensor Data Record
SDS	Solar Diffuser Screen
SDSM	Solar Diffuser Stability Monitor
SeaWiFS	Sea-viewing Wide Field-of-View Sensor

SNR	Signal-to-Noise Ratio
SIS	Spherical Integrating Source
S/MWIR	Short/Mid-Wave Infrared
SNR	Signal-to-Noise Ratio
SOLSPEC	Solar Spectrum
SSPR	Shared System Performance Responsibility
SV	Space View
SVS	Space View Source
SWIR	Short-Wave Infrared
TDI	Time Delay and Integration
TEB	Thermal Emissive Bands
TIROS	Television Infrared Observation Satellite
TOA	Top of Atmosphere
TP	Technical Publication
TV	Thermal Vacuum
VIIRS	Visible/Infrared Imager/Radiometer Suite
Vis/NIR	Visible/Near Infrared
V&V	Verification and Validation

## GLOSSARY OF SYMBOLS

Symbol	Un-notated Indices <sup>1</sup>	Description	Units
A		Area of the detector for detectors without lenslets, or area of field stop for detectors with lenslets	m <sup>2</sup>
$a_0(T_{det})$	B, d, g, m	Temperature dependent zeroth order coefficient of the response function of a detector	Photoelectrons
$a_1(T_{det})$	B, d, g, m	Temperature dependent first order (linear) coefficient of the response function of a detector. This is the effective capacitance of the detector.	Photoelectrons/V
$a_2(T_{det})$	B, d, g, m	Temperature dependent second order coefficient of the response function of a detector	Photoelectrons/V <sup>2</sup>
agg(N <sub>F</sub> )		Along-scan aggregation zone for DNB	Unitless
B		Band number	Unitless
$b_0(T_{elec})$	B, d, m	Temperature dependent zeroth order coefficient of the response function of electronics.	Volt
$b_1(T_{elec})$	B, d, m	Temperature dependent first order (linear) coefficient of the response function of electronics. This is the inverse of the gain of the combined ADC & ASP circuits.	V/count
$b_2(T_{elec})$	B, d, m	Temperature dependent second order coefficient of the response function of electronics	V/count <sup>2</sup>

<sup>1</sup> In order to reduce complexity of the notation some indices are dropped in the equations in this document. The following abbreviations are used in this column. B=band number; d=detector index; g=gain state; m=mirror side; n=cross-track pixel number

$BRDF(\phi_h, \phi_v, \lambda, t)$	B, d	Bi-directional reflectance distribution function of solar diffuser as observed from the RTA, & expressed in terms of lab angles	1/sr
$BRDF'(\phi_h, \phi_v, \lambda, t)$		Bi-directional reflectance distribution function of the SD as observed from the SDSM, & expressed in terms of lab angles	1/sr
c		Speed of light	$\mu\text{m/s}$
$C_0$	B, d, g, m	0 order coefficient of the radiance response function	$W/(m^2\mu\text{m sr})$
$C_1(T_{\text{det}}, T_{\text{elec}})$	B, d, g, m	Temperature dependent first order (linear) coefficient of the response function for radiance	$W/(m^2\mu\text{m sr cnts})$
$C_2(T_{\text{det}}, T_{\text{elec}})$	B, d, g, m	Temperature dependent second order coefficient of the response function for radiance	$W/(m^2\mu\text{m sr cnts}^2)$
$c_i[\text{agg}(N_F), N_P, N_G]$		Pre-determined DNB calibration coefficients, dependent on $N_F$ , $N_P$ , and $N_G$ .	$W/(m^2\mu\text{m sr cnts}^i)$
$C'_j(T_{\text{det}}, T_{\text{elec}})$	B, d, g, m	Temperature dependent jth order coefficient of the response function after calibration update	$W/(m^2\mu\text{m sr cnts}^j)$
$\Delta C_j$	B, d, g, m	Adjustment to coefficient of the response function	$W/(m^2\mu\text{m sr cnts}^j)$
$d_j(T_{\text{det}}, T_{\text{elec}})$	B, d, g, m	Temperature dependent jth order coefficient of the response function for reflectance	$1/\text{counts}^j$
$d_{se}(t)$		Distance from sun to earth at time $t$	Meter
$\overline{d_{se}}$		Distance from sun to earth averaged over a year	Meter
DC	B	SDSM total counts	Counts
$DC_{\text{offset}}$	B	SDSM counts offset level	Counts

$DC_{sd}$	B	SDSM total counts when viewing the solar diffuser	Counts
$DC_{sun}$	B	SDSM total counts when viewing the sun	Counts
dc(t)	B	SDSM differential counts at time $t$	Counts
$dc_{sd}(t)$	B	SDSM differential counts when viewing the solar diffuser with offset level subtracted at time $t$	Counts
$dc_{sun}(t)$	B	SDSM differential counts when viewing the sun with offset level subtracted at time $t$	Counts
DN	B,d,g,m, n	Total detector counts	Counts
DN <sub>DNB</sub>		Total DNB detector counts	Counts
DN <sub>SV_DNB</sub> [ $N_F, N_P, N_G, m$ ]		DNB space view offset LUT, as a function of $N_F, N_P, N_G$ , and $m$ .	Counts
dn	B, d, g, m, n	Differential detector counts with space view subtracted	Counts
dn <sub>DNB</sub>		Differential DNB detector counts with space view subtracted	Counts
dn <sub>ev</sub>	B, d, g, m, n	Differential detector earth view counts with space view subtracted	Counts
dn <sub>sd</sub> (t)	B, d, g, m, n	Differential detector counts at solar diffuser with space view subtracted	Counts
dn <sub>bcs</sub>	B, d, g, m, n	Differential detector counts observing BCS with space view subtracted	Counts
dn <sub>lab</sub>	B, d, g, m, n	Differential detector counts observing LABB with space view subtracted	Counts
dn <sub>obc</sub> (t)	B, d, g, m, n	Differential detector counts at OBCBB with space view subtracted at time $t$	Counts

$dn_{obc}(n,m)$	B, d, g, m, n	Differential detector counts at OBCBB with space view subtracted for frame $m$ of scan $n$ of an acquisition	Counts
$\overline{dn}_{obc}(t_n)$	B, d, g, m	Differential detector counts at OBCBB averaged over the acquisition at time $t_n$	Counts
$\overline{dn}_{sd}(t_n)$	B, d, g, m	Differential detector counts at solar diffuser averaged over the acquisition at time $t_n$	Counts
$\overrightarrow{dn}$	B, d, g, m	Set of all samples within a cal acquisition period	Counts
$\overline{DN}_{sv}$	B, d, g, m	Total detector counts per frame averaged over space view	Counts
$E(\lambda)$		Spectral irradiance	W/(m <sup>2</sup> μm)
$E_{inc}(\theta_{inc}, \phi_{inc}, \lambda)$		Spectral irradiance incident upon the solar diffuser	W/(m <sup>2</sup> μm)
$E_{bkg}(\lambda, \theta)$	n	Detected spectral irradiance at the field stop due to self-emissive background when scan angle is $\theta$	W/(m <sup>2</sup> μm)
$E_{det}(\lambda, \theta)$	n	Detected spectral irradiance on the field stop when scan angle is $\theta$	W/(m <sup>2</sup> μm)
$E_{sun}(\lambda, t), E_{sun}(\lambda, d_{se})$		Irradiance from the sun upon a surface with normal pointing toward the sun.	W/(m <sup>2</sup> μm)
$E_{sdsm_{sd}}(\phi_h, \phi_v, \lambda, d_{se})$		Spectral radiance at the SDSM when it is pointing at the solar diffuser	W/(m <sup>2</sup> μm)
$E_{sdsm_{sun}}(\lambda, d_{se})$		Spectral radiance at the SDSM when it is pointing at the sun	W/(m <sup>2</sup> μm)
F	B, d, g, m	Factor for update of the radiance coefficients	Unitless
F <sub>det</sub>	B, d	Fraction of detector illuminated by imaged aperture stop	Unitless

$F_{cav}$	B	Fraction of the reflectance off the OBCBB originating from cavity	Unitless
$F_{sh}$	B	Fraction of the reflectance off the OBCBB from shield	Unitless
$F_{tele}$	B	Fraction of the reflectance off the OBCBB originating from telescope	Unitless
G	B	Gain converting detector electron counts to radiance	W/(m <sup>2</sup> μm sr) /photoelectron
$G_{sdsms}(t)$	B	Gain converting SDSM counts to spectral irradiance	W/(m <sup>2</sup> μm sr cnt)
h		Planck Constant	J s/photon
h(t)	B	Time dependent ratio of $dc_{sun}(t)$ and $dc_{sd}(t)$ corrected for screen modulation, used to trend $H(t)$ .	Unitless
$H(t)$	B	Time dependent scale factor of BRDF of the solar diffuser	Unitless
I		Electric Current	A
$I_s$		Saturation current for a semiconductor	A
k		Boltzmann Constant	J/K
$L_{det}(\theta, \lambda)$	d	Detected spectral radiance at field stop for angle $\theta$	W/(m <sup>2</sup> μm sr)
$\overline{L_{det}(\theta, B)}$ , $\overline{L_{det}(DN)}$ , $\overline{L_{det}(dn)}$	B, d, n, m	Band-averaged detected spectral radiance at field stop for angle $\theta$ , or as a function of $DN$ or $dn$	W/(m <sup>2</sup> μm sr)
$\overline{\Delta L_{det}(\theta, B)}$	d, m	Differential band-averaged detected spectral radiance at field stop for angle $\theta$ relative to space view	W/(m <sup>2</sup> μm sr)
$\overline{L_{det\_bkg}(\theta, B)}$	d, m	Band-averaged detected spectral radiance at field stop due to self-emissive background for angle $\theta$ relative to space view	W/(m <sup>2</sup> μm sr)

$\overline{\Delta L_{det\_bkg}}(\theta, B)$	d, m	Differential band-averaged detected spectral radiance due to self-emissive background for angle $\theta$	W/(m <sup>2</sup> μm sr)
$L_{ap}(\theta, \lambda)$	d	Spectral radiance at the aperture at angle $\theta$	W/(m <sup>2</sup> μm sr)
$\overline{L_{ap}}(\theta, B)$	d	Band-averaged spectral radiance at the aperture for scan angle $\theta$	W/(m <sup>2</sup> μm sr)
$\overline{L_{det\_sd}}(\phi_h, \phi_v, B)$	d, m	Band-averaged detected spectral radiance at field stop when it is pointing at the solar diffuser	W/(m <sup>2</sup> μm sr)
$\overline{L_{nsd}}(\phi_h, \phi_v, B)$	d	Band-averaged normalized solar diffuser spectral radiance	W/(m <sup>2</sup> μm sr)
$L(T, \lambda)$		Blackbody spectral radiance according to Planck's function	W/(m <sup>2</sup> μm sr)
$\overline{L_{DNB}}$		Band-averaged spectral radiance at the aperture for Day Night Band	W/(m <sup>2</sup> μm sr)
$L_{min}$	B	Minimum spectral radiance required to meet spec	W/(m <sup>2</sup> μm sr)
$L_{max}$	B	Maximum spectral radiance required to meet spec	W/(m <sup>2</sup> μm sr)
$L_{obc\_rfl}(T_{sh}, T_{cav}, T_{tele}, \lambda)$	B, d, n	Spectral radiance emissive background from shield, cavity and telescope, and reflected off the OCB BB	W/(m <sup>2</sup> μm sr)
$L_{rfl}(\theta_{rfl}, \phi_{rfl}, \lambda)$	B, d, n	Spectral radiance reflected from the solar diffuser	W/(m <sup>2</sup> μm sr)
$N_{acq}$		Number of scans over which solar diffuser is observed	Unitless
$N_{cal}$	B	Number of frames per scan while observing OCB BB	Unitless
$N_e(DN), N_e(S)$		Number of photoelectrons for a sample as a function of digital counts or signal	Photoelectrons
$N_F$		Along-scan frame number	Unitless

$N_{\text{gain}}$	B	Number of gain states for a band: 2 for dual gain bands, otherwise 1	Unitless
$N_G$		DNB Gain stage	Unitless
$N_H$		HAM side index	Unitless
$N_{\text{op}}$	B	Number of optical elements from aperture to detectors	Unitless
$N_P$		Along-track pixel	Unitless
$N_{\text{ray}}$		Number of rays (e.g. number of rays traced in a ray-tracing program)	Unitless
$N_{\text{SDfrm}}$	B	Number of frames per scan over which the solar diffuser calibration counts are recorded, excluding frames rejected from average due to poor or missing quality	Unitless
$N_{\text{SVfrm}}$	B	Number of frames per scan over which the space view calibration counts are recorded, excluding frames rejected from average due to poor or missing quality	Unitless
$N_{\text{sd}}$		Number of scans over which SDSM is observed per acquisition	Unitless
$N_{\text{src}(i)}$		Number of emissive sources producing self-emission that enters the optical path through optical element i	Unitless
$QE(\lambda)$	B	Quantum efficiency converting photons to photoelectrons	Photoelectron /photon
$QE_{\text{sdsd}}(\lambda)$	B	Quantum efficiency of SDSM converting photons to photoelectrons	Photoelectron /photon
$RSR(\lambda)$		Relative spectral response, which combines spectral response due to transmittance and detector response normalized to have a peak of 1.0	Unitless

$RVS(\theta, B)$	d, m	Response Versus Scan function at scan angle $\theta$ for band $B$	Unitless
$RVS[N_F, N_P, N_H]$		Pre-determined Response Versus Scan for DNB, as a function of $N_F$ , $N_P$ , and $N_H$ .	Unitless
$s_{inst}$		Vector describing orientation of instrument with respect to the spacecraft	Unitless
$s_{sd}$		Vector describing orientation of solar diffuser with respect to the spacecraft	Unitless
$SNR_{acq}$	B,d,m	Calibration Signal to Noise Ratio over entire acquisition	Unitless
$SNR_{scan}$	B,d,m	Calibration Signal to Noise Ratio over one scan	Unitless
$t$		Time	Seconds
$t_i$		Time of the start solar diffuser illumination in SDSM data acquisition $i$	Seconds
$t'_i$		Time of the sun view in SDSM data acquisition $i$	Seconds
$t_n$		Time of scan $n$ of an acquisition	Seconds
$t_{i,n}$	B	Time of SDSM sample $n$ of acquisition $i$ for SD view	Seconds
$t'_{i,n}$	B	Time of SDSM sample $n$ of acquisition $i$ for sun view	Seconds
$\Delta t$	B	Integration time for sample	Seconds
$\Delta t_{frame}$	B	Time between frames or samples for detectors	Seconds
$\Delta t_{scan}$		Time between scans	Seconds
$T$		Temperature	K
$T_{cav}$		Temperature of cavity contributing to reflection off OBCBB	K

$T_{det}$		Temperature of FPA detectors	K
$T_{elec}$		Temperature of electronics module	K
$T_{labb}$		Temperature of LABB source during pre-launch characterization	K
$T_{bcs}$		Temperature of BCS source during pre-launch characterization	K
$T_{ham}$		Temperature of HAM	K
$T_{min}$		Minimum brightness temperature or EBBT as defined by sensor requirements document	K
$T_{max}$		Maximum brightness temperature or EBBT as defined by sensor requirements document	K
$T_{rta}$		Temperature of RTA	K
$T_{shld}$		Temperature of shield contributing to reflection off OBCBB	K
$T_{tele}$		Temperature of telescope contributing to reflection off OBCBB	K
$T_{obc}$		Temperature of OBCBB	K
$T_i$		Temperature of optical element i	K
$T_{i,j}$		Temperature of emissive source j entering through optical element i	K
$T_{SD/inst}$		Transformation matrix from instrument coordinate system to Solar diffuser coordinate system	K
V		Voltage	V
$V(E_{det}, T_{det}), V(DN)$	B,d,g,m,n	Analog voltage, signal output of detector	V
$V_{elec}(DN)$	B,d,g,m,n	Analog signal of detector with DC restore	V

$V_{dcr}$	B,d	Analog DC restore voltage signal	V
$W(dn_{obc}(n,m))$	B,d,g,m,n	Weight used for band M13 low gain calibration to equalize distribution over counts	Unitless
$\beta$		Efficiency of a semiconductor	Unitless
$\varepsilon$		Emissivity	Unitless
$\varepsilon_{obc}(\lambda)$		Spectral emissivity of the OBCBB	Unitless
$\varepsilon_{i,j}(\lambda)$		Spectral emissivity of emissive source j entering through optical element i	Unitless
$\theta$		Crosstrack scan angle	Radians
$\theta_{inc}$		Incidence angle onto solar diffuser relative to solar diffuser surface normal	Radians
$\theta_{rfl}$		Reflected angle off solar diffuser relative to normal	Radians
$\theta_{obc}$		Scan angle of OBCBB	Radians
$\theta_{sd}$		Scan angle at solar diffuser	Radians
$\theta_{bcs}$		Scan angle of BCS during pre-launch calibration	Radians
$\theta_{labb}$		Scan angle of LABB during pre-launch calibration	Radians
$\theta_{sv}$		Scan angle at space view	Radians
$\theta_{ev}$		Scan angle at earth view	Radians
$\theta_{sun\_inst}$		Solar angle measured off the z-axis	Radians
$\theta_{sun\_earth}$		Solar incidence angle of the sun on the earth	Radians
$\lambda$		Wavelength	$\mu\text{m}$
$\rho$		Reflectance	Unitless

$\rho_j(\lambda)$		Spectral reflectance/transmittance of the jth optical element	Unitless
$\rho_{aft}(\lambda)$		Spectral reflectance/transmittance of aft optics past the HAM	Unitless
$\rho_{fix}(\lambda)$		Spectral reflectance/transmittance of all optics except for RVS	Unitless
$\rho_{sys}(\theta, \lambda)$		Spectral reflectance/transmittance of all optics including RVS	Unitless
$\rho_{ham}(\lambda)$		Spectral reflectance of HAM	Unitless
$\rho_{rta}(\lambda)$		Spectral reflectance of RTA	Unitless
$\rho_{ev}(\theta_{ev}, \lambda)$		Earth view spectral reflectance at aperture	Unitless
$\overline{\rho_{ev}}(\theta_{ev}, B)$		Band-averaged earth view spectral reflectance	Unitless
$\overline{\rho_{sd}}(B)$		Band-averaged solar diffuser spectral reflectance detected	Unitless
$\overline{\rho_{sdeff}}(\phi_h, \phi_v, B_{sdsm})$		Band-averaged effective reflectance of solar diffuser screen	Unitless
$\tau_{sds}(\phi_h, \phi_v, \lambda, d)$		Spectral transmittance of solar diffuser screen	Unitless
$\tau_{sdsm}(\phi_{h\_sdsm}, \phi_{v\_sdsm}, \lambda)$		Spectral transmittance SDSM when viewing the sun	Unitless
$\phi_v(t)$		Vertical incidence angle of solar illumination upon the SD in laboratory coordinates	Radians
$\phi_{v\_sdsm}(t)$		Vertical incidence angle of solar illumination upon SDSM screen in SDSM reference frame	Radians
$\phi_h(t)$		Horizontal incidence angle of solar illumination upon the SD in laboratory coordinates	Radians
$\phi_{h\_sdsm}(t)$		Horizontal incidence angle of solar illumination upon SDSM screen in SDSM reference frame	Radians

$\phi_{inc}$		Azimuthal incidence angle onto solar diffuser relative to x-axis	Radians
$\phi_{rfl}$		Azimuthal reflectance angle onto solar diffuser relative to x-axis	Radians
$\phi_{sun\_inst}$		Solar angle projected on the x-y plane measured with respect to the x-axis in instrument coordinates	Radians
$\Phi_{sun}(\lambda, t)$		Spectral output power of the sun	W/ $\mu$ m
$\Omega_{sdsm}$		Solid angle of SDSM	Sr
$\Omega_{stop}$	B, d	Solid angle of aperture stop as seen from the field stop	Sr
$\Omega_{fs @ det}$	B, d	Solid angle of field stop as seen from the detector	Sr
$\Omega_{i,j}$	B, d	Solid angle as seen from the field stop of emissive source j entering through optical element i	Sr

## ABSTRACT

The Visible Infrared Imaging Radiometer Suite (VIIRS) radiometric calibration algorithm is implemented as part of the VIIRS raw data processing software in order to convert raw digital numbers (*DN*) from Earth View (EV) observations into various Sensor Data Record (SDR) radiance products. These products include calibrated top of atmosphere (TOA) radiance, TOA reflectance, and TOA brightness temperature. As part of this algorithm *DNs* from the On-Board Calibrator Blackbody (OBCBB), Space View (SV), and Solar Diffuser (SD) view are processed in order to adjust *DNs* for background signal levels and to update reflective band and emissive band calibration coefficients.

The VIIRS Environmental Data Record (EDR) algorithms require radiometrically calibrated, earth-located, spectrally defined data inputs from one or more VIIRS spectral bands. The radiance products from the SDR's provide these inputs. The SDR structures draw heavily upon the heritage of similar Level 1 products. This Algorithm Theoretical Basis Document (ATBD) shall describe the earth-location as spectral definition components of the SDR and SDR attributes as well as the radiometric calibration of the SDR products.

Much of the algorithm presented in this document is based on a first principles derivation that results in a rigorous solution that may be simplified through judicious specification of the algorithm input parameters. Design features of VIIRS that are different from its heritage instruments are accommodated. These VIIRS unique features include dual gain radiometric bands, the Day-Night Band (DNB), and the along-scan aggregation of sub-pixel detectors to limit pixel growth from nadir to end of scan.

The VIIRS algorithm applies calibration coefficients determined during pre-launch testing and updated operationally through calibration and validation (cal/val) analysis to transfer the ground calibration to on-orbit data. Provisions are included to incorporate adjustments into the radiometric calibration to account for instrument temperature, changes in incoming solar flux, and to correct for instrument degradation.

# 1. INTRODUCTION

The Visible Infrared Imaging Radiometer Suite (VIIRS) is designed to be carried aboard a sun-synchronous polar orbiting satellite – originally on each platform of the National Polar-orbiting Operational Environmental Satellite System (NPOESS). NPOESS was planned as a joint mission among the Department of Defense (DoD), the National Oceanic and Atmospheric Administration (NOAA), and the National Aeronautics and Space Administration (NASA). The VIIRS is a single visible/infrared instrument capable of satisfying the needs of all three communities, as well as the general research community. As such, the VIIRS has 2 key attributes: high spatial resolution with controlled growth off nadir, and a large number of spectral bands to satisfy the requirements for generating high quality operational and scientific products.

In February 2010, the Director of the Office of Science and Technology Policy (OSTP), as part of the Executive Office of the President, announced that NOAA and DOD will no longer jointly procure the NPOESS satellite system; instead, each agency would plan and acquire its own satellite system. NOAA is to be responsible for the afternoon orbit and the observations planned for the first and third NPOESS satellites, and DOD is to be responsible for the morning orbit and the observations planned for the second and fourth NPOESS satellites. The Joint Polar Satellite System (JPSS) is the name for the restructured civilian portion of NPOESS, where the word “joint” refers to the collaboration between NASA and NOAA. The Defense Weather Satellite System (DWSS) is the name given for the restructured military portion of NPOESS. Both JPSS and DWSS plan to include VIIRS on all of their respective satellites.

JPSS and DWSS will provide an enduring capability to measure, on a global basis, atmospheric, land, and ocean environmental parameters. The systems provide timely and accurate weather and environmental data to weather forecasters, military commanders, civilian leaders, and the scientific community. Both JPSS and DWSS satellites operate in near circular, sun-synchronous orbits. The NPOESS Preparatory Project (NPP) satellite will be launched in 2011, and will carry some of the instruments originally planned for NPOESS, including the VIIRS, whose radiometric calibration algorithm is the subject of this document. The JPSS and DWSS satellites will carry sensors operating in different frequency regions of the electromagnetic spectrum and will have nominal ascending node equatorial crossings at 1330 and 1730 local sun time. In the NPOESS specification there were approximately five dozen remote sensing products, each of which is referred to as an Environmental Data Record (EDR), to be retrieved from the radiometric data collected by NPOESS and among them six are considered to be “key” parameters. VIIRS provides 23 of these EDRs including two (imagery and sea surface temperature) that are key parameters.

## 1.1 HISTORICAL PERSPECTIVE

VIIRS can be considered as a convergence of three existing instruments; the Operational Linescan System (OLS), the Advanced Very High Resolution Radiometer

(AVHRR), and the Moderate Resolution Imaging Spectroradiometer (MODIS). The OLS and AVHRR have seen extensive operational use. MODIS on the *Terra* satellite has been operational since 1999 and MODIS on the *Aqua* satellite has been operational since 2002.

The OLS is the operational visible/infrared scanner for the DoD. Its unique strengths are controlled growth in spatial resolution through use of segmented detectors and rotation of the ground instantaneous field of view (GIFOV) and the existence of a low-level light sensor (LLLS) capable of detecting visible radiation at night. OLS has primarily served as a data source for manual analysis of imagery. The VIIRS DNB has similar capabilities and functions, and unlike OLS, can be accurately calibrated. The AVHRR is the operational visible/infrared instrument flown on the NOAA Television Infrared Observation Satellite (TIROS-N) series of satellites (Planet, 1988). Its unique strengths are low operational and production cost and the presence of five spectral channels that can be used in a wide number of combinations to produce operational and research products. In December 1999, the NASA launched the Earth Observing System (EOS) morning satellite, *Terra*, which includes a MODIS. In May 2002 a second MODIS was put into orbit onboard the EOS *Aqua* spacecraft. The third MODIS on the EOS *Aura* satellite was launched on 2004 July 15. The MODIS possesses an unprecedented array of thirty-six spectral bands at resolutions ranging from 250 m to 1 km at nadir, allowing for a wide range of satellite-based environmental measurements.

## 1.2 PURPOSE OF DOCUMENT

The main purpose of this ATBD is to provide guidelines for the production of calibrated top of atmosphere (TOA) radiances, calibrated TOA reflectances, and calibrated TOA brightness temperatures from VIIRS Raw Data Records (RDR). These calibrated data are the primary Sensor Data Record (SDR) products of the VIIRS. This document describes the required inputs, the theoretical and mathematical description of the retrieval algorithm, practical considerations for implementation, and the assumptions and limitations associated with the products.

## 1.3 SCOPE OF DOCUMENT

This document covers the algorithm theoretical basis for the operational retrieval of calibrated TOA radiances, calibrated TOA reflectances, and calibrated TOA brightness temperatures. Any derived products beyond these three SDR's are not discussed beyond brief mention. Information concerning the pre-flight calibration of VIIRS and the transfer of this calibration to on-orbit data is also included. The geolocation part of the VIIRS RDR to SDR conversion process is discussed in SDRL 147-2, which is the "*VIIRS Geolocation ATBD*" [D43776 (Y3258)].

This version of the SDRL 148-2 "*VIIRS Radiometric Calibration ATBD*" [D43777 (Y3261)] includes the radiometric calibration that is needed for the near real-time (NRT) operational conversion of raw Earth View (EV) digital numbers (DN) to calibrated TOA radiances, reflectances, and brightness temperatures and the algorithm for processing

of the once per orbit solar observations that is required to update the scaling factors that are used in the scan-by-scan reflective band radiometric calibration. The processing required to derive and update calibration coefficients and correction factors based on the results obtained during the offline analysis of on-orbit calibration mode data is summarized in Section [3.1.2](#).

This ATBD is intended to be a stand-alone document. It is organized to include introductory information in Section 1 followed by an overview section (i.e. Section 2). Section 2 includes material related to objectives, which includes a summary of requirements and a description of data products. An overview of the VIIRS instrument including its design, operations, and data are provided as well as an overview of the radiometric calibration timeline. Section 3 contains the essence of this document—a complete description of the operational radiometric calibration algorithm. Consideration is given to the overall structure, the required inputs, a theoretical description of the products, and practical implementation issues. Also included are sections to include error and uncertainty analyses when these become available and discussions about practical considerations related to the algorithm. Section 4 identifies the assumptions and limitations of the radiometric calibration algorithm and Section 5 contains a listing of document references that are cited throughout this document.

An Operational Algorithm Document (OAD) that accompanies the implementation of the radiometric calibration algorithm is based on this ATBD and various VIIRS Radiometric Calibration Component software design documents.

## 1.4 REVISIONS

Raytheon ITSS delivered the ATBD as document Y3261, Version 5, revision 4 in September 2004. At that time NG took control of the document and in February 2007 it was incorporated into the NG document control system as D43777. All changes made since then are recorded in the Revision Change Record starting on page ii at the beginning of this document. Changes made before that time are recorded in this section.

Version 5, revision 4 was prepared by the NPOESS Shared System Performance Responsibility (SSPR) contractor. It is dated September 2004. It incorporates changes made by Steve Mills and Stephanie Weiss of NGST after reviewing Version 5, revision 3. This includes changes to formatting and response to issues identified at the Algorithm Technical Interchange Meeting, and at the Algorithm Review Board.

Version 5, revision 3 is a post-VIIRS Critical Design Review (CDR) deliverable that was prepared by the NPOESS Shared System Performance Responsibility (SSPR) contractor. It is dated August 2004. The algorithm modifications documented herein were developed during a period of VIIRS algorithm continuance prior to delivery to the NPOESS Interface Data Processing Segment (IDPS) for science to operational conversion. These algorithm modifications were prescribed in “*VIIRS Radiometric Calibration Equations*” [NGST Doc. D36966]. One of the purposes of this primary

reference document was to “... *provide a single source document to revise the VIIRS Radiometric Calibration ATBD*” and much of its text has been copied or paraphrased in this ATBD. Specific modifications for Version 5, revision 3 include:

Addition of a Glossary of Symbols

Enhanced description of VIIRS design, operation, and data

Enhanced description of pre-launch instrument testing and the creation and maintenance of calibration lookup tables (LUTs)

Enhanced description of algorithm inputs and data products

Enhanced description of RDR to SDR processing

Updates to theoretical basis to include the VIIRS radiometric calibration equations document in NGST Doc. D36966

Updates to the theoretical basis for DNB calibration

Version 5 was the third working version of this document and was a VIIRS CDR deliverable. Revision 2 incorporated corrections, clarifications, and enhancements that were motivated by comments from the CDR. Version 5, Revision 2 is dated May 2002. Version 5, Revision 2 was prepared by Bill Byerly of Raytheon Information Technology and Scientific Services (ITSS) from inputs provided by Tim Dorman and Shawn W. Miller of ITSS and J. Ed Clement, Jack Engel, Richard Julian, James B. Young, and Joe A. Walker of Raytheon Santa Barbara Remote Sensing (SBRS).

The previous version number (version 4) was issued in May 2001 to address comments received from the VIIRS Preliminary Design Review (PDR). Version 3 was the first version of this ATBD. Its version number was chosen to match the delivery of the previously existing VIIRS EDR ATBDs, which had undergone two previous version releases. Shawn W. Miller and Douglas V. Hoyt authored the Version 3 ATBD (then called “*VIIRS RDR to SDR Conversion ATBD*”).

## 2. OVERVIEW

As an overview to the algorithms description this section provides the objectives of radiometric calibration, a calibration oriented overview of the VIIRS instrument and its data and operations, and the mission timeline for radiometric calibration.

### 2.1 OBJECTIVES OF RADIOMETRIC CALIBRATION

Each of the VIIRS SDR products described in this document is necessary inputs to one or more of the VIIRS EDR algorithms. All VIIRS EDR algorithms use these data either directly or indirectly. These SDR products form the link between instrument measurements reported as digital counts and the collected photons at the instrument's aperture. Collected photons relate to radiance fields at the top of the atmosphere, which in turn are related via the EDR algorithms to surface and/or atmospheric properties.

#### 2.1.1 Requirements Summary

In terms of radiometric calibration VIIRS has specific requirements in the areas of dynamic range, signal-to-noise ratio (SNR), and radiometric accuracy [PS154640-101D]. In general these requirements are specified separately for reflective solar bands, thermal emissive bands, and the DNB.

In order to have radiances that are within the required dynamic ranges for the various VIIRS EDRs (and in most cases to avoid saturation while viewing earth), VIIRS is required to have the dynamic range as specified in [Table 1](#) and [Table 2](#). For reflective bands with multiple gain states, the gain switching (ref. section [2.2.2.3.4](#)) will occur at the radiance levels specified in [Table 1](#) within the tolerance of +10% and -0%. For emissive band with multiple gain states, M13, the gain switching will occur at the brightness temperature specified in [Table 2](#) with a tolerance of +0.3K and -0.0K.

The dynamic range of the panchromatic DNB is  $3.0E-9 \text{ Watt cm}^{-2} \text{ sr}^{-1}$  to at least  $2.0E-2 \text{ Watt cm}^{-2} \text{ sr}^{-1}$ .

**Table 1: Dynamic Range for Reflective Bands**

		Single Gain		Dual Gain			
				High Gain		Low Gain	
Band	$\lambda_C$ (nm)	$L_{min}$	$L_{max}$	$L_{min}$	$L_{max}$	$L_{min}$	$L_{max}$
M1	412	-	-	30	135	135	615
M2	445	-	-	26	127	127	687
M3	488	-	-	22	107	107	702
M4	555	-	-	12	78	78	667
M5	672	-	-	8.6	59	59	651
M6	746	5.3	41.0	-	-	-	-
M7	865	-	-	3.4	29	29	349
M8	1240	3.5	164.9	-	-	-	-
M9	1378	0.6	77.1	-	-	-	-
M10	1610	1.2	71.2	-	-	-	-
M11	2250	0.12	31.8	-	-	-	-
I1	640	5	718	-	-	-	-
I2	865	10.3	349	-	-	-	-
I3	1610	1.2	72.5	-	-	-	-
$L_{min}$ = Minimum spectral radiance in units of $W\ m^{-2}\ sr^{-1}\ \mu m^{-1}$							
$L_{max}$ = Maximum spectral radiance in units of $W\ m^{-2}\ sr^{-1}\ \mu m^{-1}$							

**Table 2: Dynamic Range for Emissive Bands**

		Single Gain		Dual Gain			
				High Gain		Low Gain	
band	$\lambda_C$ (nm)	$T_{min}$	$T_{max}$	$T_{min}$	$T_{max}$	$T_{min}$	$T_{max}$
M12	3700	230	353	-	-	-	-
M13	4050	-	-	230	343	343	634
M14	8550	190	336	-	-	-	-
M15	10763	190	343	-	-	-	-
M16	12013	190	340	-	-	-	-
I4	3740	210	353	-	-	-	-
I5	11450	190	340	-	-	-	-

$T_{min}$ = Minimum brightness temperature in K
$T_{max}$ = Maximum brightness temperature in K

In order for VIIRS data to be useful in EDR retrieval it is imperative that the data have noise. The signal-to-noise ratio (SNR) of VIIRS is required to be greater than the values specified in [Table 3](#) for the reflective bands, and the Noise Equivalent  $\Delta T$  (NE $\Delta T$ ) must be less than specified in [Table 4](#) for the emissive bands. These specifications are given at “typical” radiance levels ( $L_{typ}$  and  $T_{typ}$ ), which in fact may not actually represent what is truly typical.

**Table 3: SNR for Reflective Bands**

		Single Gain SNR		Dual Gain SNR			
				High Gain		Low Gain	
Band	$\lambda_C$ (nm)	$L_{typ}$	SNR	$L_{typ}$	SNR	$L_{typ}$	SNR
M1	412	-	-	44.9	352	155	316
M2	445	-	-	40	380	146	409
M3	488	-	-	32	416	123	414
M4	555	-	-	21	362	90	315
M5	672	-	-	10	242	68	360
M6	746	9.6	199	-	-	-	-
M7	865	-	-	6.4	215	33.4	340
M8	1240	5.4	74	-	-	-	-
M9	1378	6	83	-	-	-	-
M10	1610	7.3	342	-	-	-	-
M11	2250	0.12	10	-	-	-	-
I1	640	22	119	-	-	-	-
I2	865	25	150	-	-	-	-
I3	1610	7.3	6	-	-	-	-

$L_{typ}$  = Typical spectral radiance in units of  $W\ m^{-2}\ sr^{-1}\ \mu m^{-1}$

**Table 4: Noise Requirements for Emissive Bands**

		Single Gain		Dual Gain			
				High Gain		Low Gain	
Band	$\lambda_c$ (nm)	$T_{typ}$	NEdT	$T_{typ}$	NEdT	$T_{typ}$	NEdT
M12	3700	270	0.396	-	-	-	-
M13	4050	-	-	300	0.107	380	0.423
M14	8550	270	0.091	-	-	-	-
M15	10763	300	0.070	-	-	-	-
M16	12013	300	0.072	-	-	-	-
I4	3740	270	2.500	-	-	-	-
I5	11450	210	1.500	-	-	-	-

As mentioned earlier, radiometric accuracy is critical for EDR retrieval. Thus, VIIRS must achieve a set of very stringent radiometric requirements. According to the VIIRS Sensor Specification, for the reflective bands, the calibration uncertainty for spectral reflectance given a scene with typical radiance shall be less than 2%. For the bands specified as moderate resolution emissive, the calibration uncertainty of spectral radiance shall be as specified in [Table 6](#). Given a uniform scene of brightness temperature of 267 K, the calibration uncertainty of spectral radiance for imaging emissive bands shall be as specified in [Table 6](#).

**Table 5: Absolute Radiometric Calibration Uncertainty of Spectral Radiance for Moderate Resolution Emissive Bands**

Band	Scene Temperature (K)				
	190	230	270	310	340
M12	N/A	7.0%	0.7%	0.7%	0.7%
M13	N/A	5.7%	0.7%	0.7%	0.7%
M14	12.3%	2.4%	0.6%	0.4%	0.5%
M15	2.1%	0.6%	0.4%	0.4%	0.4%
M16	1.6%	0.6%	0.4%	0.4%	0.4%

**Table 6: Radiometric Calibration Uncertainty for Imaging Emissive Bands**

Band	Calibration Uncertainty
I4	5.0%
I5	2.5%

For the DNB the radiometric calibration uncertainty of the effective, in-band radiance for a uniform scene shall be as specified in [Table 7](#). The calibration uncertainty depends on the gain state.

**Table 7: Radiometric Calibration Uncertainty for Day-Night Band**

Gain State	Calibration Uncertainty	Radiance level at which calibration uncertainty is to be evaluated
Low	5%	One-half of maximum radiance for low gain state
	10%	Minimum radiance for low gain state
Medium	10%	Maximum radiance for medium gain state
	30%	Minimum radiance for medium gain state
High	30%	Maximum radiance for high gain state
	100%	Minimum radiance for high gain state

## 2.1.2 Data Products

The radiometric calibration part of the VIIRS Data Processing Architecture (DPA) produces the following during operational NRT processing:

- Sensor Data Record (SDR)
- Onboard Calibrator Intermediate Product (IP)
- Calibrated Dual Gain IP

### 2.1.2.1 Sensor Data Records

VIIRS SDR's contain calibrated TOA radiances, reflectances (reflective 'M' and 'I' bands only), and brightness temperatures (emissive bands only) for each VIIRS Earth view pixel. The calibrated TOA radiances are reported as spectral radiance in  $W/m^2\text{-sr-micron}$  for the 'M' and 'I' bands. The DNB calibrated TOA radiances are integrated radiance in  $W/cm^2\text{-sr}$ , which is the unit expected by the VIIRS Near Constant Contrast (NCC) imagery algorithm (JPSS OAD Document for VIIRS Near Constant Contrast (NCC) Imagery Environment Data Record (EDR) Software, 474-00060). In the case of single gain bands, radiance is stored using a scaled integer representation in 15 bits. Dual gain and DNB radiances require 32 bit floating point representation. Brightness temperature is reported as scaled integers in units of K.

In addition to these radiance fields, pixel geolocation (i.e. geodetic latitude and longitude) and geolocation related data are included as part of the SDR Product. Geolocation related data includes terrain height, range, satellite and solar geometry, and (for the DNB) lunar geometry at each VIIRS Earth view pixel. Geolocation and geolocation related data are copied from the VIIRS Geolocation IPs, which are the output products of the VIIRS Geolocation algorithm.

Metadata for the VIIRS SDR's are copied from the input Verified VIIRS RDR's and VIIRS Geolocation IPs. Included are the following granule metadata:

- Granule ID – a unique identifier that identifies the VIIRS flight model, the band type (i.e. 'M', 'I', or DNB), the data start time, data version, and SDR creation time
- Ground processing software identification (module, version number, and version date)
- Time and location at start of granule
- Minimum and maximum solar, sensor, and lunar (DNB only) azimuth and zenith angles
- Geographic coverage
- Detector quality

In addition the following metadata are included for each scan:

- Scan number
- Scan start time
- Minimum and maximum solar zenith angle
- VIIRS operational mode
- Half Angle Mirror (HAM) side

Pixel level metadata are limited to quality flags. Quality flags belong to pixel level metadata. At a minimum each pixel requires a 1-bit good/bad (i.e. use/don't use) flag. Operational conversion of the VIIRS science algorithms expands quality flagging to accommodate requirements for on-orbit calibration and validation (Cal/Val).

Sub-pixel samples from the VIIRS dual gain bands are aggregated along-scan during post-calibration ground processing.<sup>2</sup> Additional flagging is required to identify cases when non-nominal sets of unaggregated data have been combined. This flagging requires three bits per pixel, which are, for the science algorithm, set according to the following convention:

- 000 good quality - nominal averaged radiance reported
- 001 aggregated pixel where some (not all) samples are saturated or unusable - average of usable samples' radiance reported
- 100 aggregated pixel where all samples unusable, but none saturated - fill value reported in radiance field

---

<sup>2</sup> Along-scan aggregation is discussed in Section 2.2.7

- 101 aggregated pixels where all samples unusable with some, but not all "saturated" fill value is reported in radiance field.
- 110 all samples unusable due to saturation - saturated DN reported in radiance field (fill value for science code)
- 011 aggregated pixel where some samples are corrupted, but none are saturated or unusable – average of all samples is reported.
- 010 and 111 are spare codes.

A description of conditions that trigger quality flags is provided under Exception Handling, section [3.4.2.2](#).

Details concerning the original format of VIIRS SDR's are in the *Operational Algorithm Description Document (OAD) for VIIRS SDR Calibration Software [D39553]*. However, the format of the IDPS Operational VIIRS SDR has changed dramatically from the original.

### **2.1.2.2 Intermediate Products**

The Onboard Calibrator IP's contain subsets of the Verified VIIRS RDR and are the primary input to offline VIIRS Cal/Val performance analysis. Included are all raw *DNs* from the space view (SV), on-board blackbody (OBCBB) view, and solar diffuser (SD) view. Also included are all engineering and housekeeping data including raw data from the Solar Diffuser Stability Monitor (SDSM). These data have been unpacked from VIIRS RDR Consultative Committee for Space Data Systems (CCSDS) packets and assembled into convenient scan cube structures during processing by the VIIRS Build RDR Module. As with the SDR's, metadata are included that uniquely identifies the IP and its content and coverage. Also included as metadata are calibrator view inventory statistics. Details concerning the format of this IP are in SDRL 148-3, *VIIRS Radiometric Calibration Component Level Detailed Design [Y2490]*. However, the format of this IP IDPS Operational code has changed dramatically from the original (Refer to JPSS OAD Document for VIIRS GEO SDR and CAL SDR Software for details).

The Calibrated Dual Gain IPs contain unaggregated, calibrated TOA radiances for those VIIRS sub-pixel samples that are aggregated along-scan during post-calibration ground processing; i.e. the calibrated M1, M2, M3, M4, M5, M7, and M13 dual gain band data from the nadir (i.e. aggregation by 3) and near-nadir (i.e. aggregation by 2) zones that would otherwise be discarded following aggregation (see Section [2.2.7](#)). Metadata are included that uniquely identifies the IP and its content and coverage. Details concerning the format of this IP are also in SDRL 148-3, *VIIRS Radiometric Calibration Component Level Detailed Design [Y2490]*. However, the format of this IP IDPS Operational code has changed dramatically from the original. (Refer to JPSS OAD Document for VIIRS GEO SDR and CAL SDR Software for details).

## 2.2 INSTRUMENT OVERVIEW

In order to develop and understand the theoretical basis of VIIRS radiometric calibration it is necessary to first understand the VIIRS instrument and data designs and the concept and capabilities of its operation. This section provides an overview of those facets of the VIIRS that are particularly relevant to radiometric calibration. An overview of the two modules that comprise the VIIRS instrument (i.e. the Opto-Mechanical Module and the Electronics Module) is presented after a description of the VIIRS spectral bands. These descriptions are followed by discussions of the on-board calibrators, the instrument operations modes, and the instrument's data output.

### 2.2.1 Spectral Bands

The VIIRS moderate resolution radiometric bands (the 'M' bands) and fine resolution imaging bands (the 'I' bands) are distributed among three Focal Plane Assemblies (FPA). Except for M16 each 'M' band consists of sixteen along-track detectors. M16 is a double row of sixteen along-track detectors that are time delay integrated (TDI) on-board. Each 'I' band consists of thirty-two along-track detectors. In addition there is a panchromatic Day-Night Band (DNB) that is mounted adjacent to the Vis/NIR FPA. The VIIRS DNB is a temperature controlled Charge Coupled Device (CCD) that has 672 sub-pixel detectors along-track, which are aggregated on-board to create sixteen constant 740 m along-track pixels for each along-scan frame.

The VIIRS spectral bands as compared to MODIS, OLS, and AVHRR are shown in [Table 8](#). The spectral response of the VIIRS 'M' and 'I' bands is illustrated in [Figure 1](#) through [Figure 4](#). These figures also illustrate spectral characteristics of the atmosphere and surface.

**Table 8: VIIRS Spectral Bands as Compared to Other Vis/IR Instruments (Parameters shown in this Table for Suomi-NPP VIIRS are from design specs. The as-built values for VIIRS can be found in Cao et al., 2013a)**

VIIRS			MODIS Equivalent			AVHRR-3 Equivalent			OLS Equivalent		
VIIRS Band	Spectral Range (um)	Nadir HSR (m)	Band(s)	Range	HSR	Band	Range	HSR	Band	Range	HSR
DNB	0.500 - 0.900								HRD PMT	0.580 - 0.910 0.510 - 0.860	550 2700
M1	0.402 - 0.422	750	8	0.405 - 0.420	1000						
M2	0.436 - 0.454	750	9	0.438 - 0.448	1000						
M3	0.478 - 0.498	750	3 10	0.459 - 0.479 0.483 - 0.493	500 1000						
M4	0.545 - 0.565	750	4 12	0.545 - 0.565 0.546 - 0.556	500 1000						
I1	0.600 - 0.680	375	1	0.620 - 0.670	250	1	0.572 - 0.703	1100			
M5	0.662 - 0.682	750	13 14	0.662 - 0.672 0.673 - 0.683	1000 1000	1	0.572 - 0.703	1100			
M6	0.739 - 0.754	750	15	0.743 - 0.753	1000						
I2	0.846 - 0.885	375	2	0.841 - 0.876	250	2	0.720 - 1.000	1100			
M7	0.846 - 0.885	750	16	0.862 - 0.877	1000	2	0.720 - 1.000	1100			
M8	1.230 - 1.250	750	5	SAME	500						
M9	1.371 - 1.386	750	26	1.360 - 1.390	1000						
I3	1.580 - 1.640	375	6	1.628 - 1.652	500						
M10	1.580 - 1.640	750	6	1.628 - 1.652	500	3a	SAME?	1100			
M11	2.225 - 2.275	750	7	2.105 - 2.155	500						
I4	3.550 - 3.930	375	20	3.660 - 3.840	1000	3b	SAME?	1100			
M12	3.660 - 3.840	750	20	SAME	1000	3b	3.550 - 3.930	1100			
M13	3.973 - 4.128	750	21 22 23	3.929 - 3.989 3.929 - 3.989 4.020 - 4.080	1000 1000 1000						
M14	8.400 - 8.700	750	29	SAME	1000						
M15	10.263 - 11.263	750	31	10.780 - 11.280	1000	4	10.300 - 11.300	1100			
I5	10.500 - 12.400	375	31 32	10.780 - 11.280 11.770 - 12.270	1000 1000	4 5	10.300 - 11.300 11.500 - 12.500	1100 1100	HRD	10.300 - 12.900	550
M16	11.538 - 12.488	750	32	11.770 - 12.270	1000	5	11.500 - 12.500	1100			

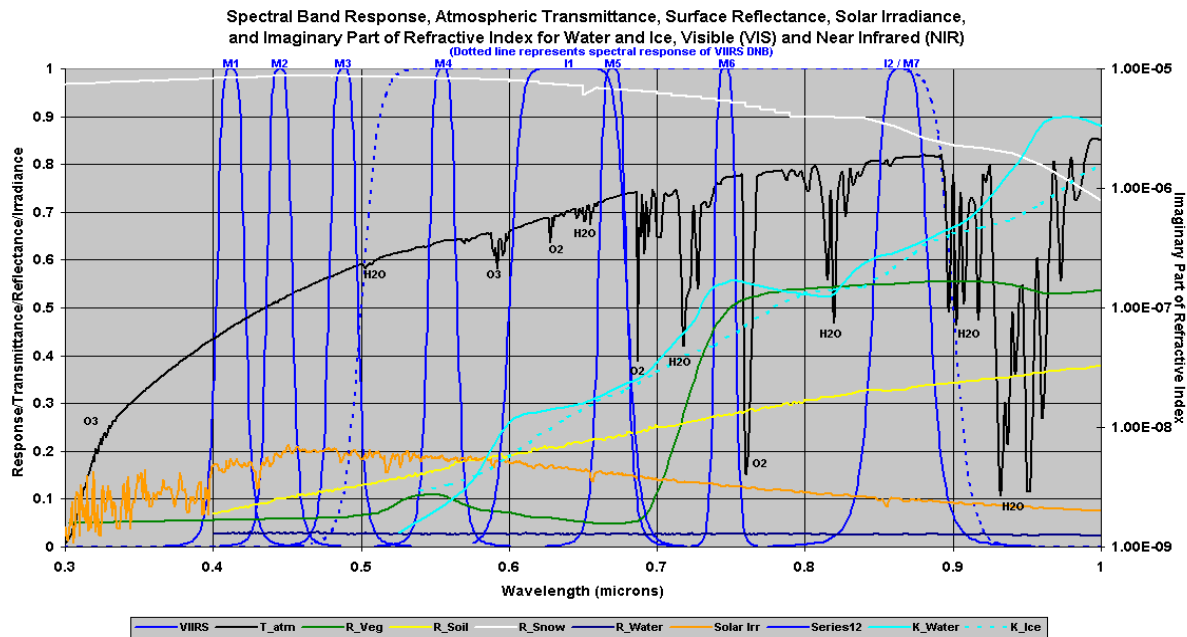


**Figure 1: VIIRS Spectral Bands; Visible and Near Infrared**

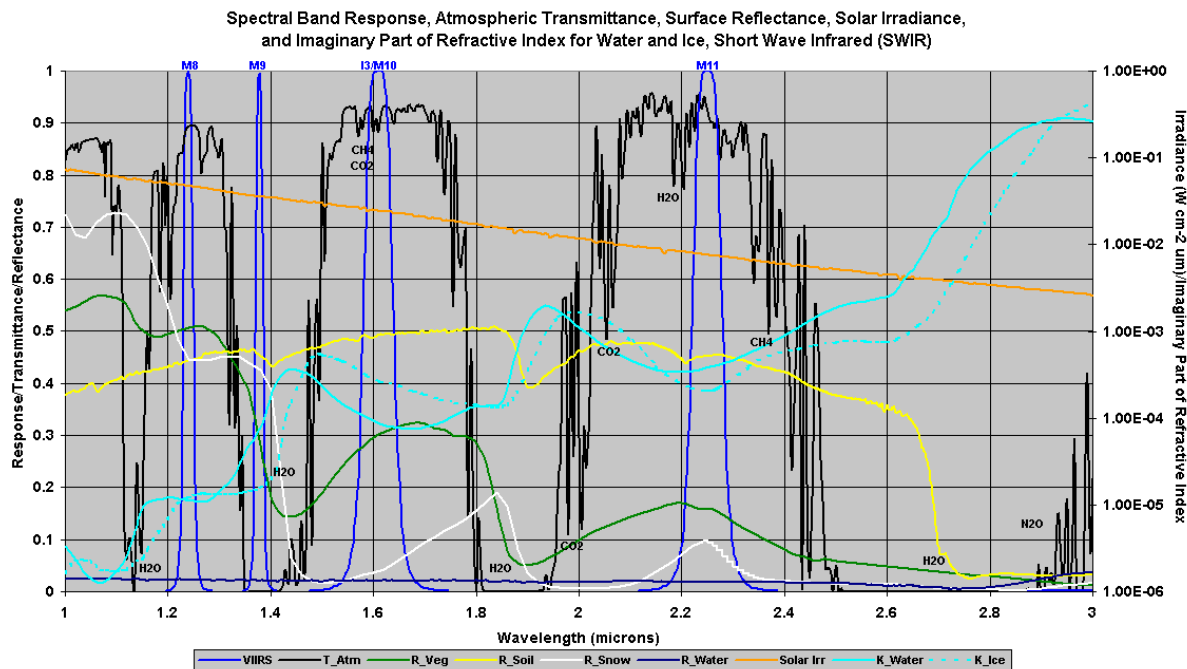


**Figure 2: VIIRS Spectral Bands; Shortwave Infrared**

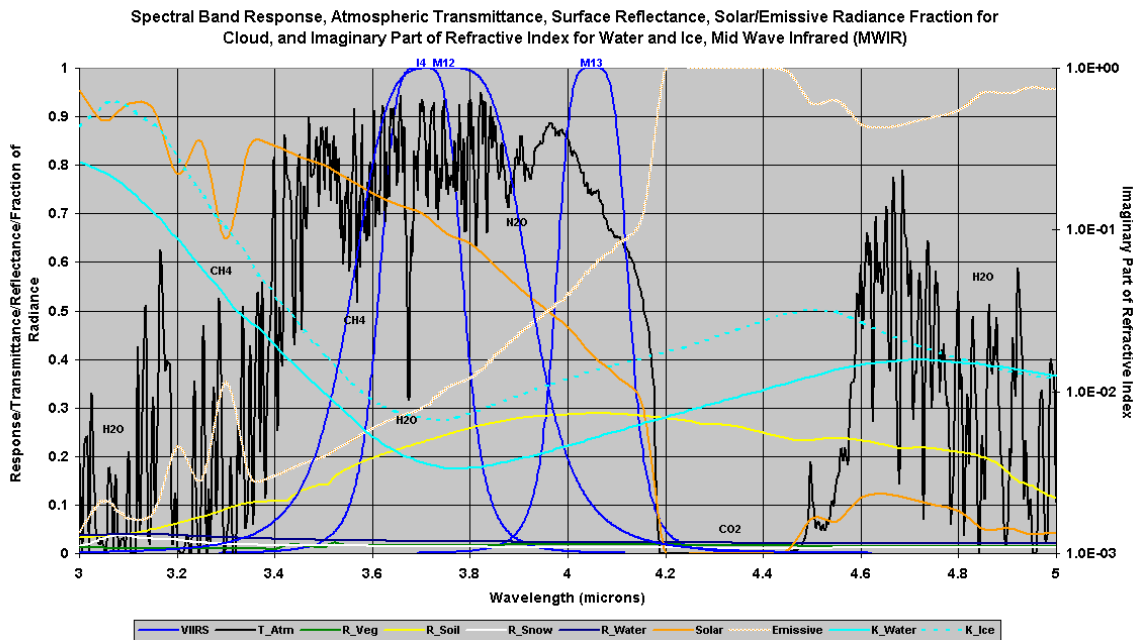


**Figure 3: VIIRS Spectral Bands; Midwave Infrared**

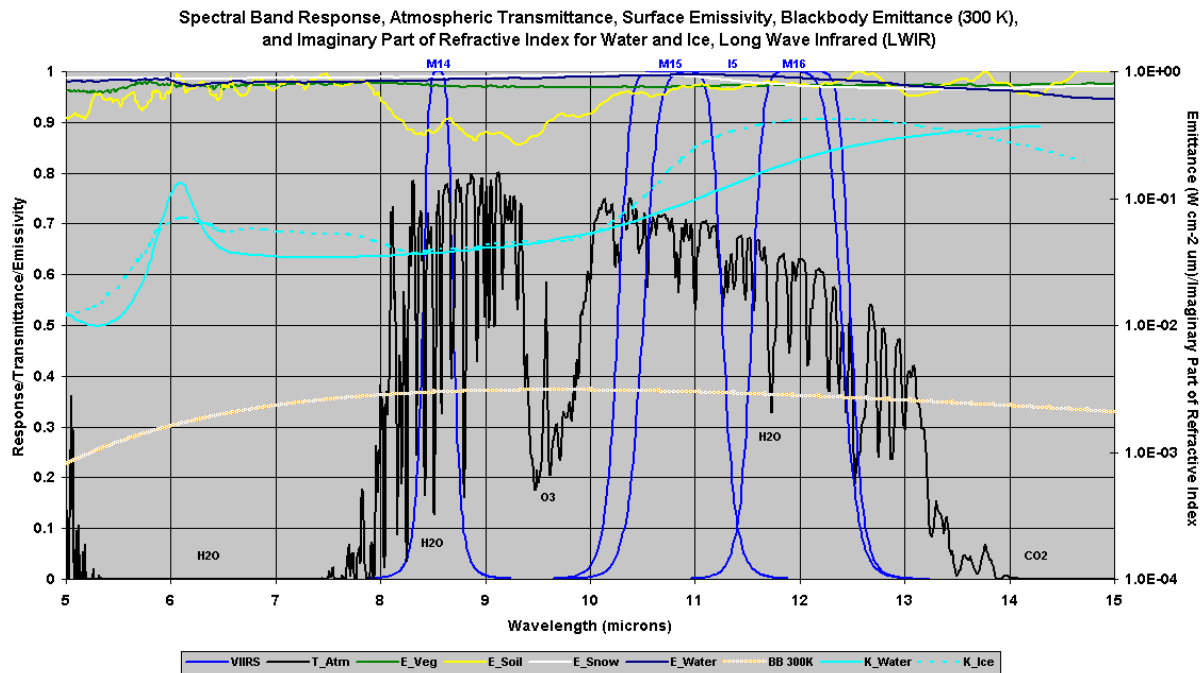


**Figure 4: VIIRS Spectral Bands, Long-wave Infrared**

## 2.2.2 Opto-Mechanical Module

The VIIRS Opto-Mechanical Module is shown in cut-out view in [Figure 5](#). This module consists of all the optical elements of the VIIRS as well as the scanning motors and encoders, the nadir doors, a passive cryoradiator, space and sun view ports, and numerous temperature sensors. Also shown in [Figure 5](#) is the Electronics Module, which is mounted separately and is the subject of Section [2.2.3](#).

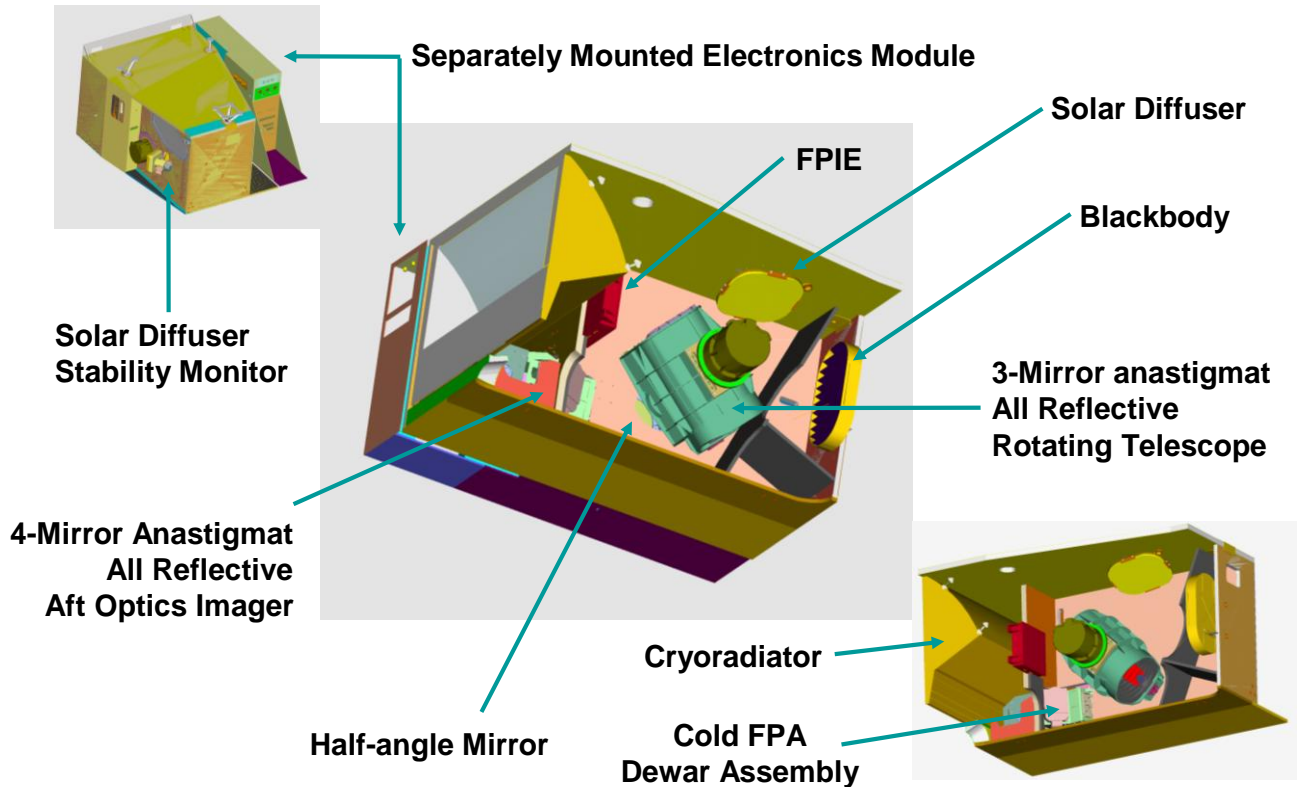


Figure 5: Cut-out View of the VIIRS Opto-Mechanical Module

The VIIRS optical elements include:

- A scanning telescope or Rotating Telescope Assembly (RTA)
- A Half Angle Mirror (HAM)
- A four-mirror anastigmat, all reflective, aft optics imager
- The three focal plane assemblies containing the 'M' and 'I' band detectors
- The DNB FPA and its Focal Plane Interface Electronics (FPIE)
- A solar diffuser
- An On-Board Calibrator Blackbody (OBCBB)

- A Solar Diffuser Stability Monitor (SDSM)

The Rotating Telescope Assembly (RTA) along with the rotating HAM produces the VIIRS cross-track scan, which is shown schematically in [Figure 6](#) and [Figure 7](#). The orientation of the velocity vector with respect to [Figure 6](#) is out of the page. VIIRS always scans from the cold side of the S/C to the warm (i.e. sunlit) side. The HAM and the RTA rotate around the same axis however the HAM is a derotator that rotates at half the speed of the RTA. The RTA and HAM are described in more detail in [Section 2.2.2.1](#) and [Section 2.2.2.2](#), respectively.

The aft optics imager contains two dichroic beam splitters that define the spectra for the optical paths leading to the three FPAs, which are described in [Section 2.2.2.3](#). It is an all reflective, four-mirror anastigmat design. [Figure 8](#) illustrates the path of photons from the entrance of the RTA to the FPAs.

There are a total of thirteen (13) optical components for the Visible/Near Infrared (Vis/NIR) bands, nineteen (19) optical components for the Short/Mid-wave Infrared (S/MWIR) bands, and eighteen (18) for the Long-wave Infrared (LWIR) bands. These are listed in Table 9, which is reproduced from NGST Doc. D36966. All of the optical elements are fixed with respect to the optical axis except for the Half Angle Mirror (HAM), which rotates to induce the cross-track scanning. The Rotating Telescope Assembly (RTA) also rotates but the optical axis remains fixed. Therefore reflectance is a function of the scan angle only for the HAM, which is the fifth component in the optical train.

The Vis/NIR, S/MWIR, and LWIR FPAs are described in [Section 2.2.2.3](#). This description includes a description of the automatic gain switching that occurs for the dual gain 'M' bands. The DNB and its interface electronics, which is part of the Opto-Mechanical Module, are described in [Section 2.2.2.4](#).

Calibration is performed onboard using a Solar Diffuser (SD) for short wavelengths and a V-groove On-Board Calibrator Blackbody (OBCBB) and deep space view for thermal wavelengths. A Solar Diffuser Stability Monitor (SDSM) is also included to track the changes to the solar diffuser reflectance. The VIIRS on-board calibrators are described in [Section 2.2.4](#).

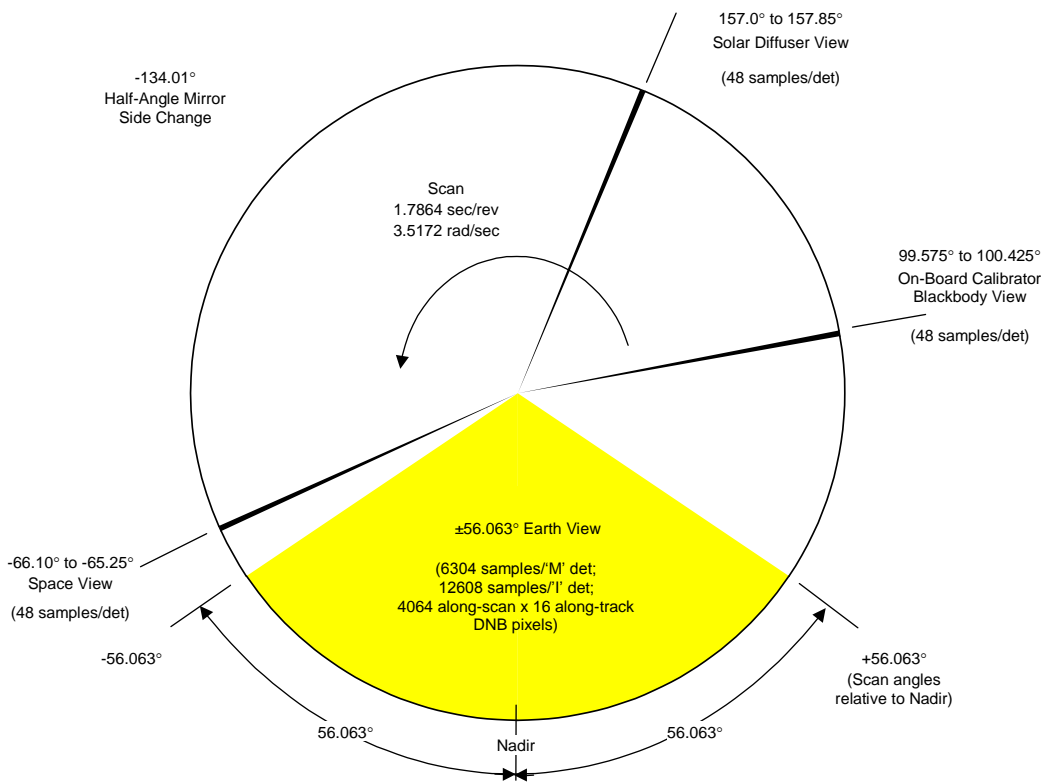


**Figure 6: Diagram of VIIRS Scan Pattern. Parameters shown in this figure are from early design specs. The as-built values for Suomi-NPP VIIRS can be found in Cao et al., 2013b.**

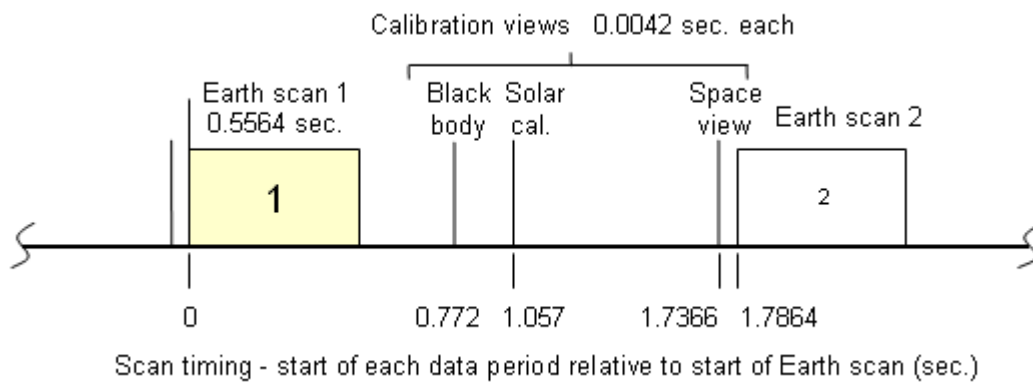


**Figure 7: Timeline of Typical VIIRS Scan**

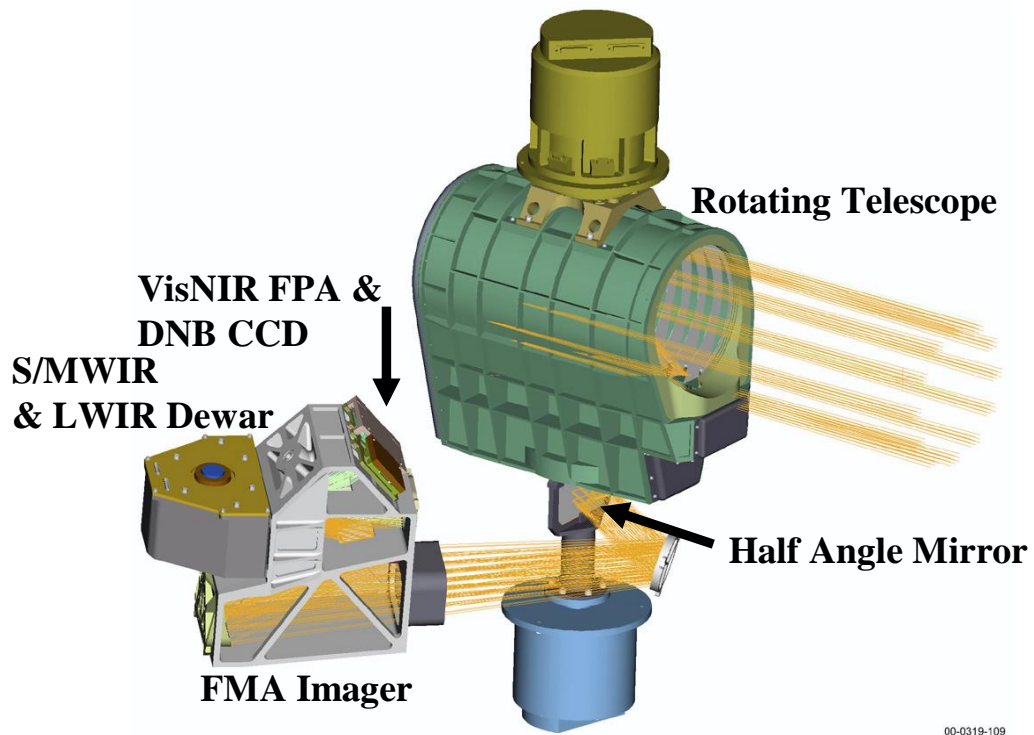


**Figure 8: VIIRS Optical Path**

**Table 9: Optical Train Components**

Component	Temp (K)	Component Numbering				
		Vis/NIR	R	DNB	SWIR	MWIR
RTA	280	1	1	1	1	1
RTA	280	2	2	2	2	2
RTA Tertiary	280	3	3	3	3	3
Fold Mirror 1	280	4	4	4	4	4
HAM	280	5	5	5	5	5
Aperture	280	6	6	6	6	6
Fold Mirror 2	280	7	7	7	7	7
Aft Optics	279	8	8	8	8	8
Aft Optics	279	9	9	9	9	9
Aft Optics	279	10	10	10	10	10
Aft Optics	279	11	11	11	11	11
Dichroic #1	279	12	12			
Dichroic #1	279			12	12	12
Dichroic #2	279			13	13	
Dichroic #2	279					13
SW/MWIR	279			14	14	
SW/MWIR	140			15	15	
SW/MWIR	80			16	16	
LWIR Dewar	279					14
LWIR Dewar	140					15
LWIR Dewar	80					16
SWIR	80			17		
MWIR	80				17	
Vis/NIR	279	13				
DNB Cover	251		13			
DNB Band	251		14			
SWIR Band	80			18		
MWIR Band	80				18	
LWIR Band	80					17
SW/MWIR	80			19	19	
LWIR	80					18
Total		13	14	19	19	18

NOTE: Temperatures vary over orbit for many of the components, so approximate mean values are given based on 17:30. The 10:30, 13:30 or 21:30 orbit temperatures are lower for many of the components

### **2.2.2.1 Rotating Telescope Assembly**

The Rotating Telescope Assembly (RTA) includes a three-mirror anastigmat (all reflective) telescope and a fold mirror that directs scene energy onto the HAM. The RTA has heritage in NASA's Sea-viewing Wide Field-of-View Sensor (SeaWiFS). The RTA rotates at a constant speed and is synchronized with the HAM once per scan. The RTA is well baffled to minimize stray light. The nominal magnification of the RTA is -4.

The RTA uses a 14 bit motor/encoder to track rotation angle versus time. The times associated with 1284 evenly spaced encoder pulses as well as the synchronization time are telemetered from each scan to the ground for determining look angles. At nadir the line of sight scans 319.4 m between pulses.

### **2.2.2.2 Half Angle Mirror**

The Half Angle Mirror (HAM) is a two-sided mirror that serves as derotator as it directs scene energy from the RTA via a fold mirror into the aft optics. It scans in the same direction as the RTA but at half its rate. [Figure 9](#) shows the synchronization of the HAM with the RTA throughout the scan.

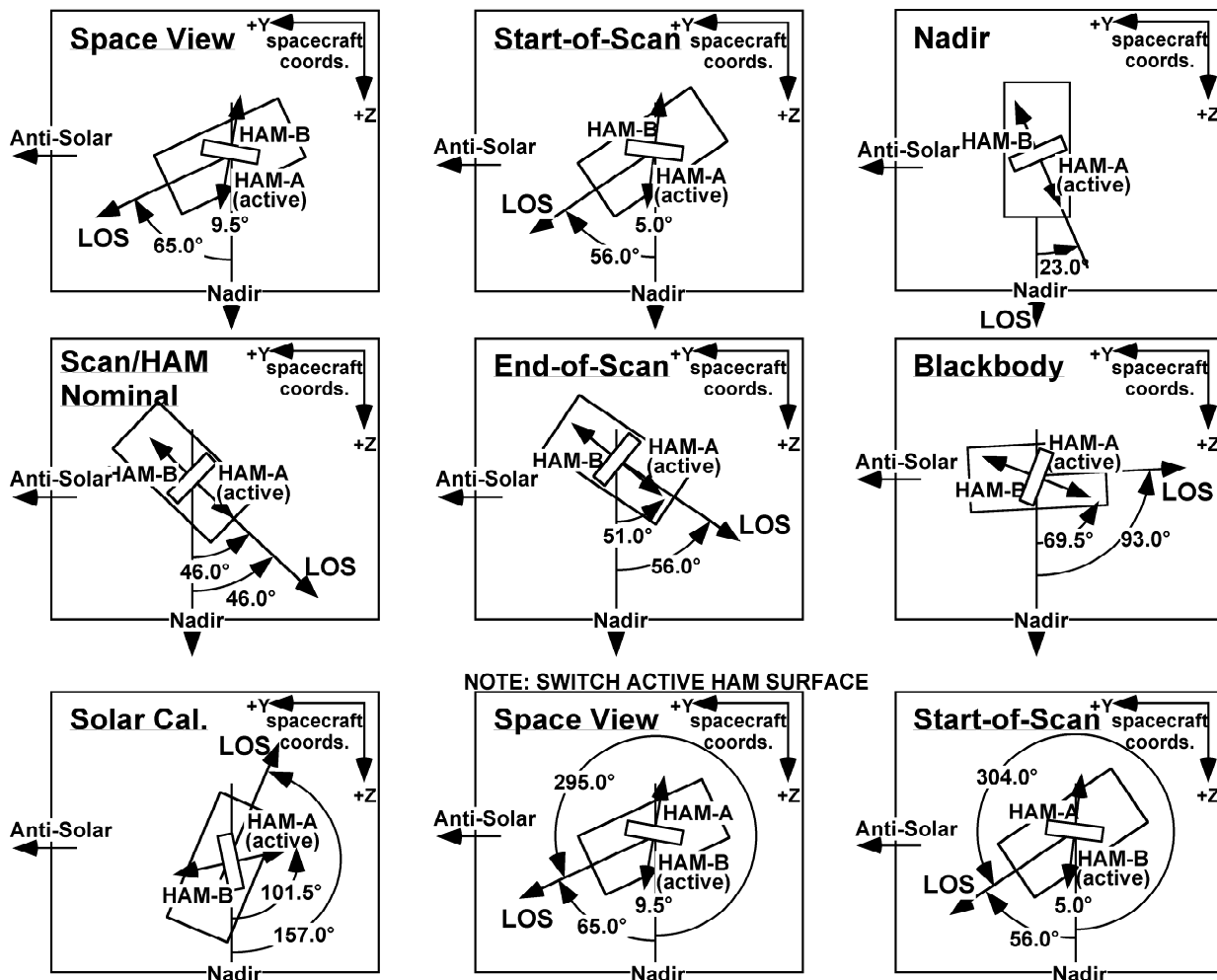


Figure 9: VIIRS RTA-HAM Synchronization throughout Scan

The start point of a scan is arbitrary but as defined here starting just after the HAM turn-around point (i.e. the side change), which occurs at approximately -134 degrees (see Figure 6). This is the point in the scan at which the HAM's angular position becomes perpendicular to the rays from the RTA, and thus the optical signal from the RTA stops falling on one side of the HAM and begins to fall on the other side. From this point, the scan proceeds in a clockwise direction (velocity vector away from viewer) to the space view, through the Earth scan (from night to Sun side), to the blackbody, solar diffuser, and then back to the HAM turn-around point. Thus each scan includes collecting data from each of the calibration sources and the Earth using only one side of the HAM, and each subsequent scan uses alternating sides of the HAM.

The HAM uses a 14 bit motor/encoder that is identical to the RTA motor/encoder to track rotation angle versus time. The times associated with 1284 evenly spaced encoder pulses are collected each scan and are telemetered to the ground as VIIRS engineering data. HAM encoder data are combined with RTA encoder data and the once per scan synchronization time to determine scan angle at individual pixel times.

### 2.2.2.3 'M' and 'I' Band Focal Plane Assemblies

The layouts of the Vis/NIR detectors are shown in [Figure 10](#) and the layouts of the detectors on the Short/Mid-Wave Infrared (S/MWIR) and Long-Wave Infrared (LWIR) FPAs are shown in [Figure 11](#). The S/MWIR and LWIR FPAs have the odd numbered detectors staggered relative to even numbered detectors whereas the Vis/NIR detectors are aligned in a single line. Band-to-band registration is performed on-board by applying time delays among the bands in order to co-align the band pixels among themselves and also to align the four nested 'I' band pixels within one 'M' band pixel. For the single gain bands, along-scan sample aggregation is performed on board, but the dual gain 'M' bands are transmitted unaggregated, and so along-scan sample aggregation is performed during ground processing following radiometric calibration of the individual samples.

It should be noted that the detector numbering in [Figure 10](#) and [Figure 11](#) follow the instrument engineer's convention of labeling the detector that first sees a target on the ground (leading edge) as detector number 1. This is opposite the "product order" convention expected by users of the VIIRS imagery and science data, which requires that the highest indexed detector in scan N lies adjacent to detector index 1 in scan N+1. Whenever the words "detector number" are used, this refers to the instrument engineer's convention. When using the product order the words "detector index" will be used. Note that in the C programming language, and others, indexing of arrays start with 0 rather than 1, and so will create an additional complexity to the indexing of detectors. All ground processing parameters and tables are designed to conform to the "product order" convention. However, the RDR packets are indexed according to the instrument engineer's convention.

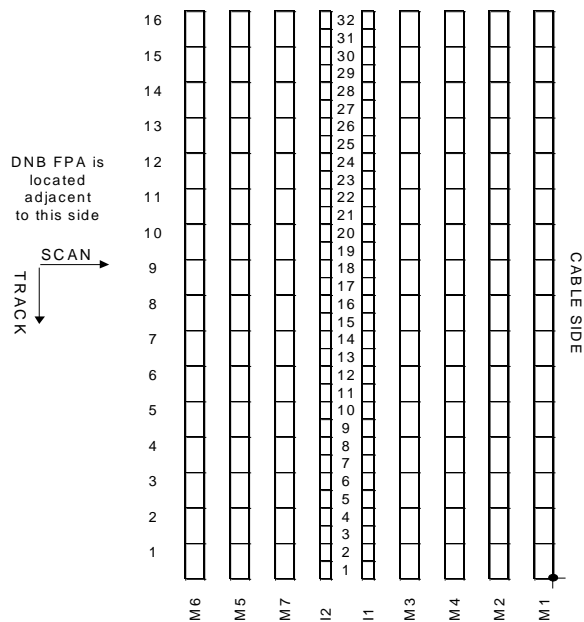
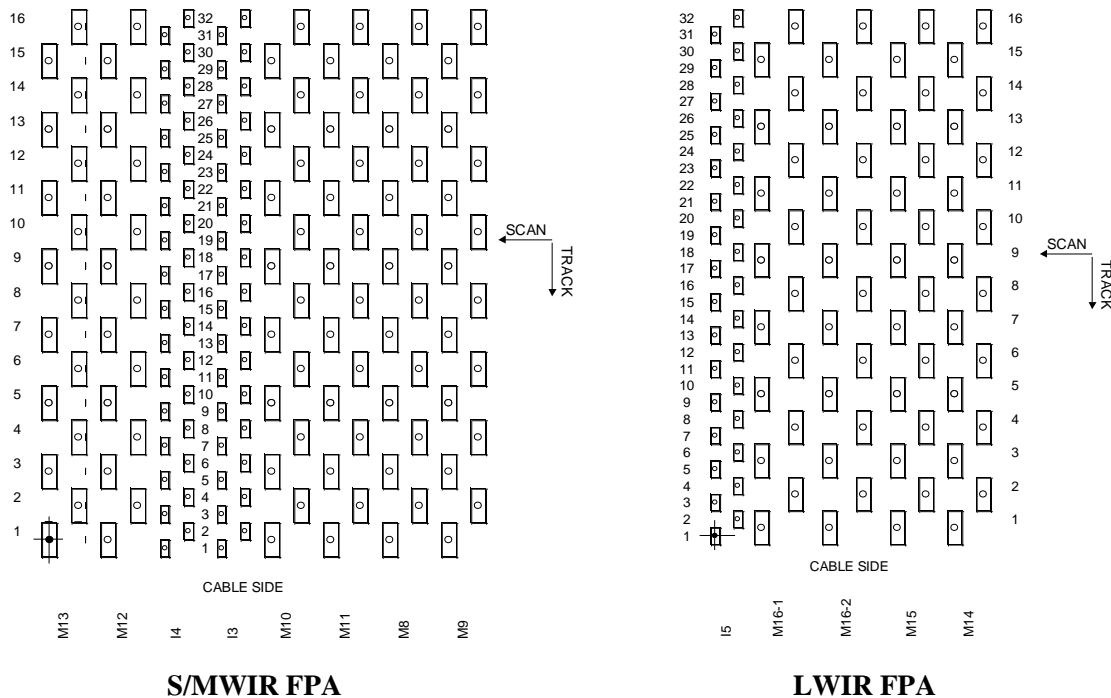


Figure 10: VIIRS Vis/NIR Detector Lay-out



**Figure 11: VIIRS S/MWIR & LWIR Detector Layout**

### 2.2.2.3.1 Vis/NIR FPA

The Vis/NIR FPA consists of a Sensor Chip Assembly (SCA) that is a detector array hybridized to a silicon Read-Out Integrated Circuit (ROIC). The ROIC integrates the output photocurrent from the detector and converts it into an output voltage.

The Vis/NIR SCA consists of nine spectral bands; seven moderate resolution ('M') radiometric bands designated M1, M2, M3, M4, M5, M6, M7 and two fine resolution imaging ('I') bands designated I1 and I2. The 'M' bands consist of 16 detectors per band arranged in a single row. The two 'I' bands consist of 32 detectors in each band, which are also arranged in a single row. Moderate resolution bands, M1 through M7, have rectangular shaped detectors. The 'I' bands have rectangular shaped detectors with dimensions of about half the size of the moderate resolution bands. Bands M1, M2, M3, M4, M5, and M7 have a dual gain capability that allows signal detection over a wide range of photon flux. The dual gain bands have a gain state for each detector that is transmitted through separate gain outputs.

### 2.2.2.3.2 S/MWIR FPA

The S/MWIR SCA consists of two HgCdTe detector arrays hybridized to a silicon ROIC. The ROIC integrates the output photocurrent from the detectors and converts it into an output voltage. The ROIC performs pixel-multiplexing functions to provide the proper output data format.

The S/MWIR SCA consists of eight spectral bands; six 'M' bands designated M8, M9, M10, M11, M12, M13 and two 'I' bands designated I3 and I4. The 'M' bands consist of 16 detectors per band arranged in two rows, with both primary and redundant detector select. The two 'I' bands consist of 32 detectors in each band, arranged in two rows, with both primary and redundant detector select. All of the S/MWIR bands have octagon shaped detectors where each pixel includes a rectangle lenslet that focuses the radiance over the pixel field of view onto the detector element which is much smaller than the lenslet. This minimizes detector area, and thus reduces 1/f noise. Band M13 has a dual gain capability, which allows signal detection over a wide range of photon flux. The dual gain band has a gain state for each detector, which is transmitted through a separate gain bit.

#### **2.2.2.3.3 LWIR FPA**

The LWIR SCA consists of two HgCdTe photovoltaic detectors hybridized to a silicon ROIC, which integrates and converts output photocurrent into output voltage.

The LWIR SCA consists of four spectral bands, three 'M' bands designated, M14, M15, M16, and one 'I' band designated I5. The 'M' bands consist of 16 detectors per band arranged in two rows. Band M16 consists of two bands M16-1 and M16-2, which are time delay integrated (TDI), in off focal plane electronics. The one imaging band consists of 32 detectors arranged in two rows. All LWIR bands have octagon shaped detectors but made rectangular with the microlens. Like the S/MWIR FPA, each pixel includes a lenslet that focuses the radiance over the pixel field onto the detector element which is much smaller than the lenslet, to minimize detector area, and thus reduces 1/f noise.

#### **2.2.2.3.4 Gain Switching**

Bands M1, M2, M3, M4, M5, M7, and M13 are dual gain bands. Transitions from high gain (low radiance) to low gain (high radiance) are done automatically at the focal plane electronics level based on a switch point bias voltage that is supplied by the Analog Signal Processor, which is a component of the Electronics Module.

[Figure 12](#) shows schematically *DN* versus radiance and the switchover from high gain to low gain. Note that for any particular *DN* there is only one radiance value. The most significant of the 13 bits used for dual-gain is used to flag the low gain mode. Because the gain and offset are different between the gain modes, calibration must be done individually for each mode. This requires a separate space view and calibration source view (OBCBB or SD). Because calibration is also done separately for each mirror side, the dual gain bands require 4 scans to complete a calibration cycle.

#### **2.2.2.4 Day-Night Band FPA and Interface Electronics**

The DNB Module includes a CCD array and a Focal Plane Interface Electronics (FPIE) located in the Opto-Mechanical Module adjacent to the Vis/NIR FPA. A DNB timing card is located in the Electronics Module. A simplified block diagram of the DNB is shown in [Figure 13](#).

The light-detecting element of the DNB, and the key to its high sensitivity and wide dynamic range, is a four-stage, backside-illuminated Charge-Coupled Device (CCD) detector chip, which is provided with a bandpass filter that limits its spectral sensitivity to the wavelengths indicated in [Table 10](#). The radiometric uncertainty requirements for the DNB are given in [Table 7](#). The architecture and features of the CCD are illustrated in [Figure 14](#). The CCD shares an optical path with, and is mounted next to but thermally isolated from, the Vis/NIR FPA. The nominal CCD operating temperature is 253K.

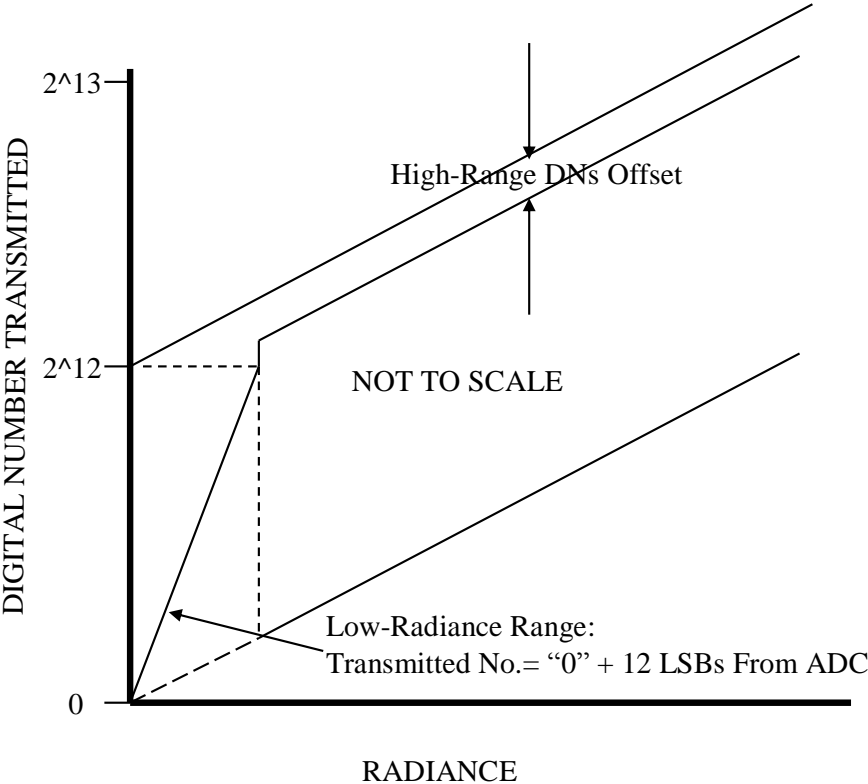


Figure 12: VIIRS Dual Gain 'M' Band Gain Switching

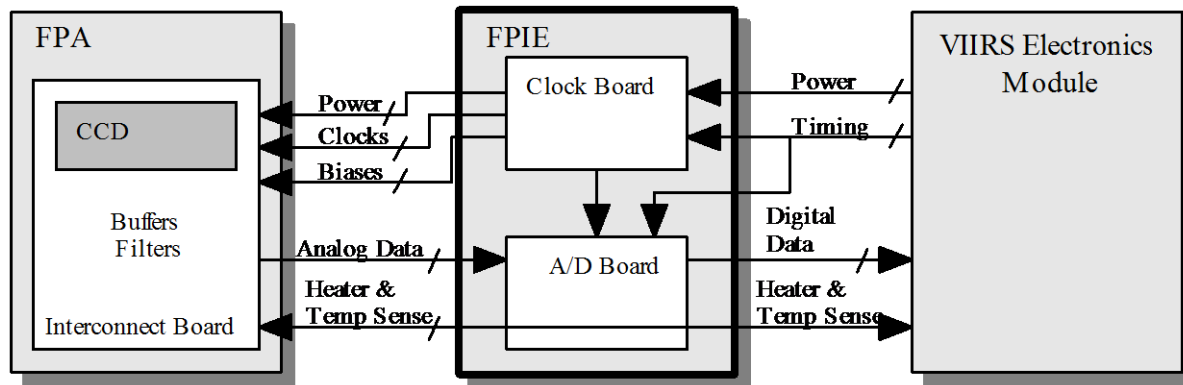
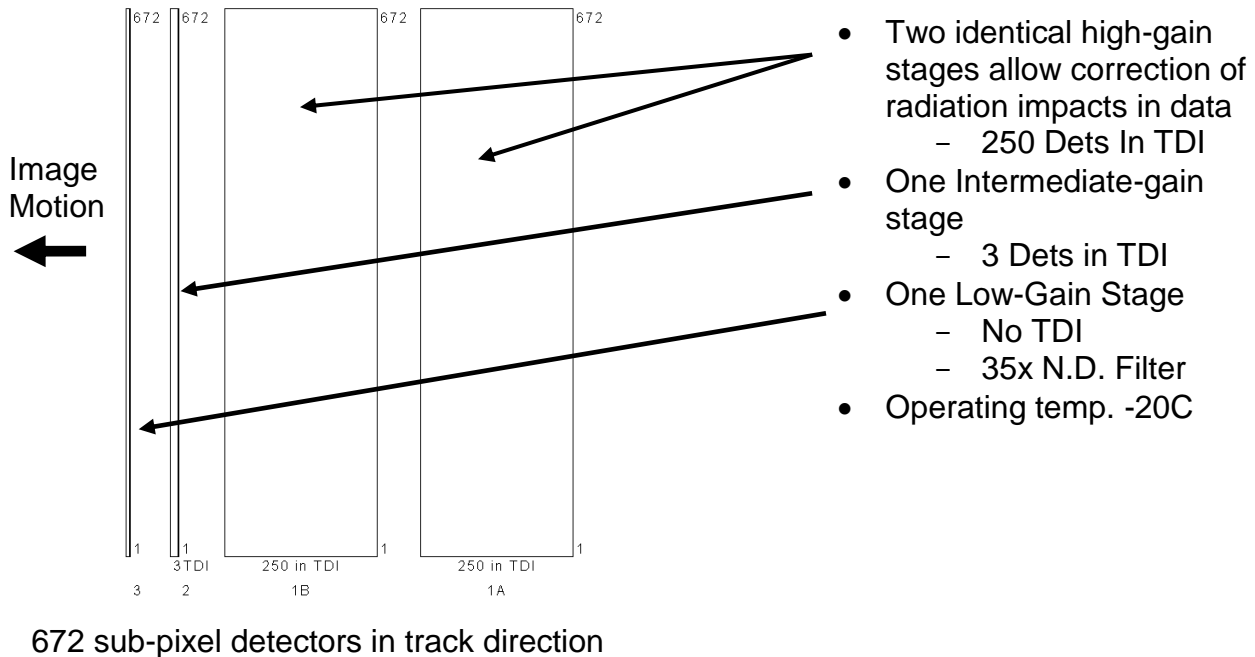


Figure 13: Simplified VIIRS DNB Block Diagram

Table 10: Key DNB Performance Requirements

Requirement No.	Description	Value
SRV0034	Band Center	700±14 nm
	Bandwidth	400±20 nm
SRV0564	Horizontal Sample Interval, track and scan (applies across the full swath)	742 m ±5%
SRV0050	Horizontal Spatial Resolution (half-cycle spatial freq. where MTF=0.5)	< 800 m
SRV0646	Lmin, High Gain Stages (HGS)	3.0E-5 W m <sup>-2</sup> sr <sup>-1</sup>
	Lmax, Low Gain Stage	200 W m <sup>-2</sup> sr <sup>-1</sup>
SRV0569	SNR @ HGS Lmin & scan angle < 53°	6
	SNR @ HGS Lmin & scan angle ≥ 53°	5



**Figure 14: VIIRS DNB CCD Layout**

As a scene is scanned a real image of the scene moves across the Vis/NIR FPA and then onto the CCD in the direction of the arrow in [Figure 14](#). The CCD covers the required dynamic range by viewing the scene with four detector arrays having three different radiometric gains. The signals from all four detector arrays are digitized in the FPIE. The digitized number most appropriate to represent the scene is selected by logic on the DNB Timing card in the VIIRS Electronics Module (EM).

The two identical large arrays at the top in [Figure 14](#) have the highest sensitivity. They are designated as Stage 1A and Stage 1B. Each one has 250 sub-pixel detectors operating in Time Delay Integration (TDI).

Two copies of Stage 1 are provided because the large area and long integration time of the Stage 1 array makes it susceptible to contamination by extra electrons produced by high-energy protons from the natural environment hitting the detector especially in the South Atlantic Anomaly (SAA) region. Since it is unlikely that proton impacts would affect the same ground pixel in both Stage 1A and 1B, the two stages can be used to detect and eliminate the radiation-induced effects. The logic for stage selection, which is performed in the Electronics' Module Digital Pre-processor, is presented in [Section 2.2.3.2](#).

The third array, identified as Stage 2, has only 3 sub-detectors in TDI. Combined with a lower output amplifier gain, this gives Stage 2 a gain that is over two orders of magnitude lower than the gain of Stages 1A and 1B. The final array, Stage 3, has only a single detector in the scan direction (no TDI). It also has a neutral-density filter and reduced amplifier gain to give an overall radiometric gain that is only 1/119,000 the gain of Stages 1A and 1B.

Analog to digital conversion from each stage is performed within the FPIE. DNB pixels are constructed through an aggregation process performed within the Electronics Module. A description of this process is in Section [2.2.3.2](#).

The DNB detector is a backside-illuminated Charge-Coupled Device (CCD) with four separate light-sensitive stages having three different gains. (Duplicate copies of the most sensitive stage are provided for use in correcting radiation effects in the data.) The detector elements in the CCD are about 3% of the size of moderate resolution channel detectors. During the course of the VIIRS active Earth scan, the DNB maintains an approximately constant Horizontal Sample Interval (HSI) and Instantaneous Field of View on the ground by aggregating the signals from various numbers of these “sub-pixel” detectors to compensate for the variations that would otherwise occur during the scan. Thirty-two different aggregation modes are used during the scan.

The CCD sensor operates in a Time Delay Integration (TDI) mode, in which the accumulating photocharge is clocked through the CCD in the same direction and at the same rate that the real image of the scene is scanned across the CCD chip. Every cycle this process delivers a row of 672 sub-detector charge packets to the downstream end of each CCD stage. The charges from a variable number of these rows of packets are accumulated in an accumulator register, thereby effectively aggregating a variable number of sub-pixels in the scan direction. The charges are then processed by applying Time Delayed Integration (TDI), with the net result being that the packets of charge delivered to the chip output amplifiers each represent the charge from  $N \times M$  sub-pixels, where  $N$  and  $M$  are the number of charge packets accumulated between readouts in the two directions. The aggregation modes used in normal DNB operation vary from 11 vertical (i.e. along-scan) x 20 horizontal (i.e. along-track) to 66 vertical x 42 horizontal. The output amplifier produces a voltage that is (nominally) a linear function of the number of electrons delivered to its input.

The CCD aggregation process described above is extremely efficient; and when the DNB is observing a uniform scene it approaches perfect efficiency. As a result it is possible to deliver to the amplifier charge packets whose relative sizes are precisely known by observing a constant uniform scene and varying the aggregation values applied. By providing an appropriate source (the on-board Solar Diffuser) and a sufficiently wide range of aggregation modes, this process is used to characterize the transimpedance (gain) of the DNB Stage 3 (high radiance range) output amplifiers.

### 2.2.3 Electronics Module

The VIIRS Electronics Module provides all of the electrical interfaces to the spacecraft. It controls the VIIRS configuration, operates the heaters and scan-control mechanisms in the Opto-Mechanical Module, and collects and formats the data from the focal planes and transmits them to the spacecraft. Several types of on-board processing are performed within the Electronics Module as shown in [Figure 15](#). The Electronics Module is mounted to a nadir facing plate in a position immediately adjacent to the VIIRS Opto-Mechanical Module (see [Figure 16](#)).

Analog data from the Vis/NIR, S/MWIR, and LWIR FPAs are processed by the Analog Signal Processor (ASP). The ASP performs analog-to-digital conversion (ADC), which is described in Section [2.2.3.1](#), and digital count (DC) restoration (DCR), which is described in Section [2.2.3.3](#). The digital output from the DNB FPIE is processed in the DNB Timing Circuit Card Assembly (CCA) where gain selection and identification is performed. Output from the ASP and DNB Timing CCA are processed by the Digital Pre-processor (DPP) to prepare the instrument data for packetization in the Single Board Computer (SBC). The DPP is described in more detail in Section [2.2.3.2](#). The data packets including the High Rate Data (HRD) packets, which provide the EV DN for radiometric calibration processing on the ground, are transmitted to the S/C for downlink over the 1394a interface. The HRD is described in more detail in Section [2.2.6](#).

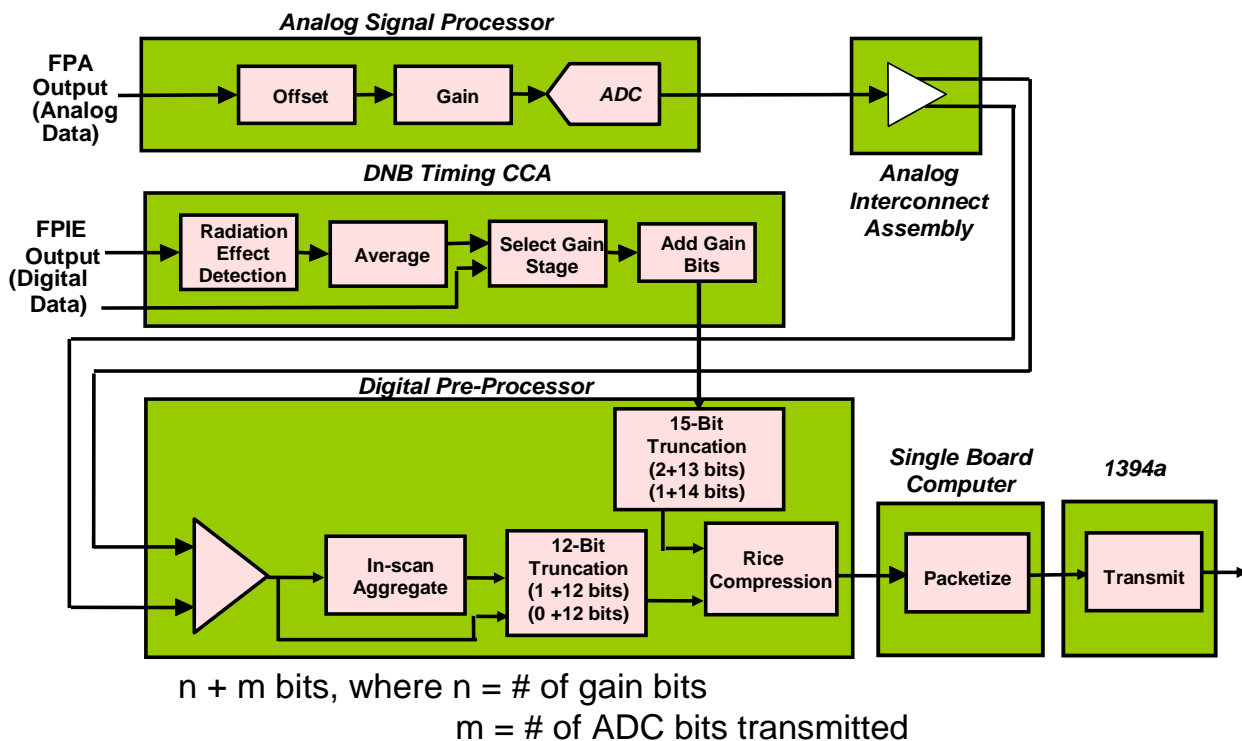
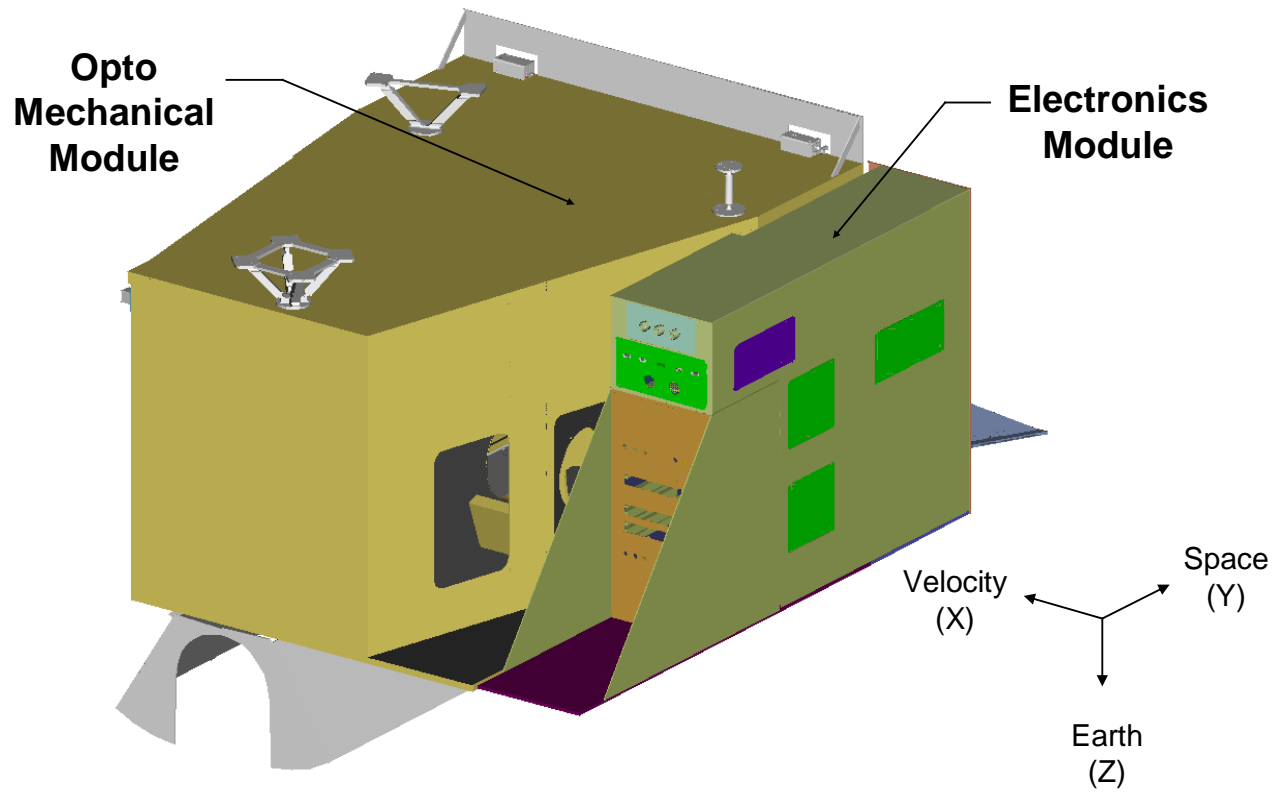


Figure 15: VIIRS Electronics Module Block Diagram



**Figure 16: VIIRS Electronics Module Orientation**

### **2.2.3.1 Analog to Digital Conversion**

The performance of the quantizing circuits or Analog to Digital Converters (ADCs) within VIIRS can have a significant effect on the overall performance of the instrument, including calibration. Specific areas of concern include integral and differential non-linearity, missing codes, and code patterns (higher and lower than expected frequency or distribution of some ADC outputs). Additionally, many aspects of the signal processing circuitry can contribute to these types of performance degradations including the analog signal processing circuitry preceding the ADC (gain and offset correction), the ADC itself, and the power, ground and control and data connections to the ADC. The design of the VIIRS Analog Signal Processor (ASP) includes provisions to address all of the above concerns in order to ensure that it provides the quality of science data required from the VIIRS instrument. Calibration data are provided in 14 bits and the earthview data are truncated to 12 bits.

### **2.2.3.2 Digital Pre-processing**

The DPP has three functions:

1. Reduce the bandwidth of the instrument data from the ASP and DNB
2. Orchestrate the timing of the ASP, DNB, Single Board Computer (SBC), and Electronics Module (EM) Power Supply
3. Capture and process RTA and HAM position telemetry

The SBC access the DPP in both operational and diagnostic modes.

[Figure 17](#) illustrates the DPP process for representing 'M' and 'I' band data. Single gain 'M' bands are stored by the ASP as 15-bit data and are grouped as 16 along-track pixels for each along-scan sample. These data are binary converted to 14 bit, with the gain bit ignored, and aggregated along-scan to form 14-bit values that are truncated to 12 bits, RICE compressed (lossless), and stored into the Lossless Data Random Access Memory (RAM). Data acquired during calibration (i.e. during SD, OBCBB, and space views) are stored into the Calibration Data RAM as their original 15-bit values. The calibration data are RICE compressed and stored in the Lossless Data RAM.

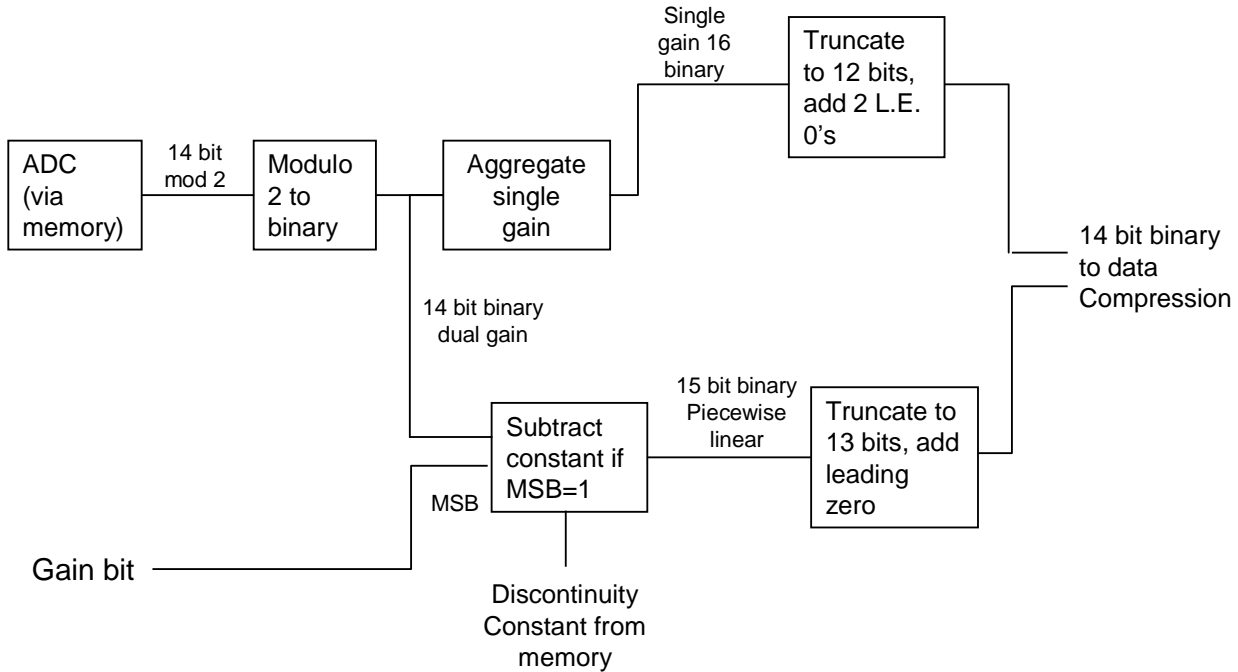


**Figure 17: VIIRS 'M' and 'I' Band Data Representation**

VIIRS has one single gain dual output band, M16A and M16B that requires averaging before the data are processed and stored. M16A is summed to M16B only after M16B is adjusted to match the gain and offset of M16A. The raw M16A and M16B Calibration data are stored in the Calibration Data RAM as their original 14-bit values.

Dual gain 'M' bands are stored by the ASP as 15-bit data consisting of 14-bit data plus 1-bit gain in the most significant bit. These data are grouped as 16 along-track pixels for each along-scan sample. These data have an offset value subtracted for values that have the gain bit set to "1", are truncated to 13-bits, RICE compressed, and stored into the Lossless Data RAM. Data acquired during calibrator views are stored into the Calibration Data RAM as their original 15-bit values.

'I' band samples are stored by the ASP as 15-bit data grouped as 32 along-track pixels for each along-scan sample. The data are binary converted to 14 bit with gain bit ignored then aggregated along-scan to form 14-bit values that are truncated to 12 bits, RICE compressed, and stored into the Lossless Data RAM. Data acquired during calibrator views are also stored into the Calibration Data RAM as their original 15-bit values.

The DPP captures DNB data from all four stages. It then selects Earth view data based on the gain selection logic shown in [Figure 18](#).

The DPP's ASP control function provides a means to write and to read from the ASP as well as controlling the FPA timing and data capture.

The DPP's Servo Monitor function monitors signals from the primary (PRI) or redundant (RDT) Servo Controller to determine the position of the telescope and HAM.

Figure 18 shows the scheme of VIIRS DNB gain selection among High Gain, Medium Gain, and Low Gain segments.

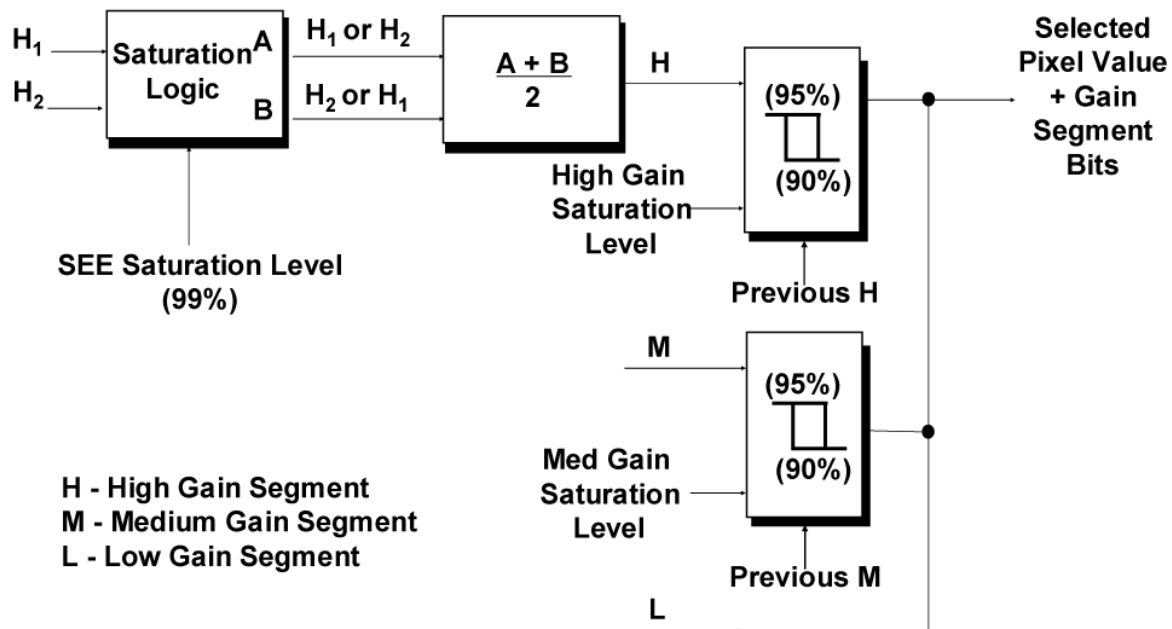


Figure 18: VIIRS DNB Gain Selection

### 2.2.3.3 DC Restore

The Digital Count (DC) restoration process for the VIIRS instrument is very similar to that employed on the MODIS, but has been modified where necessary to account for differences between the two designs. These differences include the use of dual gain bands<sup>3</sup> and the use of an RTA with a dual sided HAM derotator instead of the simpler single gain band and scan mirror architecture employed in MODIS.

<sup>3</sup> VIIRS dual gain bands include M1, M2, M3, M4, M5 and M7 on the Vis/NIR FPA and M13 on the S/MWIR FPA. The dual gain function resides within the Read-Out Integrated Circuit (ROIC) of the FPA and automatically selects between high (default) and low gain based on the input signal level detected during each integration period unless overridden.

DC Restore (DCR) is used to ensure that the FPA signals digitized by the ASP are always within the dynamic range of the ASP's ADCs. This is done by electronically summing a specific offset onto the FPA output signals for each detector channel such that their minimum, zero scene radiance output is biased to a level corresponding to approximately 200 counts out of the ADCs. This ensures that the lowest level signals from these outputs never drop below the dynamic range of the ADCs, which might otherwise result from aging and radiation effects.

This is a straightforward process for the reflective bands since their zero scene signals are already approximately zero. It is more complicated for the emissive bands since their zero scene radiance output signals are biased on a pedestal resulting from instrument self emission and detector dark current signals. The signal processing circuitry in the VIIRS is designed to remove the majority of this pedestal by restoring (offsetting) the output signal such that it corresponds to approximately 200 ADC counts when the emissive channels are viewing space.

This process is further complicated since VIIRS determines this offset based on data collected from the on-board blackbody and not the space view. The blackbody view is used for this process in order to avoid signal contamination that would otherwise result when the Moon and/or bright stars are within the space view calibration sector. Though the signals from these objects are mainly of concern to reflective band DC restoration, the architecture of the instrument requires all bands to be DC restored at the same time. Therefore, the actual offset employed for emissive band DC restoration must be calculated based on the temperature of the blackbody and the signal that should result from viewing it. This is done using an on-board look-up table that indicates the expected band output as a function of blackbody temperature, and by having the flight software adjust the offset level based on the difference between the actual and expected outputs.

The HAM introduces two variables that need to be accounted for during DC Restore and/or calibration. First, since the HAM is a two-sided mirror, differences between the reflectance (and emittance) of the two sides need to be tracked. Second, since the angle of incidence (and reflectance) of the source radiance changes as a function of HAM angle, the varying Response Versus Scan (RVS) contribution to overall instrument transmission (and emission) needs to be taken into account. This latter effect is a significant contributor to calibration, but does not impact DC restoration, since the OBC blackbody data used to compute the offset is always collected over a very small angular range centered at the fixed blackbody location.

The scan approach outlined in Section [2.2.2](#) demonstrates an additional complication with DC restoration. The data for DC restoration are collected from the OBCBB, which is towards the middle of each scan, and therefore it cannot be applied until after the scan has been completed. For calibration purposes this offset, along with biases due to self-emission and dark current, is detected as part of the space view data before the start of the earth view for each scan. Therefore it is not necessary to know the actual offset employed for DC restoration (though the offset data is included in the engineering

data packets transmitted by the Instrument), but it is important to maintain this same offset throughout the scan. The DC restore signal is used, however, to make gain and linearity adjustments as described in Section [2.3.1](#).

The two-sided HAM complicates this process since the data for each subsequent scan is collected from alternating sides of the HAM. Therefore, the flight software must keep track of the DC restore offsets calculated from one side of the HAM and save these values for use until that side of the HAM becomes active again. The bookkeeping effort associated with this side tracking and offset application process is described in *Description of DC Restore Process in the VIIRS Sensor [Y0012275]*.

The use of dual gain bands in VIIRS adds one final complication to the DC restore process. It is desirable to collect calibration data for both gain states of the dual gain bands. The dual gain bands would stay in their high gain modes when collecting the SV, OBCBB or SD views, if based on the expected signal levels from the calibration sources. However, the VIIRS includes the capability to force the dual gain bands into their low gain mode, and does so for every other pair of scans<sup>4</sup>. This allows collection of calibration data from both sides of the HAM in both gain modes. This results in an additional number of scans that must be skipped between collection and application of DC restoration data (as indicated in *[Y0012275]*) since the DC restore offsets are based on data collected while the band is in low gain mode. This is not considered a problem since the drift rate for all of the VIIRS bands is expected to be very slow compared to the DC restoration update rate, even for the dual gain bands that need to skip alternating scans.

## 2.2.4 On-board Calibrators

VIIRS is a conventional differencing radiometer that uses a space view (SV) to determine zero radiance and observations of a known radiance source to determine gain. The reflective bands' radiance source is an on-board Solar Diffuser (SD), for which the Bi-directional Reflectance Distribution Function (BRDF) is determined with pre-launch measurements. In order to determine changes with time of the SD reflectance, VIIRS uses a Solar Diffuser Stability Monitor (SDSM). Since the SDSM is basically a ratioing radiometer, it only monitors the change in magnitude of the BRDF, but does not accurately monitor changes to its directional dependence.

The known radiance source for the emissive bands is a blackbody reference. This On-Board Calibrator Blackbody (OBCBB) has a known emissivity (almost=1) and temperature. Self-emission from inside the instrument reflected off the OBCBB must be subtracted to properly determine the emissive band calibration.

---

<sup>4</sup> M13 low gain supports the Active Fires Application Related Requirement (ARR). Since the low gain signal level from M13 is expected to be on the order of four to eight ADC counts when it is viewing the on-board blackbody it is possible that it will not be forced into low gain mode as indicated in the text. This signal level is too low to be of much use and other methods are being investigated for calibrating this band when it is in the low gain mode.

#### **2.2.4.1 Solar Diffuser (SD)**

The SD is the major component of the on-board calibration source for the reflective bands. Knowledge of its bi-directional reflectance distribution function (BRDF) impacts the radiometric accuracy of VIIRS. For a perfectly Lambertian surface, BRDF would be related to the bi-directional reflectance function (BRF) by  $BRF/\pi$ . However, this does not hold exactly, since the SD surface deviates from being perfectly Lambertian. Though the SD Spectralon<sup>®</sup> panel<sup>5</sup> is expected to be nearly Lambertian, its BRDF has been measured over the expected angle of VIIRS operation. This is done prior to integration with the Opto-mechanical Module. If unfiltered, the on-orbit solar radiance reflected off the SD Spectralon<sup>®</sup> would be near the upper end of the dynamic range for most bands, therefore an attenuation screen with about 11% transmission is mounted in the SD view port to act as a neutral density filter. In actuality, the screen consists of many small holes packed closely together. This is expected to have some directional response, so the characterization includes the transmission screen characteristics as a function of solar incidence angles.

#### **2.2.4.2 Solar Diffuser Stability Monitor (SDSM)**

The SDSM monitors the stability of the SD's BRDF magnitude on orbit. The SDSM views the sun directly through an attenuation screen and indirectly via the SD. The components of the SDSM that are characterized are:

- Attenuation screen transmission
- Filter and detector spectral response
- Functional dependence of the above parameters on incident angles.

In addition, witness samples of the spectral filter and silicon detectors are maintained so that their stability over time can be monitored.

#### **2.2.4.3 On-Board Calibrator (OBC) Blackbody**

The On-board Calibrator (OBC) blackbody (OBCBB) provides the on-board calibration as well as the stability monitoring for the emissive bands. Thus it has a major impact on the radiometry of VIIRS. The major characteristics of the OBCBB that are tested before integration to Opto-mechanical Module are accuracy of the thermistors and uniformity of the blackbody temperature. The high-resolution "thermistors-in-glass-bead" temperature sensors are calibrated against National Institute of Standards and Technology (NIST) temperature standards. There is an array of six temperature sensors to measure the temperature from different parts of the OBCBB to ensure temperature uniformity. There are also redundant thermistors embedded in the OBCBB.

---

<sup>55</sup> "Spectralon" is a registered trademark of Labsphere<sup>®</sup>

## 2.2.5 Operation Modes

VIIRS has nine operation modes:

1. OFF
2. LAUNCH
3. SURVIVAL
4. SAFE
5. OUTGASSING
6. ACTIVATION
7. DIAGNOSTIC
8. OPERATIONAL-DAY
9. OPERATIONAL-NIGHT

NRT RDR to SDR processing requires that VIIRS be in either OPERATIONAL-DAY or OPERATIONAL-NIGHT mode. These operational modes as well as DIAGNOSTIC mode provide data to offline processes. The VIIRS SDR Calibration Algorithm is specifically designed to process only the Operational Mode data, and cannot process Diagnostic Mode data.

Earth view data from all VIIRS bands are packetized and sent to the S/C for downlink when in OPERATIONAL-DAY mode. In OPERATIONAL-NIGHT mode the following bands are not available for downlink: I1, I2, I3, M1, M2, M3, M4, M5, M6, M9, and M11.

## 2.2.6 Instrument Data Output

VIIRS produces the following data packet types for downlink by the S/C:

- Memory Dump
- Launch, Early Orbit and Activation (LEO&A)
- Health and Safety Telemetry
- High Rate Data (HRD), also known as Science Data (or Earth View)
- Calibration Data (SV, SD & OBCBB)
- Engineering Data

Packets of interest to the operational NRT radiometric calibration processing are the HRD, Health and Safety Telemetry, Calibration, and Engineering. Each is described in detail in “*VIIRS Command, Telemetry, Science, and Engineering Data Description*” [EDD154640-101]. These data are included in their entirety in the Verified VIIRS RDR’s (see Section [3.2.1](#)) that are produced during ground processing and provide the raw data input to the VIIRS radiometric calibration algorithm as well as the VIIRS geolocation algorithm.

## 2.2.7 Along-scan Aggregation

The *Performance Specification Sensor Specification for the VIIRS [PS154640-101]* places explicit requirements on spatial resolution for the VIIRS Imagery EDR. Specifically, the horizontal spatial resolution (HSR) of bands used to meet threshold

Imagery EDR requirements must be no greater than 400 m at nadir and 800 m at the edge of the scan. This requirement led to the development of a unique scanning approach, which optimizes both spatial resolution and signal-to-noise ratio (SNR) across the scan. This approach is described in SDRL 147-2 “*VIIRS Geolocation ATBD*” [Y3258].

The VIIRS detectors in the VIS/NIR are rectangular with the smaller dimension projecting along the scan [Cao et al., 2013b]. While in the SQIR/MWIR/LWIR, the detectors are octagonal in shape but made rectangular with the microlens. At nadir three detector samples from the Earth view are aggregated to form a single VIIRS “pixel.” Moving along the scan away from nadir the detector footprints become larger both along track and along scan due to geometric effects and the curvature of the Earth. The effects are much larger along scan. At 31.6 degrees in scan angle, the aggregation scheme is changed from 3x1 to 2x1. A similar switch from 2x1 to 1x1 aggregation occurs at 44.7 degrees. The pixel growth multiplier is limited to approximately 2 both along track and along scan, compared with a growth factor of 6 along scan which would be realized without the use of the aggregation scheme.

This aggregation is done on-board for the Earth view data from the single gain ‘M’ bands and the ‘I’ bands. The along-scan aggregations of Earth view data from the dual gain ‘M’ bands are done during ground processing to match the on-board single gain aggregations. This dual gain sample aggregation must follow radiometric calibration of the individual detector observations. The VIIRS Day/Night Band (DNB) is designed with no significant pixel growth as elements of the DNB CCD array are selected to maintain a nearly constant 742 m pixel size across scan.

## 2.3 GENERAL RADIOMETRIC EQUATIONS

With the exception of some band-pass filters and beam splitters the VIIRS is a reflective system. Transmittance and reflectance can be considered equivalent for most components. This ATBD follows the convention used in “*VIIRS Radiometric Calibration Equations*” [NGST Doc. D36966] where transmittance is represented with  $\rho$ , which is the common symbol for reflectance, even for components that may, in fact, not be reflective. The spectral transmittance through an optical system with many optical components is the product of all the transmittances (or reflectances) of each component.

The transmittance through the RTA, which contains four mirrors, as a function of wavelength  $\lambda$  is:

$$\rho_{ra}(\lambda) = \prod_1^4 \rho_j(\lambda)$$

Eq. 1.

The change in transmittance through the HAM is called Response Versus Scan (RVS) because of its scan angle dependence. An assumption is made that the scan angle dependence and the wavelength dependence are separable, which will hold true over the narrow spectral range of a single band,  $B$ .

$$\rho_s(\theta, \lambda) = \rho_{ham}(\lambda) \cdot \text{RVS}(\theta, B) \quad \text{Eq. 2.}$$

All of the optics past the HAM are referred to as the aft optics therefore:

$$\rho_{aft}(\lambda) = \prod_6^{N_{op}} \rho_j(\lambda) \quad \text{Eq. 3.}$$

where  $N_{op}$  is the number of optical elements from the aperture to the detectors. The full system transmittance is therefore:

$$\rho_{sys}(\theta, \lambda) = \prod_1^{N_{op}} \rho_j(\lambda) = \rho_{fix}(\lambda) \cdot \text{RVS}(\theta, B) \quad \text{Eq. 4.}$$

where  $\rho_{fix}(\lambda) = \rho_{rta}(\lambda) \cdot \rho_{ham}(\lambda) \cdot \rho_{aft}(\lambda)$ .

The detector signal is directly related to the irradiance on the detector field stop<sup>6</sup>. This irradiance is the sum of the irradiance from light entering the aperture and the background irradiance produced by self-emission of the optics and structure of the instrument:

$$E_{det}(\lambda, \theta) = \Omega_{stop} \cdot L_{ap}(\lambda, \theta) \cdot \rho_{sys}(\theta, \lambda) + E_{bkg}(\lambda, \theta) \quad \text{Eq. 5.}$$

where  $\Omega_{stop}$  is the solid angle of the aperture stop as seen from the field stop,  $L_{ap}(\lambda, \theta)$  is spectral radiance at the aperture at angle  $\theta$ , and  $E_{bkg}(\lambda, \theta)$  is detected spectral irradiance at the field stop due to self-emissive background at scan angle  $\theta$ .

Substitution of [Eq. 4](#) into [Eq. 5](#) yields the detected spectral irradiance on the field stop at scan angle  $\theta$ .

---

<sup>6</sup> The Vis/NIR bands have a focal plane array at the image plane of the system, so the field stop and the detector are one and the same. The S/MWIR bands and the LWIR bands, however, have a lenslet array at the focal plane with a mask to define the field stops. The lenslet array focuses the light onto the detectors.

$$E_{\text{det}}(\lambda, \theta) = \Omega_{\text{stop}} \cdot L_{\text{ap}}(\lambda, \theta) \cdot \rho_{\text{fix}}(\lambda) \cdot \text{RVS}(\theta, B) + E_{\text{bkg}}(\lambda, \theta)$$

Eq. 6

The spectral energy density is then determined by taking the product of the detected irradiance, the field stop area, and the integration time, i.e.  $\Delta t \cdot A \cdot E_{\text{det}}(\lambda, \theta)$ , in units of Joules per micron.

The number of photoelectrons per detection is

$$N_e = \int \text{QE}(\lambda) \cdot \frac{\lambda}{hc} \cdot [\Delta t \cdot A \cdot E_{\text{det}}(\lambda, \theta)] d\lambda$$

Eq. 7

where the  $\frac{\lambda}{hc}$  is Planck's formula, which gives the number of photons per Joule. Here  $h$  is Planck's constant and  $c$  is the speed of light.  $\text{QE}(\lambda)$  is the quantum efficiency converting photons to photoelectrons.

Substituting [Eq. 6](#) gives

$$N_e = \frac{\Omega_{\text{stop}} \cdot \Delta t \cdot A}{hc} \int \text{QE}(\lambda) \cdot \lambda \cdot \left[ L_{\text{ap}}(\lambda, \theta) \cdot \rho_{\text{fix}}(\lambda) \cdot \text{RVS}(\theta, B) + \frac{E_{\text{bkg}}(\lambda, \theta)}{\Omega_{\text{stop}}} \right] d\lambda.$$

Eq. 8

The Relative Spectral Response (RSR) is defined as the normalized product of the quantum efficiency, wavelength, and optical transmittance. It is normalized by the maximum value of this product.

$$\text{RSR}(\lambda) = \frac{\text{QE}(\lambda) \cdot \lambda \cdot \rho_{\text{fix}}(\lambda)}{\max(\text{QE}(\lambda) \cdot \lambda \cdot \rho_{\text{fix}}(\lambda))}$$

Eq. 9

Substituting this into [Eq. 8](#) gives

$$N_e = \frac{\Omega_{\text{stop}} \cdot \Delta t \cdot A \cdot \max(\text{QE}(\lambda) \cdot \lambda \cdot \rho_{\text{fix}}(\lambda))}{hc} \int \left[ \text{RSR}(\lambda) \cdot L_{\text{ap}}(\lambda, \theta) \cdot \text{RVS}(\theta, B) + \frac{\text{RSR}(\lambda)}{\rho_{\text{fix}}(\lambda)} \cdot \frac{E_{\text{bkg}}(\lambda, \theta)}{\Omega_{\text{stop}}} \right] d\lambda$$

Eq. 10

Defining band-averaged detectable radiance to be directly proportional to the number of photoelectron counts

$$\overline{L_{\text{det}}}(\theta, B) = G \cdot N_e$$

Eq. 11

where the gain factor  $G = \frac{h \cdot c}{\Delta t \cdot A \cdot \max(\text{QE}(\lambda) \cdot \lambda \cdot \rho_{\text{fix}}(\lambda)) \cdot \Omega_{\text{stop}} \int \text{RSR}(\lambda) d\lambda}$ .

Substituting [Eq. 10](#) into [Eq. 11](#) gives

$$\overline{L_{\text{det}}}(\theta, B) = \text{RVS}(\theta, B) \cdot \frac{\int \text{RSR}(\lambda) \cdot L_{\text{ap}}(\lambda, \theta) d\lambda}{\int \text{RSR}(\lambda) d\lambda} + \overline{L_{\text{det\_bkg}}}(\theta, B) \quad \text{Eq. 12}$$

Here the band-averaged background radiance is defined as

$$\overline{L_{\text{det\_bkg}}}(\theta, B) = \frac{\int E_{\text{bkg}}(\theta, \lambda) \cdot \frac{\text{RSR}(\lambda)}{\rho_{\text{fix}}(\lambda)} d\lambda}{\Omega_{\text{stop}} \int \text{RSR}(\lambda) d\lambda} \quad \text{Eq. 13}$$

Band averaging of a wavelength dependent function  $F(\lambda)$  can be represented with the notation

$$\overline{F(\lambda)} = \frac{\int \text{RSR}(\lambda) \cdot F(\lambda) d\lambda}{\int \text{RSR}(\lambda) d\lambda} \quad \text{Eq. 14}$$

The limits of the integrals over wavelength are not given, but should be taken to be the measurement range of the RSR, including Out-of-Band (OOB) portion of the response. Because the OOB RSR was carefully measured in test, it is included it. To simplify notation [Eq. 13](#) can be rewritten as

$$\overline{L_{\text{det\_bkg}}}(\theta, B) = \frac{1}{\Omega_{\text{stop}}} \cdot \left[ \frac{E_{\text{bkg}}(\theta, \lambda)}{\rho_{\text{fix}}(\lambda)} \right] \quad \text{Eq. 15}$$

The space view provides a calibration zero reference for radiance entering the aperture when  $L_{\text{ap}}(\lambda, \theta) = 0$ . Subtracting the space view detected radiance from detected radiance at a given angle,  $\theta$ , then applying [Eq. 12](#) to the detected radiance difference gives

$$\begin{aligned} \overline{\Delta L_{\text{det}}}(\theta, B) &= \overline{L_{\text{det}}}(\theta, B) - \overline{L_{\text{det}}}_{\text{sv}}(\theta, B) \\ &= \text{RVS}(\theta, B) \cdot \overline{L_{\text{ap}}}(\lambda, \theta) + \overline{\Delta L_{\text{det\_bkg}}}(\theta, B) \end{aligned} \quad \text{Eq. 16}$$

where

$$\overline{\Delta L_{\det\_bkg}}(\theta, B) = \overline{L_{\det\_bkg}}(\theta, B) - \overline{L_{\det\_bkg}}(\theta_{sv}, B) \quad \text{Eq. 17}$$

Substituting [Eq. 15](#) into [Eq. 17](#) gives

$$\overline{\Delta L_{\det\_bkg}}(\theta, B) = \frac{1}{\Omega_{stop}} \cdot \left[ \frac{(E_{bkg}(\theta, \lambda) - E_{bkg}(\theta_{sv}, \lambda))}{\rho_{fix}(\lambda)} \right] \quad \text{Eq. 18}$$

Band-averaged aperture radiance can be defined as

$$\overline{L_{ap}}(\theta, B) = \overline{L_{ap}}(\lambda, \theta) \quad \text{Eq. 19}$$

Combining [Eq. 16](#) and [Eq. 19](#) results in

$$\overline{L_{ap}}(\theta, B) = \frac{\overline{\Delta L_{\det}}(\theta, B) - \overline{\Delta L_{\det\_bkg}}(\theta, B)}{\text{RVS}(\theta, B)} \quad \text{Eq. 20}$$

### 2.3.1 Combining Detector and Electronics Subsystem Response

The response of the instrument is considered the combined response of the detectors in the Focal Plane Array (FPA) and the responses of the amplifiers in the Analog Signal Processor (ASP) and Analog to Digital Converter (ADC) electronics. This two-stage approach is valid as long as there is no ASP feedback into the FPA detector electronics. The output signal from a detector in the FPA is assumed to be directly related to  $N_e$ , which can be represented with a second order polynomial

$$N_e(V) = \sum_{i=0}^2 a_i \cdot V^i \quad \text{Eq. 21}$$

where  $V$  is detector output voltage.

Each  $a_0$ ,  $a_1$  and  $a_2$  coefficient has physical meaning. Coefficient  $a_0$  is a measure of the charge collected from the dark current through the detector. Coefficient  $a_1$  is the effective capacitance of the detector, which can be converted to farads by multiplying it by the elementary charge constant,  $e$ . The  $a_2$  coefficient is the change per volt in capacitance of the detector.

In order to convert the signal to a digital number ( $DM$ ), a DC restore voltage  $V_{dcr}$  is subtracted from  $V$  before it is input to the ASP and ADC.

$$V_{elec} = V - V_{dcr}$$

**Eq. 22**

The ADC and the ASP electronics may introduce some non-linearity therefore the electronics signal is expressed as a second order polynomial of the digital number

$$V_{elec}(DN) = \sum_{i=0}^2 b_i \cdot DN^i$$

**Eq. 23**

The total signal voltage as a function of counts can therefore be determined from [Eq. 22](#) and [Eq. 23](#)

$$V(DN) = V_{dcr} + \sum_{i=0}^2 b_i \cdot DN^i$$

**Eq. 24**

Substituting [Eq. 24](#) into [Eq. 21](#) gives

$$N_e(DN) = \sum_{i=0}^2 a_i \cdot \left( V_{dcr} + \sum_{j=0}^2 b_j \cdot DN^j \right)^i$$

**Eq. 25**

Substituting this into [Eq. 11](#) gives the nonlinear expression for detected radiance

$$\overline{L}_{det}(DN) = G \cdot \sum_{i=0}^2 a_i \cdot \left( V_{dcr} + \sum_{j=0}^2 b_j \cdot DN^j \right)^i$$

**Eq. 26**

Representing [Eq. 16](#) as a function of  $DN$  gives

$$\overline{\Delta L}_{det}(DN) = G \cdot \sum_{i=0}^2 a_i \cdot \left[ \left( V_{dcr} + \sum_{j=0}^2 b_j \cdot DN^j \right)^i - \left( V_{dcr} + \sum_{j=0}^2 b_j \cdot DN_{sv}^j \right)^i \right]$$

**Eq. 27**

The number of space view counts is subtracted from the total digital counts and this adjusted digital number ( $dn$ ) is used in calibration

$$dn = DN - \overline{DN}_{sv}$$

**Eq. 28**

Using  $dn$  in [Eq. 27](#) gives

$$\overline{\Delta L_{\text{det}}}(dn) = G \cdot \sum_{i=0}^2 a_i \cdot \left[ \left( V_{\text{dcr}} + \sum_{j=0}^2 b_j \cdot (dn + \overline{DN}_{sv})^j \right)^i - \left( V_{\text{dcr}} + \sum_{j=0}^2 b_j \cdot \overline{DN}_{sv}^j \right)^i \right] \quad \text{Eq. 29}$$

[Eq. 29](#) can be expanded and expressed as a fourth order polynomial in terms of  $dn$ :

$$\overline{\Delta L_{\text{det}}}(dn) = \sum_{i=0}^4 c_i \cdot dn^i \quad \text{Eq. 30}$$

The values for  $c_i$  are given in Table 11.

**Table 11: Fourth Order Calibration Coefficients**

Coefficient	Formula for $c_n(G, a_0, b_0, a_1, b_1, a_2, b_2, \overline{DN}_{sv}, V_{dcr})$
$c_0$	0
$c_1$	<b><math>G \cdot [a_1 \cdot b_1 + 2a_2 \cdot b_0 \cdot b_1 + 2a_1 \cdot b_2 \cdot \overline{DN}_{sv} + 4a_2 \cdot b_0 \cdot b_2 \cdot \overline{DN}_{sv} + 6a_2 \cdot b_1 \cdot b_2 \cdot \overline{DN}_{sv}^2 + 4a_2 \cdot b_2^2 \cdot \overline{DN}_{sv}^3 + 4a_2 \cdot b_2 \cdot \overline{DN}_{sv} \cdot V_{dcr} + 2a_2 \cdot b_1^2 \cdot \overline{DN}_{sv} + 2a_2 \cdot b_1 \cdot V_{dcr}]</math></b>
$c_2$	<b><math>G \cdot (2a_2 \cdot b_2 \cdot V_{dcr} + 2a_2 \cdot b_0 \cdot b_2 + 6a_2 \cdot b_1 \cdot b_2 \cdot \overline{DN}_{sv} + a_2 \cdot b_1^2 + a_1 \cdot b_2 + 6a_2 \cdot b_2^2 \cdot \overline{DN}_{sv}^2)</math></b>
$c_3$	<b><math>G \cdot (2a_2 \cdot b_1 \cdot b_2 + 4a_2 \cdot b_2^2 \cdot \overline{DN}_{sv})</math></b>
$c_4$	$G \cdot a_2 \cdot b_2^2$

Though [Eq. 30](#) and [Table 11](#) describe a 4<sup>th</sup> order equation, the existing algorithm design calls for only a second order equation to represent non-linear effects as,

$$\overline{\Delta L_{det}}(dn) = \sum_{i=0}^2 c_i \cdot dn^i \quad \text{Eq. 31}$$

For the expected VIIRS values of  $G, a_i, b_i, \overline{DN}_{sv}, V_{dcr}$ , only the terms in [Table 11](#) that are in bold are significant; all the other terms contribute less than 0.01% to the radiance. Therefore there is potential for considerable simplification when computing these coefficients.

To minimize the error produced by truncating the expansion to second order the expected value of this error can be distributed over the zeroth, first, and second order terms. The fraction of the error that is adjusted by each term is expressed by  $\Delta c_i$  for  $i=0, 1,$  and  $2$ . Statistical analysis determines the optimal values of  $\Delta c_i$ . The goal is to minimize the error function

$$Err = \text{RMS} \left( 2Ga_2b_2b_1 \cdot \left( \frac{\overline{L}_{ap}}{c_1} \right)^3 - \sum_{i=0}^2 \Delta c_i \cdot \left( \frac{\overline{L}_{ap}}{c_1} \right)^i \right) \quad \text{Eq. 32}$$

Since the first order term will dominate, it is a good approximation to assume

$$dn \approx \frac{\overline{\Delta L_{\text{det}}}(dn)}{c_1} \quad \text{Eq. 33}$$

Since  $c_0$  and  $c_2$  are expected to be small, this approximation will not introduce any significant error. The RMS in [Eq. 32](#) will depend on the expected  $dn$  distribution, which from [Eq. 33](#) is directly related to  $\overline{\Delta L_{\text{det}}}$ . The approximation  $\overline{\Delta L_{\text{det}}} \approx \overline{L_{\text{ap}}}$  ([Eq. 20](#)) implies that scene radiance distributions can be used from other satellite measurements such as from MODIS. Therefore an equation for the error can be written that does not depend on scene counts. Substituting [Eq. 33](#) into [Eq. 32](#) and making the approximation  $\overline{\Delta L_{\text{det}}} \approx \overline{L_{\text{ap}}}$  gives

$$Err = 2Ga_2b_2b_1 \left\langle \frac{\overline{L_{\text{ap}}}}{c_1} \right\rangle^3 \text{RMS} \left( \left( \frac{\overline{L_{\text{ap}}}}{\left\langle \frac{\overline{L_{\text{ap}}}}{c_1} \right\rangle} \right)^3 - \sum_{i=0}^2 \frac{\Delta c_i}{2Ga_2b_2b_1} \left\langle \frac{\overline{L_{\text{ap}}}}{c_1} \right\rangle^{i-3} \cdot \left( \frac{\overline{L_{\text{ap}}}}{\left\langle \frac{\overline{L_{\text{ap}}}}{c_1} \right\rangle} \right)^i \right) \quad \text{Eq. 34}$$

where  $\left\langle \frac{\overline{L_{\text{ap}}}}{c_1} \right\rangle$  is computed pre-launch and should not be recomputed based on on-orbit changes in  $c_1$ .

Minimizing the error is a straightforward process using [Eq. 34](#) once  $c_1$  is known and a distribution  $\overline{L_{\text{ap}}}$  is available. The proper coefficients to use with the second order calibration [Eq. 31](#) are given in [Table 12](#).

During EDU testing the following observations were made:

- For certain mid-wave infrared (MWIR) bands and/or detectors, a 3<sup>rd</sup> order equation may more accurately represent the detected radiance difference ([Eq. 31](#)).
- Out-of-family detectors sometimes have a significant 3<sup>rd</sup> order response which makes it impossible to meet the strict uniformity requirement (SRV0613). Allowing for a 3<sup>rd</sup> order correction could bring these detectors into compliance with the uniformity requirement.

For this reason a 3<sup>rd</sup> order coefficient ( $c_3$ ) has been added in the relevant equations. This coefficient will nominally be set to zero for bands or detectors where it is not needed. Because a 3<sup>rd</sup> order correction is considered the exception rather than the rule, all summations are shown only to the second order. Second order correction is still considered the baseline approach. It will be difficult to maintain 3<sup>rd</sup> order coefficients on orbit, but for out-of-family detectors, the third order coefficient can be adjusted to provide good uniformity with respect to the other detectors, which are corrected to second order.

The 3<sup>rd</sup> order correction is performed entirely by using the  $\Delta c_3$  term as shown in [Table 12](#).

**Table 12: Second Order & 3<sup>rd</sup> Order Calibration Coefficients**

Coefficient	Formulas for $c_n$
$c_0(T_{det}, T_{elec})$	$\Delta c_0(T_{det}, T_{elec})$
$c_1(T_{det}, T_{elec}, V_{dcr})$	$G \cdot b_1(T_{elec}) \cdot [a_1(T_{det}) + 2a_2(T_{det}) \cdot V_{dcr}] + \Delta c_1(T_{det}, T_{elec})$
$c_2(T_{det}, T_{elec}, V_{dcr})$	$G \cdot [ \{ a_1(T_{det}) + 2a_2(T_{det}) \cdot V_{dcr} \} \cdot b_2(T_{elec}) + a_2(T_{det}) \cdot b_1(T_{elec})^2 ] + \Delta c_2(T_{det}, T_{elec})$
$c_3(T_{det}, T_{elec})$	$\Delta c_3(T_{det}, T_{elec})$ (set to zero in most cases)

In some cases the assumption that sensor response depends only on detector and electronics temperature along with the  $V_{dcr}$  may be faulty. In actual testing, temperature dependencies were seen in the SWIR bands that were strongly correlated with Opto-Mech Module (OMM) temperature. Therefore, the definition of  $T_{det}$  may include temperatures other than the actual focal plan array temperature, such as the OMM temperature. In these cases, however, the dependence on DC restore voltage shown in [Table 12](#) does not make sense, so it should be dropped. This can be done by setting  $a_2 = 0$ . Also,  $T_{det}$  is generalized to the name  $T_a$ . The products of the  $a$  and  $b$  coefficients produce what is effectively a bilinear interpolation over 2 temperature variables. This is shown in [Table 13](#).

**Table 13: Alternative Second Order & 3<sup>rd</sup> Order Calibration Coefficients**

Coefficient	Formulas for $c_n$
$c_0(T_a, T_{elec})$	$\Delta c_0(T_a, T_{elec})$
$c_1(T_a, T_{elec})$	$G \cdot a_1(T_a) \cdot b_1(T_{elec}) + \Delta c_1(T_a, T_{elec})$
$c_2(T_a, T_{elec})$	$G \cdot a_1(T_a) \cdot b_2(T_{elec}) + \Delta c_2(T_a, T_{elec})$
$c_3(T_a, T_{elec})$	$\Delta c_3(T_a, T_{elec})$ (set to zero in most cases)

### 2.3.2 Response and Thermal Dependence

The coefficients in [Table 12](#) are explicitly dependent on two temperatures; detector temperature  $T_{det}$  and electronics temperature  $T_{elec}$ . For the emissive bands there is also an implicit dependence on the self-emissive background temperature of the optics. This is because the DC Restore (DCR) voltage acts to offset this emissive background and is therefore a good measure of it.

As the self-emissive background changes, the additional flux shifts the detector to a different part of its response curve. Since the response is approximately parabolic the slope of the response changes slightly with this shift. Therefore this change in slope is compensated for in [Table 12](#) by adding  $2a_2 \cdot V_{dcr}$ , which represents an adjustment to the effective capacitance of the detector, to  $a_1$ . For the reflective bands  $V_{dcr}$  is not expected to change very much since it compensates only for the detector dark current, which is fairly constant.

Since coefficients  $a_1$  and  $a_2$  describe the response of the detectors they will show a dependence on detector temperature. While varying the temperature and measuring the response in pre-launch thermal vacuum tests could be used to characterize this temperature dependence, the current test plans do not call for this. Also, these tests could be done at the detector sub-system level since the coefficients are dependent only on detector characteristics, but again current test plans do not call for this (ref. TP154640-118 & TP154640-274). The ramifications of not characterizing the thermal dependence of the detector response are discussed in [Section 2.4.1.2](#).

Likewise, coefficients  $b_1$  and  $b_2$  describe the response of the electronics. These coefficients are dependent only on the temperature of the electronics subsystem. Varying the temperature and measuring the response in pre-launch tests will be used to characterize this temperature dependence. These tests could be done at the electronic sub-system level since the coefficients are dependent only on electronics characteristics but test plans do not call for this (ref. TP154640-118 & TP154640-274).

### 2.3.3 General Equations for Emissive Bands

The irradiance  $E(\lambda)$  upon the field stop from some emissive source is the product of four factors:

1. Transmittance from the source to the field stop,  $\tau(\lambda)$
2. Effective solid angle  $\Omega$  of the source as seen from the field stop
3. Emissivity of source  $\varepsilon(\lambda)$
4. Blackbody spectral radiance

$$E(\lambda) = \tau(\lambda) \cdot \Omega \cdot \varepsilon(\lambda) \cdot L(T, \lambda)$$

Eq. 35

Blackbody spectral radiance as a function of temperature and wavelength based on Planck's formula is

$$L(T, \lambda) = \frac{2c^2 h \cdot 10^{-6}}{\lambda^5 \left( \exp\left(\frac{hc}{kT\lambda}\right) - 1 \right)} \quad \text{Eq. 36}$$

where  $c$  is the speed of light,  $h$  is Planck's constant, and  $k$  is Boltzmann's constant.

All physical constants and wavelength are given here in meter-kilogram-second (mks) units, and therefore Planck's formula would output in mks units of  $\text{W}/\text{m}^3/\text{sr}$ , except that it is multiplied by the factor  $10^{-6}$  to convert to units of  $\text{W}/\text{m}^2/\mu\text{m}/\text{sr}$ .

The total background irradiance is the sum from all emissive sources. A double sum is used here, where the sum over index  $i$  is over each of the optical elements and the sum over  $j$  is over all of the emissive sources entering the optical path at optical component  $i$ . The emission from the previous optical element is also included.

$$E_{bkg}(\lambda, \theta) = \sum_{i=2}^{N_{op}+1} \left\{ \prod_{k=i}^{N_{op}+1} \rho_k(\lambda) \cdot \left[ \Omega_{i-1} \cdot \varepsilon_{i-1}(\lambda) \cdot L(T_{i-1}, \lambda) + \sum_{j=1}^{N_{src}(i)} \Omega_{i,j} \cdot \varepsilon_{i,j}(\lambda) \cdot L(T_{i,j}, \lambda) \right] \right\} \quad \text{Eq. 37}$$

where  $N_{op}$  is the number of optical elements from the aperture to the detectors and  $N_{src}(i)$  is the number of emissive sources producing self-emission that enters the optical path through optical element  $i$ .

Note that both the sum and the product in [Eq. 37](#) go up to  $N_{op}+1$ . This is done so that any sources between the last optical element and the field stop are included. The transmittance of empty space is one leading to the assumption that  $\rho_{N_{op}+1}(\lambda) = 1$ . The optical components themselves are emissive sources, so the emissivity and temperature for  $i-1$  refers to the optical component just preceding component  $i$ .

The notation in [Eq. 37](#) where  $\Omega$ ,  $\varepsilon$  or  $T$  has one index (e.g.  $\Omega_{i-1}$ ) the reference is to the solid angle, emissivity, or temperature of the respective optical elements. Where  $\Omega$ ,  $\varepsilon$  or  $T$  has two indices (e.g.  $\Omega_{i,j}$ ) the reference is to emissive sources entering the optical path starting at optical component  $i$ , for example, the instrument structure around the optical elements.

The values of  $\Omega_{i,j}$  represent the effective solid angles of the surrounding structure that is visible to the detector. The effective solid angle of an emissive surface is determined by tracing a large number of rays,  $N_{ray}$ , from the detector into a hemisphere and determining the number that intersect the surface in question. The number of rays that intersect divided by  $2\pi \cdot N_{ray}$  yields the solid angle.

A ray-tracing program such as ASAP is used for determining this effective solid angle. The effective solid angle must be scaled to adjust for the change in magnification from

the detector to the field stop. From the optical invariant rule the magnification factor of solid angle caused by the lenslet is  $\frac{\Omega_{stop}}{F_{det} \cdot \Omega_{fs@det}}$  where  $\Omega_{stop}$  is the solid angle of aperture stop (optical component 6 as identified in [Table 9](#)) as seen from the field stop,  $F_{det}$  is the fraction of detector illuminated by imaged aperture stop, and  $\Omega_{fs@det}$  is the solid angle of field stop as seen from the detector

$$\Omega_{i,j} = \frac{\Omega_{stop}}{F_{det} \cdot \Omega_{fs@det}} \cdot 2\pi \cdot N_{ray} \quad \text{Eq. 38}$$

The relationship between emissivity and reflectance for a highly specular surface (such as a mirror) is<sup>7</sup>

$$\varepsilon(\lambda) = 1 - \rho(\lambda) \quad \text{Eq. 39}$$

The aperture stop (optical component 6) blocks all self-emission outside the solid angle of the stop, therefore

$$\begin{aligned} \Omega_{i,j} &= 0 \quad \text{if } i < 6 \\ \Omega_i &= \Omega_{stop} \quad \text{if } i < 6 \end{aligned} \quad \text{Eq. 40}$$

Application of [Eq. 2](#), [Eq. 3](#), [Eq. 39](#) and [Eq. 40](#) to [Eq. 37](#) gives

$$\begin{aligned} E_{bkg}(\lambda, \theta) &= \rho_{aft}(\lambda) \cdot \Omega_{stop} \cdot \left\{ \begin{aligned} &\rho_{ham}(\lambda) \cdot \text{RVS}(\theta) \cdot \sum_{i=1}^4 \left[ (1 - \rho_i(\lambda)) \cdot L(T_i, \lambda) \prod_{k=i+1}^4 \rho_k(\lambda) \right] \\ &+ (1 - \rho_{ham}(\lambda)) \cdot \text{RVS}(\theta) \cdot L(T_{ham}, \lambda) \end{aligned} \right\} \\ &+ \sum_{i=7}^{N_{op}+1} \left\{ \prod_{k=i}^{N_{op}+1} \rho_k(\lambda) \cdot \sum_{j=1}^{N_{src}(i)} \Omega_{i,j} \cdot \varepsilon_{i,j}(\lambda) \cdot L(T_{i,j}, \lambda) \right\} \end{aligned} \quad \text{Eq. 41}$$

One simplifying assumption that can be made is that all components of the RTA have the same temperature, that is

$$T_{rta} = T_1 = T_2 = T_3 = T_4 \quad \text{Eq. 42}$$

<sup>7</sup> To be exact, the emittance in a given direction is 1 minus the hemispherical-to-directional reflectance in the same direction. The reflectance in [Eq. 37](#) is given as a specular reflectance, not a hemispherical-to-directional reflectance, but for a specular surface the quantitative difference is small. It should be noted that this is an approximation.

Actual thermal models have shown significant temperature differentials within the RTA of several K. Nevertheless, sensitivity analysis that has been performed show that making this assumption does not cause a significant increase in calibration error.<sup>8</sup>

Applying [Eq. 1](#) and [Eq. 42](#) to [Eq. 41](#) gives

$$E_{bkg}(\lambda, \theta) = \rho_{aft}(\lambda) \cdot \Omega_{stop} \cdot \left\{ \begin{aligned} & \rho_{ham}(\lambda) \cdot \text{RVS}(\theta) \cdot (1 - \rho_{rta}(\lambda)) \cdot L(T_{rta}, \lambda) \\ & + (1 - \rho_{ham}(\lambda)) \cdot \text{RVS}(\theta) \cdot L(T_{ham}, \lambda) \end{aligned} \right\} \\ + \sum_{i=7}^{N_{op}+1} \left\{ \prod_{k=i}^{N_{op}+1} \rho_k(\lambda) \cdot \sum_{j=1}^{N_{src}(i)} \Omega_{i,j} \cdot \varepsilon_{i,j}(\lambda) \cdot L(T_{i,j}, \lambda) \right\} \quad \text{Eq. 43}$$

After substitution of [Eq. 43](#) into [Eq. 16](#) and application of [Eq. 4](#)

$$\overline{\Delta L_{det\_bkg}}(\theta, B) = (\text{RVS}(\theta, B) - \text{RVS}(\theta_{sv}, B)) \cdot \left( \frac{\{(1 - \rho_{rta}(\lambda)) \cdot L(T_{rta}, \lambda) - L(T_{ham}, \lambda)\}}{\rho_{rta}(\lambda)} \right) \quad \text{Eq. 44}$$

Analysis shows that the band averaging in [Eq. 44](#) is separable.<sup>9</sup> The analysis showed that some error results for the MWIR bands, but this error is small and almost entirely alleviated if the band averaged value of  $\rho_{rta}$  is taken as a weighted average using the emissive Planck spectrum for the weighting for a temperature at the average instrument temperature of approximately 280K.

Combination of equations [Eq. 31](#), [Eq. 20](#) and [Eq. 44](#) yields

$$\overline{L_{ap}}(\theta, B) = \frac{\sum_{i=0}^2 c'_i \cdot dn^i - (\text{RVS}(\theta, B) - \text{RVS}(\theta_{sv}, B)) \cdot \frac{\{(1 - \overline{\rho_{rta}}(\lambda)) \cdot \overline{L(T_{rta}, \lambda)} - \overline{L(T_{ham}, \lambda)}\}}{\overline{\rho_{rta}}(\lambda)}}{\text{RVS}(\theta, B)} \quad \text{Eq. 45}$$

## 2.4 RADIOMETRIC CALIBRATION TIMELINE

Radiometric calibration starts early in the VIIRS development process and continues through the instrument's pre-launch testing and mission operations phase. During the pre-launch phase, calibration and characterization ground tests are performed. Once on orbit an intensive period of calibration update and instrument performance

<sup>8</sup> Mills, Steve, "VIIRS IR calibration uncertainty as a function of sensor characterization uncertainty", NGST Doc. #D36947, 5 May 2003.

<sup>9</sup> Mills, Steve, "Analysis of Band Averaging Approximation in VIIRS Calibration Equations", NGST Engineering Memo, 16 December 2003.

verification occurs, which is followed by a continuous period of long-term monitoring and sustaining calibration and validation.

### 2.4.1 Pre-Launch

Prior to launch tests are performed at Raytheon facilities under ambient and thermal vacuum (TV) conditions to characterize VIIRS' performance and to determine its calibration coefficients. Pre-launch characterization is an integral part of VIIRS instrument performance verification. The purpose of this characterization is to verify that the instrument design meets requirements per the "*Performance Specification Sensor Specification*" [PS154640-101] and to quantify specific instrument parameters that are required for ground data processing (e.g. radiometric calibration). Furthermore, it is necessary to verify that the instrument has adequate radiometric performance to permit calibration. The testing process evaluates performance over the entire range of expected on-orbit environmental and operating conditions.

The philosophy of the calibration and validation program for VIIRS is to validate the performance parameters as early as possible in the assembly process. Radiometric calibration, spatial response and spectral response are the three major categories of performance parameters to be characterized. The impacts of various subassemblies on these performance parameters include:

- Telescope Assembly (Includes baffle) : Polarization, optical transmission, stray light impacts
- Aft Optics Assembly (Includes back-end optics): Polarization, optical transmission impacts
- Half Angle Mirror (HAM) Assembly: Angular reflectance, variable polarization impacts
- Focal Plane Assemblies: Quantum efficiency, dynamic range, noise, temperature sensitivity, linearity, operability impacts
- Electronics Assemblies: Noise, temperature characteristics impacts
- Solar Diffuser (SD): Bi-directional reflectance distribution function (BRDF) impacts
- SDSM: Transmission screen, detector stability, filter stability, integrating sphere stability impacts
- OBC Blackbody: Temperature accuracy, uniformity impacts

Tests that demonstrate that the requirements are satisfied are performed primarily at the VIIRS instrument level; however, some are repeated at multiple levels of assembly to check the validity of the instrument radiometric model at multiple stages. The variation of each parameter as a function of environment and time is also characterized.

Specific pre-launch testing for VIIRS includes:

1. Responsivity and offset - performed during payload TV to transfer calibration to VIIRS from NIST standard.

2. On-board Calibrator (OBC) Blackbody Characterization - performed during payload TV to transfer calibration to the OBC blackbody.
3. Internal Calibration Source Stability - Collect VIIRS data while viewing a known radiance source then collect data while viewing OBC blackbody. Performed as often as possible; at least once a day during payload I&T. Provides data to demonstrate long-term stability of SD/OBC blackbody.
4. Noise Sensitivity to Electronics Module Temperature - Measure the temporal variance in response to any known radiance source while varying the signal processing electronics box temperature. Performed during ambient payload component testing. Involves only FPA and signal processing electronic boxes. Provides data about possible electronic timing induced coherent noise.
5. Responsivity Sensitivity to FPA Temperature -performed during payload T/V to provide data about variation in instrument responsivity as function of FPA temperature for possible calibration correction.
6. Responsivity Sensitivity to Scan Angle – performed during payload TV to provide data about variation in instrument responsivity as function of VIIRS HAM position for possible calibration correction.
7. Flat-Fielding – Performed while scanning and viewing the Blackbody Calibration Source (BCS). Data is collected to test both sides of HAM. At the end of the scan collect data from OBC blackbody. Performed during payload TV to provide data to demonstrate the ability of internal calibration sources to remove pixel-to-pixel response variation. (This demonstrates the severity of any 'striping' problem).
8. Linearity – performed during payload TV to provide information about the instrument response as function of radiance level for incorporation into calibration procedure.
9. Polarization - performed during payload ambient testing to measure polarization sensitivity of the reflective bands for later use in calibration correction.
10. Dynamic Range - performed during payload TV to measure the response of the instrument when exposed to the maximum expected radiance (Provides information about the maximum observable radiance without A/D saturation).
11. Signal to Noise Ratio - performed during ambient or payload TV testing to measure the temporal mean and variance of the instrument response to a constant, uniform scene at multiple radiance levels. Provides the signal to noise ratio of the instrument at multiple radiance levels within the required dynamic range.
12. SD coordinate system - measured pre-launch to define the transformation from the z-axis normal to the Solar Diffuser Screen (SDS) and the x-axis in the along-track direction.

#### **2.4.1.1 Subsystem Tests**

Either several pre-launch subsystem measurements need to be made or data needs to be collected from subsystem manufacturers in order to implement the calibration algorithms. These measurements are:

- Angular alignment measurements to determine the position of the solar diffuser relative to the instrument coordinate system.
- Quantum efficiency of each band as a function of wavelength,  $QE(\lambda)$ , that includes the wavelength range of all VIIRS bands. Wavelengths are to be across the entire band, including Out of Band (OOB) spectral response. The data available from detector manufacturers is sufficient.
- Spectral reflectance/transmittance of the RTA optics  $\rho_{rta}(\lambda)$  for wavelengths to cover all the emissive bands, or a band-averaged measurement over  $\lambda$ , weighted for a Planck blackbody emissive spectrum at about 280 K.
- Solar diffuser BRDF  $(\phi_h, \phi_v, \lambda, 0)$  measured at wavelengths representing all the reflective bands, or a band-averaged measurement over  $\lambda$ , and over ranges of  $\phi_v$  and  $\phi_h$  sufficient to cover all possible illumination angles.
- Solar diffuser screen transmittance,  $\tau_{sds}(\phi_h, \phi_v, \lambda)$  measured at wavelengths representing all the reflective bands, and over ranges of  $\phi_v$  and  $\phi_h$  sufficient to cover all possible illumination angles, or a band-averaged measurement over  $\lambda$ .
- Emissivity of the OBCBB,  $\varepsilon_{obc}(\lambda)$  measured at wavelengths representing all the emissive bands, or a band-averaged measurement over  $\lambda$ .
- The fractional reflectance factors  $F_{sh}$ ,  $F_{cav}$  and  $F_{tele}$  representing reflectance off the OBCBB from each of the three sources: OBCBB shield, cavity and telescope, respectively.

#### 2.4.1.2 System Tests

Several pre-launch system measurements need to be made in order to implement the calibration algorithms. These are:

- Response Versus Scan,  $RVS(\theta)$ , for all reflective bands using SIS(100) lamps
- Response Versus Scan,  $RVS(\theta)$ , for all emissive bands using the Laboratory Ambient Blackbody (LABB) by varying  $\theta_{labb}$ .
- Detector response for emissive bands at the system level using the BCS, measuring  $dn_{bcs}$  as a function of  $\overline{L(T_{bcs}, \lambda)}$  by varying  $T_{bcs}$ . The radiance measurements must include a zero radiance measurement for  $DN_{sv}$ . These should be measured at several temperatures as defined in the test plan, and are within the expected operating range of the detectors. The S/MWIR and LWIR detectors have operating temperature set points at 76K, 78K and 80K.<sup>10</sup> These measurements are repeated at three thermal plateaus for the instrument.

---

<sup>10</sup> Test plans call for measurement at only one set point 80 K.

- Detector response at the system level for reflective bands using the SIS(100), measuring  $dn$  as a function of  $\overline{L_{ap}}$ . These measurements are repeated at three thermal plateaus for the instrument.
- Measurement of the RSR for each band, including coarser measurements for OOB response.

Thermal vacuum testing is summarized in [Table 14](#).

**Table 14: Summary of TV Testing**

Test	Name	Description	GSE Used
RC-1	Radiometric response & sensitivity, ambient	This test is done at ambient temperature. Part 1 tests the emissive bands using the LABB & TMC BB at several brightness temperatures. Part 2 tests the reflective bands at several SIS100 radiances. Part 3 tests the DNB response characterization. Part 4 tests dual gain transitions.	LABB, SVS TMC BB, SIS100
RC-2	Reflective band radiometric response and sensitivity	This tests the radiometric response of the reflective bands using the SIS100 as a source. Radiance levels are varied to determine full response. This includes the DNB.	SVS. SIS100 TMC SIS
RC-3	Radiometric response stability	This tracks the response of all the bands during transition between thermal plateaus. It determines temperature sensitivity of the gain for all bands.	BCS, SVS SIS100
RC-5	Emissive band radiometric response and sensitivity	This tests the radiometric response of the emissive bands using the BCS as a source. Brightness temperature levels are varied to determine full response.	BCS, SVS

#### **2.4.1.2.1 System Level Calibration from Pre-Launch Testing**

Referring back to Section [2.3](#) if the temperature dependence of coefficients  $a_0$ ,  $a_1$ ,  $a_2$ ,  $b_0$ ,  $b_1$ , and  $b_2$  are characterized then coefficients  $c_0$ ,  $c_1$ , and  $c_2$  are determined as a function of detector temperature  $T_{det}$  and electronics temperature  $T_{elec}$  by using the equations given in [Table 12](#). The coefficients  $\Delta c_i$  allow for fitting the subsystem measurements of  $a_1$ ,  $a_2$ ,  $b_1$ , and  $b_2$  to system level measurements of coefficients  $c_0$ ,  $c_1$ , and  $c_2$ . However, current test plans do not call for characterization sufficient to determine  $\Delta c_i$ ,  $a_1$  or  $a_2$  (ref. TP154640-118 & TP154640-274).

So even though some pre-launch subsystem measurements of the detector and electronic response are part of acceptance testing, this characterization does not determine the coefficients  $a_i$  and  $b_i$  accurately or thoroughly enough to be used for calibration as described in [Table 12](#). It is also not certain whether these values measured at a subsystem level, would remain stable through the life of the mission. This created a concern that there was a potential gap in pre-launch characterization.<sup>11</sup>

Since the actual responses of the detectors has been measured and temperature dependency at least partially understood, a more informed discussion about modeling temperature dependence in response coefficients can be made. This describes the process of determining calibration coefficient temperature dependence. It may not be perfect, but this represents a starting point before launch. The following principles guided the decision about how temperature dependence is applied:

<sup>11</sup> De Luccia, Frank J. , "Memo for the Record, VIIRS as a Two-Stage System", 6 February 04.

1. Minimize changes to the calibration algorithm. For example, changes to have separate ASP temperatures for each FPA, while desirable, is not in the existing coefficients as described in [Table 12](#).
2. Temperature dependencies should have a physically explainable mechanism. As noted below, the SWIR aperture stop dependency created a problem here.
3. It should be maintainable on orbit. For example, having second order coefficients for both  $a_2$  and  $b_2$  complicate recomputation of coefficients.
4. It should avoid confusion. As noted below, substituting the Opto-Mech Module (OMM) temperature for the detector temperature may work, but it may also cause confusion.
5. The results should converge to the measured coefficients at the 3 plateau temperatures.

The following temperature dependencies of the gains based on correlations between temperature and response observed in test RC-3 (described in [Table 14](#)) have been determined:

**Table 15: Relative change in Response per K observed in RC3**

	Bands	FPA	ASP	Aperture Stop	OMM
Vis/NIR	I1	-2e-4	≈0	≈0	≈0
	I2	≈0	≈0	≈0	≈0
	M1	5e-5	2e-5	≈0	≈0
	M2 & M3	≈0	-1e-4	≈0	≈0
	M4 & M5	1e-3	1e-4	≈0	≈0
	M6	4e-4	≈0	≈0	≈0
	M7	8e-4	1e-4	≈0	≈0
SWIR	I3	N/A	≈0	3e-4	≈0
	M8 & M10	N/A	≈0	2e-4	≈0
	M9 & M11	N/A	≈0	≈0	≈0
MWIR	I4	N/A	≈0	≈0	Significant
	M12 & M13	N/A	≈0	≈0	Significant
LWIR	I5	N/A	≈0	≈0	Significant
	M14 - M16	N/A	≈0	≈0	Significant

The stability requirement for the Thermal Emissive Bands (TEB) is 0.1% and for the Reflective Solar Bands (RSB) it is 0.3%. This requirement is on the stability to be maintained between successive calibrations. Temperatures for most of the instrument change only a few degrees over an orbit, so the stability requirement would likely be met even if there was no calibration compensation for temperature change. Temperatures for different parts of the sensor are highly correlated, so even if the optimal thermistor is not found, others should do almost as well. Some of the dependencies indicated in the table are not easily explained, and the current SDR

calibration algorithm does not have a mechanism to easily apply the temperature dependencies for OMM or aperture stop.

The ASP actually has separate cards for each of the focal planes, and each of these focal planes has a separate thermistor. Ideally, we should have in the SDR algorithm a separate  $T_{elec}$  for the electronics of each focal plane. These three temperatures, while not exactly equal, should be very strongly correlated, and it should be sufficient to use the average of the three as  $T_{elec}$ .

### Vis/NIR Bands

For the Vis/NIR bands the following assumptions are made and the justification is given:

1. Because there is no background for the RSB, the DC restore dependence will not be significant. Therefore, one assumption that simplifies the equations significantly is that the detector response is linear with  $a_2 = 0$ .
2. Source stability was an issue during RSB testing and so it must be assumed that relative gain change between the plateaus is not well known. Therefore,  $c_1$  is not well known, but only the values of  $c_0/c_1$  and  $c_2/c_1$  are meaningful.
3. Temperature change of the gain is best determined from the RC-3 rather than RC-2 tests.
4. The nonlinearity described by  $c_2/c_1$  is assumed to depend only on the electronic temperature.
5. An average ASP electronic temperature represents the temperature for the ASP for the LWIR and MWIR processors.

From assumption 1 the equations simplify to:

$$\begin{aligned} c_1(T_{det}(n), T_{elec}(n)) &= G \cdot a_1(T_{det}(n)) \cdot b_1(T_{elec}(n)) \\ c_2(T_{det}(n), T_{elec}(n)) &= G \cdot a_1(T_{det}(n)) \cdot b_2(T_{elec}(n)) \end{aligned} \quad \text{Eq. 46}$$

where  $n$  refers to the plateau, with  $n=1, 2$  or  $3$  for cold, nominal and hot respectively. Taking the ratio of these gives

$$\frac{c_2(n)}{c_1(n)} = \frac{b_2(T_{elec}(n))}{b_1(T_{elec}(n))} \quad \text{Eq. 47}$$

From the RC-3 test the values of  $q$  and  $r$  have been determined. These are summarized by the values in the [Table 15](#) but exact values for each detector should be used. The values of  $q$  and  $r$  are the relative change in gain as a function of temperature for the detector and ASP electronics temperatures respectively. The relationship between the plateaus for  $a_1$  and  $b_1$  can be expressed as

$$a_1(T_{det}(1)) = (1 + Q_{12}) \cdot a_1(T_{det}(2))$$

$$b_1(T_{elec}(1)) = (1 + R_{12}) \cdot b_1(T_{elec}(2))$$

where

Eq. 48

$$Q_{12} = q \cdot (T_{det}(1) - T_{det}(2))$$

$$R_{12} = r \cdot (T_{elec}(1) - T_{elec}(2))$$

The same relationships apply likewise between the nominal and hot plateaus (2 and 3 respectively). Based on the individual curve fits for each plateau, the ratios  $c_0/c_1$  and  $c_2/c_1$  represent each combination of band, detector, mirror-side and gain state for all 3 plateaus.

The process is to project these gain dependencies to the other plateaus based on the nominal plateau. Details of the process are given in NP-EMD-2010.510.0030.

### **SWIR Bands**

It is difficult to determine one specific mechanism for the SWIR gain dependence on aperture stop temperature. Several mechanisms have been suggested. It may be that this is actually the result of a change in effective focal length which may be correlated with aperture stop temperature. The concern about this mechanism is that it cannot explain why other SWIR RSB is sensitive to this. The second possibility may be some type of crosstalk from the MWIR bands which are sensitive to self emission from the aperture stop. Another possibility could be some type of vignetting. For SW/MWIR FPA as well as the LWIR FPA the optics do not image the radiance directly onto the detector material, but instead image onto lenslets, which then image the aperture stop onto the detectors. If there is a shift in alignment of the stop with the aft optics due to temperature changes, then it is possible that this could slightly affect the amount of light falling on the detector.

None of these possibilities fully explains the observed temperature dependence, and it is possible that the effect is actually a combination of these. The effect is not very large, and the aperture stop is not expected to undergo large temperature changes over an orbit. Therefore, it is recommended to model temperature dependence for SWIR in the same way as for the Vis/NIR for the cases of bands with ASP electronics dependence. Since the SWIR FPA is temperature controlled, the value of  $T_{det}$  *should* be replaced with the OMM temperature. This is admittedly a substitution that could cause confusion, and is violation for the 4<sup>th</sup> principle listed above. It is recommended to change the code and the documentation to refer to it as  $T_a$  rather than  $T_{det}$ .

For the SWIR bands many of assumptions are made the same as with the Vis/NIR. Following is a list with the justification given:

1. Because there is no background for the RSB/SWIR, the DC restore dependence will not be significant. Therefore, one assumption that simplifies the equations significantly is that the detector response is linear with  $a_2 = 0$ .

2. Source stability was an issue during RC-2RSB/SWIR testing and so it must be assumed that relative gain change between the plateaus is not well known. Therefore,  $c_1$  is not well known, but only the values of  $c_0/c_1$  and  $c_2/c_1$  are meaningful.
3. Temperature change of the gain is best determined from the RC-3 rather than RC-2 tests.
4. RC-3 determined that the aperture stop temperature is the best predictor of gain change. The OMM temperature, which is an average of several thermistors including the aperture stop thermistor, is used to represent this.
5. There is no electronic temperature dependence for gain. Therefore  $r = 0$  for SWIR.
6. The OMM temperature is used as the “detector” temperature for the SWIR.
7. The nonlinearity described by  $c_2/c_1$  is assumed to depend only on the electronic temperature.
8. An average ASP electronic temperature represents the temperature for the ASP for the LWIR and MWIR processors.

The process for the SWIR bands is similar to that used for Vis/NIR process except that rather than use the detector temperature the change is relative to  $T_{OMM}$ . Details of the process are given in NP-EMD-2010.510.0030.

### **Thermal Emissive Bands (TEB)**

For TEB, the gains show the strongest correlation with OMM temperature. This can be explained as being the result of the change in self-emissive background. There may also be changes due to the same mechanisms that are seen for the SWIR bands.

Rather than make this a direct temperature dependence in the coefficients, one approach is using the DC restore voltage,  $V_{dcr}$  which is a direct response to the emissive background, and from in [Table 12](#) this dependence is clearly seen with

$$c_1(T_{det}, T_{elec}, V_{dcr}) = G \cdot b_1(T_{elec}) \cdot (a_1(T_{det}) + 2a_2(T_{det}) \cdot V_{dcr}) \quad \text{Eq. 49}$$

Note that  $a_2$  is the multiplier that controls the impact of  $V_{dcr}$  on the gain. Also note the relative change in the second order coefficient is dependent on the DC restore voltage as seen by taking the ratio  $c_2/c_1$  for the values given in [Table 12](#)

$$\frac{c_2(T_{det}, T_{elec}, V_{dcr})}{c_1(T_{det}, T_{elec}, V_{dcr})} = \frac{b_2(T_{elec})}{b_1(T_{elec})} + \frac{a_2(T_{det}) \cdot b_1(T_{elec})}{(a_1(T_{det}) + a_2(T_{det}) \cdot 2V_{dcr})} \quad \text{Eq. 50}$$

Since detector temperatures for all TEB are controlled, the  $T_{det}$  dependency can be removed.

However, an alternative approach is to simply recognize the temperature dependency from the OMM. The value of  $T_{det}$  is then replaced with the OMM temperature. As was pointed out for the SWIR this is admittedly a substitution that could cause confusion,

and is violation for the 4<sup>th</sup> principle listed above, and it is recommended to change the code and the documentation to refer to it as a more generic  $T_a$  rather than  $T_{det}$ . The advantage of this method is that it does not depend on the DC-restore voltage model, and all the assumptions associated with that. Both methods are described below. Alternative II is being used to produce the initial delivery of the calibration coefficients, but during intensive cal/val experimenting with alternative I is recommended.

### Alternative I – Use the DC Restore Voltage Values

The following process computes the TEB coefficients for  $b_1$ ,  $a_2$ , and  $b_2$ . The process starts with the nominal Raytheon model values for the gains, and then computes  $a_2$ . Then  $b_1$  is adjusted and finally  $b_2$  and  $c_0$  are computed. This process takes into account how the change in background impacts nonlinearity.

$$b_2(T_{elec}(n)) = b_1(T_{elec}(n)) \cdot \left\{ \frac{c_2(n)}{c_1(n)} - \frac{a_2 \cdot b_1(T_{elec}(n))}{(a_1 + a_2 \cdot 2V_{dcr}(n))} \right\} \quad \text{Eq. 51}$$

The following assumptions are made for this process:

1. Because of the self emissive background in the TEB, the gain dependence  $V_{dcr}$  is significant. Since in the equations  $a_2$  is always a multiplier for  $V_{dcr}$  then  $a_2$  should be non zero.
2. Source stability was very good during TEB RC-5 testing and so it can be assumed that relative gain change between the plateaus reflects the actual change in gain. Therefore,  $c_1$  should be derived from RC-5.
3. There is electronic temperature dependence for gain.
4. The nonlinearity described by  $c_2$  is assumed to depend on the electronic temperature and  $V_{dcr}$ .
5. An average ASP electronic temperature represents the temperature for the ASP for the LWIR and MWIR processors.

### Alternative II – Use OMM Temperature

This process would be the same as the Vis/NIR bands, except that the Aperture Stop Temperature is used as the detector temperature.

The following assumptions are made for this process:

1. Because of the self emissive background in the TEB, the gain dependence on OMM temperature significant.
2. Source stability was very good during TEB RC-5 testing and so it can be assumed that relative gain change between the plateaus reflects the actual change in gain. Therefore,  $c_1$  should be derived from RC-5.
3. There is no electronic temperature dependence for gain.
4. The nonlinearity described by  $c_2$  is assumed to depend on the ASP electronic and OMM temperature.

5. An average ASP electronic temperature represents the temperature for the ASP for the LWIR and MWIR processors.

#### 2.4.1.2.2 Reflective Band RVS

As a pre-launch test, measurements are taken for all the reflective bands using a 100-cm SIS(100) lamp placed at twelve (12) different scan angles. Measurements of  $dn$  are taken with the SIS lamp illuminated at four different power levels (including 0).<sup>12</sup> With the known radiances ( $\overline{L_{ap}}(\theta_{ev}, B)$ ) for the four powers a least squares fit can be used with the following equation to determine the RVS at each angle as well as the values for the calibration coefficients  $c_i$ :

$$\begin{aligned} \overline{L_{ap}}(\theta_{ev}, B) &= \frac{\overline{\Delta L_{det}}(\theta_{ev}, B)}{\text{RVS}(\theta_{ev}, B)} \\ &= \frac{F \cdot \sum_{i=0}^2 c_i \cdot dn_{ev}^i}{\text{RVS}(\theta_{ev}, B)} = \frac{\sum_{i=0}^2 c'_i \cdot dn_{ev}^i}{\text{RVS}(\theta_{ev}, B)} \end{aligned} \quad \text{Eq. 52}$$

The minimum reflectance angle off the HAM is when  $\theta = +46^\circ$  away from nadir. Therefore the RVS and the Emission Versus Scan (EVS) should be symmetric about this angle because the reflectance is always the same in either direction. It should therefore be true that

$$\text{RVS}(46^\circ + \alpha, B) = \text{RVS}(46^\circ - \alpha, B) \quad \text{Eq. 53}$$

The symmetry assumption given in [Eq. 53](#) is important in the calibration process, since in the test procedure the RVS is not measured for the scan angles of the two calibration sources:

- Solar diffuser source, which is located at when  $\theta = +157^\circ$ , so from [Eq. 53](#)  $\text{RVS}(+157^\circ, B) = \text{RVS}(-65^\circ, B)$
- On-board calibration source, which is located at  $\theta = +100^\circ$ , so from [Eq. 53](#)  $\text{RVS}(+100^\circ, B) = \text{RVS}(-8^\circ, B)$ .

#### 2.4.1.2.3 Pre-Launch Calibration Coefficients from the BCS

In pre-launch testing a Blackbody Calibration Source (BCS) is used to measure the detector response as a function of radiance for the emissive bands.<sup>13</sup> The BCS is

<sup>12</sup> "VIIRS Program Test Procedure for Response Versus Scan Angle (FP-10)," TP154640-250

<sup>13</sup> "VIIRS Program Test Procedure for Emissive Band Calibration," TP154640-274

designed so that its emissivity is 1; that is, it is a near-perfect blackbody. If its temperature is measured, the radiance it emits can be exactly known from Planck's formula as described in [Eq. 36](#). By varying the temperature of the BCS the detector response of the emissive bands can be determined. The scan angle at which the BCS is observed is referred to here as  $\theta_{bcs}$ .

$$L_{ap}(\theta_{bcs}, \lambda) = L(T_{bcs}, \lambda)$$

**Eq. 54**

Taking the band-average of [Eq. 54](#)

$$\overline{L}_{ap}(\theta_{bcs}, B) = \overline{L}(T_{bcs}, \lambda)$$

**Eq. 55**

Setting [Eq. 45](#) equal to [Eq. 55](#) at the BCS scan angle, and expressing in terms of the quadratic series

$$\sum_{i=0}^2 c_i \cdot \overline{dn}_{bcs}^i = \text{RVS}(\theta_{bcs}, B) \cdot [\overline{L}(T_{bcs}, \lambda)] + (\text{RVS}(\theta_{bcs}, B) - \text{RVS}(\theta_{sv}, B)) \cdot \frac{\{(1 - \overline{\rho}_{rta}(\lambda)) \cdot \overline{L}(T_{rta}, \lambda) - \overline{L}(T_{ham}, \lambda)\}}{\overline{\rho}_{rta}(\lambda)}$$

**Eq. 56**

By varying the temperature  $T_{bcs}$  and recording  $\overline{dn}_{bcs}$  [Eq. 56](#) can be used to determine the calibration coefficients  $c_0$ ,  $c_1$ , and  $c_2$  for each detector by fitting the data. Of course all the temperatures and reflectances in [Eq. 56](#) must also be known. This includes the RVS. The differential detector counts observing the BCS (with zero offsets removed),  $\overline{dn}_{bcs}$ , is shown as an averaged value since it should be taken several times per setting of  $T_{bcs}$ . The RVS may be arbitrarily set to one at any angle. Setting  $\theta_{bcs} = \theta_{sv}$ , and arbitrarily defining  $\text{RVS}(\theta_{sv})=1$  transforms [Eq. 56](#) into the very simple form of

$$\sum_{i=0}^2 c_i \cdot \overline{dn}_{bcs}^i = [\overline{L}(T_{bcs}, \lambda)].$$

However, it is not possible to do this, because  $\overline{dn}_{bcs} = \overline{DN}_{bcs} - \overline{DN}_{sv}$  and in order to measure  $\overline{DN}_{sv}$  a simulated Space View Source (SVS) must be placed at  $\theta_{sv}$ . Nevertheless, it is highly recommended that  $\theta_{bcs}$  be as close as possible to  $\theta_{sv}$  in order to keep the RVS difference in [Eq. 56](#) to a minimum, which reduces the effect of the background term. When the background contribution is minimized the effect of any uncertainties in reflectance/emittance and temperature on the accuracy of the coefficients is also minimized.

There is a problem using [Eq. 56](#) to solve for the calibration coefficients  $c_i$ , because it requires knowledge of the RVS, while the equation to determine the RVS requires knowledge of the calibration coefficients. The only way to reconcile this is to iteratively solve the two equations. The number of iterations required for convergence can be minimized by making  $\theta_{bcs}$  as close as possible to  $\theta_{sv}$ .

One problem with varying the temperature  $T_{bcs}$  and measuring detector response over time is that there will be small changes in the coefficients from one measurement to the next. According to the VIIRS specification detectors are to be linear to within 1%, so the first order coefficients  $c_1$  will dominate. Therefore, if  $c_1$  fluctuates by even a small fraction of a percent from one  $T_{bcs}$  setting to the next it will cause an error in the computing  $c_0$  or  $c_2$  that is on the order of that fluctuation. To avoid this measurements should be taken while cycling  $T_{bcs}$  settings several times.

#### 2.4.1.2.4 Emissive Band RVS

The Laboratory Ambient Blackbody (LABB) is used to measure the RVS. Like the BCS, it is a 100% emissive blackbody.<sup>14</sup> It can be placed at various positions within the VIIRS scan and the change in signal used to determine the RVS. [Eq. 56](#) for the BCS also applies to the LABB. As with BCS observations the RVS can be arbitrarily assigned for one scan angle; e.g.

$$\text{RVS}(\theta_{sv}, B) = 1 \quad \text{Eq. 57}$$

Substituting  $\theta_{labb}$  for  $\theta_{bcs}$ , and solving [Eq. 56](#) for RVS using [Eq. 57](#) yields

$$\text{RVS}(\theta_{labb}, B) = \frac{\sum_{i=0}^2 c_i \cdot \overline{dn}_{labb}^i + \frac{\{(1 - \overline{\rho}_{rta}(\lambda)) \cdot \overline{L}(T_{rta}, \lambda) - \overline{L}(T_{ham}, \lambda)\}}{\overline{\rho}_{rta}(\lambda)}}{\left( \overline{L}(T_{labb}, \lambda) + \frac{\{(1 - \overline{\rho}_{rta}(\lambda)) \cdot \overline{L}(T_{rta}, \lambda) - \overline{L}(T_{ham}, \lambda)\}}{\overline{\rho}_{rta}(\lambda)} \right)} \quad \text{Eq. 58}$$

Using [Eq. 57](#) at  $\theta_{labb} = \theta_{sv}$  [Eq. 58](#) becomes

$$\overline{L}(T_{labb}, \lambda) = \sum_{i=0}^2 c_i \cdot \overline{dn}_{labb}(\theta_{sv})^i \quad \text{Eq. 59}$$

Substituting [Eq. 59](#) back into [Eq. 58](#) gives

$$\text{RVS}(\theta_{labb}, B) = \frac{\sum_{i=0}^2 c_i \cdot \overline{dn}_{labb}(\theta_{labb})^i + \frac{\{(1 - \overline{\rho}_{rta}(\lambda)) \cdot \overline{L}(T_{rta}, \lambda) - \overline{L}(T_{ham}, \lambda)\}}{\overline{\rho}_{rta}(\lambda)}}{\sum_{i=0}^2 c_i \cdot \overline{dn}_{labb}(\theta_{sv})^i + \frac{\{(1 - \overline{\rho}_{rta}(\lambda)) \cdot \overline{L}(T_{rta}, \lambda) - \overline{L}(T_{ham}, \lambda)\}}{\overline{\rho}_{rta}(\lambda)}} \quad \text{Eq. 60}$$

If  $T_{labb}$  is held very stable during the test then [Eq. 60](#) can be used effectively to determine RVS. It is preferable to [Eq. 58](#) because it does not require exact knowledge of  $T_{labb}$ , though it does require knowledge of  $T_{ham}$  and  $T_{rta}$ .

#### 2.4.1.3 Creating Calibration Tables

Several look-up tables and other data required for calibration are generated using the pre-launch measurements. These include:

<sup>14</sup> "VIIRS Program Test Procedure for Response Versus Scan Angle (FP10)," TP154640-250

- Determination of the transformation matrix from solar diffuser coordinates into instrument coordinates,  $\mathbf{T}_{SD/inst}$ , using angular alignment measurements
- Computation of the band average functions  $\overline{\tau_{sds}}(\phi_h, \phi_v, B_{sds})$  by averaging (using [Eq. 14](#)) using the RSR of the SDSM bands
- Computation of a LUT for  $\overline{\text{BRDF}}'(\phi_h, \phi_v, B_{sds}, 0)$  using:

$$\overline{\text{BRDF}}'(\phi_h, \phi_v, B_{sds}, 0) = \overline{\text{BRDF}}(\phi_h, \phi_v, \lambda_{sds}, 0)$$

Eq. 61

The description and derivation of [Eq. 61](#) is given in Section [3.3.3.1](#).

- Computation of the band average functions  $\overline{\text{BRDF}}(\phi_h, \phi_v, \lambda, 0)$  and  $\overline{\tau_{sds}}(\phi_h, \phi_v, B)$  using the RSR for each reflective band and [Eq. 14](#)
- Computation of a complete  $\text{RVS}(\theta)$  LUT for all bands by using the symmetry defined in [Eq. 53](#)
- Computation of a LUT for band-averaged OBCBB reflective radiance,  $(1 - \overline{\varepsilon_{obc}}(\lambda)) \cdot \overline{L(T, \lambda)}$ , using the RSR of each emissive band
- Computation of a LUT for band-averaged OBCBB emissive radiance,  $\overline{\varepsilon_{obc}}(\lambda) \cdot \overline{L(T, \lambda)}$ , using the RSR of each emissive band
- Computation of a LUT for band-averaged RTA emissive radiance,  $\left( \frac{1}{\overline{\rho_{rta}}(\lambda)} - 1 \right) \cdot \overline{L(T, \lambda)}$ , using the RSR of each emissive band
- Computation of a LUT for band-averaged HAM emissive radiance,  $\frac{\overline{L(T, \lambda)}}{\overline{\rho_{rta}}(\lambda)}$ , using the RSR of each emissive band
- Determination of detector response coefficients,  $a_i(T_{det})$ , by fitting data from the  $V(E_{det}, T_{det})$  measurements. The detected spectral irradiance on the field stop,  $E_{det}$ , is converted into  $N_e$  using [Eq. 7](#) and the measurements of  $V(E_{det}, T_{det})$  by fitting the data to a quadratic polynomial with coefficients  $a_i$ . This conversion uses [Eq. 21](#) for each temperature measurement and a least squares optimization to minimize fitting error.

- Determination of electronic response coefficients,  $b_i(T_{elec})$ , by fitting data from the  $DN(V, V_{dcr}, T_{elec})$  measurements to a quadratic polynomial with coefficients  $b_i$ . This uses [Eq. 24](#) for each temperature measurement and a least squares optimization to minimize fitting error
- Determination of emissive band system response coefficients,  $c_i(T_{det}, T_{elec})$ , by fitting data from the system detector response. System detector response is measured by varying the BCS temperature and fitting the coefficients  $c_i$  using [Eq. 56](#) and a least squares optimization to minimize fitting error. The optimization process should also include iterative variation of RVS in [Eq. 56](#) to get a best fit.
- Determination of reflective band system response coefficients,  $c_i(T_{det}, T_{elec})$ , by fitting data from the system detector response. System detector response was measured by varying the SIS(100) source and fitting the coefficients  $c_i$  using [Eq. 52](#) and a least squares optimization to minimize fitting error. The optimization process should also include iterative variation of RVS in [Eq. 52](#) to get a best fit.
- Computation of coefficients  $c_i(T_{det}, T_{elec})$  from coefficients  $a_i(T_{det})$  and  $b_i(T_{elec})$  using equations in [Table 12](#). These should be computed for the same temperatures ( $T_{det}$  and  $T_{elec}$ ) that were used in the previous determination of system response coefficients.

## 2.4.2 Early Orbit Activation and Evaluation

VIIRS will undergo a systematic activation and early orbit checkout following the successful launch of each spacecraft. The details and phasing of this sequence is planned through coordination of the spacecraft, payload, and cal/val teams.

During instrument checkout various VIIRS health and status parameters will be checked against range threshold values and will be compared to pre-launch values to verify that VIIRS is operating within its nominal performance range. After the completion of the VIIRS early orbit checkout, the sensor will be declared as ready for on-orbit instrument calibration and data product validation.

A notional sequence for the VIIRS instrument would include:

- Turn survival heater power ON
- Activate ON State
- Open nadir and cryoradiator doors
- Start outgassing sequence
- End outgassing sequence
- Focal plane cool down
- Instrument checkout and testing

VIIRS can be commanded into any of the following modes regardless of the operational mode of any other instrument:

- OFF Mode
- OUTGASSING
- ACTIVATION
- DIAGNOSTIC /EARLY ORBIT CHECKOUT
- OPERATIONAL
- SAFE HOLD
- SURVIVAL

VIIRS will be in the OFF Mode during the launch phase and during orbit acquisition. In the OFF Mode, no power is supplied to the instrument. Over a period of time it will go through the following sequence of modes:

- SURVIVAL
- ACTIVATION
- OUTGAS
- return to ACTIVATION
- DIAGNOSTIC/EARLY ORBIT CHECKOUT

Adjustments to the reflective, emissive, and DNB radiometric calibration LUTs may be made as necessary prior to entering the operational phase.

### **2.4.3 Operations Phase**

During the operations phase VIIRS radiometric calibration occurs during ground processing early in the VIIRS data retrieval process; immediately following geolocation of the raw pixel data. The calibrated TOA radiances SDR product (SDR\_RAD) is generated for all active bands. The calibrated TOA reflectances SDR product (SDR\_REF) is generated for all active reflective bands during day and terminator operations. The calibrated TOA brightness temperatures SDR product (SDR\_BT) is generated for all active emissive bands at all times. [Table 16](#) summarizes the bands for which each product is retrieved.

The LUTs that are established with pre-launch data and updated (as needed) during early orbit activation and evaluation are essentially static during the operations phase. During normal operations the pre-launch tables are used in combination with measurements from the on-board calibration sources to support a dynamic on-orbit calibration process. Though the pre-launch tables are nominally static, post-launch

validation is done to identify shortcomings in the tables that would require post-launch corrections.

One occasional change will involve the LUT for  $\Phi_{sun}(\lambda)$ , the spectral output power of the sun.  $\Phi_{sun}(\lambda)$  changes slightly over time due to solar activity. More importantly, knowledge of the solar spectrum will improve as better measurements become available. Updates to the solar spectral power will use the best available data. Also the moon is occasionally visible in the space view and analysis of these data is planned in order to verify calibration of the reflective bands. For the emissive bands, a cycling at regular intervals (TBD) of the OBCBB temperature from ambient temperature to 315K will be performed. In these cases the data will be used to verify the calibration coefficients, and if changes are observed modifications to the response curves will be considered. Any such changes will not be performed automatically but will instead involve a formal process of review and approval.

**Table 16: Bands Included in the Three Primary VIIRS SDR's.**

Band	Center (μm)	SDR_RAD	SDR_REF	SDR_BT	Notes
M1	0.412	X	X		Dual Gain
M2	0.445	X	X		Dual Gain
M3	0.488	X	X		Dual Gain
M4	0.555	X	X		Dual Gain
I1	0.645	X	X		Imagery Resolution
M5	0.672	X	X		Dual Gain
M6	0.751	X	X		
I2	0.865	X	X		Imagery Resolution
M7	0.865	X	X		Dual Gain
M8	1.240	X	X		
M9	1.378	X	X		
I3	1.610	X	X		Imagery Resolution
M10	1.610	X	X		
M11	2.250	X	X		
M12	3.700	X		X	
I4	3.740	X		X	Imagery Resolution
M13	4.050	X		X	Dual Gain
M14	8.550	X		X	
M15	10.783	X		X	
I5	11.450	X		X	Imagery Resolution
M16	12.013	X		X	2 bands in TDI
DNB	0.700	X			NCC Imagery is the DNB Reflectivity Product

*[This page is intentionally blank]*

### 3. ALGORITHM DESCRIPTION

The VIIRS radiometric calibration algorithm was developed for use in the operational environment of the ground system. Radiometric calibration processing as well as algorithm inputs are described as a precursor to the theoretical description of the algorithm. Following the theoretical description practical considerations are discussed.

#### 3.1 PROCESSING OUTLINE

[Figure 19](#) illustrates the VIIRS Radiometric Calibration Component processing architecture. Here are shown four major processes that operate independently on four different time scales. The granule-by-granule near real-time (NRT) process is the radiometric calibration of EV *DN*, which is shaded in yellow. This processing will be discussed in Section [3.1.1](#). Other processes include 1) cross-granule processing of SD view *DN*, which occurs once per orbit, 2) typically multi-orbit processing of SDSM data, and 3) various offline processes that are performed on an occasional or as needed basis to update the calibration LUTs. SD processing is described in Section [3.1.1](#) and SDSM and other offline processing are discussed in Section [3.1.2](#).

Interfaces between the processes of the VIIRS Radiometric Calibration Component include Intermediate products produced during RDR to SDR processing and various LUTs and input parameters. Intermediate products include the Geolocation IPs, which are described in SDRL 147-3 “*VIIRS Geolocation Unit Detailed Design Document*” [Y3245] and the On-Board Calibrator IP that is listed as a product of the VIIRS Radiometric Calibration Component and whose description can be found in SDRL 148-3 “*VIIRS Radiometric Calibration Component Detailed Design Document*” [Y2490]. LUTs and input parameters are described in Section [3.2.3](#).

The operational ground system environment requires near real-time production of calibrated SDR products. As described in this section the initialization and updates required to maintain SDR performance throughout the mission also require various offline processes.

NRT radiometric calibration of Earth View (EV) *DN*s proceeds following the geolocation of VIIRS pixels (see SDRL 148-6 “*VIIRS Radiometric Calibration Component Level Software Architecture*” [Y2479b]). Raw instrument counts (i.e. *DN*) are scaled and calibration coefficients are applied in accordance with the algorithm presented in [Section 3.3](#). As part of this process the calibration coefficients and correction factors that are read in at run-time from radiometric calibration LUTs are adjusted to remove background and instrument artifacts and to accommodate the current on-orbit environment and to account for changes in the instrument.

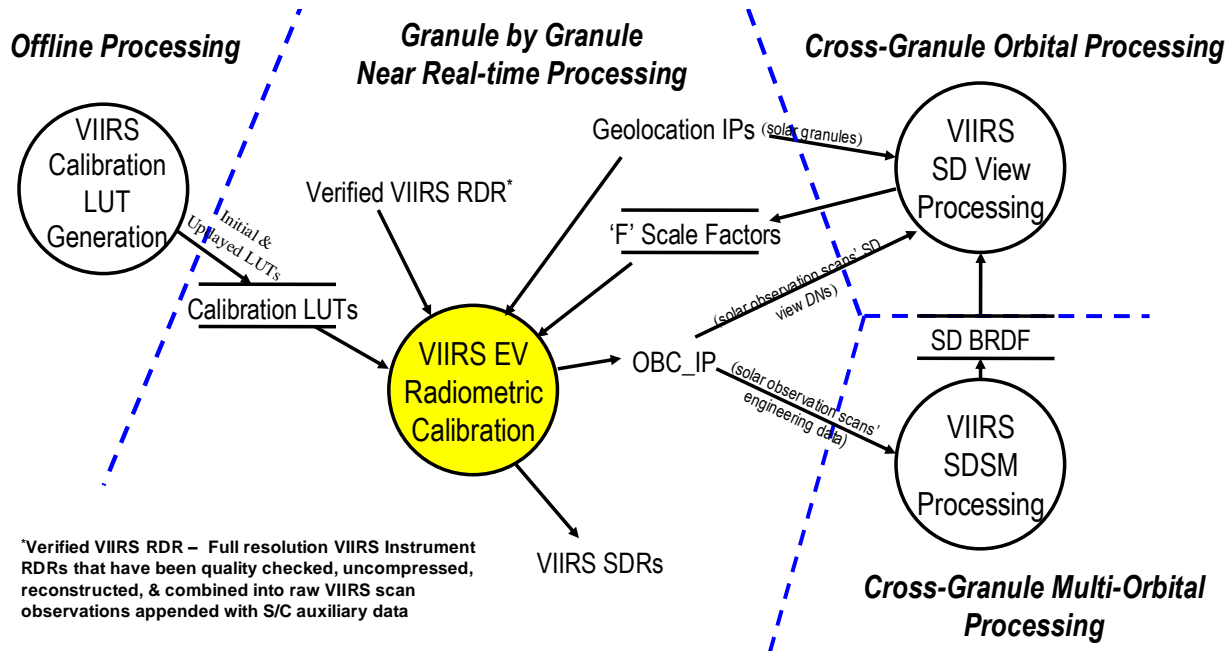
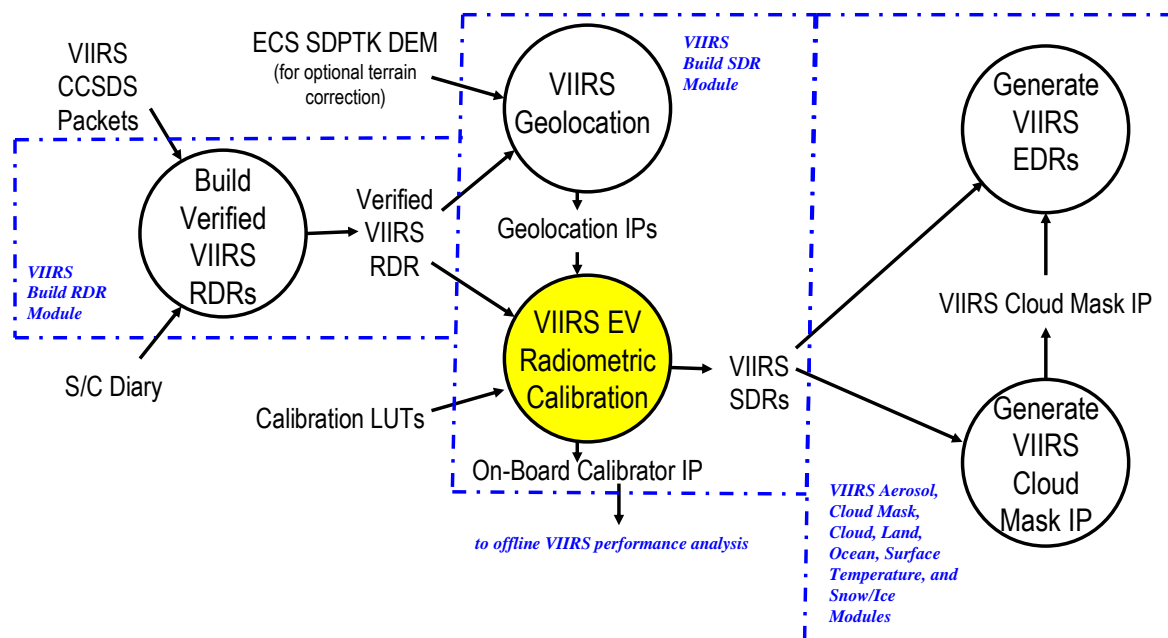


Figure 19: Architecture of the VIIRS Radiometric Calibration Component

### 3.1.1 Near Real-time Processing

In the context of this ATBD near real-time (NRT) processing refers to the radiometric calibration that is performed as part of the operational timeline from receipt of downlinked VIIRS RDR's to completion of the corresponding VIIRS EDRs. In general this includes the processing necessary to determine the appropriate zero offsets and correction factor updates to apply to the current Earth View *DN*s.

[Figure 20](#) shows the data flow through the NRT VIIRS RDR to SDR processing algorithms. As shown the VIIRS EV Radiometric Calibration Unit (shaded in yellow) is a part of the VIIRS Build SDR Module that executes following VIIRS Geolocation. Both the Geolocation and EV Radiometric Calibration Units read Verified -VIIRS RDR's that are produced by the VIIRS Build RDR Module. In addition to the Verified VIIRS RDR's, which are described in [Section 3.2.1](#), the VIIRS EV Radiometric Calibration Unit reads Geolocation IPs produced by the VIIRS Geolocation Unit and pre-determined Calibration LUTs, which are described in [Section 3.2.3](#). The resultant VIIRS SDR's, which are summarized in [Section 2.1.2](#) and described in detail in SDRL 148-3 "VIIRS Radiometric Calibration Component Detailed Design Document" [Y2490], are subsequently processed by the VIIRS Cloud Mask IP Component and the various VIIRS EDR modules.



**Figure 20: VIIRS Granule-by-Granule Near Real-Time Processing**

Except for the terminator orbit (i.e. 17:30 local ascending node crossing time) the Solar Diffuser (SD) is illuminated during a sequence of consecutive scans once per orbit. Once a complete orbital sequence of scans is available these SD view data are processed automatically to produce scale factors that are used in subsequent NRT EV radiometric calibration. These scale factors are accumulated and combined over a number of orbits (TBD) before an update to the operational scale factors.

### 3.1.2 Offline Processing

Offline processing includes the processing required to analyze instrument performance, assess instrument degradation, and adjust the slowly varying calibration coefficients that are read into the VIIRS Radiometric Calibration Component during NRT SDR production. The known adjustments to calibration coefficients are mostly done using off-line procedures called Algorithm Support Functions (ASF). Offline C/V processing includes the following:

- Thermal Emissive Bands (TEB) response and Noise Equivalent Differential Temperature (NEdT) trending
- Reflective Solar Bands (RSB) response and Signal-to-Noise Ratio (SNR) trending
- Solar Diffuser (SD) degradation analysis using SDSM and ASF
- Half Angle Mirror (HAM) degradation analysis
- Analysis of lunar observations through the space view port
- Calibration and instrument performance evaluation after configuration change

- Key telemetry points monitoring (Blackbody(BB), instrument, HAM, Focal Plane Assembly [FPA])
- Striping reduction study
- Analog to Digital Conversion (ADC) bit pattern analysis
- HAM side correlated noise monitoring

NPP orbital (roll) maneuvers will be scheduled in order to view the Moon through the space view port under carefully chosen viewing conditions. These observations will provide, through offline analysis, time dependent RVS for the reflective solar bands and will be useful in validating band-to-band registration and other instrument performance parameters.<sup>15</sup> Other NPP orbit maneuvers will facilitate offline calibration with respect to deep space at various scan angles (pitch maneuver) and offline calibration of the SD with respect to solar incidence angle (yaw maneuver). These processes are described in more detail in the VIIRS SDR Calibration/Validation Plan.

## 3.2 ALGORITHM INPUTS

Inputs to the VIIRS Radiometric Calibration Component include data produced by VIIRS as well as several types of non-VIIRS data, input parameters, and LUTs.

### 3.2.1 VIIRS Data

The required inputs for the generation of SDR products are Verified VIIRS RDR's, which contain the basic *DN*s to be converted into calibrated top of atmosphere (TOA) radiances, reflectances, and brightness temperatures as well as engineering data, health and safety data, and onboard calibrator view data that are required by the radiometric calibration algorithm. The VIIRS Build RDR Module produces the Verified VIIRS RDR's. These RDR's contain unprocessed *DN*s from all viewing sectors as well as various engineering and housekeeping data. These data are unpacked from VIIRS RDR CCSDS packets and assembled into scan cube structures. As part of the unpacking these data are uncompressed, band de-referenced, and quality checked through a re-computation of embedded checksums. The format and content of Verified VIIRS RDR's are described in detail in the *VIIRS Build RDR Module Level Detailed Design Document [Y2488]*.

As described in [Section 2.2.2.3](#), the detector numbering in [Figure 10](#) and [Figure 11](#) follow the instrument engineer's convention of labeling the detector that first sees a target on the ground as detector number 1.

Solar zenith angles are required to radiometrically calibrate the reflective bands. These data are available from the resolution specific VIIRS Geolocation IPs that are produced as part of RDR to SDR processing prior to execution of the VIIRS EV Radiometric

---

<sup>15</sup> Xiong, X. et al, "MODIS On-orbit Characterization Using the Moon".

Calibration Unit. The format and content of VIIRS Geolocation IPs are described in detail in SDRL 147-3 *VIIRS Geolocation Unit Level Detailed Design Document [Y3248]*.

### 3.2.2 Non-VIIRS Data

Radiometric calibration of VIIRS' reflective solar bands requires an extraterrestrial solar irradiances database. A solar irradiance database created from data observed by the Solar Spectrum (SOLSPEC) instrument flown on the Atmospheric Laboratory for Applications and Science (ATLAS) spacecraft<sup>16</sup> is utilized for processing of solar diffuser view data. Other solar spectra exist and the choice of which one will be used will be made during the final update of the SDR Look-up Tables before launch. For Suomi NPP, the solar spectrum used in the IDPS is from MODTRAN 4.3. For detailed discussion on this issue, see Cao et al. (2013b).

### 3.2.3 LUTs and Input Parameters

The VIIRS radiometric calibration algorithm requires many inputs in the form of input parameters and look-up tables (LUT). These inputs are specific to VIIRS and in many cases are initialized and updated on an instrument by instrument basis. This section describes each LUT and input parameter and prescribes the initialization of each and the criteria for update during early orbit and operational phases. The LUTs and input parameters are listed here for reference when going through the theoretical description in [Section 3.3](#).

The radiometric calibration LUTs that are used directly in the per pixel radiometric calibration of Earth view data include:

1. OBCBB Reflective Radiance
2. OBCBB Emissive Radiance
3. RTA Emissive Radiance
4. HAM Emissive Radiance
5. Radiance to Effective Blackbody Temperature (EBBT)

The OBCBB Reflective Radiance LUT  $\overline{(1 - \varepsilon_{obc}(\lambda)) \cdot L(T, \lambda)}$ , the OBCBB Emissive Radiance LUT  $\overline{\varepsilon_{obc}(\lambda) \cdot L(T, \lambda)}$ , the RTA Emissive Radiance LUT  $\overline{\left(\frac{1}{\rho_{rta}(\lambda)} - 1\right) \cdot L(T, \lambda)}$ , and the HAM Emissive Radiance LUT  $\overline{\left(\frac{L(T, \lambda)}{\rho_{rta}(\lambda)}\right)}$  contain band-averaged radiance

---

<sup>16</sup> Thuillier, G. et al, "The Solar Spectral Irradiance from 200 to 2400 nm as Measured by the SOLSPEC Spectrometer from the ATLAS and EURECA Missions", Solar Physics, 214: 1-22, 2003.

determined from the Relative Spectral Responses (RSR) over the band-dependent temperature ranges, with 0.25 K increment (see Table 14).

The Radiance to EBBT LUT contains EBBT (i.e. brightness temperature as a function of band-averaged radiance over band dependent EBBT ranges) for the emissive bands (i.e. I4, I5, M12- M16). These radiance values are evenly tabulated in the LUT . Using pre-launch measurements several look-up tables and other data required for calibration are generated:

Use angular alignment measurements to determine the transformation matrix from solar diffuser coordinates into instrument coordinates,  $\mathbf{T}_{SD/inst}$ .

Use the RSR of the SDSM bands to compute the band average functions  $\overline{\tau_{sds}}(\phi_h, \phi_v, B_{sds})$ ,  $\overline{\tau_{sds}}(\phi_{h\_sds}, \phi_{v\_sds}, B_{sds})$  and  $\overline{BRDF}(\phi_h, \phi_v, \lambda_{sds}, 0)$  by averaging over the SDSM bandpass. Because the SDSM has no transmissive optics  $RSR_{sds}(\lambda) = QE_{sds}(\lambda)$ . Otherwise, use the band-averaging equation given in [Eq. 14](#).

Compute a LUT for  $\overline{\rho_{SDeff}}(\phi_h, \phi_v, B_{sds})$ .

Use the RSR for each reflective band to compute the band average functions  $\overline{BRDF}(\phi_h, \phi_v, \lambda, 0)$  and  $\overline{\tau_{sds}}(\phi_h, \phi_v, B)$  using [Eq. 14](#).

Compute the complete Look-up table for  $RVS(\theta)$ , for all bands by using the symmetry defined in [Eq. 53](#).

Use the RSR of each emissive band to compute the band-averaged radiance found in eq. 107,  $(1 - \overline{\epsilon_{obc}}(\lambda)) \cdot \overline{L}(T, \lambda)$ . Compute this over the temperature ranges 240 K to 320K at increments given in Table 17. This will be referred to as the **OBCBB Reflective Radiance LUT**.

**Table 17: LUT Limits and Increments**

Band	Increment (K)	T <sub>min</sub> (K)	Lowest Detectable EBBT (K)	T <sub>max</sub> (K)	Highest Detectable EBBT (K)
M12	0.25	230	203	368	368
M13	0.25	230	192	683	683
M14	0.25	190	128	365	365
M15	0.25	190	111	381	381
M16	0.25	190	103	382	382
I4	0.25	210	208	367	367
I5	0.25	190	110	380	380

Use the RSR of each emissive band to compute the band-averaged radiance,  $\varepsilon_{obc}(\lambda) \cdot \overline{L(T, \lambda)}$  (the computation is shown in [Section 3.3.4.1](#), [Eq. 112](#) and [Eq. 117](#)). Compute this over the temperature ranges 240 K to 320K at increments given in Table 15. This will be referred to as the **OBCBB Emissive Radiance LUT**.

Use the RSR of each emissive band to compute the band-averaged radiance, which is defined as  $\left( \frac{1}{\rho_{rtt}(\lambda)} - 1 \right) \cdot \overline{L(T, \lambda)}$  (the computation is shown in [Section 3.3.4.1](#), [Eq. 112](#), [Eq. 115](#), and [Eq. 117](#)). Compute this over the temperature ranges 240 K to 320K at increments given in [Table 17](#). This is the **RTA Emissive Radiance LUT**.

Use the RSR of each emissive band to compute the band-averaged radiance, which is defined as  $\frac{\overline{L(T, \lambda)}}{\rho_{rtt}(\lambda)}$  (the computation is shown in [Section 3.3.4.1](#), [Eq. 112](#), [Eq. 115](#), and [Eq. 117](#)). Compute this over the temperature ranges 240 K to 320K at increments given in Table 15. This is the **HAM Emissive Radiance LUT**.

An **EBBT LUT** is to be prepared as a function of band-averaged radiance over the ranges listed in [Table 17](#) in the columns “Lowest Detectable EBBT” (LDEBBT) and “Highest Detectable EBBT” (HDEBBT). The increment of temperature used in the LUT should be less than or equal to what is listed in [Table 17](#). Inside the LUT, the radiance values are evenly spaced. These increments are fine enough so that linear interpolation

would not add any significant error, the criterion being less than 1 digital count of error due to interpolation, worst case. The LDEBBT listed in [Table 17](#) is defined either as the signal level where the detectors have an SNR of  $\frac{1}{2}$  or where the expected  $dn = 1$ , whichever is greater. The HDEBBT is the expected EBBT when the signal level is 1.5 times the signal of  $T_{max}$  as defined by the sensor specification. Since the VIIRS design is to set saturation at approximately 1.2 times the signal of  $T_{max}$ , it is unlikely that the HDEBBT values listed in [Table 17](#) will ever be detected. The value of 1.5 was chosen to allow ample margin, since gain may drift from its design value. All computed EBBT values less than  $T_{min}$  should have a quality flag set indicating this condition. Any EBBT that is less than LDEBBT should be replaced with LDEBBT and should have a quality flag set indicating this condition. If an EBBT is greater than  $T_{max}$ , then a quality flag should be set indicating this condition. The detectors will saturate before reaching HDEBBT, so a quality flag is not necessary to indicate this condition. However, saturation flags should already have been set for the radiance values, and these should be carried over into the EBBT quality flags.

Compute for all bands listed in [Table 17](#) over the temperature range from LDEBBT to HDEBBT.

Determine the detector response coefficients  $a_i(T_{det})$  by fitting data from the  $V(E_{det}, T_{det})$  measurements. Convert  $E_{det}$  into  $N_e$ , using [Eq. 7](#) and the measurements of  $V(E_{det}, T_{det})$  by fitting the data to a quadratic polynomial with coefficients  $a_i$  using [Eq. 21](#) for each temperature measurement, and a least squares optimization to minimize fitting error.

Determine the electronic response coefficients  $b_i(T_{elec})$  by fitting data from the  $DN(V, V_{dcr}, T_{elec})$  measurements to a quadratic polynomial with coefficients  $b_i$  using [Eq. 24](#) for each temperature measurement, and a least squares optimization to minimize fitting error.

For emissive bands determine the system response coefficients  $c_i(T_{det}, T_{elec})$ , by fitting data from the system detector response that was measured by varying the BCS temperature and fitting the coefficients  $c_i$  using [Eq. 56](#) and a least squares optimization to minimize fitting error. The optimization process should also include iterative variation of RVS in [Eq. 56](#) to get a best fit.

For reflective bands determine the system response coefficients  $c_i(T_{det}, T_{elec})$ , by fitting data from the system detector response that was measured by varying the SIS(100) source, and fitting the coefficients  $c_i$  using [Eq. 70](#), and a least squares optimization to minimize fitting error. The optimization process should also include iterative variation of RVS in [Eq. 70](#) to get a best fit.

Use equations in [Table 12](#) to compute coefficients  $c_i(T_{det}, T_{elec})$ , from coefficients  $a_i(T_{det})$  and  $b_i(T_{elec})$ . Compute these for the same temperatures  $T_{det}$  and  $T_{elec}$  as were used in the system response coefficients described in the previous 2 steps. The result should agree closely.

A LUT for  $\Phi_{sun}(\lambda)$ , the spectral output power of the sun, should be created based on the best available data from solar observatories.

As stated in [Section 2.2.2.3](#) all detector dependent LUTs shall use the “product order” convention; i.e. the highest number detector in scan N lies adjacent to detector index 1 in scan N+1.

### 3.3 THEORETICAL DESCRIPTION

The theoretical description of the VIIRS radiometric calibration algorithm is arranged to first discuss specific processes that are needed to support the calibration equations specific to each band type. Secondly separate sub-sections are allocated for details related to reflective and emissive bands. The Day-Night Band is quite unique from the ‘M’ and ‘I’ bands in its design, operation, and calibration requirements and methods and is therefore described in a separate section. The terminator orbit presents a special challenge for reflective band calibration as solar observations cannot be made in this orbital configuration. The current method for addressing this challenge is described in [Section Error! Reference source not found.](#)

The VIIRS radiometric calibration algorithm makes extensive use of pre-determined LUTs along with measured instrument temperatures and reference observations of the Solar Diffuser (SD) (which is illuminated by the sun for a sequence of scans once per orbit), the On-Board Calibrator Blackbody (OBCBB), and views of deep space.

The LUTs are initially populated with constants or values inferred from pre-launch instrument testing and are updated as needed during the initial on-orbit period of intensive instrument calibration and validation (cal/val) as well as throughout normal operations. In general these LUTs are flight model and instrument configuration specific. The radiometric calibration algorithm has the flexibility to accommodate any LUT update frequency.

The ‘M’ and ‘I’ band radiometric calibration algorithm theory presented in [Section 3.3.3](#) and [Section 3.3.4](#) is based on the first principles derivation documented in “*VIIRS Radiometric Calibration Equations*” [NGST Doc. D36966]. The LUTs for the ‘M’ and ‘I’ bands are designed to accommodate temperature dependencies that may be present by including detector, electronics, cavity, shield, RTA, HAM, and OBCBB temperature dimensions where appropriate.

#### 3.3.1 Zero Offset Determination

Because VIIRS is a differencing radiometer there is always some background level in the downlinked *DN*s that inflate their value beyond what would be present from the scene radiances alone. The methods for determining these zero offsets are band type specific. The following sub-sections describe the methods and provide details for

selection and processing of data to ascertain zero offsets for the ‘M’ and ‘I’ bands and for the DNB.

### 3.3.1.1 ‘M’ and ‘I’ Band Zero Offsets

Single gain ‘M’ band and ‘I’ band background level is removed from each detector sample by subtracting from each observed (i.e. Earth view or calibrator view) *DN* an average *DN* obtained from NRT processing of the current scan’s deep space view. This is done by using the views of cold space that are available once per scan when VIIRS views the space view port. Care must be taken in selection of the space view to ensure that the same HAM side used for the observed *DN* was used for the space view.

In the case of imagery bands, there are two sub-frames per moderate resolution frame (see Figure 11.) This requires that each earthview sample have the appropriate space view sub-frame average subtracted from it.

In the case of the dual gain bands the on-board calibrator sources are viewed with alternating gain ranges so that a complete set of gain range-HAM side combinations is

acquired every four scans. The radiometric calibration algorithm selects the data from the appropriate scan’s calibrator view to use when processing a scan according to the scheme shown in [Table 18](#). Table 18: Space View Selection for Dual Gain Bands

Scan No.	Gain State for Cal-views	HAM Side	V <sub>DCRestore</sub> Value From	SV Offset From	
				Low Gain Sample	High Gain Sample
N	Low	1	N-4	Scan N	Scan N-2
N+1	Low	2	N-3	Scan N+1	Scan N-1
N+2	High	1	N	Scan N+4	Scan N+2
N+3	High	2	N+1	Scan N+5	Scan N+3
N+4	Low	1	N	Scan N+4	Scan N+2
N+5	Low	2	N+1	Scan N+5	Scan N+3
N+6	High	1	N+4	Scan N+8	Scan N+6
N+7	High	2	N+5	Scan N+9	Scan N+7

A *DN* that has been corrected for this zero offset background is referred to as a *dn*.

For the M13 band, the OBC *DN* must be selected from the same scan as the SV Offset in Table 18.

N is the true scan line number from the sensor and not the row index within the granule. Granules can contain 47 or 48 scan lines.

### 3.3.1.2 Day-Night Band Zero Offsets

Unlike the VIIRS ‘M’ and ‘I’ bands the zero offsets for the DNB are not obtained during NRT processing of space view data and applied immediately in the NRT processing of downlinked EV data. Instead they are pre-determined in an offline analysis process and uploaded to VIIRS to be applied to future DNB observations during on-board data processing. [Section 3.3.5.2.](#) shows details for the determination of these zero offsets. Nonetheless the ground processing algorithm will include a facility for a zero offset correction via a pre-determined LUT to remove any residual offset that is not removed on-board. This zero offset LUT includes values for each HAM side and each gain stage for each along-track pixel in each along-scan frame.

### 3.3.2 Determination of Instrument Temperatures

As will be shown in [Section 3.3.3](#) and [Section 3.3.4](#) the reflective and emissive band algorithms use knowledge of actual instrument component temperatures to determine scan specific coefficients. These scan specific coefficients are based on pre-determined calibration coefficients that are valid for specific temperature values. This section describes how specific thermistor readings are chosen and processed to provide the component temperature required for the algorithm.

The instrument component temperatures required for radiometric calibration are a combination of the various thermistor readings telemetered to the ground as VIIRS Engineering data and Health and Safety Telemetry data. Except for the OBCBB the radiometric calibration algorithm assigns component temperatures based on weighted sums of pre-determined thermistor readings that have been converted to temperature using 5<sup>th</sup> order polynomial conversions. The coefficients for the 5<sup>th</sup> order polynomial conversion are tabulated in SBRS’ “VIIRS Command, Telemetry, Science and Engineering Data Description” [[EDD154640-101](#)].

The OBCBB temperature is determined from an average of the six active thermistors that are embedded in the OBCBB. A conversion from raw data *DN* values measured by thermistors to temperature is performed as described in [Appendix A](#), which is based on SBRS Engineering Memo *Y0012889*, and the Engineering Data Description (EDD)

### 3.3.3 Reflective ‘M’ and ‘I’ Band Calibration

The reflective ‘M’ and ‘I’ bands’ Earth View (EV) SDR products are spectral reflectance and spectral radiance. The calibration source for these bands is an on-board SD, for which the BRDF is well known. The radiance at the entrance to the instrument’s aperture when pointing to the SD is solar irradiance attenuated by the SDS and the BRDF

$$L_{ap}(\theta_{sd}, \lambda) = \tau_{sds}(\phi_h, \phi_v, \lambda, d) \cdot E_{sun}(\lambda, d_{se}) \cdot \cos(\theta_{inc}) \cdot \text{BRDF}(\phi_h, \phi_v, \lambda),$$

Eq. 62

where  $\tau_{sds}(\phi_h, \phi_v, \lambda, d)$  is transmittance of the SDS;  $\phi_h$  and  $\phi_v$  are the horizontal and vertical incidence angles of solar illumination upon the SD attenuation screen, respectively;  $d$  is detector index;  $E_{sun}(\lambda, d_{se})$  is solar irradiance onto a surface normal to the sun;  $d_{se}$  is the distance from the sun to the earth; and  $\theta_{inc}$  is the incidence angle onto the SD relative to normal. The definition of  $\phi_v$  and  $\phi_h$ , are given in section [3.3.3.2](#). Typically BRDF is expressed as a function of four angles, two describe the vector of the incident irradiance and two describe the vector of the reflected radiance. However since the RTA always observes the SD from approximately the same angle the angles of the reflected light can be dropped. The reason for wavelength and detector dependence of SDS transmittance is explained in [Appendix B](#).

There is no significant self-emitted thermal background radiance in the reflective bands therefore this term can be dropped from [Eq. 16](#). Substituting [Eq. 62](#) into [Eq. 16](#) with the background term dropped yields

$$\begin{aligned} \overline{\Delta L_{det\_sd}}(\phi_h, \phi_v, B) &= \overline{\Delta L_{det}}(\theta_{sd}, B) \\ &= RVS(\theta_{sd}, B) \cdot \cos(\theta_{inc}) \cdot \left[ \overline{\tau_{sds}(\phi_h, \phi_v, \lambda, d) \cdot E_{sun}(\lambda, d_{se}) \cdot BRDF(\phi_h, \phi_v, \lambda)} \right] \end{aligned} \quad \text{Eq. 63}$$

Combining [Eq. 31](#) and [Eq. 63](#) gives

$$\sum_{j=0}^2 c_j \cdot dn_{sd}^j = \cos(\theta_{inc}) \cdot RVS(\theta_{sd}, B) \cdot \overline{\tau_{sds}(\phi_h, \phi_v, \lambda, d) \cdot E_{sun}(\lambda, d_{se}) \cdot BRDF(\phi_h, \phi_v, \lambda)} \quad \text{Eq. 64}$$

All the variables on the right side of [Eq. 64](#) are based on preflight measurements and angles that can be determined from the geometry. The BRDF, however, is updated at regular monthly intervals based on the trending of the SDSM output. All values on the right are known; the three  $c$  coefficients are unknowns.

[Equation 64](#) is used to update the  $c_j$  coefficients on orbit. Since there are three unknowns and only one equation some assumptions or constraints need to be made in order to solve for the coefficients. The assumption made here is that the shape of the response curve is preserved so that the same scale factor is applied to all three coefficients. The updated coefficients are designated as  $c'_j$ . Assuming that some factor,  $F$ , represents the change in scale (or gain) of the response, and that this scales all three coefficients equally, the coefficients in [Eq. 64](#) are substituted with

$$c'_j = F \cdot c_j \quad \text{Eq. 65}$$

Applying [Eq. 65](#) to [Eq. 64](#) gives

$$F = \frac{\cos(\theta_{inc}) \cdot RVS(\theta_{sd}, B) \cdot \overline{(\tau_{sds}(\phi_h, \phi_v, \lambda, d) \cdot E_{sun}(\lambda, d_{se}) \cdot BRDF(\phi_h, \phi_v, \lambda))}}{\sum_{j=0}^2 c_j \cdot dn_{sd}^j} \quad \text{Eq. 66}$$

Here the horizontal and vertical solar illumination incidence angles on the SD,  $\phi_h$  and  $\phi_v$ , will change not only from one calibration acquisition to the next, but also during a single acquisition itself. Therefore Eq. 66 needs to be averaged over all solar diffuser scans.

Normalized solar diffuser radiance can be defined as

$$\begin{aligned} \overline{L_{nsd}}(\phi_h, \phi_v, B) &= \overline{(\tau_{sds}(\phi_h, \phi_v, \lambda, d) \cdot E_{sun}(\lambda, d_{se}) \cdot BRDF(\phi_h, \phi_v, \lambda))} \\ &= \frac{1}{4\pi \cdot \overline{d_{se}}^2} \cdot \overline{(\tau_{sds}(\phi_h, \phi_v, \lambda, d) \cdot \Phi_{sun}(\lambda) \cdot BRDF(\phi_h, \phi_v, \lambda))} \end{aligned} \quad \text{Eq. 67}$$

where  $\overline{d_{se}}$  is the mean distance from the earth to the sun.

The scale factor,  $F_n$  for scan n at time  $t_n$  is

$$F_n = \frac{RVS(\theta_{sd}, B)}{N_{acq}} \cdot \left( \frac{\overline{d_{se}}}{d_{se}} \right)^2 \frac{\cos(\theta_{inc}(t_n)) \cdot \overline{L_{nsd}}(\phi_h(t_n), \phi_v(t_n), B)}{\sum_{j=0}^2 c_j \cdot \overline{dn_{sd}}(t_n)^j} \quad \text{Eq. 68}$$

where the average counts per scan viewing the solar diffuser is

$$\overline{dn_{sd}}(t_n) = \frac{1}{N_{SDfrm}} \sum_{m=0}^{N_{SDfrm}} DN_{sd}(t_n + m \cdot \Delta t_{frame}) - \frac{1}{N_{SVfrm}} \sum_{m=0}^{N_{SVfrm}} DN_{sv}(t_n + m \cdot \Delta t_{frame}) \quad \text{Eq. 69}$$

The number of frames per scan over which the SD calibration counts are recorded is  $N_{SDfrm}$  and  $N_{SVfrm}$  for the space view. This is set to 48 in the current design for the 'M' bands, and 96 for the 'I' bands. The value of the scale factor,  $F_n$ , computed over a single scan is not sufficient to correctly calibrate reflective bands. The SD is illuminated once per orbit, but the exact length of this period varies somewhat depending on the time of orbital plane of the spacecraft, and the time of year, but approximately 32 scans per orbit have full SD illumination. Since a separate value of F must be computed for each mirror side and gain state, the dual gain bands have about  $32 \div 4 = 8$  scans per orbit and the single gain bands have  $32 \div 2 = 16$ . Because of modulations that occur on the SD signal due to the holes from the screen, one orbit's worth of SD observations will not be sufficient to calibrate the reflective bands. Therefore, data aggregated over multiple orbits must be used to estimate the values of F to use in the LUT. This process is described in [Appendix B](#).

The calibration coefficients change as a function of electronics temperature  $T_{elec}$ , and detector temperature  $T_{det}$ , and can be expressed as  $c_0(T_{det}, T_{elec})$ ,  $c_1(T_{det}, T_{elec})$  and

$c_2(T_{det}, T_{elec})$ . Here  $c_j(T_{det}, T_{elec})$  is the coefficient computed from the formula given in [Table 12](#) and  $c'_j(T_{det}, T_{elec})$  is the corrected coefficient using the factor  $F$  from [Eq. 65](#) and [Eq. 68](#).

The Earth View radiances for the reflective bands are determined by dropping the background from [Eq. 20](#) and combining it with [Eq. 31](#) and [Eq. 64](#)

$$\begin{aligned} \overline{L_{ap}}(\theta_{ev}, B) &= \frac{\overline{\Delta L_{det}}(\theta_{ev}, B)}{\text{RVS}(\theta_{ev}, B)} \\ &= \frac{F \cdot \sum_{i=0}^2 c_i \cdot dn_{ev}^i}{\text{RVS}(\theta_{ev}, B)} = \frac{\sum_{i=0}^2 c'_i \cdot dn_{ev}^i}{\text{RVS}(\theta_{ev}, B)} \end{aligned} \quad \text{Eq. 70}$$

The reflectance equations are similar to the radiance equations. Reflectance is defined here as the Earth View spectral radiance divided by the spectral radiance from a 100% Lambertian reflector. The spectral reflectance of the solar diffuser is given by the ratio of the irradiance observed reflecting from the solar diffuser, and to the known irradiance incident on the diffuser

$$\begin{aligned} \rho_{sd}(\lambda) &= \frac{\pi \cdot L_{ap}(\theta_{sd}, \lambda)}{\cos(\theta_{inc}) \cdot E_{sun}(\lambda, d_{se})} \\ &= \frac{\pi \cdot \tau_{sds}(\phi_h, \phi_v, \lambda) \cdot E_{sun}(\lambda, d_{se}) \cdot \cos(\theta_{inc}) \cdot \text{BRDF}(\phi_h, \phi_v, \lambda)}{\cos(\theta_{inc}) \cdot E_{sun}(\lambda, d_{se})} \\ &= \pi \cdot \tau_{sds}(\phi_h, \phi_v, \lambda) \cdot \text{BRDF}(\phi_h, \phi_v, \lambda) \end{aligned} \quad \text{Eq. 71}$$

The value  $\pi$  is from the solid angle normalization. Like the band-averaged radiance, the band-averaged reflectance integral includes weighting for the RSR, but unlike the radiance, it also is weighted for solar irradiance

$$\overline{\rho}(B) = \frac{\int \text{RSR}(\lambda) \cdot E_{sun}(\lambda, d_{se}) \cdot \rho(\lambda) d\lambda}{\int \text{RSR}(\lambda) \cdot E_{sun}(\lambda, d_{se}) d\lambda} \quad \text{Eq. 72}$$

After substituting Eq. 71 into Eq. 72

$$\overline{\rho}_{sd}(B) = \frac{\pi \cdot \int \text{RSR}(\lambda) \cdot \tau_{sds}(\phi_h, \phi_v, \lambda) \cdot E_{sun}(\lambda, d_{se}) \cdot \text{BRDF}(\phi_h, \phi_v, \lambda) d\lambda}{\int \text{RSR}(\lambda) \cdot E_{sun}(\lambda, d_{se}) d\lambda} \quad \text{Eq. 73}$$

Combining [Eq. 63](#) with [Eq. 73](#)

$$\overline{\rho_{sd}}(B) = \frac{\pi}{\cos(\theta_{inc})} \cdot \frac{\overline{\Delta L_{det\_sd}}(\phi_h, \phi_v, B)}{E_{sun}(\lambda, d_{se}) \cdot RVS(\theta_{sd}, B)} \quad \text{Eq. 74}$$

Substituting Eq. 30 yields

$$\overline{\rho_{sd}}(B) = \frac{\pi}{E_{sun}(\lambda, d_{se}) \cdot RVS(\theta_{sd}, B) \cdot \cos(\theta_{inc})} \cdot \sum_{j=0}^2 c'_j dn_{sd}^j \quad \text{Eq. 75}$$

After defining

$$d_j = \frac{\pi}{E_{sun}(\lambda, d_{se})} \cdot c'_j, \quad \text{Eq. 76}$$

[Eq. 75](#) becomes

$$\overline{\rho_{sd}}(B) = \frac{\sum_{j=0}^2 d_j dn_{sd}^j}{RVS(\theta_{sd}, B) \cdot \cos(\theta_{inc})} \quad \text{Eq. 77}$$

Similar to deriving spectral reflectance for the solar diffuser in Eq. 71 above, the spectral Earth-View reflectance is

$$\rho_{ev}(\theta_{ev}, \lambda) = \frac{\pi \cdot L_{ap}(\theta_{ev}, \lambda)}{\cos(\theta_{sun\_earth}) \cdot E_{sun}(\lambda, d_{se})} \quad \text{Eq. 78}$$

From [Eq. 72](#), the band-averaged reflectance is defined as

$$\overline{\rho_{ev}}(\theta_{ev}, B) = \frac{\pi \cdot \int RSR(\lambda) \cdot L_{ap}(\theta_{ev}, \lambda) d\lambda}{\cos(\theta_{sun\_earth}) \cdot \int RSR(\lambda) \cdot E_{sun}(\lambda, d_{se}) d\lambda} \quad \text{Eq. 79}$$

Combining [Eq. 19](#) with [Eq. 79](#) results in

$$\begin{aligned} \overline{\rho_{ev}}(\theta_{ev}, B) &= \frac{\pi \cdot \int RSR(\lambda) d\lambda}{\cos(\theta_{sun\_earth}) \cdot \int RSR(\lambda) \cdot E_{sun}(\lambda, d_{se}) d\lambda} \cdot \overline{L_{ap\_ev}}(\theta_{ev}, \lambda) \\ &= \frac{\pi \cdot \overline{L_{ap\_ev}}(\theta_{ev}, \lambda)}{\cos(\theta_{sun\_earth}) \cdot \overline{E_{sun}}(\lambda, d_{se})} \end{aligned} \quad \text{Eq. 80}$$

Substituting [Eq. 70](#) and [Eq. 76](#) into [Eq. 80](#) gives

$$\begin{aligned}\overline{\rho_{ev}}(\theta_{ev}, B) &= \frac{\pi \cdot \sum_{j=0}^2 c'_j dn_{ev}^j}{\text{RVS}(\theta_{ev}, B) \cdot \cos(\theta_{sun\_earth}) \cdot \overline{E_{sun}}(\lambda, d_{se})} \\ &= \frac{\sum_{j=0}^2 d_j dn_{ev}^j}{\text{RVS}(\theta_{ev}, B) \cdot \cos(\theta_{sun\_earth})}\end{aligned}\tag{Eq. 81}$$

This equation is identical to [Eq. 77](#) except that the solar incidence angle upon the diffuser is replaced with the solar incidence angle upon the earth.<sup>17</sup>

### 3.3.3.1 Solar Diffuser Stability Monitor Equations

The Solar Diffuser Stability Monitor (SDSM) is used to track changes in solar diffuser BRDF. Recall from Section 3.3.3 that the view angles from RTA to SD are dropped from the description of the BRDF due to the fact that the RTA always views the SD from approximately the same angle. However the SDSM views the SD from a different angle and therefore "sees" a different BRDF, defined as BRDF' to distinguish it. In an analogous manner that "dn" represents the VIIRS signal difference between scene/calibration signal (i.e. DN) and space view, "dc" represents an equivalent digital count difference obtained by subtracting the offset value from the SDSM detector signal (i.e. DC) when viewing either the SD or the sun. The SDSM digital counts remove a signal offset by observing the dark, unilluminated internal cavity,

$$\begin{aligned}dc_{sun} &= DC_{sun} - DC_{offset} \\ dc_{sd} &= DC_{sd} - DC_{offset}\end{aligned}\tag{Eq. 82}$$

The irradiance on the SDSM when viewing the SD is

$$\begin{aligned}E_{sdsm\_sd}(\phi_h, \phi_v, \lambda, d_{se}) &= \cos(\theta_{inc}) \cdot E_{sun}(\lambda, d_{se}) \cdot \tau_{sds}(\phi_h, \phi_v, \lambda) \cdot \Omega_{sdsm} \text{BRDF}'(\phi_h, \phi_v, \lambda) \\ &= \cos(\theta_{inc}) \cdot \frac{\Phi_{sun}(\lambda)}{4\pi \cdot d_{se}^2} \cdot \tau_{sds}(\phi_h, \phi_v, \lambda) \cdot \Omega_{sdsm} \text{BRDF}'(\phi_h, \phi_v, \lambda),\end{aligned}\tag{Eq. 83}$$

where  $\theta_{inc}$  is the solar incidence angle onto the SD relative to normal,  $\tau_{sds}(\phi_h, \phi_v, \lambda)$  is the spectral transmittance of the SDS,  $\Omega_{sdsm}$  is the solid angle subtended by the SDSM solar diffuser viewing cone, and the solar irradiance is

<sup>17</sup> Note that the earth reflectance is not dependent on the sun-to-earth distance,  $d_{se}$ . This is evident from [Eq. 80](#), since both  $\overline{L_{ap}}(\theta_{ev}, \lambda)$  in the numerator and  $\overline{E_{sun}}(\lambda, d_{se})$  in the denominator are inversely proportional to the square of  $d_{se}$  and thus this inverse square effect cancels.

$$E_{sun}(\lambda, d_{se}) = \frac{\Phi_{sun}(\lambda)}{4\pi \cdot d_{se}^2} \quad \text{Eq. 84}$$

Here  $E_{sun}(\lambda, d_{se})$  is the irradiance on a surface with its normal facing the sun and  $\Phi_{sun}(\lambda)$  is the spectral output power of the sun in W/ $\mu\text{m}$ . The irradiance on the SDSM when viewing the sun is

$$E_{sds\_sun}(\lambda, d_{se}) = E_{sun}(\lambda, d_{se}) \cdot \tau_{sds}(\phi_{h\_sds}, \phi_{v\_sds}, \lambda) = \frac{\Phi_{sun}(\lambda)}{4\pi \cdot d_{se}^2} \cdot \tau_{sds}(\phi_{h\_sds}, \phi_{v\_sds}, \lambda) \quad \text{Eq. 85}$$

where  $\tau_{sds}(\phi_{h\_sds}, \phi_{v\_sds}, \lambda)$  is the spectral transmittance of the SDSM screen when viewing the sun. The subscripts  $h\_sds$  and  $v\_sds$  are the horizontal and vertical sun incidence angles on the SDSM screen.

An SDSM detector is assumed to have a linear gain with zero offset,  $G_{sds}(t)$ , therefore

$$E_{sds\_sd}(\lambda) = G_{sds} \cdot dc_{sd} \quad \text{Eq. 86}$$

and

$$E_{sds\_sun}(\lambda) = G_{sds} \cdot dc_{sun} \quad \text{Eq. 87}$$

Equating [Eq. 83](#) with [Eq. 86](#) and solving for BRDF' gives

$$\text{BRDF}'(\phi_h, \phi_v, \lambda) = \frac{4\pi \cdot d_{se}^2 \cdot G_{sds} \cdot dc_{sd}}{\tau_{sds}(\phi_h, \phi_v, \lambda) \cdot \Omega_{sds} \cdot \cos(\theta_{inc}) \cdot \Phi_{sun}(\lambda)} \quad \text{Eq. 88}$$

Combining [Eq. 87](#) with [Eq. 88](#) yields

$$\text{BRDF}'(\phi_h, \phi_v, \lambda) = \frac{4\pi \cdot d_{se}^2 \cdot E_{sds\_sun}(\lambda) \cdot dc_{sd}}{\tau_{sds}(\phi_h, \phi_v, \lambda) \cdot \Omega_{sds} \cdot \cos(\theta_{inc}) \cdot \Phi_{sun}(\lambda) \cdot dc_{sun}} \quad \text{Eq. 89}$$

Solving Eq. 85 for  $\tau_{sds}(\phi_{h\_sds}, \phi_{v\_sds}, \lambda)$  and substituting into [Eq. 89](#), the expression for BRDF' reduces to

$$\text{BRDF}'(\phi_h, \phi_v, \lambda) = \frac{\tau_{sds}(\phi_{h\_sds}, \phi_{v\_sds}, \lambda) \cdot dc_{sd}}{\tau_{sds}(\phi_h, \phi_v, \lambda) \cdot \Omega_{sds} \cdot \cos(\theta_{inc}) \cdot dc_{sun}} \quad \text{Eq. 90}$$

The values for  $\tau_{sds}$  and  $\tau_{sds m}$  are not expected to change during flight<sup>18</sup> and are based on a fixed look-up table. Sun-Earth distance,  $d_{se}$ , actually changes over time, and there is an assumption here that it is the same for the sun view as for the SD view. These are only one scan apart and the change in distance is negligible over that period.

The band averaged BRDF can be expressed as,

$$\begin{aligned} \overline{\text{BRDF}'(\phi_h, \phi_v, \lambda)_{sds m}} &= \overline{\text{BRDF}(\phi_h, \phi_v, B_{sds m})} \\ &= \left( \frac{\tau_{sds m}(\phi_{h\_sds m}, \phi_{v\_sds m}, \lambda)}{\tau_{sds}(\phi_h, \phi_v, \lambda)} \right) \cdot \frac{dc_{sd}}{\Omega_{sds m} \cdot \cos(\theta_{inc}) \cdot dc_{sun}} \end{aligned} \quad \text{Eq. 91}$$

Here  $B_{sds m}$  indicates averaging over the SDSM band, which has different spectral characteristics than the VIIRS bands.

Although the BRDF changes slowly over time, its relative directional dependence is assumed to be invariant. This assumption is supported by analysis of solar diffusers in heritage instruments such as MODIS and SeaWiFS. With these assumptions the time dependence of the BRDF is completely described by a scale factor. Note that in the following expressions the BRDF term has two values of time  $t$ ; the first sets the incident angle, and the second is the time at which the BRDF is measured. With an additional assumption that the spectral dependence of the BRDF does not change over the SDSM bandwidth, the degradation over time of the post-launch BRDF' can be modeled as

$$\overline{\text{BRDF}'(\phi_h, \phi_v, B_{sds m}, t)} = H(t) \cdot \overline{\text{BRDF}'(\phi_h, \phi_v, B_{sds m}, t_0)} \quad \text{Eq. 92}$$

The value  $t_0$  indicates the time of the BRDF prelaunch characterization. Therefore, by definition  $H(t_0)=1$ .

Note that since  $\tau_{sds}$  and  $\tau_{sds m}$  are almost constant with respect to wavelength over the band, the band-averaged value can be substituted and factored out of the integral over the ratio in [Eq. 91](#). The band-averaged  $\tau_{sds}$  and  $\tau_{sds m}$  can be expressed as

$$\begin{aligned} \overline{\tau_{sds}(\phi_h, \phi_v, B_{sds m})} &= \overline{\tau_{sds}(\phi_h, \phi_v, \lambda)} \\ \overline{\tau_{sds m}(\phi_{h\_sds m}, \phi_{v\_sds m}, B_{sds m})} &= \overline{\tau_{sds m}(\phi_{h\_sds m}, \phi_{v\_sds m}, \lambda)} \end{aligned} \quad \text{Eq. 93}$$

Also note that variation of  $\tau_{sds m}$  with wavelength is actually due to the placement of the detector inside the SDSM integrating sphere and is not truly wavelength dependent. The SD screen transmittance,  $\tau_{sds}$ , however, includes a stray light term, which is wavelength dependent, and which is discussed in [Appendix B](#).

<sup>18</sup> These screens are simply a thin sheet with drilled holes and black paint on one side to prevent multiple reflections. The only possible way that this could change in transmittance is if the holes changed size or if the black paint changed reflectance. The paint reflectance will probably change somewhat, but not enough to make a measurable difference since the contribution from multiple reflection is very small.

Combining Eq. 91 and Eq. 93 yields

$$\overline{\text{BRDF}}(\phi_h, \phi_v, B_{sdsm}) = \frac{\overline{\tau_{sdsm}}(\phi_{h\_sdsm}, \phi_{v\_sdsm}, B_{sdsm})}{\overline{\tau_{sds}}(\phi_h, \phi_v, B_{sdsm})} \cdot \frac{dc_{sd}}{\Omega_{sdsm} \cdot \cos(\theta_{inc}) \cdot dc_{sun}} \quad \text{Eq. 94}$$

Eq. 94 provides an absolute measurement of the SD BRDF, and could, in theory, be used to track all change in BRDF over time without depending on the prelaunch characterization of the BRDF. The problem with this is that there are measurement uncertainties associated with all the values in the equation. In addition to inherent measurement uncertainties associated with the characterization test set-up,  $\tau_{sdsm}$  has significant modulations over the two angles, and characterization in the azimuthal dimension was coarsely sampled. Similarly,  $\tau_{sds}$  has coarsely sampled modulations, and also includes a stray light term, as discussed in [Appendix B](#). The value of the SDSM solid angle  $\Omega_{sdsm}$  is based on the design, but manufacturing tolerances makes this imperfect. Because of these uncertainties, [Eq. 94](#) is only used during the early days of intensive Cal/Val to verify that the BRDF has not changed from its prelaunch characterization. The assumption is made that the BRDF has not changed significantly between the time of characterization and the time of post launch with first-light on the SD, designated as beginning of life (BOL). Mathematically this assumption is expressed as for  $H(t_{BOL}) = H(t_0) = 1$ . However, if the difference between the characterized BRDF' and the BRDF' from [Eq. 94](#) is greater than what could be explained by the uncertainties discussed here, then a value for  $H(t_{BOL})$  based on [Eq. 94](#) and other data<sup>19</sup> would be considered.

After initial determination of the value of  $H(t_{BOL})$ , the SDSM is used to track relative change of the BRDF. Combining [Eq. 92](#) with [Eq. 94](#) gives an expression for the relative change in  $H$  between time  $t_1$  and  $t_2$  as,

$$\frac{H(t_1)}{H(t_2)} = \frac{\left( \frac{\overline{\tau_{sdsm}}(t'_1)}{\overline{\tau_{sds}}(t_1)} \cdot \frac{dc_{sd}(t_1)}{\cos(\theta_{inc}(t_1)) \cdot dc_{sun}(t'_1)} \right)}{\left( \frac{\overline{\tau_{sdsm}}(t'_2)}{\overline{\tau_{sds}}(t_2)} \cdot \frac{dc_{sd}(t_2)}{\cos(\theta_{inc}(t_2)) \cdot dc_{sun}(t'_2)} \right)} \cdot \frac{\overline{\text{BRDF}}'(\phi_h(t_2), \phi_v(t_2), t_0)}{\overline{\text{BRDF}}'(\phi_h(t_1), \phi_v(t_1), t_0)} \quad \text{Eq. 95}$$

Here the following shorthand is used

$$\overline{\tau_{sdsm}}(t'_i) = \overline{\tau_{sdsm}}(\phi_{h\_sdsm}(t'_i), \phi_{v\_sdsm}(t'_i), B_{sdsm}), \quad \text{Eq. 96}$$

$$\overline{\tau_{sds}}(t_i) = \overline{\tau_{sds}}(\phi_h(t_i), \phi_v(t_i), B_{sdsm}), \quad \text{Eq. 97}$$

<sup>19</sup> This data could include witness sample measurements or Spectralon<sup>®</sup> aging tests.

where  $t'_i$  and  $t_i$  are the times of the sun and solar diffuser views, respectively.<sup>20</sup> The functional dependency on  $B_{sds m}$  in the BRDF and the screen transmittance terms has been dropped here for brevity.

The SDSM acquires data over a period close to one minute, or approximately 33 RTA scans. However, not all data is used as there are acceptance limits restricting the data to a specific angular range that is within the design limits of both the solar diffuser attenuation screen and the SDSM screen. Due to a design slip of the SDSM unit, a separate check must be performed for the SD and SDSM angles [ref. Y22114]. If  $N_i$  is the number of samples in the SDSM data acquisition  $i$ , then the sample-averaged version of [Eq. 95](#) is

$$\frac{H(t_j)}{H(t_i)} = \frac{\frac{1}{N_j} \sum_{n=1}^{n=N_j} \overline{\text{BRDF}'(\phi_h(t_{j,n}), \phi_v(t_{j,n}), t_0) \cdot \cos(\theta_{inc}(t_{j,n})) \cdot \frac{dc_{sun}(t'_{j,n}) \cdot \overline{\tau_{sds}}(t_{j,n})}{dc_{sd}(t_{j,n}) \cdot \overline{\tau_{sds m}}(t'_{j,n})}}}{\frac{1}{N_i} \sum_{n=1}^{n=N_i} \overline{\text{BRDF}'(\phi_h(t_{i,n}), \phi_v(t_{i,n}), t_0) \cdot \cos(\theta_{inc}(t_{i,n})) \cdot \frac{dc_{sun}(t'_{i,n}) \cdot \overline{\tau_{sds}}(t_{i,n})}{dc_{sd}(t_{i,n}) \cdot \overline{\tau_{sds m}}(t'_{i,n})}}}$$

**Eq. 98**

To understand this equation it is important to know how the sequence in which the SDSM collects the data. It performs a three-scan cycle, sequentially looking at a dark view, a solar diffuser view and a sun view. For each of the three scans, five samples are taken, as shown in [Figure 21](#). The SDSM motor operation and data collect are clocked to correspond to times between the earth and cal views in order to eliminate any interference and crosstalk. The five samples are taken at 0.1-second intervals just after the RTA passes the SD. Before the next SDSM data collection the motor is moved during the times shown in the figure. The times given in [Eq. 98](#) can be computed as,

$$t_{i,n} = t_i + 0.83 + 0.1 \cdot \text{mod}(n-1, 5) + 3 \cdot \text{floor}((n-1)/5) \cdot \Delta t_{scan}$$

**Eq. 99**

and

$$t'_{i,n} = t_{i,n} + \Delta t_{scan}$$

**Eq. 100**

The definition of  $t_i$ , the SDSM acquisition time, is somewhat arbitrary. In [Eq. 99](#), it is set as the nadir point for the first SD view scan. The SD view is the second scan of the three-scan cycle, so this does not represent the actual start of the acquisition. The definition of “SDSM acquisition” as used here refers to all samples from one orbit that fall within the angular limits of the intersection of the SDSM and SD solar illumination window.

<sup>20</sup> Note that the time  $t$  associated with  $T_{sds m}$  is the sampling time of the sun view and is different from that associated with the BRDF or  $T_{sds}$ . In the current configuration, the sun view occurs one scan after the solar diffuser view.

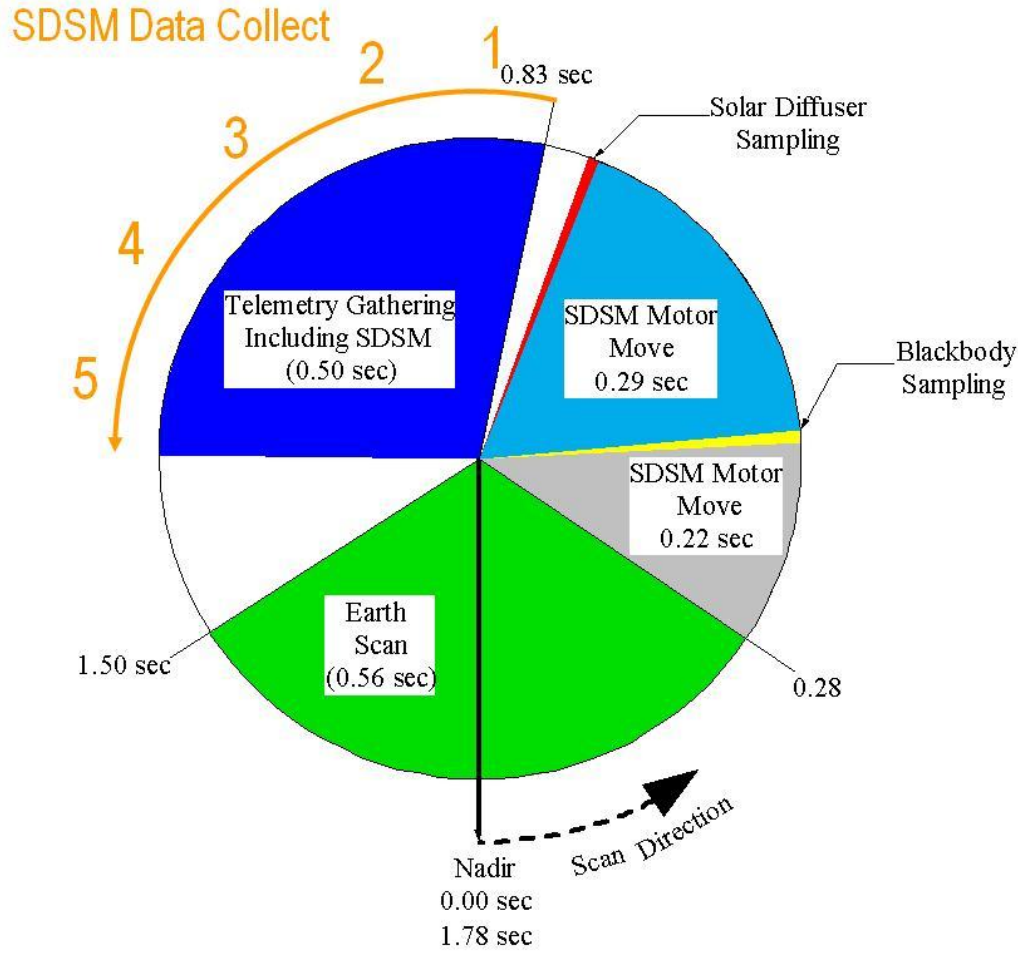


Figure 21: Timing of SDSM collect

The SD reflectance will be measured with the SDSM every orbit and these measurements will be accumulated, trended and projected in order to provide an update. The update frequency will depend on how much change is seen in trending these data.

For this periodic data analysis,  $H(t_i)$  is not directly calculated, instead  $h(t_i)$  is produced by the algorithm, where

$$h(t_i) = \frac{1}{N_i} \sum_{n=1}^{n=N_i} \overline{\text{BRDF}'(\phi_h(t_{i,n}), \phi_v(t_{i,n}), t_0) \cdot \cos(\theta_{inc}(t_{i,n}))} \cdot \frac{dc_{sun}(t'_{i,n}) \cdot \overline{\tau_{sds}(t_{i,n})}}{dc_{sd}(t_{i,n}) \cdot \tau_{sds}(t'_{i,n})} \quad \text{Eq. 101}$$

thus:

$$\frac{H(t_i)}{H(t_j)} = \frac{h(t_j)}{h(t_i)} \quad \text{Eq. 102}$$

Therefore,  $H(t_i)$  is directly proportional to the inverse of  $h(t_i)$ . An algorithm support function (ASF) will be used on orbit to trend the changes to  $h(t_i)$ . The on-orbit operational SDR algorithm outputs the values of  $h(t_i)$  for each acquisition along with the standard deviation of the individual components inside the summation given in [Eq. 101](#). Anomalous acquisitions are filtered out by the ASF using standard deviation thresholds. During intensive cal/val the SDSM data will be analyzed to determine what constitutes an anomalously high standard deviation. Most of the variation here comes from the uncertainties in modulations of the SD attenuation screen and SDSM screen transmittances.

After the ASF filters the data for anomalies, it will trend the data. [Figure 22](#) shows the MODIS Terra values of  $H(t_i)$  trended over 1000 days. The effect where the blue bands degrade faster than the red and NIR bands is called yellowing, and is evident in this plot. Similar trends are expected for VIIRS. Note the strong, correlated modulations that can be seen in the data trend. These modulations are evidently due to the screens, and the ASF will have the ability to filter out correlated modulations. Although the degradations seen in [Figure 22](#) are fairly linear, it is possible for them to stabilize over longer periods of time. The ASF will allow the data to be fit to higher order degradation curves

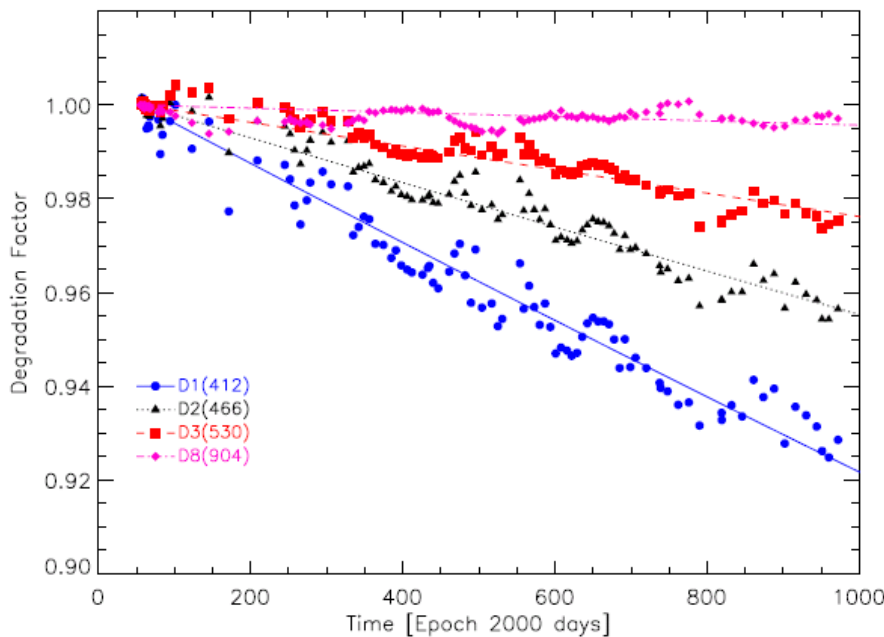


**Figure 22: Changes to MODIS Terra SD reflectance trended over 1000 days.**

### 3.3.3.2 Solar Diffuser Geometry

The unit vector describing the orientation of the sun with respect to the instrument,  $\mathbf{s}_{inst}$ , is computed by the VIIRS Geolocation Algorithm, output in the Geolocation IP,

and is read in by the SD algorithm as part of the SD View Processing. The sun to earth distance  $d_{se}$  is also read in from the Geolocation IP.

The solar angles measured off the instrument coordinates are determined from  $\mathbf{s}_{inst}$  defined as:

$$\mathbf{s}_{inst} = \begin{bmatrix} x_{inst} \\ y_{inst} \\ z_{inst} \end{bmatrix}$$

$$d_{se} = |\mathbf{s}_{inst}| = \sqrt{x_{inst}^2 + y_{inst}^2 + z_{inst}^2} \quad \text{Eq. 103}$$

The vector describing the orientation of solar diffuser with respect to the spacecraft,  $\mathbf{s}_{sd}$ , is computed using  $\mathbf{s}_{inst}$  and a transformation matrix,  $\mathbf{T}_{SD/inst}$ . The Geolocation Algorithm produces solar diffuser angles,  $\theta_{inc}$ ,  $\phi_{inc}$ , from the instrument coordinate system solar vector,  $\mathbf{s}_{inst}$ , as follows:

$$\begin{aligned} \mathbf{s}_{sd} &= \mathbf{T}_{sd/inst} \mathbf{s}_{inst} \\ &= |\mathbf{s}_{sd}| \cdot \begin{bmatrix} \sin(\theta_{inc}) \cos(\phi_{inc}) \\ \sin(\theta_{inc}) \sin(\phi_{inc}) \\ \cos(\theta_{inc}) \end{bmatrix} = \begin{bmatrix} x_{sd} \\ y_{sd} \\ z_{sd} \end{bmatrix} \end{aligned}$$

where

$$\mathbf{T}_{sd/inst} = \begin{bmatrix} \cos \alpha \cos \beta \cos \gamma - \sin \alpha \sin \gamma & \sin \alpha \cos \beta \cos \gamma + \cos \alpha \sin \gamma & -\sin \beta \cos \gamma \\ -\cos \alpha \cos \beta \sin \gamma - \sin \alpha \cos \gamma & -\sin \alpha \cos \beta \sin \gamma + \cos \alpha \cos \gamma & \sin \beta \sin \gamma \\ \cos \alpha \sin \beta & \sin \alpha \sin \beta & \cos \beta \end{bmatrix} \quad \text{Eq. 104}$$

$$\begin{aligned} \therefore \theta_{inc} &= \frac{\pi}{2} - \arctan 2 \left( z_{sd}, \sqrt{x_{sd}^2 + y_{sd}^2} \right) \\ \phi_{inc} &= \arctan 2(y_{sd}, x_{sd}) \end{aligned}$$

The SD coordinate system is defined with the z-axis normal to the Solar Diffuser (SD), the y-axis is aligned with the cross-track scan angle, and the x-axis completes the right-hand coordinate system. The transformation matrix,  $\mathbf{T}_{SD/inst}$ , is determined by accurate pre-launch measurements. Vertical and horizontal incidence angles of solar illumination,  $\phi_v$  and  $\phi_h$ , are with respect to the SDS. Since the SDS is oriented to be parallel to the y-z plane of the instrument, the instrument coordinate system and the SDS coordinate system are identical with the exception of the horizontal angle. Here, the sign is reversed because the solar diffuser is on the negative y side of the instrument. The angles are computed using the following equations:

$$\phi_v = -\arctan 2(z_{inst}, x_{inst}) \quad \text{Eq. 105}$$

$$\phi_h = -\phi_{sun\_inst}$$

Eq. 106

The BRDF of the SD for each scan in an acquisition is determined by interpolating  $\phi_v$ ,  $\phi_h$ , and a BRDF LUT. Likewise, the transmittance of the SDS,  $\tau_{sds}$ , is determined as a function of  $\phi_v$ , and  $\phi_h$ , by interpolating the SDS transmittance LUT.

### 3.3.4 Emissive ‘M’ and ‘I’ Band Calibration

The known radiance source for the emissive bands is a blackbody reference. This On-Board Calibrator Blackbody (OBCBB) has a known emissivity and temperature. Self-emission from inside the instrument must be subtracted to properly determine the emissive band radiance being observed from the earth. Therefore, the emissivities and temperatures of several instrument components, including optical components, must also be used in the calibration equations. The SDR product requirements for the emissive bands are calibrated top-of-atmosphere radiance and brightness temperature.

#### 3.3.4.1 Earth View Emissive Band Radiometric Calibration

The OBCBB is used to allow for adjustment of the calibration coefficients during operation after launch. The radiance when observing the OBCBB,  $L_{ap}(\theta_{obc}, \lambda)$ , is the sum of the emissive radiance from the OBCBB and the reflected radiance off the OBCBB which are originally emitted from the cavity, blackbody shield or telescope.. This can be expressed as,

$$L_{ap}(\theta_{obc}, \lambda) = \varepsilon_{obc}(\lambda) \cdot L(T_{bcs}, \lambda) + L_{obc\_rfl}(T_{sh}, T_{cav}, T_{tele}, \lambda)$$

Eq. 107

where  $\varepsilon_{obc}(\lambda)$  is spectral emissivity of the OBCBB,  $L(T_{bcs}, \lambda)$  is blackbody spectral radiance according to Planck’s function, and

$$L_{obc\_rfl}(T_{sh}, T_{cav}, T_{tele}, \lambda) = (1 - \varepsilon_{obc}(\lambda)) \cdot (F_{sh} \cdot L(T_{sh}, \lambda) + F_{cav} \cdot L(T_{cav}, \lambda) + F_{tele} \cdot L(T_{tele}, \lambda))$$

Eq. 108

The factors  $F_{sh}$ ,  $F_{cav}$  and  $F_{tele}$  represent the fraction of the reflectance off the OBCBB originating from each of the three sources: blackbody shield, cavity, and telescope. These factors represent an integration of the BRDF of the OBCBB over the integration limits defined by the solid angle subtended by each of the three source's solid angles. [Equation 108](#) assumes that the emissivity of the 3 sources is 1.0, so it therefore follows that

$$F_{sh} + F_{cav} + F_{tele} = 1$$

Eq. 109

Even though the emissivities of any of the sources is less than 1.0, their combined effective emissivity will be 1.0 due to multiple internal reflections within the OBCBB cavity.

By substituting [Eq. 108](#) into [Eq. 107](#) and setting all temperatures equal to  $T_{obc}$  it can be seen that the radiance is that of a perfect blackbody, that is, with an emissivity of 1.0. Though these temperatures are rarely exactly equal, they are fairly close so the OBCBB acts more like a blackbody than might be assumed simply based on its emissivity.

Taking the band-average of [Eq. 107](#) we get,

$$\overline{L_{ap}}(\theta_{obc}, B) = \overline{[\varepsilon_{obc}(\lambda) \cdot L(T_{obc}, \lambda) + L_{obc\_rfl}(T_{sh}, T_{cav}, T_{tle}, \lambda)]} \quad \text{Eq. 110}$$

Setting [Eq. 45](#) equal to [Eq. 110](#) at the OBCBB scan angle and expressing the result in terms of the quadratic series

$$\sum_{i=0}^2 c_i \cdot dn_{obc}^i = \text{RVS}(\theta_{obc}, B) \cdot \overline{[\varepsilon_{obc}(\lambda) \cdot L(T_{obc}, \lambda) + L_{obc\_rfl}(T_{sh}, T_{cav}, T_{tle}, \lambda)]} \\ + (\text{RVS}(\theta_{obc}, B) - \text{RVS}(\theta_{sv}, B)) \cdot \frac{\{(1 - \overline{\rho_{rta}}(\lambda)) \cdot \overline{L(T_{rta}, \lambda)} - \overline{L(T_{ham}, \lambda)}\}}{\overline{\rho_{rta}}(\lambda)} \quad \text{Eq. 111}$$

[Equation 111](#) is used on-orbit to update the coefficients. However since there are three unknowns in one equation, some assumptions or constraints need to be made in order to solve for the coefficients. Making the assumption that the shape of the response curve is preserved allows the application of the same scale factor,  $F$ , to all three coefficients. The updated coefficients, designated as  $c'_j$ , are scaled equally by the change in scale (or gain) of the response. Substituting  $c'_j = F \cdot c_j$  into [Eq. 111](#) and recognizing that the band averaged OBC emissivity can be separated out gives

$$F = \frac{\text{RVS}(\theta_{obc})}{\sum_{j=0}^2 c_j \cdot dn_{obc}^j} \cdot \left\{ \left( 1 - \frac{1}{\text{RVS}(\theta_{obc})} \right) \cdot \left[ \left( \frac{1}{\overline{\rho_{rta}}(\lambda)} - 1 \right) \cdot \overline{L(T_{rta}, \lambda)} - \frac{\overline{L(T_{ham}, \lambda)}}{\overline{\rho_{rta}}(\lambda)} \right] \right. \\ \left. + \overline{\varepsilon_{obc}}(\lambda) \cdot \overline{L(T_{obc}, \lambda)} + \overline{L_{obc\_rfl}}(T_{sh}, T_{cav}, T_{tle}, \lambda) \right\} \quad \text{Eq. 112}$$

Averaging all frames of each scan then gives,

$$F = \text{RVS}(\theta_{obc}) \frac{\left\{ \left( 1 - \frac{1}{\text{RVS}(\theta_{obc})} \right) \cdot \left[ \left( \frac{1}{\rho_{rta}(\lambda)} - 1 \right) \cdot \overline{L(T_{rta}(t), \lambda)} - \frac{\overline{L(T_{ham}(t), \lambda)}}{\rho_{rta}(\lambda)} \right] \right.}{\left. + \varepsilon_{obc}(\lambda) \cdot \overline{L(T_{obc}(t), \lambda)} + L_{obc\_rfl}(T_{sh}(t), T_{cav}(t), T_{tele}(t), \lambda)} \right\}}{\sum_{j=0}^2 c_j \cdot \overline{dn_{obc}(t)}^j} \quad \text{Eq. 113}$$

where,  $t$  is the start time of the acquisition period and where the average counts per scan viewing the OBCBB is

$$\overline{dn_{obc}(t)} = \frac{1}{N_{cal}} \sum_{m=0}^{N_{cal}} dn_{obc}(t + m \cdot \Delta t_{frame}) \quad \text{Eq. 114}$$

The number of frames per scan over which the OBCBB counts are recorded is  $N_{cal}$ . This is set to 48 in the current design for the 'M' bands and 48 for each of the first and second sub-frame averages for the 'I' bands, see Section 3.4.6.

The band-averaged OBCBB reflected radiance is,

$$\overline{L_{obc\_rfl}(T_{sh}, T_{cav}, T_{tele}, \lambda)} = F_{sh} \cdot (1 - \varepsilon_{obc}(\lambda)) \cdot \overline{L(T_{sh}, \lambda)} + F_{cav} \cdot (1 - \varepsilon_{obc}(\lambda)) \cdot \overline{L(T_{cav}, \lambda)} + F_{tele} \cdot (1 - \varepsilon_{obc}(\lambda)) \cdot \overline{L(T_{tele}, \lambda)} \quad \text{Eq. 115}$$

Expressing [Eq. 45](#) with all temperature dependencies shown gives,

$$\overline{L_{ap}}(\theta_{ev}, B) = \frac{(1 - \text{RVS}(\theta_{ev}, B)) \cdot \left[ \left( \frac{1}{\rho_{rta}(\lambda)} - 1 \right) \cdot \overline{L(T_{rta}, \lambda)} - \frac{\overline{L(T_{ham}, \lambda)}}{\rho_{rta}(\lambda)} \right] + F \cdot \sum_{i=0}^2 c_i(T_{det}, T_{elec}) \cdot \overline{dn_{ev}}^i}{\text{RVS}(\theta_{ev}, B)}$$

Eq. 116

Since the number of thermal plateaus at which measurements are taken in pre-launch testing is limited to three, it is expected that there will not be enough data to accurately determine the separability in  $c_i(T_{det}, T_{elec})$ . This being the case, it will be necessary to use the simplified [Eq. 50](#) rather than [Table 12](#) to compute coefficients. During the pre-launch test procedure the DC restore value changes over the period of the test, and needs to be recorded. Also, the temperatures  $T_{det}$  and  $T_{elec}$  need to be recorded. During characterization, the measurements using SIS(100) lamp for the reflective bands<sup>21</sup>, or the measurements with the BCS for the emissive bands are repeated for three thermal plateaus that produce three values of detector temperature  $T_{det}$ , and electronic

<sup>21</sup> "VIIRS Program Test Procedure for Reflective Band Calibration," TP154640-271

temperature  $T_{elec}$ . With this a temperature dependent  $c_i(T_{det}, T_{elec})$  is to be determined. In Section [2.3.1](#) it was shown that  $c_i$  is expressible in terms of two other sets of coefficients:  $a_i(T_{det})$  used in a polynomial to describe the response of the detectors as a function of detector signal; and  $b_i(T_{elec})$  used in a polynomial to describe the response of detector signal as a function of the output counts. The coefficients  $a_i$  are dependent only on detector temperature  $T_{det}$ , and  $b_i$  depend only on the electronic temperature  $T_{elec}$ , so with these coefficients  $a_i$  and  $b_i$  being accurately determined there is separability in determining dependent  $c_i(T_{det}, T_{elec})$ .

The emissive band radiometric calibration requires not only the radiance but also a brightness temperature (also known as Equivalent Black Body Temperature [EBBT]). To get the band-averaged radiance from a blackbody at temperature  $T$ , take average over the band in [Eq. 36](#)

$$\overline{L(T, \lambda)} = 2c^2 h \cdot 10^{-6} \left( \lambda^{-5} \cdot \left( \exp\left(\frac{hc}{kT\lambda}\right) - 1 \right)^{-1} \right) \quad \text{Eq. 117}$$

Since the band averaging in [Eq. 117](#) represents an integral there is no way to derive a closed-form solution that expresses EBBT as a function of band-averaged radiance. However, [Eq. 117](#) can be used to generate band-averaged radiances at fine intervals of  $T$ , and these data can then be used to generate a LUT of blackbody temperature, EBBT, as a function of radiance (see Section [3.2.3](#)).

#### **3.3.4.1.1 M13 Low Gain**

The low gain mode of band M13 is intended for fire detection, and consequentially has a very high  $T_{max}$  of 634K. This creates calibration problems since, at the OBCBB's nominal temperature of 292K, there are only approximately four counts detected per sample. This relationship between temperature and counts is illustrated in [Figure 23](#). This produces a very low SNR of 6.5 which does not improve during aggregation because the error is not random. That is, if one sample detects four counts then all other samples will also detect exactly four counts.

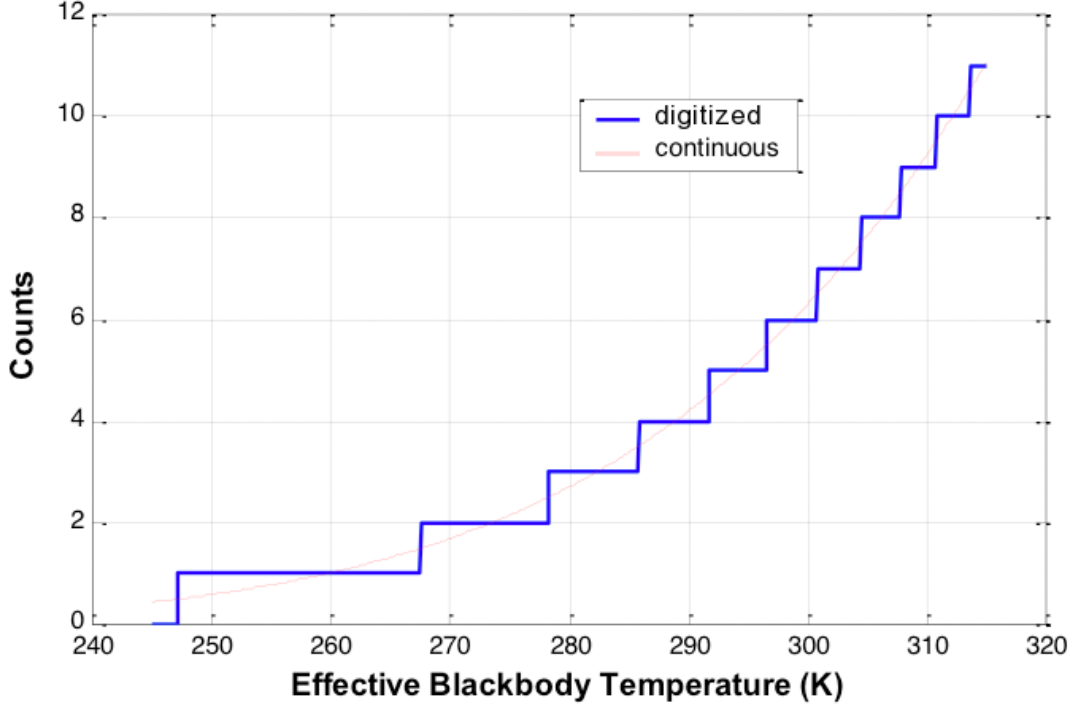


Figure 23:  $dn$  as a function of EBBT for band M13 in the low gain mode

Calibration is possible for the M13 low gain mode if data can be collected while varying the OBCBB temperature. Therefore the OBCBB should be cycled biweekly using the OBCBB heater, over a range from ambient (260K to 292K) up to 315K. The number of counts will not increase linearly as a function of time since counts are not a linear function of temperature (see [Figure 23](#)). Therefore, it is important to weight the measurements so that all counts get equal weighting, as follows.

A modified equation for  $F$  with weighting to equalize the counts is based on [Eq. 112](#)

$$F = \text{RVS}(\theta_{obc}) \cdot \sum_{n=0}^{N_{acq}-1} \left\{ \left( 1 - \frac{1}{\text{RVS}(\theta_{obc})} \right) \cdot \left[ \left( \frac{1}{\rho_{rta}} - 1 \right) \cdot \frac{\overline{L(T_{rta}(t_n))} - \overline{L(T_{ham}(t_n))}}{\rho_{rta}} \right] \right. \\ \left. + \frac{\overline{\varepsilon_{obc}} \cdot \overline{L(T_{obc}(t_n))} + \overline{L_{obc\_rfl}(T_{sh}(t_n), T_{cav}(t_n), T_{tele}(t_n))}}{\rho_{rta}} \right\} \cdot \frac{\sum_{m=0}^{N_{cal}} W(dn_{obc}(n, m))}{\sum_{j=0}^2 c_j \cdot dn_{obc}(n, m)^j},$$

Eq. 118

where  $dn_{obc}(n, m) = dn_{obc}(t_n + m \cdot \Delta t_{frame})$ .

The weighting function is defined as,

$$W(dn) = \begin{cases} \frac{1}{[\max(\overline{dn}) - \min(\overline{dn}) - 2]} \cdot \text{hist}(dn, \overline{dn}) & \text{if } (\min(\overline{dn}) < dn < \max(\overline{dn})) \\ 0 & \text{if } \left( \begin{array}{l} dn = \min(\overline{dn}) \\ \text{or } dn = \max(\overline{dn}) \end{array} \right) \end{cases} \quad \text{Eq. 119}$$

In [Eq. 119](#)  $\overline{dn}$  is the set of all samples measured within the calibration period and  $\text{hist}(dn, \overline{dn})$  is a histogram function giving the number of occurrences of  $dn$  within the set  $\overline{dn}$ . Also it can be seen that the weighting function is set to zero for the lowest and highest number of counts. This is done because these bins are not fully spanned by the range of radiances produced. Therefore, rather than let these bins skew the results, they are discarded.

### 3.3.4.1.2 M13 Band Aggregation

M13 is the only dual gain band in the thermal IR that is aggregated. From the individual space view and blackbody  $DN$ s from the correct scan (see [Table 18](#)), the radiance is calculated per [Eq.114](#), where  $dn_{obc} = DN_{obc} - DN_{sv}$ ,

In the middle three aggregation zones, the radiance is averaged over two, three, and two samples, respectively. The aggregated radiance is then converted to Brightness Temperature. Both the radiance and brightness temperatures are reported across the scan.

### 3.3.5 Day-Night Band Calibration

An overview of the DNB FPA and its interface electronics is presented in Section [2.2.2.4](#). The DNB Calibration requirements [PS154640-101D], which are based on OLSand are considered fairly loose, range from 5% on the LGS to 100% for the HGS. Refer to [Table 7](#) for details.

However, the user's need for visually acceptable imagery calls for a tighter calibration or at least more elaborate processing than would be needed to simply meet the requirement.

#### 3.3.5.1 Overview

Pre-launch analysis indicates that DNB data can potentially meet calibration accuracy requirements without the use of a quadratic term in the calibration equation. The analysis also shows that additional offline refinements to the offset correction performed by VIIRS on-orbit may not be needed. However more rigorous correction, including

accounting for HAM side differences, is needed for optimal image quality and to mitigate sixteen pixel-wide striping in the along-scan direction.

Each stage of the DNB CCD creates free electrons in response to photons, aggregates the electrons over rectangular areas of scene (which vary in angular extent during the scan in 32 different aggregation modes), and generates an output voltage for each pixel that is nominally linearly related to the number of electrons. These output voltages are converted linearly into digital form.

There are eight analog outputs. Each sample from each of the eight analog output ports will have an analog offset, and many of these offsets will be very large compared to signals at the lowest end of the radiance ranges. While the offsets can be predicted within a few percent based on the aggregation mode and “pixel” number in track (more specifically, where the sample falls in the sequential readout from the CCD), this prediction is not adequate for satisfactory removal of the offsets. Instead it is necessary to measure the offsets directly by means of a full scan of a “dark scene”. The data produced by the dark scene represent the offsets; and these will be stored in the on-board memory for every pixel in the earth scan for each CCD stage. VIIRS will subtract the appropriate offset value from each transmitted pixel value prior to transmission. Note that the dark scene data stored and used for offset correction consists of 4,064 (along-scan) samples x 16 (along-track) detectors x 4 stages = 260,096 words.

Many important details relating to offset correction will require analysis of data on-orbit. A few of these are:

- The stability of these individual offset values over time in orbit
- The extent to which any changes can be predicted from parameters such as temperature or power supply voltage
- The extent to which ground processing might correct for small changes in the offsets
- How to acquire updated dark scene data (offsets)
- The process of updating the stored offset values in VIIRS memory

Based on on-orbit analysis, the frequency of the processed described in the following subsections may be revised.

The DNB radiometric gains for even-numbered scans will differ from those for odd-numbered scans due to differences in the the reflectivities of the two sides of the Half-Angle Mirror (HAM).

The nominal radiometric gains of a particular CCD output will be proportional to the number of sub-pixels aggregated, and thus will vary during the scan. The range of gains within the eight pixels read by an output in one aggregation mode, and the deviation of the gains from the ideal proportionality to aggregation, should be small compared to the specified calibration uncertainty.

However even if the transfer functions were initially identical it would still be necessary to derive and track separate gain values for the pixels. This is because radiation

damage can manifest itself either as leaky sub-pixels or as dead sub-pixels, which would impact the offset & gain of any aggregated pixel that included the affected sub-pixel.

The nominal radiometric gains of the CCD stages are quite different. They will be in the ratio of 1 for Stage 3, 477 for Stage 2, and 119,000 for Stages 1.

The right and left outputs of a stage will have slightly different gains due to dedicated amplifiers and ADCs.

For each output the transfer function from radiance into  $DN$  is expected to be very linear over most of its range (the only significant nonlinearity is due to the analog CCD output amplifier). It will be possible to measure nonlinearity on orbit by observing the SD calibration source with many different aggregation modes.

The processes described in the following sections are implemented as an Algorithm Support Function (ASF).

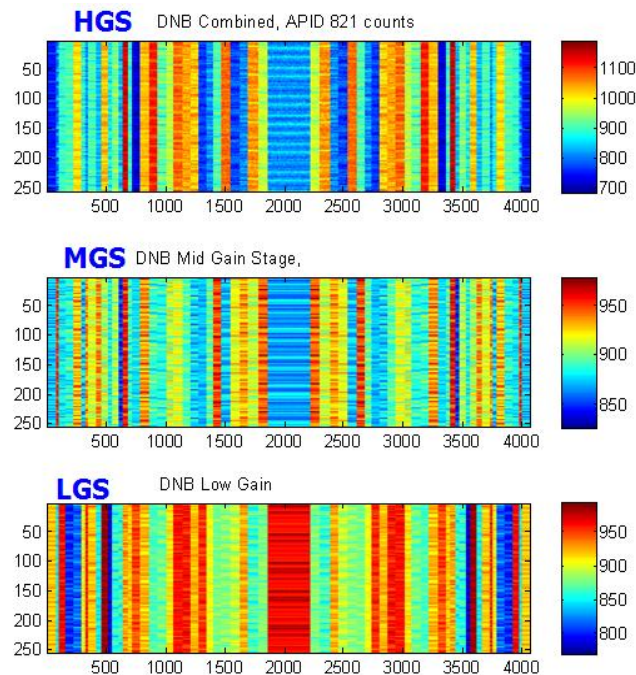


**Figure 24: Simulated raw counts for 16 scans of dark earthview data for LGS, MGS and HGS**

### 3.3.5.2 Offset Determination On Orbit

The space view provides a zero radiance offset which is subtracted from the solar diffuser view for on orbit determination of LGS gain. However the zero offset observed in the calibration views is slightly different from the zero offset observed in the EV. A more accurate method of determining  $DN_{off}$  requires the use of dark views collected within EV.

The darkest scenes of the earth are during a new moon. During these events, data is collected from all three gain stages. During normal operations, only the HGS is transmitted at night. However, it is possible to specifically command VIIRS to downlink DNB MGS and LGS earth view data. [Figure 24](#) shows simulated data for the 3 gain stages that would be collected over a dark earth scene. The vertical banding clearly shows the 32 aggregation zones (repeated twice and symmetric about nadir – approximately sample 2000) with a different offset for each. There is also clearly striping from detector to detector, and since these images represent 16 scans of data, there is a pattern of the striping repeated 16 times.

After the dark earth view data have been collected and geo-located, they require further filtering. Populated areas with enough nighttime lights bias the offset, particularly in the HGS. Therefore, regions with known human habitation are removed. A conservative approach is to eliminate all land, but the baseline threshold will be to use only regions with less than 4 persons per km<sup>2</sup> based on population density maps.

Another possible light source is aurora activity. By eliminating data from north or south latitudes greater than  $\pm 50$  degrees almost all aurora activity will be suppressed. However, even with these filters some sources of stray radiance will remain (e.g. ships on the ocean, lightning or mid-latitude auroras).

To further eliminate stray radiance, data is binned by detector,  $m$ , in-scan pixel,  $n$  and gain stage,  $j$ . Once enough data is collected, statistics are taken determining mean, standard deviation, skew and kurtosis. The skew and kurtosis are used to determine whether any constituent pixels contain stray radiance. The skew and kurtosis of the distribution is computed, and if a bin has values well beyond what is expected for a normal distribution then outliers are identified and removed and the average value of the offset is retaken.

### **3.3.5.3 On-Orbit Determination of Gain for LGS**

The calibration of the LGS uses the SD view and is similar to the process used for the other reflective bands, which has been described in Section 3.3.3.. Since the MGS and HGS detectors saturate when viewing the illuminated SD, the LGS is the only stage able to directly use the SD for calibration. As with the reflective M and I bands, the LGS calibration process compares expected radiance on the solar diffuser with the counts from solar diffuser with space view subtracted, yielding a value for gain. However unlike the other bands, the DNB requires each of the 32 aggregation zones to be calibrated separately.

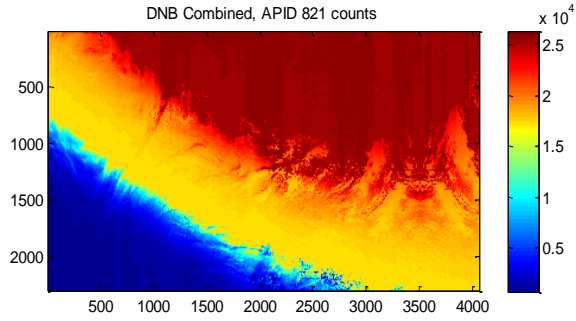


**Figure 25: Simulated DNB earth view scene.**  
Data modeled from EVEREST. by 3000 km

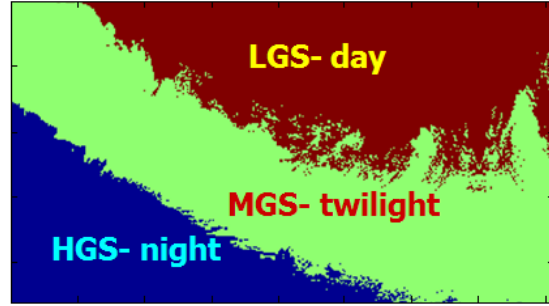


**Figure 26: Corresponding gain stages selected by DNB during normal operation.**

The gain is computed as follows:

$$A(d, m, N_{agg}, 1) = \frac{L_{sd}(\bar{\theta}, d_{se})}{dn_{SD}(d, m, N_{agg}, 1)}$$

where,

$$dn_{SD}(d, m, N_{agg}, 1) = DN_{SD}(d, m, N_{agg}, 1) - DN_{SV}(d, m, N_{agg}, 1),$$

$$L_{sd}(\bar{\theta}, d_{se}) = RVS_{sd} \cdot \pi \cdot \bar{E}_{sol} \cdot \cos(\theta_{inc}) \cdot \rho(\bar{\theta}) \cdot \tau(\bar{\theta}) \cdot \left(\frac{\bar{d}_{se}}{d_{se}}\right)^2$$

and,

$L_{sd}$  = computed radiance of SD

$RVS_{sd}$  = RVS at the SD scan angle

$DN_{SD}$  = scan averaged SD counts

$DN_{SV}$  = scan averaged SV counts

$dn_{SD}$  = scan averaged, offset adjusted SD counts

$d$  = detector index

$m$  = mirror side

$\rho$  = Reflectivity of SD

$\tau$  = band-averaged transmittance of the SDS

$\bar{\theta}$  = 2-dimensional angle of the sun relative to the sensor

$\theta_{inc}$  = angle of incidence of the sun on the SD; is a function of  $\bar{\theta}$

$d_{se}$  = sun-to-earth distance

$\bar{d}_{se}$  = annually-averaged sun-to-earth distance

$\bar{E}_{sol}$  = annually-averaged solar spectral irradiance

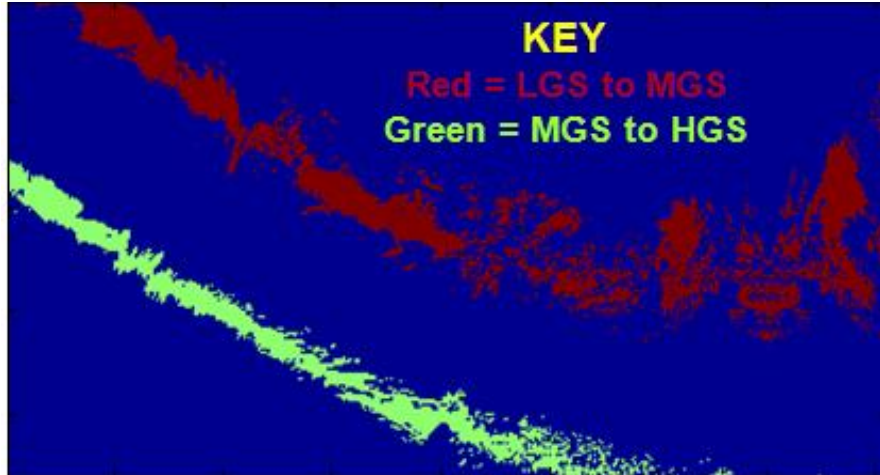


Figure 27: Transition region used to determine MGS/LGS & HGS/MGS gain ratio

### 3.3.5.4 On-Orbit Gain Transfer for MGS & HGS

Since MGS and HGS saturate when the SD is illuminated, calibration is accomplished indirectly using the EV data in the transition regions between the stages. VIIRS is capable of transmitting data from each of the gain stages separately, and this is needed to perform cross-calibration between the stages.

Figure 25 shows a simulated DNB scene computed using EVEREST data, depicting a region crossing the terminator where radiance levels span six orders of magnitude. This range of radiance covers all 3 gain stages as is shown in Figure 25. In this range, there exists a limited region where the LGS is sensitive but the MGS is not saturated. The calibration process identifies these regions and then computes the ratio of the data to determine a relative gain in a process explained in more detail below. In this crossover region the LGS SNR is low, and the lower threshold is determined by where the SNR drops below an acceptable level (initially set to 25 and tunable). A similar process is done to determine the crossover region between MGS and HGS. In Figure 27 **Error! Reference source not found.**, these two regions are shown for the scene in Figure 25.

Once the LGS to MGS gain transition region is identified, the ratio of  $dn_{EV}$  from the MGS to LGS is computed for each pixel. These ratios are binned by detector number,  $d$ , and aggregation zone,  $N_{agg}$ . When the number of points in each bin exceeds a threshold ( $>1000$ ) the ratios in each bin are averaged, and the gain for MGS is computed using the equation

$$A(d, N_{agg}, 2) = \overline{R_{M:L}}(d, N_{agg}) \cdot A(d, N_{agg}, 1)$$

where  $\overline{R_{M:L}}$  = averaged MGS : LGS  $dn_{EV}$  ratio

A similar process is used to compute the HGS gain with the equation

$$A(d, N_{agg}, 3) = \overline{R_{H:M}}(d, N_{agg}) \cdot A(d, N_{agg}, 2)$$

where  $\overline{R_{H:M}}$  = averaged HGS : MGS  $dn_{EV}$  ratio

### 3.3.5.5 Conversion From DN To Radiometric Units

The conversion from *DN* as received on the ground into radiometric units to within the required calibration accuracy can be accomplished as a first-order operation where the gain coefficient is a function of pixel number in track (1 of 16), CCD gain stage (1 of 3), aggregation mode (1 of 36), and HAM side (1 of 2). The residual offsets, which are expected to be very near zero<sup>22</sup>, will be a function of pixel number in track and CCD stage.

Further refinement of this conversion may be desired to improve the quality of the final imagery products. These refinements would be aimed at “de-stripping” the image to eliminate 1) streaks in the scan direction due to detector non-uniformity and 2) bands in the track direction corresponding to the aggregation modes. These refinements will be developed based on long-term statistics in the DNB data corrected as above. Among other possibilities, refinements could correct the values of gain described above, allow for individual pixel offset corrections below the quantization step level, and describe the transfer functions from *DN* into radiance using higher-order polynomials. In principle these corrections could all vary as a function of sample number even within an aggregation mode.

A complete calibration of the DNB involves calibration of four detector stages in each of 32 aggregation modes. The ratio of the lowest to the highest radiance needed is approximately 6.9 million to one. The facilities for such a calibration are difficult to provide on the ground, and are totally impractical in space. Fortunately, an adequate calibration is possible with just the single accurately-known radiance provided by the SD, supplemented by occasional diagnostic mode observations of the Earth in the neighborhood of the terminator. In addition, observing one or more Earth scenes under very low but known illumination such as moon can verify the calibration [Shao et al., 2013]. On-orbit DNB calibration takes advantage of a VIIRS capability to transmit both the highest and lowest-radiance VIIRS stages simultaneously (in the night mode only) with the composite DNB data when the Earth is being observed.

The process provides in-flight calibration of the high-range output amplifiers over essentially their entire anticipated operating range. The accuracy of the calibration is limited by the uncertainty in knowledge of the SD radiance and by the response non-uniformity of the sub-pixel detectors. (CCD Charge Transfer Inefficiency is a second-order effect that essentially disappears for uniform scenes such as the calibrator.)

---

<sup>22</sup> Note that this is possible only because the large offsets introduced by the CCD have nominally been corrected by subtraction of a full-scan “dark scene” within the VIIRS instrument

One of the primary effects of radiation on orbit is expected to be degradation in sub-pixel response uniformity. Recent radiation tests provide data indicating the magnitude of any degradation. In addition, the impact of non-uniformity on the aggregated pixels is directly measurable in the observations of the SD. These data can be used along with accumulated Earth data statistics to develop the equations for “de-stripping” the DNB Earth image data.

**Error! Reference source not found.** shows the NRT processing of DNB  $DN$ s from Verified VIIRS RDR’s through to the Near Constant Contrast (NCC) imagery that is part of the VIIRS Imagery EDR. The first step is conversion of  $DN$ s to DNB SDR radiances in unit of  $W/cm^2\text{-sr}$  through the DNB Radiometric Calibration process. Here pre-determined float\*32 calibration coefficients  $c_0$ ,  $c_1$ , and  $c_2$ , which are dimensioned by aggregation mode (32), along-track pixel (16), and gain (3), are read as calibration LUTs. Other pre-determined calibration LUTs are float\*32 values of RVS for each along-scan frame (4064), gain (3), and HAM side (2) and integer\*16 values of residual zero offset,  $DN_{sv\_DNB}$  for each along-scan frame (4064), along-track pixel (16), gain (3), and HAM side (2). Verified RDR’s provide the raw  $DN$  ( $DN_{DNB}$ ), the frame and pixel numbers, gain, and HAM side. The calibration equation that yields DNB TOA radiance is

$$\frac{L_{DNB}}{RVS} = \frac{\sum_{i=0}^2 c_i [agg(N_F), N_P, N_G] \cdot dn_{DNB}^i}{RVS[N_F, N_P, N_H]} \quad \text{Eq. 120}$$

$$dn_{DNB} = DN_{DNB} - DN_{sv\_DNB}[N_F, N_P, N_G] \quad \text{Eq. 121}$$

where  $dn_{DNB}$  is the raw  $DN$  after subtraction of residual zero offset, given by Eq. 120,  $c_0$ ,  $c_1$ , and  $c_2$  are pre-determined coefficients dependent on along-scan aggregation zone,  $agg(N_F)$ , along-track pixel,  $N_P$ , and gain stage,  $N_G$ , and  $RVS$  is pre-determined and a function of along-scan frame number,  $N_F$ , along-track pixel,  $N_P$ , and HAM side,  $N_H$ . VIIRS Geolocation IP’s provide geolocation and derived geolocation parameters need for building the DNB SDR’s.

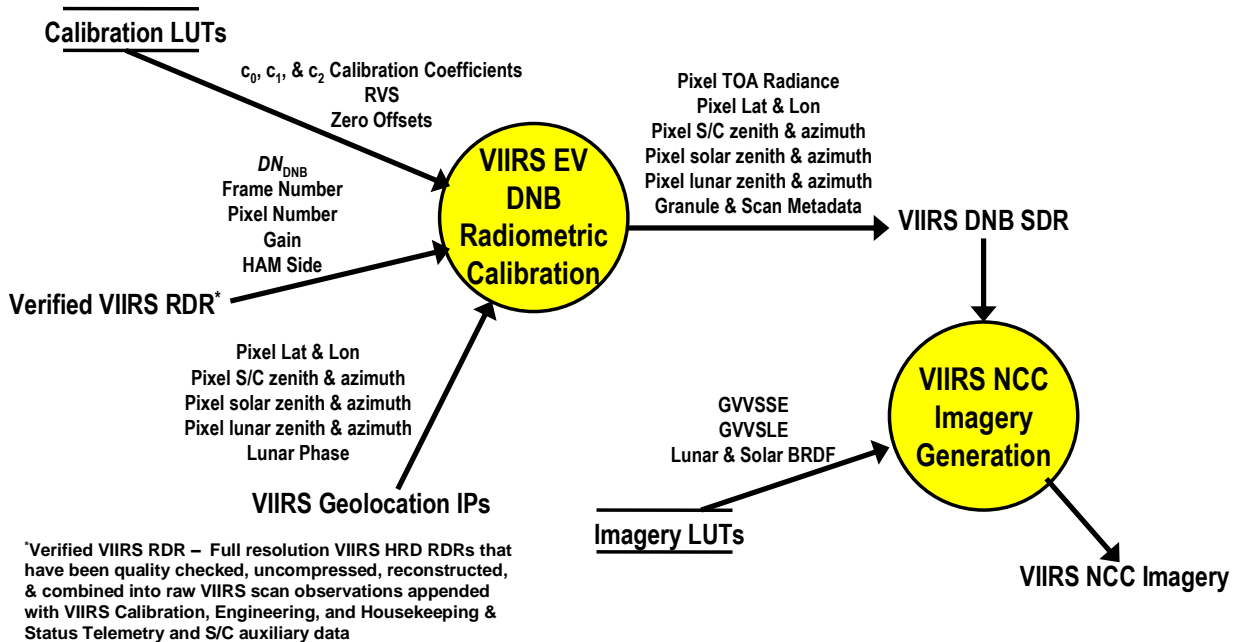


Figure 28: Near Real-time DNB Processing

Each DNB SDR is read by the VIIRS NCC Imagery Generation process to produce VIIRS NCC Imagery. LUT input to this process includes Gain Value Versus Scene Solar Elevation (GVVSSE), Gain Value Versus Scene Lunar Elevation (GVSLE), and lunar and solar BRDF.

### 3.4 PRACTICAL CONSIDERATIONS

Applying the theory to practice requires consideration of issues related to numerical computation, algorithm initialization, and product validation, which are discussed in the following sub-sections. A special consideration has to do with striping that is expected whenever multiple detectors per band are employed in an instrument such as VIIRS. Strategies for dealing with striping are discussed in Section 3.4.5.

#### 3.4.1 Numerical Computation Considerations

The scientific SDR and EDR algorithms must be convertible into operational code that is compatible with data latency requirements. This essentially means that most EDRs must be completely processed from VIIRS raw data, including calibration and georeferencing, within 30 minutes from the time the raw data are available<sup>23</sup>.

<sup>23</sup> see specification in in the LIRD Appendix A of LIRD Reqs Supplement

The complexity of the calculations used for VIIRS radiometric calibration is similar to those in routine MODIS processing and are therefore expected to perform within a reasonable allocation of the operational timeline.

### **3.4.2 Programming and Procedural Considerations**

It is expected that some adjustments will have to be made to the calibration coefficients and/or radiance/reflectance values to account for on-orbit changes in instrument characterization and to account for small differences in individual detector throughput and the optical characteristics of the two sides of the VIIRS HAM. The nature of these adjustments may not be known before the VIIRS Radiometric Calibration software is complete. To meet this challenge, the VIIRS radiometric calibration algorithm, through the use of external band-detector-HAM side LUTs, has been designed to be flexible enough to accommodate adjustments if and when needed.

#### **3.4.2.1 Quality Control**

The VIIRS radiometric calibration algorithm includes many checks on the reasonableness of input data and output product. Quality bits associated with each pixel's SDR radiance, as described in Section [2.1.2.1](#), are set should some problem be detected during radiometric calibration.

Additional quality flags are likely to be identified and implemented during the operational conversion of the RDR to SDR algorithm to facilitate data quality monitoring and post-launch Cal/Val activities.

#### **3.4.2.2 Exception Handling**

Implementation of the VIIRS radiometric calibration algorithm includes the issuance of warning and error messages. As part of the operation conversion of the code implementation additional graceful degradation scenarios is included.

In the process of verifying the RDR data, quality flags, triggered by missing or corrupted data, are included along with the earth view counts, the space view counts, the OCBDB counts and the solar diffuser view counts. If any of these are flagged as bad, this quality flag (QF) is passed through to the SDR output quality flag for each pixel. In the cases of calibrator quality flags, a bad detector in the calibrator causes a bad quality flag to be set for the entire scan or scans that use that calibration data.

In the case of missing or corrupted calibration data, when this is encountered in the data processing calibration data from other scans are searched for substitute calibration data. The earth view data is calibrated with this, but is flagged as poor quality. Likewise, if telemetry data used to determine temperatures used in the calibration is missing or corrupted, then other scans are search for substitute telemetry and the earth view data is flagged as poor. For the reflective bands, if space view data cannot be found, the process allows for the OCBDB view data to be used as a zero DN offset. For details regarding this process refer to Section [3.4.7](#)

To determine when the moon intrudes on the space view, the calibration algorithm receives a unit vector defining the direction to the moon in instrument coordinates as an input from the geolocation algorithm. This moon vector is used to compute the lunar angles using the same set of equations that are used to compute the solar angles,  $\phi_v$  and  $\phi_h$ , (see eqns. 102, 104 and 105). The algorithm defines angular limits of the space view, and the checks to determine whether the lunar angles fall within these limits. If so, the space view event is flagged as unusable, and this is processed in the same way as missing calibration data as described above, where a substitute dark view is searched for. Therefore, the quality flag flows down through the SDR earth view output for all earth view data in the scan or scans affected. The following table describes implementation of quality flags.

**Table 19: Conditions triggering quality flags and fill value**

Condition	Science Code			Operational Code		
	Scan QF	Pixel QF	Fill Value	Scan QF	Pixel QF	Fill Value
Missing Cal Data	yes	DG only	yes	yes	Yes	yes
Substitute Cal Data	yes	no	no	yes	poor	no
Moon in SV	yes	no	no	yes	poor	no
Missing Thermistor Data	yes	no	no	yes	poor	no
Cal temperature out of range	no	DG only	yes	no	Yes	yes
Dual gain anomaly	no	DG only	no	no	poor	no
DNB Stray light	no	yes	no	no	poor	no
Missing EV data	no	yes	Yes	no	Yes	Yes
Some Saturated then aggregated	No	DG only	No	No	poor	No
All saturated	No	DG only	yes	No	Yes	Highest value
Saturated and Bad, none good	No	DG only	Yes	No	Yes	Yes
Radiance out of range	No	No	yes	No	Yes	yes
Reflectance out of range	No	No	yes	No	Yes	yes
Brightness temp. out of range	No	No	Yes	No	Yes	Yes
DNB Stray Light Correction	NA	NA	NA	Yes	Yes	No

### 3.4.3 Initialization

Initialization is accomplished by populating the reflective, emissive, and DNB LUTs. Prior to launch of VIIRS a set of instrument specific LUTs will be constructed using the best available analysis results from pre-launch testing.

Should an anomaly occur that requires a switch to redundant electronics or power supply, a new set of LUTs that are prepared specifically for the particular instrument configuration will be installed into the processing systems.

#### **3.4.4 Validation**

The validation of SDR radiances is associated with the instrument characterization discussed in previous sections. In addition, the calibrated radiances that are stored in the VIIRS SDR's by the radiometric calibration algorithm must be validated. This validation involves pre-launch verification that the operational code implements the radiometric calibration algorithm correctly and that the algorithm will produce calibrated radiances from the on orbit data that meet the accuracy and precision requirements. On orbit validation will consist of an early orbit activity and a long-term activity, which are described in detail in “*VIIRS SDR Calibration and Validation Plan for NPP*” [D47854-01].

##### **3.4.4.1 Pre-Launch Verification**

The System Engineering Integrated Product Team (SE IPT) receives science algorithms (including those for conversion of RDR's to SDR's) from the instrument vendor and delivers these algorithms to the Interface Data Processing Segment (IDPS) for conversion to operational programs. The SE IPT independently verifies the functionality and suitability of the science algorithms prior to the delivery to the IDPS. Simulated instrument data and substitute instrument data are used to test retrieval algorithms over a wide variety of scene conditions.

It is anticipated that VIIRS SDR algorithms may continue to be refined after the drop to IDPS. Refinement possibilities include:

- Modifications to adapt to emerging VIIRS instrument modifications
- Incorporation of additional algorithm modifications as warranted from peer review by VIIRS Operational Algorithm Team (VOAT) scientists and science consultants
- Modifications of parts of the SDR algorithm that may not be able to be made to meet the data latency requirements of the IDPS

Pre-launch instrument characterization and calibration provides opportunities to validate the functional form of the radiometric calibration function of the RDR to SDR algorithm. Here known radiances from National Institute of Standards and Technology (NIST) traceable sources provide a stimulus for the VIIRS detectors and analysis of the instrument response leads to pre-launch calibration coefficients. When these calibration coefficients are installed into the input parameters for the SDR algorithms and run against the raw instrument output digital numbers (DN) the known radiance should be retrieved thereby validating the radiometric calibration algorithm.

##### **3.4.4.2 On Orbit Validation**

Once on orbit, VIIRS will undergo an activation and early orbit checkout that will verify functionality of detectors and scanning mechanisms and proper environmental control. Following this checkout will be an intensive verification and validation (V&V) of

radiometric calibration, spatial calibration, and spectral calibration. These V&V activities provide the first opportunity to validate SDR's from on-orbit observations.

As part of radiometric calibration V&V instrument performance is compared to pre-launch test results. This analysis may result in an update to the pre-launch calibration coefficients that will be installed into the operational IDPS following established CM procedures.

The SDR radiance products will then be compared to external truth data. These external truth data include coincident surface, airborne, and space-based measurements. In the case of VIIRS on Suomi-NPP, NASA's MODIS instruments will provide particularly useful truth data. MODIS measurements can be compared with VIIRS using well established intercomparison techniques such as SNOs over radiometrically stable and homogenous sites. In addition, monitoring VIIRS radiometric stability and calibration accuracy over vicarious calibration sites is also highly useful. Also MERIS and AATSR data from the European Space Agency (ESA) Envisat will provide correlative data. For the later JPSS and DWSS missions cross validation with Suomi-NPP/VIIRS and other VIIRS in the constellation, and radiometers flown on the ESA's MetOp satellites (e.g. AVHRR) will provide validation data.

#### **3.4.4.3 Long Term Monitoring**

Monitoring SDR performance will be an on-going process throughout the spacecraft mission. The primary method for tracking instrument performance for the reflective bands is through the analysis of calibration data from the VIIRS solar diffuser view and data from the Solar Diffuser Stability Monitor (SDSM). Updates to the SD BRDF will be made when changes observed in trending is significant. Any updates will be installed into the IDPS software and followed by an intensive SDR validation similar to that which is planned following the initial on orbit update. In the case of the emissive bands, the on-board blackbody will provide the source of data for long-term monitoring. Following a calibration coefficient update SDR radiance products will be compared to external truth data for on orbit validation.

#### **3.4.5 Striping and Mitigation Strategies**

Striping is a phenomenon that can manifest itself in many ways in a multi-detector scanning instrument such as VIIRS. Striping may indicate a calibration problem or may just be a residual low-level variability that remains under certain scene conditions even when all calibration requirements are met. The former degrades EDR performance while the latter is an aesthetic concern for imagery. The possible striping mechanisms that have been identified within the VIIRS system are:

- Noisy or dead detectors
- Non-uniform illumination or emission of calibration source
- Variation in solar diffuser screen transmittance due to finite number of holes
- Earth shine pollution on solar diffuser
- Stray light in space view

- Illuminated space view (moon, planet or star)
- Errors in non-linear response characterization
- Uncorrected variations in response due to temperature changes to detectors or electronics
- Errors in RVS characterization and variation with mirror side
- 1/f noise
- High frequency drifts in detector gain
- High-frequency drifts in instrument background
- Electronic crosstalk
- Optical crosstalk

It should be emphasized that these are only potential sources of striping, and most are not currently expected to be a problem. Of course the extent of these effects will not be known until sensor characterization tests are complete. Often when striping is discussed, there is an assumption that it is a single problem. The truth is it is a large set of possible problems that run the whole gamut of sensor design. Because of this, diagnosing striping can be a difficult problem that requires significant engineering detective work. Minimizing striping requires careful characterization of detector response across the full dynamic range, accounting for HAM side differences, and characterization of the SD over the full range of sun angles. This careful characterization begins during pre-launch testing (see Section [2.4.1](#)) and continues throughout each VIIRS mission as SDR performance is continually analyzed and calibration coefficients are updated.

For example consider that each detector sees a different part of the SD and that the diffuser is not evenly illuminated.<sup>24</sup> Therefore the band-averaged transmittance of solar diffuser screen,  $\tau_{sds}(\phi_h, \phi_v, \lambda)$ , is slightly dependent on each field angle at the detector's field stop and it is assumed that the solar diffuser screen transmittance is separately defined for each detector. Any errors in characterizing the field angle dependence of  $\tau_{sds}(\phi_h, \phi_v, \lambda)$  could contribute to striping of the calibrated radiances or reflectances. This dependence can be characterized using an optical model and pre-launch tests<sup>25</sup> to determine the ripple in the illumination over the diffuser, so a field angle dependent  $\tau_{sds}(\phi_h, \phi_v, \lambda)$  should be produced using this model.

---

<sup>24</sup> The solar diffuser screen consists of a fine grid of very small holes. Each hole produces a pinhole camera image of the sun on the solar diffuser and these images overlap to produce a fairly even irradiance upon the diffuser. It is not perfectly even, however. This effect produces a ripple in the illumination level over the diffuser, and is believed to have produced some striping for the MODIS instrument Vis/NIR bands, which use a similar solar diffuser design to VIIRS. The VIIRS design, however, uses holes spaced 3 times closer together so this is not expected to cause very much striping.

<sup>25</sup> "VIIRS Program Test Procedure for Solar Diffuser Screen Characterization," TP154640-247

The transmission must be measured at the component level and then measured again as a SD 'system' with illuminated Spectralon<sup>®</sup>. The component level data must agree with the 'system' level data since the component data is used in the reflected band calibration. If the component level data fails to agree with 'system' level data, additional characterization must be performed until two sets of data are brought to agreement. Failure to properly characterize the entire Spectralon<sup>®</sup>/transmission screen system will result in undesirable radiometric anomalies such as 'striping' of calibrated radiance image, instability and inaccuracy in absolute calibration. In addition to this testing, witness samples of the SD and the transmission screen will be maintained at the instrument vendor to monitor degradation over time as well as provide a test unit for anomaly resolution.

For imagery products, striping is more than simply a radiometric issue since it involves the ability of an analyst to interpret an image. It is always preferable to remove striping as part of the SDR calibration rather than to apply a post-process algorithm to improve the image cosmetically. Cosmetic enhancement of an image may inadvertently remove real features. Because the emissive imagery bands do not have the strict radiometric requirements (ref. [Table 7](#)) unlike the one that are imposed on the moderate resolution bands, it is reasonable to adjust the calibration coefficients to reduce striping. This is done as an off-line process by determining the level of striping in the imagery band by taking response statistics as a function of detector and mirror side to determine the variation in gain and offset from detector to detector, and then update the coefficients so as to minimize striping error.

### **3.4.6 Sub-frame Offset for Imagery Bands**

#### **3.4.6.1 Hardware Case and Test Observations**

In VIIRS tests, when a dark scene is being observed, a phenomenon has been observed whereby there is a difference in offset between the first and second sub-frames for the Imagery (IMG) bands. This is referred to as Sub-frame Offset because the Imagery band detectors are sampled two samples per one Moderate Resolution (MOD) sample (see [Figure 11](#).) These two samples are referred to as 1st sub-frame sample and 2nd sub-frame sample. It is likely that this offset difference is related to interference from the MOD frames. The first IMG sub-frames read out while the MOD frame is still collecting, while the second IMG sub-frames read out at the same time that the MOD frames read out. There may be cross-talk in the read-out signals, but since the offset is observed even when all the bands are dark, it is observed that this cross-talk is not caused only by the magnitude of MOD signal. The DN values are steady over the increasing illumination conditions. In this test a slit was focused on band I1 only, so none of the other bands are illuminated. Because the signal is steady, this demonstrates that there is not a gain component in this offset issue. A similar test was done with flood illumination across all the bands, and the signals are no longer steady as illumination increases. This clearly demonstrates a crosstalk issue. Tests done in December 2006 determined the cross-talk on the Vis/NIR focal plane. It was determined that crosstalk did exist but was not strong enough to make algorithmic

compensation necessary. The algorithm changes described here will not compensate for these variations due to crosstalk.

Offset differences between the sub-frame samples of a single IMG detector have been observed by Raytheon and requirements have been specified to set limits. Raytheon System Engineering has determined that radiometric requirements cannot be met unless the sub-frame offset is compensated in the VIIRS SDR Calibration Algorithm.

Further work has shown that there is an additional complication due to the difference in timing between even and odd detectors which varies according to band. The timing offset among the bands is necessary so that bands are co-registered (refer to section [2.2.2.3](#)). Analysis of data from the VIIRS instrument TVAC tests confirm this behavior and were documented in "Parity of Imagery Band Odd-Even Offset," by Lushalan Liao [virrs.cvtm.07.11.01].

**Table 20: Original Calibration Pixel Matching, Current Matching with Even Detectors Swapped**

Detector - Frame			Detector - Frame			Detector - Frame			Detector - Frame		
1-1	1-2	...	1-1	1-2		1-1	1-2	...	1-1	1-2	
2-1	2-2		2-1	2-2		2-1	2-2		2-2	2-1	
3-1	3-2		3-1	3-2		3-1	3-2		3-1	3-2	
4-1	4-2		4-1	4-2		4-1	4-2		4-2	4-1	
...			...			...			...		
Earth View			Calibration Views			Earth View			Calibration Views		

The calibration selectively swaps the first and second sub-frame averages for the calibration sources (SV and OBCBB) to compensate for this timing difference. This swap is only performed for calibrating the earthview: the OBCIP output retains the original ordering when reporting the calibration data. Whether to swap or not is determined by new configurable parameters, either true or false, two per band: one for even detectors and one for odd.

The swap configuration is currently stored in the odd detector swap and even detector swap arrays (from `swapEvenOdd.h`):

```
/* set 1 to swap 1st/2nd frame average for odd detectors, set 0
to leave alone*/
const int oddDetSwap[5] = {0,0,0,1,1};
const int evenDetSwap[5] = {0,0,1,0,0};
```

This configuration currently calibrates VIIRS TVAC test data correctly.

To avoid confusion, a few terms are defined here, though these definitions may not necessarily be perfectly consistent with other VIIRS documents. For the purposes of this document :

- “sample” - refers to an individual time sample of the IMG band before it is aggregated on-board.
- “Frame” refers to the sample time for the MOD band

- “sub-frame” refers to one of the two IMG samples in each MOD frame.
- “Pixel” is used to refer to IMG data after the on-board aggregation. Pixels are referred to as even or odd, counting from 1 at the start of the scan.
- “even” and “odd” will refer to the detector where odd is the first, third, fifth etc and even are the second, fourth, sixth etc. regardless of whether indexing started at one or zero. Note that this refers to the detector index in product order, not the instrument engineer’s convention as described in Section [2.2.2.3](#). Detectors that are even in one convention are odd in the other.
- Sub-frames are described as “first” or “second” sub-frame instead of “odd” or “even” sub-frame (although some earlier documents referred to the “even/odd sub-frame offset”).

The algorithm changes that are described here will compensate for the first/second sub-frame differences that are found in the IMG offsets. These offset differences are discussed in Raytheon document Y17827. This issue has been recognized and is discussed in greater detail in Raytheon Document Y16894.

### **3.4.6.2 Algorithm Overview**

#### **3.4.6.2.1 Calculating the Space View Offset**

To compensate for the differences between the first and second sub-frames, there are two different averages calculated for the Space view (SV) offset DN. For the MOD bands, a single average is taken over all the samples from the SV scan (96 samples). For the IMG bands, two averages are taken from the 48 first sub-frames and the 48 second sub-frames.

#### **3.4.6.2.2 Calculating the Black Body Offset**

To compensate for the differences between the first and second sub-frames, there are two different averages calculated for the Black body (BB) offset DN. For the MOD bands, a single average is taken over all 96 samples from the BB view. For the IMG bands, two averages are taken from the 48 first sub-frames and the 48 second sub-frames.

#### **3.4.6.2.3 Swapping the First/second Sub-frame Averages, Robust Substitution**

To correct the timing offset issue described above between even and odd detectors, the first and second sub-frame SV and BB averages are swapped according to the configuration arrays. Next, the SV and BB averages undergo substitution to improve calibration if there are problems with the calibration data. For details on this process refer to Section 3.4.7.

#### **3.4.6.2.4 Calibrating the Reflective Bands (I1, I2, I3)**

During the calibration of the reflective bands, the Space view DN is subtracted from the Earth view (EV) DN (DN<sub>ev</sub>) to obtain an Earth view DN with background subtracted (dn<sub>ev</sub>). This value is used in the radiance calculation. The value subtracted will change depending on which EV pixel is selected. Due to the fact that the IMG pixels

have already been aggregated, the number to subtract is not a simple matter of subtracting the second sub-frame or first sub-frame averages (see Section [3.4.6.2.6](#)).

### 3.4.6.2.5 Calibrating the Emissive Bands (I4, I5)

During calibration of the Emissive bands, the Space view DN is subtracted from the EV DN (DN\_ev) to obtain an EV with background subtracted (dn\_ev). This value is used in the radiance calculation. The Black body DN value is also used in the radiance calculation. Due to the fact that the IMG pixels have already been aggregated, for the EV data the number to subtract is not a simple matter of subtracting the even sub-frame or first sub-frame averages (see Section [3.4.6.2.6](#)).

### 3.4.6.2.6 Aggregation of IMG band samples

The IMG bands are aggregated within the hardware. The aggregation scheme is shown in the following table and reduces the data from 12608 samples to 6400 pixels. For the aggregation area that is 1:1, the first sub-frame and second-sub-frame averages must be subtracted from the first and second sub-frame samples, as would be expected. For the aggregation area that is 1:2, a single combined average of the first and second sub-frames can be used since each aggregated pixel is made up of 1 first sub-frame and 1 second sub-frame sample. For the 1:3 aggregations, there are also two averages but they alternate between:

- Offset DN for even EV pixel = 1/3 first average + 2/3 second average
- Offset DN for odd EV pixel = 2/3 first average + 1/3 second average.

This is because when aggregating 3 samples the resulting aggregated pixels are made up of either 1 first sub-frame sample combined with 2 second sub-frame sample, or vice versa. The IMG aggregation scheme is shown in [Table 21](#).

**Table 21: Aggregation from Samples to Pixels**

<i>Raw Sample ranges</i>	<i>Size</i>	<i>Aggregation Pixel:Sample</i>	<i>Aggregated Pixel ranges</i>	<i>Size</i>	<i>Offset scheme</i>
1	1280	1:1	1	1280	Two averages: first/second sub-frames
1280			1280		
1281	1472	1:2	1281	736	single average
2752			2016		
2753	3552	1:3	2017	1184	two averages: 1/3 odd + 2/3 even; 2/3 odd + 1/3even
6304			3200		
6305	3552		3201	1184	
9856			4384		
9857	1472	1:2	4385	736	single average
11328			5120		
11329	1280	1:1	5121	1280	two averages: first/second sub-frames
12608			6400		

### 3.4.7 SDR Robust Algorithm Processes

#### 3.4.7.1 *Deviations from Optimal Calibration Conditions*

Deviations from optimal conditions during data collection will cause errors or failures in the final calibrated Top of Atmosphere (TOA) radiances, reflectances and brightness temperatures. The data collection comes from these sources: Earth view (EV), Solar Diffuser view (SD), Space view (SV), Black Body view (BB), thermistor temperature and DC restore voltage. Errors in any of this data can lead to errors in calibration. Algorithm modifications are made to use alternate data sources for the Space view, Black Body view and DC restore data if they have errors. Without special robust processes, missing data would usually end the calibration of any EV pixels that require the missing data. A quality flag indicates this and the pixel is assigned a fill value, but no radiance is computed. A robust process using alternate data sources increases coverage, while still flagging the calibration as less reliable since it depends on alternate sources. In some cases, the algorithm will resort to using default values.

Each scan contains data for all four views, DC restore voltages for each detector and temperature data from the thermistors. The data collected during a scan is used in the calibrations for the same scan. [Figure 6](#) shows the VIIRS scanning pattern. Note that only one side of the half angle mirror (HAM) is used during a scan. Also, calibration is acquired separately for each gain range for the dual gain bands. To obtain all HAM side and gain combinations, a dual gain band requires 4 scan cycles and a single gain band requires 2 scan cycles for calibration. This fact must be taken into account when devising a plan for alternate data sources.

The Space view data is used as an offset to remove background levels from the M and I bands. Ideally, the Space view is completely filled with a view of cold space. Lunar intrusion into the view will corrupt the data. The algorithm contains a subroutine (Check\_For\_Moon\_in\_SV\_KOB) to set a flag to indicate the presence of the moon in or near the Space view. Missing data and variation test failures will also cause problems. The lunar contaminated SV data is marked with a fill value, which is a flag to the algorithm to do no data retrieval. The SV data is critical due to the fact that the zero offset that it establishes is subtracted from all the other view data (EV, SD, and BB). By identifying an alternate substitute value, the algorithm can continue to calibrate.

The Black Body view data is used as a known radiance source for the emissive bands. It provides the on-board calibration and stability monitoring for these bands. The BB value is used in the calibration equations to adjust gain. Error sources are missing data and variation test failure.

The Black Body view is also used in the hardware for DC Restore. DC Restore insures that the FPA signals digitized by the analog signal processor (ASP) are always within

range of the dynamic range of the analog to digital converters. The blackbody view (instead of the Space view) is used to avoid signal contamination from the moon or stars. The DC restore voltages are reported as part of the engineering packets from the instrument. These values are used in generating the coefficients table used during calibration. It is important in the calibration process to use a calibration source that has the same DC restore voltage as the EV data that is being calibrated, so the algorithm uses a scheme to apply the SV offset and cal source depending on gain state and mirror side.

The Earth view data is the actual data being calibrated to create the SDR products. The Earth view data can be corrupted by the Sun during the 1730 orbit. Adding a subroutine (similar to Check\_For\_Moon\_in\_SV\_KOB) would allow a flag to be set that would indicate that stray light from the Sun is intruding on the Earth view. This is only an issue during the 1730 orbit. The solar angles with respect to the satellite are computed for use in determining the angles incident upon the solar diffuser. This same angle would be used to determine if part of the EV data is in a solar stray light exclusion zone. Of course, because the sun is so much brighter than the moon, the stray light exclusion zone around the sun is much larger than the zone around the moon that is used for the SV exclusion. This is not being implemented currently (Feb. 2007), since the NPP orbit will not be a 1730 orbit. FU2 is planned to be a 1730 orbit, and this should be implemented before that time.

The Solar Diffuser view data is the known radiance source for the reflective bands. No alternate data sources are being considered for this view because the SD view occurs for a short period (less than a minute) once per orbit. Using less than perfect data other than SD view data for the on-board reflective calibration would impact the entire orbit, and possibly many orbits if the multi-orbit SD calibration is applied.

The thermistor data is critical to all the data collections. The thermistors are measuring temperatures for the FPA detectors (Tdet), Electronics (Telec), Half angle mirror HAM (Tham), Black Body (Tbb), Shield (Tsh), and Cavity (Tcav), as well as indirect measurement of the Rotating Telescope Assembly (Trta and Ttele). [Table 22](#) shows the number of thermistors used in calculations for a given temperature. Under ideal conditions, all thermistors would be functioning and calibrated correctly. The temperatures are then calculated based on averages of the thermistors for that area.

**Table 22: Number of thermistors assigned to given temperature readings**

<b>Areas Measured</b>	<b>Maximum number of thermistors used in calculation</b>	<b>Alternates in linear combination</b>
Black Body (BB)	6	0
Cavity	1	2
Electronics	1	9
FPA- LWIR	1	1
FPA- S/MWIR	1	1

Half angle mirror (HAM)	2	0
RTA, Shield, Telescope	2	0

Accurate temperature data is critical. The calibration coefficients can vary based on the temperatures of the FPA detectors and electronics. The black body radiance relies on temperatures from the black body, cavity, shield, mirror and telescope. The emissive background term, referred to as Emission vs. Scan (EVS) that is used in the emissive bands calibration is based on the temperature of the RTA and HAM.

Noisy or corrupted pixels can be a problem in any view. The algorithm handles outliers by removing those pixels that are outside of 3 sigma (standard deviations) limits. In the case of a noisy view, a maximum sigma would be an input from a lookup table and if a view exceeds this value then the entire view is rejected as corrupted, and is not used. This is not currently in the algorithm. Rejecting a view as corrupted/noisy triggers the search for an alternate in the same way that missing data does.

### 3.4.7.2 *Alternate data sources*

Alternative data sources are listed in order of priority. Any EV calibrations that depend on an alternate source will be flagged as poor quality, but a calibrated value will be reported. For the calibration data where the alternate source has a lunar intrusion, is missing, is noisy or is corrupted, then the next source is considered. If the process finds no alternate sources, and the bottom of the list is encountered, then any EV data that depends on this data is flagged as bad, and a fill value is reported for the EV pixel. In cases where a default value is used, the defaults are input to the algorithm as tunable parameters in a table in the source code.

- Earth view counts -
  - no alternatives
- Solar Diffuser view counts -
  - no alternatives
- Space View (SV) counts, dual gain (M1-M5, M7 & M13);
  - SV from 4 scans earlier than designated low gain or high gain scans, if in granule
  - SV from 4 scans later than designated low gain or high gain scans, if in granule
  - SV from 8 scans earlier than designated low gain or high gain scans, if in granule
  - SV from 8 scans later than designated low gain or high gain scans, if in granule
  - SV from N scans earlier than designated low gain or high gain scans, if in granule, where N is a multiple of 4
  - SV from N scans later than designated low gain or high gain scans, if in granule, where N is a multiple of 4
  - Repeat N earlier/later cycle, increasing N by 4 until outside the granule
  - Black body view (BBV) from designated low gain or high gain scans, except for M13

- BBV from 4 scans earlier than designated low gain or high gain scans, if in granule, except for M13
  - BBV from 4 scans later than designated low gain or high gain scans, if in granule, except for M13
  - BBV from N scans earlier than designated low gain or high gain scans, if in granule, where N is a multiple of 4, except for M13
  - BBV from N scans later than designated low gain or high gain scans, if in granule, where N is a multiple of 4, except for M13
  - Repeat N earlier/later cycle, except for M13, increasing N by 4 until outside the granule
- Space View (SV) counts, single gain bands (M6, M8 to M11, I1 to I5); Emissive bands are M12, M14 to M16, I4 and I5, and should not use the black body view (BBV) as an alternative.
    - SV from 2 scans earlier than current scan, if within granule
    - SV from 2 scans later than current scan, if within granule
    - SV from N scans earlier than current scan, if within granule, where N is a multiple of 2
    - SV from N scans later than current, if within granule, where N is a multiple of 2
    - Repeat N earlier/later cycle, increasing N by 2 until outside the granule
    - BBV of current scan, except for emissive
    - BBV from 2 scans earlier, if in granule, except for emissive
    - BBV from 2 scans later, if in granule, except for emissive
    - BBV from N scans earlier, if in granule, except for emissive where N is a multiple of 2
    - BBV from N scans later, if in granule, except for emissive, where N is a multiple of 2
- Black Body View (BBV) counts, dual gain, M13 high-gain only.
    - BBV from 4 scans earlier than designated high gain scans, if in granule
    - BBV from 4 scans later than designated high gain scans, if in granule
    - BBV from N scans earlier than designated high gain scans, if in granule, where N is a multiple of 4
    - BBV from N scans later than designated high gain scans, if in granule, where N is a multiple of 4
- Black Body View (BBV) counts, single gain emissive, M12, M14 - M16 I4 and I5;
    - BBV from 2 scans earlier than current scan, if in granule
    - BBV from 2 scans later than current scan, if in granule
    - BBV from N scans earlier than current scan, if in granule, where N is a multiple of 2
    - BBV from N scans later than current scan, if in granule, where N is a multiple of 2
- OBC black body thermistors (6 total)
    - Take average of remaining thermistors for BB temperature. Limit is at least 1 thermistor for average.

- Thermistors from N scans earlier than current scan, if in granule, where N is iteratively decreased by 1
- Thermistors from N scans later than current scan, if in granule, where N is iteratively increased by 1
- Default value
- All other thermistors
  - Thermistors from N scans earlier than current scan, if in granule, where N is iteratively decreased by 1
  - Thermistors from N scans later than current scan, if in granule, where N is iteratively increased until edge of granule reached
  - Default temperature
- DC restore voltage (DCRV), single gain bands, M6, M8-M16, I1 to I5
  - DCRV from 2 scans earlier than current scan, if in granule
  - DCRV from 2 scans later than current scan, if in granule
  - DCRV from N scans earlier than current scan, if in granule, where N is a multiple of 2
  - DCRV from N scans later than current scan, if in granule, where N is a multiple of 2
- DCRV, dual gain, M1-M5, M7 & M13
  - DCRV from 4 scans earlier than current scan, if in granule
  - DCRV from 4 scans later than current scans, if in granule
  - DCRV from N scans earlier than current scans, if in granule, where N is a multiple of 4
  - DCRV from N scans later than current scans, if in granule, where N is a multiple of 4

### 3.4.8 Bright Pixel Identification

Scattered light can contaminate pixels in the vicinity of bright objects in VIIRS scenes. Also, bright objects can lose light that is scattered to darker areas. Although the fraction of scattered light is low, for a sufficiently bright source near a dim nearby pixel, the scattered contribution can dominate the radiometric uncertainty. This condition is easily understood by considering the ocean's color and VIIRS ability to determine that color with a bright cloud in the nearby scene. Several EDRs (ocean color, land albedo, and sea-surface temperature) have exclusion conditions in the NPOESS & NPP System Spec around bright pixels, and call for a flag to indicate when scattering is above an acceptable level. Here we describe an algorithm to identify pixels that are likely to be contaminated by scattered light and to produce the flags required by the EDR algorithms. It will be applied to the Moderate resolution bands, M1 to M16, and the imagery resolution bands, I1 to I5, but not to the DNB. The output of this algorithm is a 4-bit flag for each pixel in each band that characterizes the level of contamination of signal by scattered light.

The percentage of scattered light is defined to be:

$$\% \text{ scattered light} = \left| \frac{S_{scat}}{S_{meas}} \right| * 100 \quad \text{Eq. 122}$$

4-bit state flag:

0000	0.0 - 0.01% scattered light
0001	0.0 - 0.02% scattered light
0010	0.02 - 0.05% scattered light
0011	0.05 - 0.1% scattered light
0100	0.1 - 0.2% scattered light
0101	0.2 - 0.5% scattered light
0110	0.5 - 1.0% scattered light
0111	1.0 - 2.0% scattered light
1000	2.0 - 5.0% scattered light
1001	5 - 10% scattered light
1010	>10% scattered light
1111	calculation unreliable

### 3.4.8.1 Estimating % Scattered Light

Scattered light distribution is a property of the telescope & focal plane and is referred to as the near-field scattering. We model the scattering with a point-spread function that is composed of a delta function with small epsilon tails. The measured scene is the true scene convolved with the PSF.

Definitions:

$$S_{true} = \text{true scene}$$

$$S_{meas} = \text{measured scene including scattered light}$$

$$P_{true} = \text{true PSF}$$

$$P_{meas} = \text{measured PSF}$$

$$\delta = \text{Dirac Delta Function}$$

$$\delta(i, j) = \begin{cases} 1 & \text{if } i = i_{center} \text{ \& } j = j_{center} \\ 0 & \text{otherwise} \end{cases}$$

$$i = \text{in-track sample index}$$

$$j = \text{in-scan sample index}$$

Eq. 123

$$S_{meas} = P_{true} * S_{true} \quad \text{Eq. 124}$$

The PSF here is a full optical PSF, including all the effects of Near-Field Scattering (NFS). This is sometimes also referred to as a Point Source Transmittance (PST), but it will be referred to as PSF here. The effect of NFS can be considered as a perturbation,  $\epsilon$ , with respect to the Dirac Delta function

$$\begin{aligned}
P_{true} &= \delta + \varepsilon_{true} \\
P_{meas} &= \delta + \varepsilon_{meas}
\end{aligned}
\tag{Eq. 125}$$

The following normalization conditions apply to both the measured and the true PSF

$$\begin{aligned}
\sum_i \sum_j P(i, j) &= 1 \\
\sum_i \sum_j \varepsilon(i, j) &= 0
\end{aligned}
\tag{Eq. 126}$$

The true scattering in the scene is the difference between the measured scene and the true scene

$$\begin{aligned}
S_{scat} &= S_{meas} - S_{true} = P_{true} * S_{true} - \delta * S_{true} \\
&= (P_{true} - \delta) * S_{true} \\
&= \varepsilon_{true} * S_{true}
\end{aligned}
\tag{Eq. 127}$$

If we convolve the measured scene again with the PSF, we find:

$$\begin{aligned}
S_{doubleconv} &= P_{meas} * S_{meas} \\
&= (\delta + \varepsilon_{meas}) * (\delta + \varepsilon_{true}) * S_{true} \\
&= (\delta * \delta + \varepsilon_{meas} * \varepsilon_{true} + \varepsilon_{meas} + \varepsilon_{true}) * S_{true}
\end{aligned}
\tag{Eq. 128}$$

Subtracting the measured scene from this gives what will be referred to as  $S'_{scat}$

$$\begin{aligned}
S'_{scat} &= S_{doubleconv} - S_{meas} = P_{meas} * S_{meas} - \delta * S_{meas} \\
&= (\delta + \varepsilon_{meas} - \delta) * S_{meas} \\
&= \varepsilon_{meas} * S_{meas} \\
&= \varepsilon_{meas} * (\delta + \varepsilon_{true}) * S_{true}
\end{aligned}
\tag{Eq. 129}$$

Then we can write:

$$\begin{aligned}
S'_{scat} - S_{scat} &= (\varepsilon_{meas} + \varepsilon_{meas} * \varepsilon_{true} - \varepsilon_{true}) * S_{true} \\
&OR \\
S'_{scat} &= S_{scat} + (\varepsilon_{meas} - \varepsilon_{true} + \varepsilon_{meas} * \varepsilon_{true}) * S_{true}
\end{aligned}
\tag{Eq. 130}$$

which reduces to

$$S_{scat} = S'_{scat} \text{ when } \varepsilon_{true} \cong \varepsilon_{meas} \text{ and } \varepsilon_{true} * \varepsilon_{meas} * S_{true} \cong 0
\tag{Eq. 131}$$

As long as the measured NFS is a good estimate of the true NFS, and NSF is a small contribution to the whole PSF, then the difference between the doubly convolved scene and the measured scene is a good estimate of the scattering. Our estimate of scattered light then is:

$$\% \text{ scattered light} = \frac{S_{scat}}{S_{meas}} * 100 \cong \frac{S'_{scat}}{S_{meas}} * 100 \cong \frac{\varepsilon_{meas} * S_{meas}}{S_{meas}} * 100
\tag{Eq. 132}$$

In addition to the above requirements that the measured scattering distribution be close to the real one and much smaller than 1, there is another requirement here, that  $S_{meas} \gg S'_{scat}$ . Very close to a bright object, where the % scattered light is close to or greater than 1, the exact value will become very uncertain. However, there is no uncertainty that the scattering is large, but the only thing that is uncertain is how large. Since we choose the highest threshold of 10% for the flags, anything above this is flagged as >10% scattered light, so it will not matter whether it is, say 20% or 40%. Either way, the error is too large to provide a meaningful EDR.

### 3.4.8.2 $\mathcal{E}_{meas}$ as an estimate of $\mathcal{E}_{true}$

SBRS measures the LSF and Near-Field scattering. Until such measurements become available for the flight unit, the in-track and cross-track NFS contribution to the PSF will be based on a fit to a Harvey-Shack (H-S) BRDF model. We will translate the H-S BRDF into  $\mathcal{E}_{meas}$ , using the angular separations in the BRDF to describe the scattering to adjacent samples in the in-track and in-scan direction,

$$PSF = \delta + \mathcal{E}_{meas} \quad \text{Eq. 133}$$

The true scattering function,  $\mathcal{E}_{true}$ , is expected to differ from this, especially over the life of VIIRS as optical surfaces degrade with time, and SBRS has models to estimate this impact. So that our flags are conservatively pessimistic, we will use the end-of-life (EOL) estimates over the entire mission.

### 3.4.8.3 “Calculation Unreliable” Flag

The tails of the scattering distribution are notoriously difficult to measure since they are several orders of magnitude lower than the peak. The VIIRS near-field response (NFR) test FP-14 uses bright sources that saturate the central pixels to measure the tails and we therefore expect to know  $\mathcal{E}_{meas}$  over several orders of magnitude. There will be some point, however, when the measured tails become unreliable. Computing the scattering fraction becomes problematic when both  $S_{meas}$  and  $S'_{scat}$  become very small, since the uncertainty of both is inversely related to the value.

A reasonable approach is to set minimum thresholds for each. The flag is then set if both  $S_{meas}$  and  $S'_{scat}$  are below their associated thresholds. For  $S_{meas}$ , a dim pixel threshold  $S_{lo\_thresh}$  is defined for each band. A reasonable choice for  $S_{lo\_thresh}$  is  $L_{min}$  or, for the emissive bands, is the black body radiance associated with  $T_{min}$ .

For  $S'_{scat}$  a threshold,  $S_{scat\_thresh}$ , will be based on test data. We will determine the minimum  $\mathcal{E}_{meas}$  that is reliable and flag possible conditions where a reference bright target could scatter significant light beyond the measured tails. The bright target, as

defined by the spec is at Lmax and has an angular extent of 12 by 12 milliradians per the System Spec. If  $\theta$  is the angle which defines the limit of the measurement of the NFS, then  $S_{scat\_thresh} = S'_{scat}(\theta)$  where  $S'_{scat}(\theta)$  is computed for the bright target.

#### **3.4.8.4 Creation of Non-Saturated Scene**

We have considered determining the percentage of scattered light using the measured scene and a PSF; however, there is a difference between the scene needed to do this computation and a VIIRS SDR. The SDR is not a continuous field of radiance, and it is necessary to do the convolution described above. Therefore, there are several features of the VIIRS SDR which need to be addressed to produce a continuous scene from the SDR.

##### **3.4.8.4.1 Saturated radiance**

We assign a proxy band that has highly correlated radiances and substitute scaled radiances of the proxy band in place of the saturated data in cases where the pixel is saturated. Which proxy bands to use and the scale factors will be controlled by a changeable LUT.

If no suitable proxy band is found, or if the radiance in the proxy band is saturated or missing, then default radiance based on maximum reflectance or brightness temperature will be used. This would be higher than Tmax or Lmax values and lead to a conservative upper estimate of the scattering.

##### **3.4.8.4.2 In-scan angular resolution and Aggregation**

The PSF is a function of uniformly spaced pixels on the focal plane. Because of the size of the scattering PSF it is faster to convolve using an FFT. Computationally an FFT convolution requires a regular sample interval. Because the in-scan angular resolution changes across an aggregation zone boundary, each aggregation zone has a different angular resolution in-scan. To overcome this problem the aggregated pixels will be “de-aggregated” by repeating them by the number of samples that were used in the original aggregation. A guard band would be added that would avoid aliasing of the FFT.

##### **3.4.8.4.3 Bowtie and Edge of scan effects**

We need to re-pixelize between the scans because of the “bowtie” overlap with adjacent scans. IDPS developed a utility that properly finds adjacent pixels across scan boundaries. The IDPS implementation uses this tool to bring in adjacent scans for processing. We can also use a simplified approach for testing the science grade code so that flags are computed at the Beginning of scan (BOS) and EOS. This algorithm will make a guard region beyond each end of the scan and assign the radiance of the last pixel of the scene for that scan line.

#### 3.4.8.4.4 Missing radiance

If the gap in radiance data is small, such as a single pixel, or a row of pixels, then the pixels are estimated by interpolating the nearest neighbors. If the gap is large, then it will be filled in with proxy bands.

#### 3.4.8.4.5 Scan & Granule limits

The PSF will be as wide as or wider than a scan in the in-track direction. Reliable convolution depends on having guard regions around the scene that are about the size of the PSF. Granules will be processed so that the granule before and the granule after is always available, so that scans adjacent to the first and last scan of the granule are available.

#### 3.4.8.4.6 Scene edges

In the usual processing mode, there is always a granule before and after the current granule. In the case where the process is just starting up, the IDPS algorithm should create a guard region by reflecting the first or last granule in the processing chain so that the flags can be calculated. The alternative is to set the “calculation unreliable” flag until the 2<sup>nd</sup> or 3<sup>rd</sup> scan. This is not part of the Science Grade Code.

### 3.4.9 Dual Gain Anomaly Flagging

A nonlinear anomaly occurs over a narrow part of the dynamic range of the high gain for the dual gain bands. When the earth view DN is in this region, the Dual Gain quality flag is set to warn of possible degraded data. The DN values still may be used in the radiance and reflectance computations. The situation may be seen in [Figure 29](#).

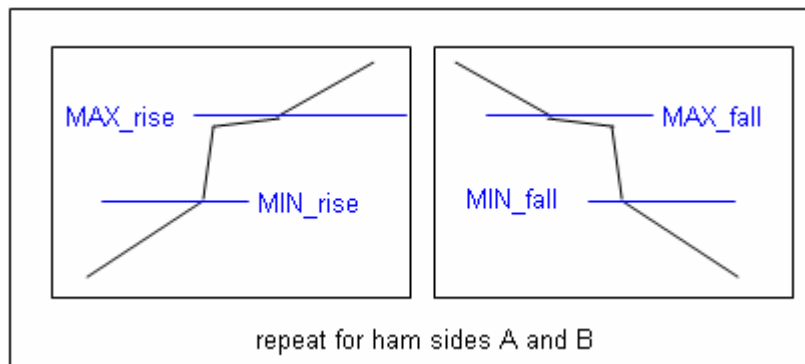


**Figure 29: Response seen for dual gain anomaly.**

Earth view DNs in the region between MIN\_rise and Max\_rise and between MIN\_fall and MAX\_fall are suspect. In order to be conservative, the minimum of the MIN\_rise and MIN\_fall values for both ham sides (and the maximum of the maximums) has been used to define the flagged region. The DG quality flag for each detector of dual gain bands is set to a unique number (96) to warn of this condition.

Whenever

$$\text{Min\_anomaly\_DN}(\text{band, detector}) < \text{DN\_ev} < \text{Max\_anomaly\_DN}(\text{band, detector})$$

then DG\_quality\_flag = DG\_ANOMALY\_DATA\_FLAG (96).

The algorithm includes a look-up table that describes the maximum and minimum DN values for every detector of a dual gain band. This anomaly will need to be monitored on orbit and the tables adjusted if necessary.

### 3.4.10 DNB Stray Light Flagging

Though the VIIRS instrument was designed to be resistant to stray light, on orbit analysis of DNB imagery data showed a haze in the earthview that occurred after the terminator, see [Figure 30](#). It is characterized as a positive offset of about 1 to  $5 \times 10^{-9}$   $\text{Wcm}^{-2}\text{sr}^{-1}$  and is fairly uniform across the scan. This is thought to be due to a light leak along the optical path as the contamination ends when the sun is eclipsed by the earth relative to the satellite about 8 minutes post terminator. In the southern hemisphere, there is an increase in stray light that occurs after the instrument comes out of eclipse--this is due to light entering the solar diffuser screen which is only illuminated during the southern terminator crossing, see [Figure 31](#).

An analysis showed this light leak was characterized to be dependent on the spacecraft (S/C) solar zenith and azimuth angles, as well as detector and frame. A correction algorithm was developed to remove the stray light offset and improve the DNB imagery. The correction is performed by a lookup table that has the dimensions of earth hemisphere, spacecraft solar zenith angle, detector, frame, and half-angle mirror side. The S/C solar azimuth angle varies over the course of a year and is adjusted for by using twelve tables, one for each month.

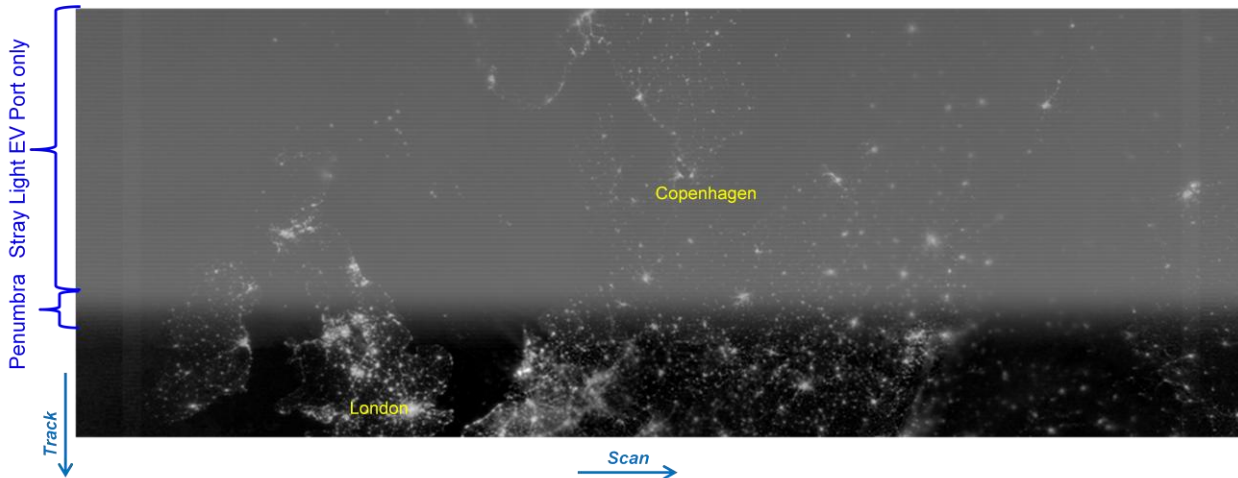


**Figure 30: Northern Hemisphere Stray Light Contamination**



**Figure 31: Southern Hemisphere Stray Light Contamination**

The DNB stray light correction table is generated by an offline process that analyzes the calibrated earthview scenes during the new moon over dark areas of the earth to determine the offset value. A human image analyst must first stage stray light

contaminated dark scenes and set fiducial regions and fit parameters. Once these steps are taken, the correction LUT is generated by the following process:

- Read in data and reduce noise by aggregating N frames to produce 4064/N bins
- Filter out all data points that are over city lights, have significant twilight, are above a preset radiance level, and outside of the specified S/C solar zenith angle range
- Take the median value in each bin
- Adjust for nightglow based on darkest parts of the granule where there is no stray light contamination
- For the steep transitions, such as the penumbra region, perform a centering and scaling transformation of radiance versus S/C solar zenith angle
- Perform polynomial fits (see [Figure 32](#)) of binned data as a function of the S/C solar zenith angle or transformed S/C solar zenith angle for different contaminated areas that are shown in Figure 32a and Figure 32b.
- Estimate stray light in twilight region through extrapolation
- After determining the fit parameters for different contaminated areas, an interpolation process creates a full LUT that is indexed to the hemisphere, solar zenith angle, in-scan pixels (frames), detector, and HAM side.

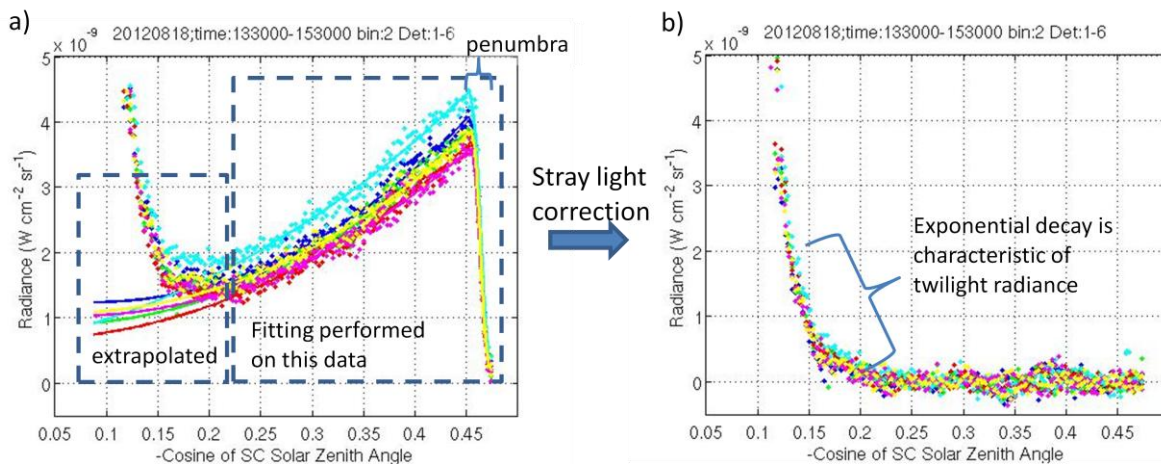


**Figure 32: a) Fitting of Earth view data to create stray light offset. Data are shown as dots and fits are shown as solid lines. Only data for detectors 1-6 are shown in the figure. b) Radiances corrected for stray light.**

The DNB stray light correction is applied after the radiance has been calibrated. If the spacecraft solar zenith angle (SZA) is within the stray light affected range, the QF2 scan level flag is set to indicate a stray light condition and pixel level test will be performed. For each pixel, if the calibrated radiance is below the threshold for significant

contamination, the correction will be performed and the QF1 pixel level flag will be set to poor (see [Figure 33](#)).

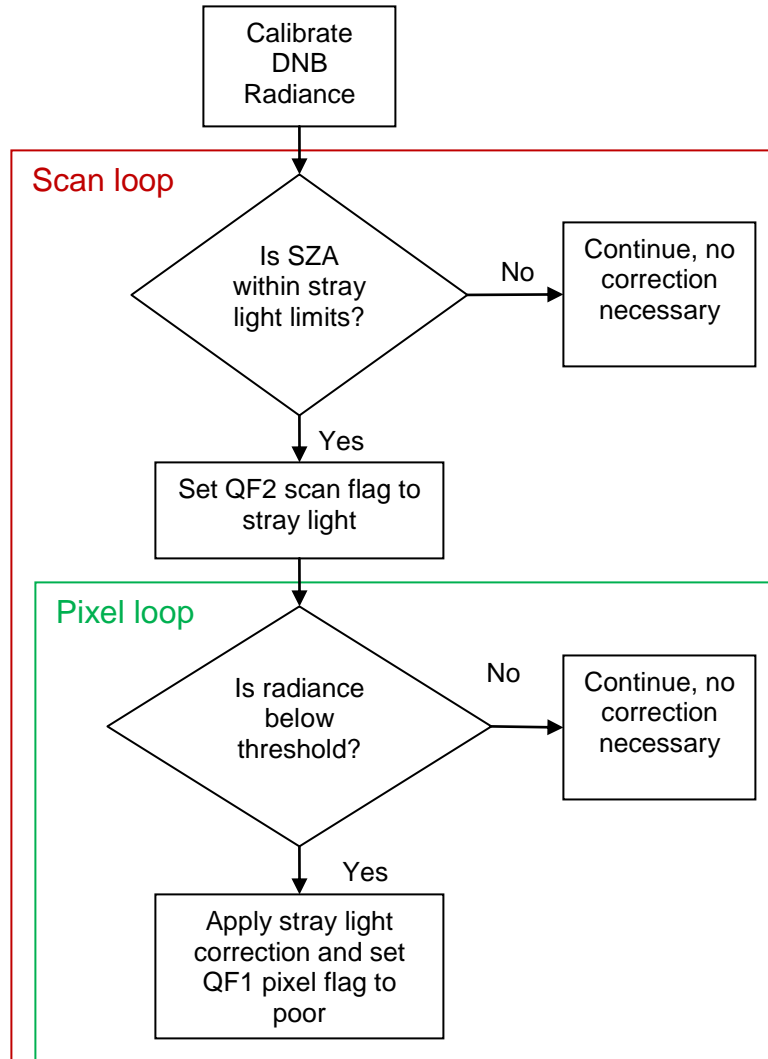


**Figure 33: Flowchart of Stray Light Correction**

The lookup table, SZA thresholds, and radiance thresholds are all tunable parameters. The correction is applied by interpolating the solar zenith angle of the current scan to the appropriate bins of the LUT and retrieving the stray light offset which is subtracted from the earthview radiance.

Twelve correction tables, one for each month, will be created to provide the appropriate adjustment in S/C solar azimuth angle which has a seasonal dependence. The LUTs will be replaced at appropriate times during the course of a year. It is assumed that since the primary dependence is on the angle of sun light impinging on the instrument,

little correction to these tables should be necessary over the life of the mission after the initial twelve are created. Proper image adjustment is confirmed by visual inspection of imagery corrected with the algorithm.

With the stray light correction in place, the DNB imagery is improved dramatically and dynamic range is extended by 2 orders of magnitude, to as low as  $1 \times 10^{-10} \text{ Wcm}^{-2} \text{ sr}^{-1}$ . Examples of the stray light corrected radiances are in [Figure 34](#) and [Figure 35](#).

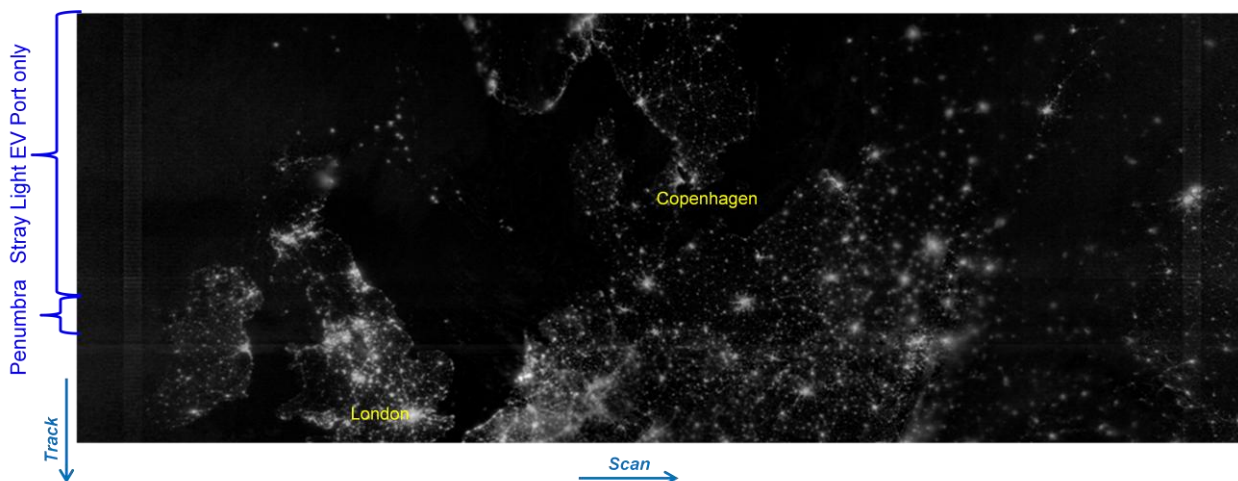


**Figure 34: Northern Hemisphere Stray Light Corrected Radiances**

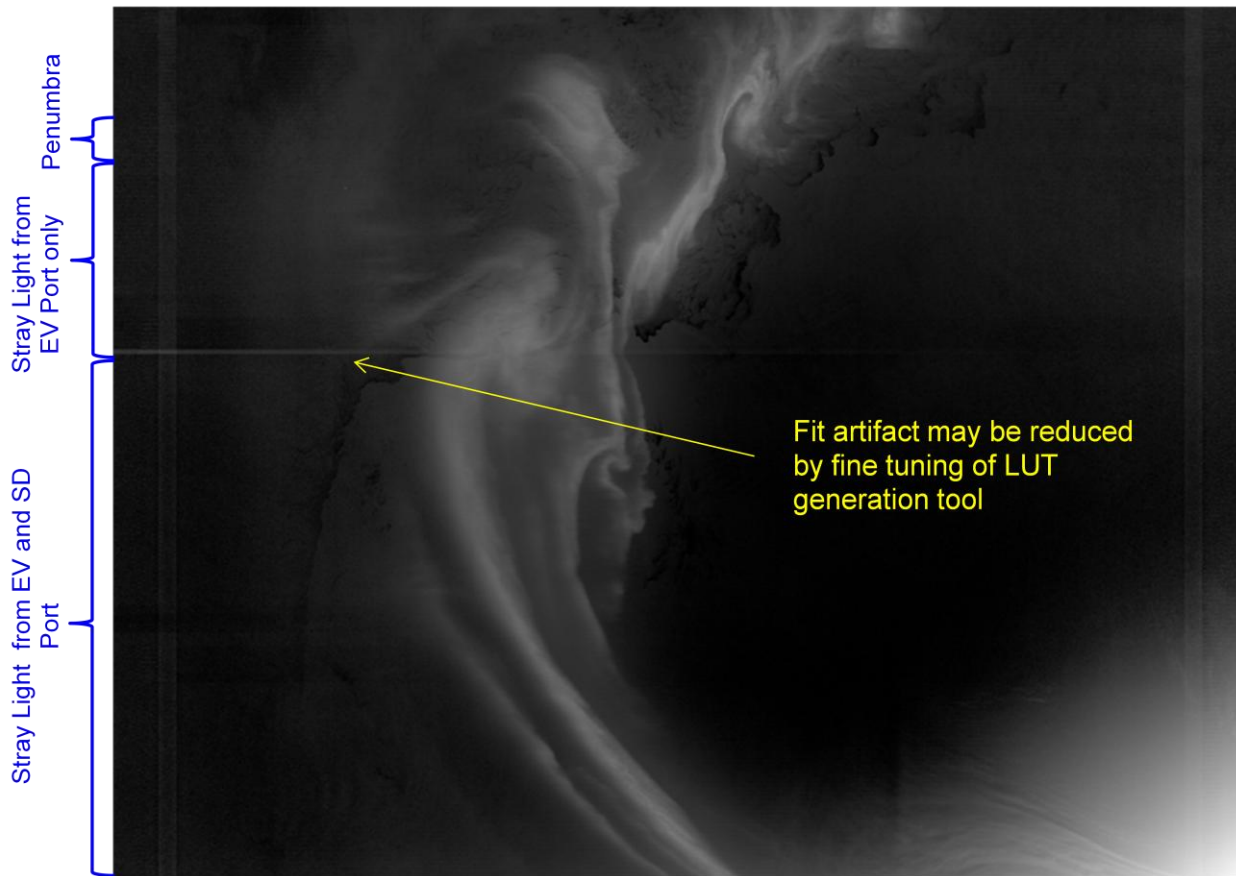


Figure 35: Southern Hemisphere Stray Light Corrected Radiances

### 3.4.11 Spike Noise Filter for Thermistor Data

Accurate thermistor readings are critical to good calibration as can be seen in section [2.4.1.2.1](#). During Electro-Magnetic Interference (EMI) testing it was discovered that some thermistors were affected with noise and spikes. In order to mitigate this and to improve thermistor temperature prediction in general, a filtering process is applied. It should be noted that temperature is over-sampled and so spikes may be filtered out without reducing accuracy of temperature measurement.

The following process is applied to the temperatures from each of the thermistors, with the exception of the OBC BB thermistors:

1. Temperature data is fitted by a 2<sup>nd</sup> order polynomial function.
2. Points are filtered if the residual exceeds a threshold value.
3. The remaining points are again fitted.
4. Residuals (including omitted points) are again filtered.
5. Steps 2 to 4 are repeated until there are no more changes as a result of this fitting and filtering process.
6. The fitted function is returned for each LRV.

- a. If there are insufficient points to fit the data, the original data is returned.

An example of the effect of this filter is shown in [Figure 36](#). The white noise on the thermistor is greatly exaggerated to show the effect of the filter.

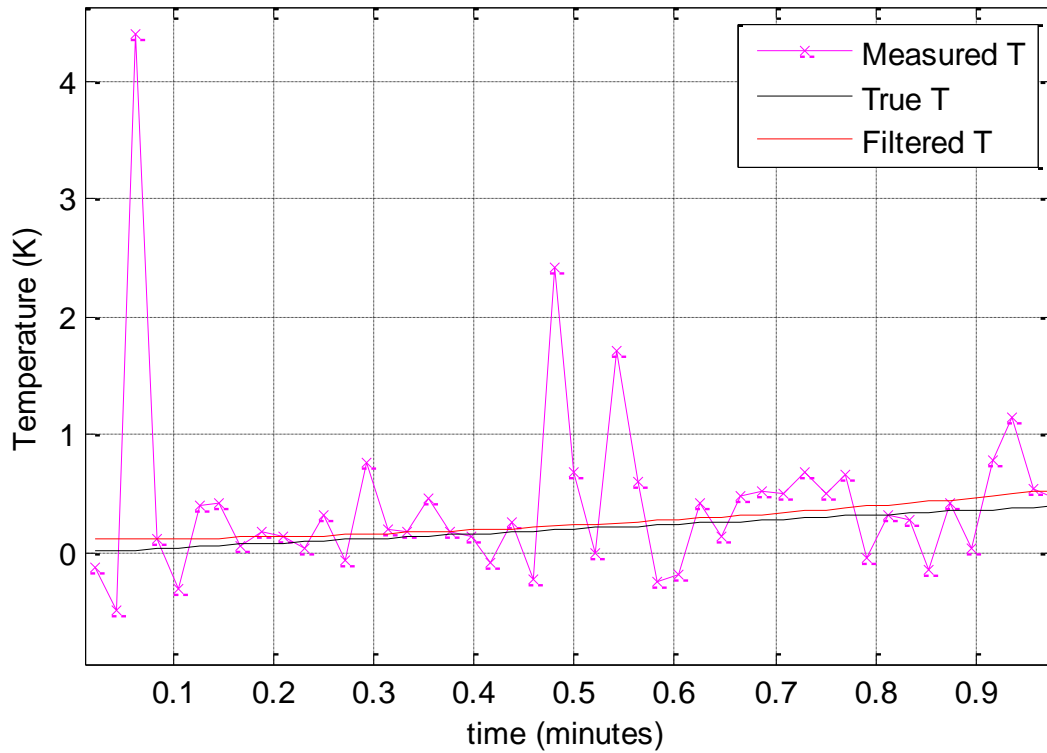


**Figure 36: Noise and spike filtering applied to a simulated thermistor measurement with 3 spikes.**

## 4. ASSUMPTIONS AND LIMITATIONS

This ATBD assumes that the equations and methods described in “*VIIRS Radiometric Calibration Equations*” [NGST Doc. D36966, Rev. 1] are complete and correct. Also the VIIRS radiometric calibration algorithm described in this ATBD makes some assumptions with respect to on-board processing, input data content, and inputs from pre-launch calibration testing.

### 4.1 ONBOARD PROCESSING

It is assumed that the on-board processing as described in Section [2.2.2.4](#) (DNB) and Section [2.2.3](#) (Electronics Module) is correct and complete.

It is further assumed that onboard processing aggregates the imagery resolution and single gain moderate resolution band *DN*'s as is described in Section [2.2.2](#).

### 4.2 INPUT DATA

It is assumed that the detector numbering convention used for all inputs is the “product order” convention expected by users of the VIIRS imagery and science data who require that the highest number detector in scan N lies adjacent to detector number 1 in scan N+1. This is opposite the detector numbering shown in [Figure 10](#) and [Figure 11](#), which follows the instrument engineer’s convention of labeling the detector that first sees a target on the ground as detector number 1.

It is assumed that the reflective band, emissive band, and DNB LUTs are populated with complete and correct calibration parameters.

It is assumed that the content of the Verified VIIRS RDR input is as described in Section [3.2.1](#) and that the Geolocation IP's that correspond to the Verified VIIRS RDR's are available at the time the VIIRS Earth View radiometric calibration process' execution is initiated.

### 4.3 PRE-LAUNCH CALIBRATION

It is assumed that pre-launch calibration for each VIIRS flight model is adequate to characterize the instrument and provide the data needed for the reflective, emissive, and DNB radiometric calibration LUTs.

It is assumed that the pre-launch calibration testing summarized in Section [2.4.1](#) and described in “*VIIRS SDR Calibration and Validation Plan for NPP*” [D47854-01], and “*VIIRS SDR Calibration and Validation Plan for NPOESS*” [D47854-2] is complete and correct.

*[This page is intentionally blank]*

## 5. REFERENCES

This version of the VIIRS Radiometric Calibration ATBD has several VIIRS specific reference documents as well as several non-VIIRS reference documents.

### 5.1 VIIRS DOCUMENTS

The following VIIRS documents are references for this ATBD. They are identified using their SSPR or Raytheon SBRS document number (when available) in italicized brackets, e.g., [*Y12345*]:

- [D31409-02]        *NPOESS Calibration and Validation Plan Volume 2: VIIRS*
- [D36966]        Mills, Steve, “*VIIRS Radiometric Calibration Equations*”, Rev 1, August 2004.
- [D36947]        Mills, Steve, “*VIIRS IR calibration uncertainty as a function of sensor characterization uncertainty*”, May 2002
- [D39553]        *Operational Algorithm Description Document (OAD) for VIIRS SDR Calibration Software*
- [D47854-01]     Liao, Lusalan, *VIIRS SDR Calibration and Validation Plan for NPP*
- [D47854-02]     Liao, Lusalan, *VIIRS SDR Calibration and Validation Plan for NPOESS*
- IPO MFR        De Luccia, Frank J., “*VIIRS as a Two-Stage System*”, IPO Memo for the Record, 6 February 04.
- [*EDD154640-101*] *VIIRS Command, Telemetry, Science and Engineering Data Description*
- [NP-EMD-2010.510.0030] Steve Mills, Lushalan Liao & Jodi Christiansen, *VIIRS SDR RSB Calibration Coefficient LUT Temperature Dependence Report*, 11 March 2010
- [*PS154640-101D*] *Performance Specification, Sensor Specification for the VIIRS Raytheon Corp.*, 19 June 2008
- [*PS154640-102*] *Performance Specification Algorithm Specification for the VIIRS*
- [*PS154640-124*] *DNB Module Performance Specification NPOESS*
- [*PS154640-360*] *Digital Preprocessor Product Specification for VIIRS*
- [*PS154640-380*] *DNB CCA Product Specification for VIIRS*
- [*TP154640-001*] *VIIRS System Verification and Validation Plan*

[TP154640-118]	<i>VIIRS Characterization and Calibration Plan</i>
[TP154640-247]	<i>VIIRS Program Test Procedure for Solar Diffuser Screen Characterization</i>
[TP154640-250]	<i>VIIRS Program Test Procedure for Response Versus Scan Angle (FP10)</i>
[TP154640-274]	<i>VIIRS Program Test Procedure for Emissive Band Calibration</i>
[virrs.cvtm.07.11.01]	Liao, Lushalan, <i>Parity of Imagery Band Odd-Even Offset</i> , Engineering Memo, 1 November 2007
[Y2466a]	<i>VIIRS Imagery ATBD</i>
[Y0012275]	<i>Description of DC Restore Process in the VIIRS Sensor</i>
[Y2479b]	<i>VIIRS Radiometric Calibration Component Level Software Architecture (SDRL 148-6)</i>
[Y2487]	<i>VIIRS Build RDR Module Level Detailed Design</i>
[Y2490]	<i>VIIRS Radiometric Calibration Component Level Detailed Design Document (SDRL 148-3)</i>
[Y3245]	<i>VIIRS Geolocation Unit Level Detailed Design Document (SDRL 147-3)</i>
[Y3258]	<i>VIIRS Geolocation ATBD (SDRL 147-2)</i>
[Y5235]	<i>Methodology to characterize VIIRS non-linearity - micro and macro</i>
[Y6875]	<i>Terminator Orbit Calibration</i>
[Y0012275]	<i>Description of DC Restore Process in the VIIRS Sensor</i>
[Y0012416]	<i>VIIRS Cross-Calibration Method for Terminator Orbit Sensors</i>

## 5.2 NON-VIIRS DOCUMENTS

The following non-VIIRS documents are references for this ATBD:

1. Barnes, W.L., Thomas S. Pagano, and Vincent V. Salomonson, (July 1998), *Prelaunch Characteristics of the Moderate Resolution Imaging Spectroradiometer (MODIS) on EOS-AM1*, IEEE Transactions on Geoscience and Remote Sensing, Vol. 36, No. 4, July 1998. 13 pp.
2. Che, N.B., et al, Results of Calibrations of the NOAA-11 AVHRR Made by Reference to Calibrated SPOT Imagery at White Sands, NM, Proc. SPIE Vol. 1943-21, 1991.

3. Fitzgerald, A.E., et al., *Basic Electrical Engineering*, 4<sup>th</sup> Ed., McGraw-Hill, 1975.
4. Guenther, B. et al, (July 1998), Prelaunch Algorithm and Data Format for the Level 1 Calibration Products for the EOS-AM1 Moderate Resolution Imaging Spectroradiometer (MODIS), IEEE Transactions on Geoscience and Remote Sensing, Vol. 36, No. 4, July 1998. 10 pp.
5. IPO (2002), *NPOESS Technical Requirements Document (TRD) Version 7*, National Polar-Orbiting Operational Environmental Satellite System (NPOESS), NPOESS/IPO, Silver Spring,, MD.
6. MODIS Characterization Support Team (May 1997). *MODIS Level 1B Algorithm Theoretical Basis Document Version 2.0*, MCST Document #MCM-ATBD-01-U-DNCN, NASA/GSFC, Greenbelt, MD.
7. MODIS Characterization Support Team (2000). *MODIS Level 1B Product User's Guide, for Level 1B Version 2.3.x*, Release 2, MCST Document #MCM-PUG-01-U-DNCN, NASA/GSFC, Greenbelt, MD.
8. Planet, W.G. (ed.), (1988). *Data Extraction and Calibration of TIROS-N/NOAA Radiometers*. NOAA Technical Memorandum NESS 107 – Rev. 1, Oct. 1988. 130 pp.
9. Scott, K. P., Radiometric Calibration of On-Orbit Satellite Sensors Using an Improved Cross-Calibration Method, Ph.D. Dissertation, Univ. of Arizona, 1998.
10. Scott, K. P., K. J. Thome, and M. R. Brownlee, *Evaluation of the Railroad Valley playa for use in vicarious calibration*, Proc. SPIE Vol. 2818, 1996.
11. Teillet, P. M., P. N. Slater, Y. Ding, R. P. Santer, R. D. Jackson, and M. S. Moran, *Three methods for the absolute calibration of the NOAA AVHRR sensors in-flight*, Remote Sens. Environ., 31:105-120, 1990.
12. Thuillier, G. et al, "The Solar Spectral Irradiance from 200 to 2400 nm as Measured by the SOLSPEC Spectrometer from the ATLAS and EURECA Missions", Solar Physics, 214: 1-22, 2003.
13. Xiong, X., J. Sun, K. Chiang, S. Xiong and W. Barnes "MODIS On-orbit Characterization Using the Moon". In: Fujisada H (ed) Proceedings Sensors, Systems, and Next Generation Satellites VIII. SPIE 4881: 299–307, 2002.
14. S. Mills et al., Computer Modeling of Earthshine Contamination on the VIIRS Solar Diffuser" SPIE remote sensing 2005
15. S. Mills, S. Weiss, T. Ohnuki, D. Searcy, M. Plonski, E. Jacobson, J. McCarthy, and J. Jaron, Calibration of the VIIRS Day/Night Band (DNB), 6th Annual Symposium on Future National Operational Environmental Satellite Systems- NPOESS and GOES-R, Jan 21, 2010.
16. Cao, C., F. DeLuccia, X. Xiong, R. Wolfe, F. Weng, Early On-orbit Performance of the Visible Infrared Imaging Radiometer Suite (VIIRS) onboard the Suomi National Polar-orbiting Partnership (S-NPP) Satellite, IEEE Trans. Geosci. and Remote Sens., in press, DOI:10.1109/TGRS.2013.2247768, 2013a.

17. Cao, C., J. Xiong, S. Blonski, Q. Liu, S. Uprety, X. Shao, Y. Bai, *and* F. Weng, Suomi NPP VIIRS sensor data record verification, validation, and long-term performance monitoring, *J. Geophys. Res. Atmos.*, 118, *doi:10.1002/2013JD020418*, 2013b.
18. Shao, X., C. Cao, and S. Uprety, Vicarious calibration of S-NPP/VIIRS day-night band, *SPIE Proceedings Vol. 8866, Earth Observing Systems XVIII*, James J. Butler; Xiaoxiong (Jack) Xiong; Xingfa Gu, Editors, 88661S, DOI: 10.1117/12.2023412, 2013.
- 19.

*[This page intentionally blank]*

## Appendix A: Description of VIIRS OBC BB Thermistor Temperature Processing<sup>26</sup>

This section covers the OBC BB thermistor characteristics, the passive analog electronic circuits for processing them, the generation of raw data DN values, and the determination of temperature from DN values using  $1/\ln(R)$  equations.

The thermistors are thermally sensitive resistors that have a negative temperature coefficient. GSFC Spec S-311-P-18 issued in 1974, defines 10 dash numbers that cover two temperature ranges  $-55^{\circ}$  to  $70^{\circ}/90^{\circ}\text{C}$  with variations in resistance @  $25^{\circ}\text{C}$ , tolerances and lead configurations. VIIRS uses the 10 Kohm @  $25^{\circ}\text{C}$  thermistor by YSI for general temperature sensors and a Fenwal SBRS Spec SC6G02 5K ohm @  $25^{\circ}\text{C}$  thermistor for the Blackbody, both over smaller temperature ranges for a balance of needed range and resolution. Thermistors can be used in passive analog circuits (as described here) or in active analog circuits.

[Figure 37](#) is a simplified diagram of the generic passive analog telemetry process for generating raw DN data. Thermistor and parallel resistance differs for the general versus Blackbody circuits. The steps [1] to [4] summarize the major activity items. Added detail is that a pulse of excitation current,  $I_e$ , generates a voltage,  $V_{tot}$ , across the total resistance of the thermistor and parallel resistance. An offset voltage ( $V_o$ ) is added to  $V_{tot}$  and the sum  $V_{tot}+V_o$  is passed through a -1 unity amplifier to produce the telemetry voltage ( $V_t$ ).  $V_t$  is routed to the input of a  $\pm 2.5\text{V}$ , 14-bit, 2's complement ADC. The ADC digital telemetry output is  $DN$  that is expected to range from -8192 DN to +8191 DN for 14 bits. In the figure it is noted that three Mux functions are not shown. Details will be folded in after the general description of Temperature Recovery.

1.  $V_{tot} = I_e * R_{tot}$
2. Based on the equation for parallel resistors  $R_{tot} = (R_{th} R_p) / (R_{th} + R_p)$  in ohms
3.  $V_t = -(V_{tot} + V_o)$  volts, which has a -2.5V to +2.5V range for ADC
4. 14-bit ADC delivers 2's complement data, from -8192 DN to +8191 DN

The design CTA values are

- General circuit:  $I_e = 0.000707\text{A}$ ,  $V_o = -3.49\text{V}$ ,  $R_p = 10\text{K ohms}$
- Blackbody circuit:  $I_e = 0.00139\text{A}$ ,  $V_o = -3.49\text{V}$ ,  $R_p = 5\text{K ohms}$

---

<sup>26</sup> Parts of this appendix are based on Raytheon SBRS Engineering Memo Y0012889

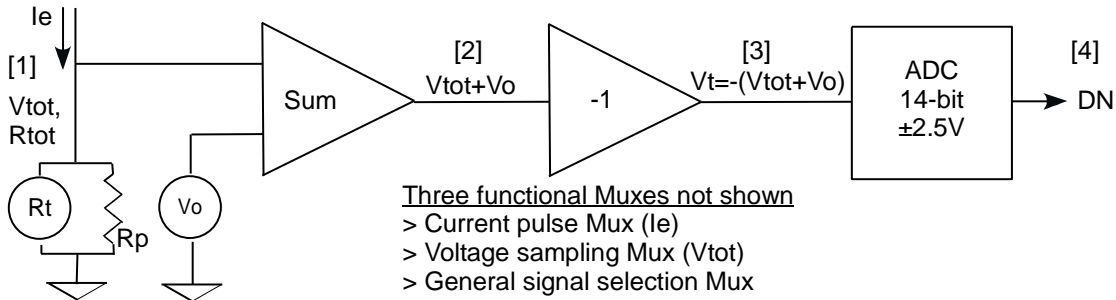


**Figure 37: VIIRS simplified generic passive analog telemetry circuit**

Unfortunately the design CTA values given above vary with temperature, and are not stable enough to be used explicitly to determine  $R_{tot}$ . However, there are 3 reference resistors that are part of the circuit, and for which DN counts are reported every scan. A linear fit of the 3 known resistances to the reported DN values provides accurate gain and offset which can be used to determine  $R_{tot}$  from the reported counts from each of the 6 OBC BB thermistors. The values to use in the equations below are provided in the Engineering Data Description (EDD).

To determine temperature vs. DN it is best to break it into 4 parts:

1. Determine the gain and offset of the circuit using a linear fit to the 3 reference resistors.
2. Use this gain and offset to determine  $R_{tot}$  as a function of DN.
3. Compute  $R_{th}$  from  $R_{tot}$  and  $R_p$  from the equation for parallel resistors

$$R_{th} = \frac{1}{\frac{1}{R_{tot}} - \frac{1}{R_p}}$$

The value for  $R_p$  is provided in the EDD separately for the 6 OBC BB thermistors.

4. Determine temperature as a function of  $R_{th}$  with the equation

$$T = \frac{1}{\sum_0^3 A_n (\ln R_{th})^n}$$

The values for  $A_n$  are provided separately in the EDD for the 6 OBC BB thermistors.

## Appendix B: Solar Diffuser Calibration Multi-Orbit Aggregation

### Introduction

In considering the design of multi-orbit aggregation of the solar diffuser (SD) data, the capabilities of the SD as a calibration source must be considered as well as the interaction of a calibration analyst during processing. Both the SDSM and the SD cal aggregation approach depend on system stability and as yet uncharacterized errors in the SD and SDSM. Initially, during the cal/val phase, interpreting the F factors and applying them to the calibration coefficient LUTs will require analyst in the loop. Analyst may also have to go back to the raw cal data to understand any observed flukes in the F factors. There is no reason, however, why computing the F factors cannot eventually be an on-line, automated process.

If during this initial phase the process becomes sufficiently predictable, it would be prudent to implement the application of the F factors to the EV data as an automated approach, involving some aggregation or filtering of the F factors. If the detector gains turn out to be unstable on the order of hours, and for reasons of data latency, there may be no choice but to automate this process. Advice from user community to define the initial form of this trending/ integration will be sought out. The approach described here is not the final approach. We fully realize that any approach defined before launch would almost certainly need to be modified during cal/val, but with the structuring of the program sufficiently well defined to allow various options, it will require minimum modification.

[Figure 38](#) shows the general flow of data in the Solar Diffuser Calibration Multi-Orbit Aggregation algorithm. A history database is updated to retain all relevant data regarding solar diffuser calibration for some N number of orbits. A best fit of the data is produced to project a current best estimate of the values of the F factors described in [Eq. 68](#). Using a least-square linear fit an F factor is estimated along with an estimate of the rate of change of F. This is computed for each detector on each band for each gain state and for each mirror side. These values provide data that an analyst can use to update the current F values in the Look-up Tables (LUT) actually used by the reflective calibration algorithm. In order to aid the analyst in the decision about whether to apply the revised F values to the LUT, estimation error predictions and confidence probabilities are provided.

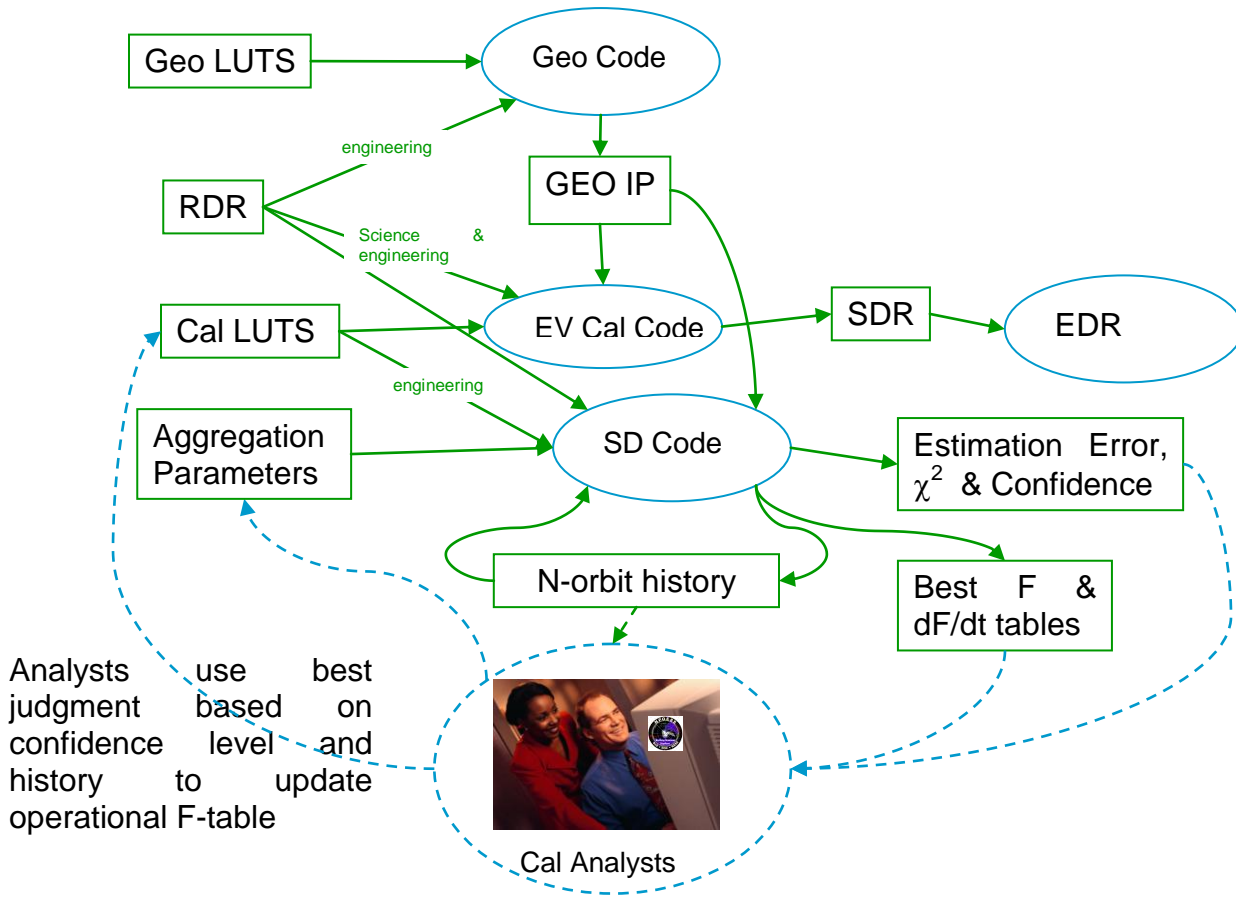


Figure 38: Flow diagram of SD Multi-orbit history and aggregation

### Update history file

The history file is updated every time the SD module is run. The module can process up to 4 granules at a time, though for expediency IDPS may choose to run the process for each granule.

The process adds new records to the history file scan by scan for each band and detector. The Signal to Noise Ratio (SNR) is an important measure of the quality of an individual scan, and is determined with the following equation,

$$SNR = \frac{\langle DN_{sd} \rangle - \langle DN_{sv} \rangle}{\sqrt{\frac{1}{12} + \frac{\sigma^2(DN_{sd})}{N_{sdfrm}} + \frac{\sigma^2(DN_{sv})}{N_{svfrm}}}}$$

where the means and variances are taken over frames without error flags, and are inside  $3\sigma$  (or  $n\sigma$ ) test

Eq. 134

The 1/12 value is to account for round-off or quantization error in the digital output. This insures that the SNR is never infinite even if the variances are 0.  $N_{sdfrm}$  or  $N_{svfrm}$  are 0 then the SNR should be set to 0.

DN data is reported as average values over 48 or 96 SD & SV frames. [Table 23](#) lists items saved in the history file.

**Table 23: Parameters reported in the History File**

Symbol	Description	Reference
$t_{i,n}$	scan time	N/A
$g$	gain state	N/A
$V_{dcr}$	DC restore voltage	N/A
$DN_{sd}$	Solar diffuser digital number including mean, standard deviation and maximum value	<a href="#">Eq. 69</a>
$DN_{sv}$	Space view digital number including mean, standard deviation and maximum value	<a href="#">Eq. 69</a>
$N_{svfrm}$	Number of frames with good SV quality flags	N/A
$c_0$ , $c_1$ & $c_2$	Calibration coefficients applicable to the given scan	<a href="#">Table 12</a>
$RVS_{SD}$	RVS at the SD for a given band	<a href="#">§2.4.1.2.2</a>
$\phi_v$	Vertical SD angle	<a href="#">Eq. 105</a>
$\phi_h$	Horizontal SD angle	<a href="#">Eq. 106</a>
BRDF	Bi-directional Reflectance Distribution Function	<a href="#">Eq. 63</a>
$\tau_{sds}$	SD screen transmittance	<a href="#">Eq. 63</a>
SNR	Signal to Noise Ratio	eq. 134
$\cos(\theta_{inc})$	Cosine of the SD angle of incidence	N/A
$d_{se}$	Sun to Earth Distance Factor	N/A
$L_{ap}$	Measured EV radiance	<a href="#">Eq. 70</a>
$L_{nsd}$	Predicted SD radiance	<a href="#">Eq. 67</a>
$F_i$	Calibration F factor for scan i	<a href="#">Eq. 68</a>

### SD Scan Filter Process

The filtering process is defined by a LUT of threshold parameters. It loops through all records in the history file and rejects ones that do not meet the following requirements.

- Require measured data within tolerances for  $\langle DN_{sd} \rangle$ ,  $std(DN_{sd})$  &  $\langle DN_{sv} \rangle$   $std(DN_{sv})$ ,
- Require minimum SNR of SD signal per band and gain state
- Requires valid geometry

## SD Aggregation Process

The combined aggregation of data in the history file or database is used to compute a best fit for the values of F. It performs the following function every time the process is run. The process is run every time the history file is updated. Using a Least Square linear fit or simple average depending on flag, it performs the following steps:

- Shift the times to be relative to the time of the most recent scan in the history

$$t'_i = t_i - \max(t) \quad \text{Eq. 135}$$

- Compute weights for each scan, per detector, per band with the equation

For simple average

$$w_i = 1$$

otherwise for linear fit

$$w_i = \frac{1}{\left(\frac{F_i}{\text{SNR}_i}\right)^2 + \sigma_{\text{mod}}^2} \quad \text{Eq. 136}$$

where  $\sigma_{\text{mod}}$  = modulation error for  $F_i$

- Compute a rate of change,  $dF/dt$ , with the equation

if linear fit

$$\frac{dF}{dt}_{\text{best}} = \frac{\sum_i w_i \cdot (t'_i - \langle t \rangle) \cdot F_i}{\sum_i w_i^2 \cdot (t'_i - \langle t \rangle)^2}$$

otherwise if simple average = 0

where

$$\langle t \rangle = \frac{\sum_i w_i t'_i}{\sum_i w_i}$$

Eq. 137

- Compute a offset in F due to the gradient computed in eq. 136

For simple average

$$\Delta F = 0$$

otherwise for linear fit

$$\Delta F = \langle t \rangle \frac{dF}{dt}_{\text{best}}$$

Eq. 138

- produce a best-fit F with the equation

$$F_{best} = \frac{\sum_i w_i \cdot F_i}{\sum_i w_i} - \Delta F \quad \text{Eq. 139}$$

summations taken over all  $i$  scans that pass filter test

Values of F are differenced from the predicted F value based on the fit. If F values are outside three standard deviations it removes those values and again performs the fit. The 3 standard deviation test may be changed in the parameters file to a lower or higher value at the analyst's discretion.

### Confidence and Error Estimation Process

As described above, estimation errors and confidence statistics need to be calculated as following.

- Generate an estimate of the standard deviation of F with the following equation:

$$\sigma(F_{best}) = \sqrt{\frac{1}{\sum_i w_i} + \frac{\left(\sum_i w_i \cdot F_i\right)^2}{\sum_i w_i^2 \cdot (t'_i - \langle t \rangle)^2 \times \left(\sum_i w_i\right)^2}} \quad \text{Eq. 140}$$

summations taken over all  $i$  scans that pass filter test

- Generate an estimate of the standard deviation of the rate of change of F, dF/dt, with the following equation:

$$\sigma\left(\frac{dF}{dt}_{best}\right) = \sqrt{\frac{1}{\sum_i w_i^2 \cdot (t'_i - \langle t \rangle)^2}}$$

summations taken over all  $i$  scans that  
pass filter test

Eq. 141

- Compute estimation error  $\chi^2$  with the following equation:

$$\chi^2 = \sum_i w_i \cdot \left( F_i - F_{best} - t'_i \cdot \frac{dF}{dt}_{best} \right)^2 \quad \text{Eq. 142}$$

summations taken over all  $i$  scans that pass filter test

- Compute Goodness of Fit Probability using the incomplete gamma function with the following equation:

$$P_{GOF}(\chi^2 | N) = 1 - P\left(\frac{N-2}{2}, \frac{\chi^2}{2}\right)$$

= Goodness of Fit Probability

where

$$P(a, x) = \frac{1}{\Gamma(a)} \int_0^x e^{-t} t^{a-1} dt \quad \text{Eq. 143}$$

= incomplete gamma function

N = number of fitted values of  $F$

### SD Transmittance Screen Wavelength Dependence

One of the reasons for multi-orbit aggregation of the SD calibration is that there is expected to be some modulation in the SD signal, and averaging over many orbits will reduce the error caused by this modulation. As seen in [Eq. 62](#), the SDS transmittance has wavelength and detector dependence. The SDS includes direct transmittance that is not wavelength dependent or detector dependent. This represents the transmittance that would be measured at the component level. The direct transmittance is only affected by the geometry of the screen mask, and this is independent of wavelength (the holes are large enough that diffraction is not important). But there is also an indirect component due to stray light that bounces off the inside of the SD cavity. This is represented by the equation

$$\tau_{sds}(\phi_h, \phi_v, \lambda, d) = \tau_{sds\_direct}(\phi_h, \phi_v) + \tau_{sds\_stray}(\phi_h, \phi_v, \lambda, d) \quad \text{Eq. 144}$$

The stray light transmittance component is wavelength dependent because stray reflections occur off surfaces which have different reflectances for different wavelengths. It is also detector index dependent because each detector sees a somewhat different footprint on the SD, and stray light does not usually illuminate the SD evenly. In pre-launch tests, stray light has been observed bouncing off the SD, retro reflecting from the telescope and back onto the telescope. This produces a concentration of stray light at a local spot upon the SD. This effect has been confirmed by some stray light models. Other stray light paths include multiple bounces off the inside of the cavity before hitting the SD.

An end to end test of the SD system could be used to determine wavelength dependence or detector dependence of SDS transmittance. Alternately stray light analysis which demonstrates that these dependencies are negligible would suffice. So far, however, this has not been done.

Generally, stray light models are sufficient to predict that a problem does or does not exist, but not sufficient to substitute for characterization. A LUT for SDS transmittance derived from stray light analysis would require a strong burden of proof to show that it could be used in the calibration algorithm.

## **Appendix C: Description of Reflective Solar Band (RSB) Calibration Process Implemented to Compensate for Anomalous On-Orbit Throughput Degradation**

On December 5, 2012, 38 days after the launch of Suomo NPP and 14 days after the opening of the nadir door, an anomalous degradation in VIIRS reflective band response in the longer wavelength Vis/NIR bands was discovered. Trending of the reflective band response scale factor  $F$  defined in Eq. 66 above showed a sharp increase in the rate of change of the  $F$  factor in these bands after the nadir door was opened during orbit 344 on November 21, 2012. The subsequent anomaly investigation revealed that the root cause of the response degradation was tungsten contamination of the coatings of the four mirrors in the Rotating Telescope Assembly. UV exposure of the tungsten contaminated coatings produces color centers that darken these mirrors, thereby reducing their combined throughput. The RTA mirrors are exposed to solar UV every orbit near the South Pole when the sun illuminates the Solar Diffuser. However, the time averaged rate of UV exposure increased dramatically when the nadir door was opened and the instrument began observing sunlight reflected from the earth (earthshine). As a result the rate of optical throughput degradation increased dramatically at this time, and, since the  $F$  factor is inversely proportional to optical throughput, this effect was clearly observable in the  $F$  factor trending.

The original plan for RSB calibration was to follow the MODIS paradigm of updating the look-up table (LUT) containing  $F$  values whenever the response changes by an amount greater than an agreed-upon threshold (0.2% in the case of MODIS). The MODIS  $F$  LUTs for Terra and Aqua were updated approximately weekly during Intensive Calibration and Validation (ICV) and approximately biweekly later in the Terra and Aqua missions. Due to the throughput anomaly, VIIRS response in the VisNIR bands affected most severely (M7 and I2) changed at a rate of 7% per week in the first week after opening of the nadir door. This worst case rate of response change has decreased to somewhat less than 1% per week at the time of this writing. Response is expected to continue changing due to the anomaly throughout the mission life, albeit at lower rates over time. Since as a practical matter the  $F$  LUT can be updated no more frequently than once per week and since the EDR community desires highly stable RSB calibration, ideally without any abrupt temporal changes in calibration error, the strategy for RSB calibration was modified during ICV to perform scan-by-scan updating of the  $F$  values within the operational ground processing performed by IDPS.

The scan-by-scan updating of  $F$  factors within the operational code entailed only a slight change in the theoretical basis of the VIIRS RSB calibration for the DNB. A HAM side dependence was incorporated into the LGS gain as defined in Sec. 3.3.5.3, On-Orbit Determination of Gain for LGS. This modification improves the quality of the DNB imagery by reducing striping, as the instrument exhibits slightly different throughput for the two HAM sides. The calibration equations for the non-DNB RSB remained exactly as described in the body of this document. The manner in which the algorithms

implement these equations via a combination of online and offline processing did change and is described at a top level in what follows. The detailed description of the code changes associated with scan-by-scan updating of F factors are described in the Operational Algorithm Description for VIIRS Geolocation (GEO) Sensor Data Record (SDR) and Calibration (CAL) SDR [474-00090]. The detailed description of the new and modified LUTs are described in the Configuration Description and Format Control Book, Volume VIII, (474-0001-08 B0122).

As indicated in Eq. 65 the F factor for non-DNB bands is applied to rescale all three calibration coefficients. For the DNB the Low Gain Stage (LGS) gain is the analog of the F factor defined for the other bands. This gain is defined in Sec. 3.3.5.3, On-Orbit Determination of Gain for LGS, and is referred to as the DNB F factor in what follows. The F factors for all reflective bands are calculated offline and trended over time. The trends are fitted to either an exponential form as shown in Eq. 145 or a quadratic form as shown in Eq. 146 below,

$$F = F0 + F1 * \exp(F2 * (T - T_{REF})) \quad \text{Eq. 145}$$

$$F = F0 + F1 * (T - T_{REF}) + F2 * (T - T_{REF})^2 \quad \text{Eq. 146}$$

where the parameters F0, F1 and F2 are determined from the fits and the reference time  $T_{REF}$  is the midpoint of the last solar calibration period used in the fitted F data. In the implementation of the RSB calibration algorithms performed initially in ICV, the above equations were used to predict ahead and populate LUT updates, specifically the F LUT for non-DNB bands and the DNB gain LUT. The time T was chosen based on the typical time between LUT submission into the code/LUT change process and the time of insertion of the updated LUTs into the IDPS. In the implementation performed in IDPS code update Mx6.2 and thereafter, the above equations were incorporated in the operational code to calculate F factor updates on a scan by scan basis. The time T is the start time of the scan being calibrated, and the values of the parameters F0, F1, F2 and  $T_{REF}$  are read from LUTs. This strategy provides near continuous RSB calibration and much smaller impacts to calibration error when LUTs are updated.

## **Appendix D: Description of Theoretical Basis for Reflective Solar Band (RSB) Automated Calibration (RSBAutoCal) Algorithm**

### **D1. Introduction**

A fully automated algorithm for calibration of the RSB has been implemented to eliminate the predict-ahead errors in SDR radiances and reflectances associated with the prior offline calibration process that relied upon weekly updates of non-DNB RSB calibration scale factors and DNB LGS gains and their trends. The calculation and application of DNB offsets and gain ratios have also been automated by exploiting calibration sector data. The automation of the DNB calibration eliminates artifacts in imagery due to the prior offline calibration process in which offsets and gain ratios were corrected monthly via look-up table (LUT) updates derived from EV data acquired during special operations.

For the non-DNB RSB the RSBAutoCal algorithm migrates offline calculations of calibration parameters as described in the body of this ATBD into the operational algorithm implemented in the IDPS code, allowing update and application of these parameters every orbit. The scan-by-scan calibration functionality described in Appendix C remains in effect to smoothly interpolate between the per-orbit updates. Consequently, there are no changes to the algorithm theoretical basis involved in these branches of the algorithm, which calculate non-DNB RSB calibration scale factors (F factors) and the SD BRDF degradation factors (H factors) for SDSM detectors. The same is true of the branch of the automated algorithm that calculates the DNB LGS gains from solar calibration data. Therefore, these three branches of the algorithm are described very briefly in what follows.

The feasibility of calculating DNB gain ratios from reflected earthshine signals in the calibration sectors was not realized until post-launch ICV. Therefore, this branch of the RSBAutoCal algorithm will be described in some detail in what follows. It is arguable that the theoretical basis for gain ratio determination is the same as described in the body of this ATBD for the method using EV data collected in special operations, since it is principally the radiance source that is different when calibration sector data are exploited for this purpose. The key concept of collecting signals from different gain states viewing a common scene radiance simultaneously is the same, whether the common radiance is viewed in the EV or calibration sectors. However, the key equations for an algorithm utilizing calibration sector data are not described in the body of this ATBD, so a description of these equations and the top-level functionality of this algorithm is warranted in this appendix.

Similarly, the feasibility of utilizing calibration sector data to measure and compensate for offset drift was not realized until post-launch ICV. EV measurements are still needed to measure offset patterns within aggregations zones, but these patterns are now known to be extremely stable, so that the EV measurements can be much less frequent

than monthly. The branch of the automated algorithm that calculates and applies the offset drift correction based on calibration sector data will therefore also be described in some detail in this appendix.

Greater detail on all aspects of the RSBAutoCal algorithm may be found in the Joint Polar Satellite System (JPSS) Operational Algorithm Description (OAD) Document for VIIRS Geolocation (GEO) Sensor Data Record (SDR) and Calibration (CAL) SDR Software [D1].

## **D2. RSB Calibration Scale Factor Determination**

The RSB calibration scale factors, or “F” factors, are calculated as described in Sec. 3.3.3, in particular Eq. 66. There is no change in algorithm theoretical basis for determination of these scale factors associated with the RSBAutoCal algorithm. The F factors are computed every orbit in this algorithm shortly after the solar calibration data are acquired. Outlier rejection and smoothing are performed using Robust Holt Winters (RHW) filtering operating on the current observed F factor values and prior smoothed F factor values [D2]. The RHW filter also calculates the local temporal trends in F factors as part of its functionality. The calibration coefficients are rescaled as described in Eq. 65 using the most recently calculated F factors and their trends. The F factors are applied scan by scan as described in Eq. 146 in Appendix C, using the linear trend only for propagation to the time of the current scan.

## **D3. Solar Diffuser BRDF Degradation Factor Determination**

The Solar Diffuser BRDF degradation factors, or “H” factors, are calculated as described in Sec. 3.3.3.1 for the eight SDSM detectors. There is no change in algorithm theoretical basis for determination of these scale factors associated with the RSBAutoCal algorithm. The H factors are updated every orbit using measured data from the most recent operation of the SDSM. In the very early phase of the mission the SDSM was operated once per orbit but it is now operated once per day. The automated algorithm can ingest new SDSM data acquired on any cadence. Outlier rejection and smoothing are performed using Robust Holt Winters (RHW) filtering operating on the current observed H factor values and prior smoothed H factor values for the eight SDSM detectors. The RHW filter also calculates the local temporal trends in H factors as part of its functionality. The H factors are updated every orbit using the most up-to-date calculated trend data.

The H factor is applied to rescale the Solar Diffuser BRDF at the wavelength of each SDSM detector as described in Eq. 66. Interpolation and extrapolation of all eight H factors are used to extend the corrected BRDF over the support of the Relative Spectral Response of a given RSB, and it is this corrected BRDF that is used in the spectral integration required to calculate the F factor as described in Eq. 66.

#### **D4. DNB LGS Gain Determination**

The DNB LGS gain is calculated as described in Sec. 3.3.5.3 for each aggregation zone, detector and mirror side. There is no change in algorithm theoretical basis for determination of the DNB LGS gains associated with the RSBAutoCal algorithm. The gains are computed every orbit in this algorithm shortly after the solar calibration data are acquired. Outlier rejection and smoothing are performed using Robust Holt Winters (RHW) filtering operating on the current observed gain values and prior smoothed gain values. The RHW filter also calculates the local temporal trends in gains as part of its functionality. The DNB LGS gains are updated scan by scan as described in Eq. 146 in Appendix C, in the same way F factors are updated for non-DNB reflective bands, using the linear trend only for propagation to the time of the current scan.

#### **D5. DNB Offset Determination**

DNB offsets are determined from Earth View (EV) data acquired during new moon periods when the instrument is viewing dark, uniform ocean scenes and from calibration sector data acquired every scan (Solar Diffuser (SD), On-Board Calibrator Blackbody (OBC BB), and Space View (SV)). The EV dark scene data are used to generate offsets for every detector, every sample across the EV scan, both Half Angle Mirror (HAM) sides and all three DNB gain stages. The calibration sector data are used to compensate for drift over time in these offsets. Based on observation of offset patterns and their temporal behavior over more than a year of on-orbit instrument operation at the time of this writing, it is believed that the complementary use of the two data sets will provide highly accurate offsets at all times. The automated algorithm updates the offsets every orbit, and offsets have been observed to drift slowly by small amounts on time scales much longer than an orbital period.

DNB offsets are subtracted from the signal both by the instrument flight software (FSW) in on-board processing and also in the SDR ground processing code implemented in the IDPS. The FSW uses four uploaded offset LUTs, one per DNB gain state (HGA, HGB, MGS, LGS), that incorporate common target values for all detectors and frames in each DNB gain state, so that the on-board signal is highly uniform after the offset correction. Notionally, the on-board offset LUT values represent “dark signal minus target value”, where the dark signal varies significantly from detector to detector and across frames within and across aggregation zones. However, after subtracting the on-board LUT offsets from the signal when the instrument is viewing a dark scene, the resulting value of all signals across detectors and frames is approximately equal to the target value at the instrument output. The offset corrected dark signals are not perfectly uniform due to random noise and the fact that the on-board LUT offsets are not perfectly accurate. The uniformity of on-board offset corrected signals is needed for the proper operation of the radiation spike suppression algorithm performed by the FSW subsequent to offset correction.

The on-board LUTs have been updated only once post launch after more than a year of instrument operation on orbit due to the remarkable stability of the DNB dark signals. The small dark signal changes that are measured each month in special operations performed during new moon periods are incorporated in the ground offset LUT, which is updated in the IDPS every month. Since the offsets do drift by small amounts, particularly in aggregation zones 28-32 in which timing feedthrough effects are much larger than in other aggregation zones, artifacts in SDR images are most noticeable just before LUT replacement when drift effects have accumulated over the month since the prior LUT update. When the RSB calibration code is operating in automated mode, however, drift effects are compensated on a nearly continuous basis, largely obviating the need for monthly special operations to view dark ocean scenes and the associated monthly LUT changes. Because the DNB electronic timing is different in the calibration sectors relative to the EV portion of the scan, and because only 16 samples per aggregation zone and gain state are acquired each scan, it is not possible to use calibration data for differential offset correction within aggregation zones. Therefore, it is anticipated that special operations to view dark ocean scenes may still be needed occasionally to update the on-board and ground processing offset LUTs, but such updates will be needed much less frequently than monthly, perhaps yearly or even less frequently based on analyses of on-orbit offsets performed to date.

The drift correction performed by the SDR Cal code uses calibration objects calculated by the RSBAutoCal algorithm and stored in a Cal History file that captures all the outputs of the RSBAuto Cal algorithm. This drift correction depends on sequence order  $N_{seq}$ , not on frame index, where sequence order is related to aggregation zone  $N_{agg}$  by the following relationship:

$$N_{seq} = 33 - N_{agg} \quad \text{Eq. 147}$$

for  $N_{agg} = 1, 2, 3, \dots, 32$ .

The static offset reference appropriate for determining offset drift is the dark signal derived from the calibration sector for the orbit  $N_{orb,ref}$  in which the EV data are collected for an EV derived offset LUT update. The dark signal derived from the calibration sector is a function of sequence order, detector, mirror side and gain:

$$DNO_{static,ref}(N_{seq}, d, m, g) = DNO_{cal}(N_{orb,ref}, N_{seq}, d, m, g)$$

where:

$DNO_{static,ref}$  = static dark signal reference

$DNO_{cal}$  = dark signal derived from calibration sector

and all other parameters have been defined above.

The static dark signal reference is calculated offline and stored in a LUT.

The drift correction is given by the difference between the dark signal acquired from the calibration sector data for an arbitrary orbit and the static dark signal reference:

$$DNO_{drift}(N_{orb}, N_{seq}, d, g, m) = DNO_{cal}(N_{orb}, N_{seq}, d, m, g) - DNO_{static,ref}(N_{seq}, d, m, g)$$

Eq. 148

where:

$DNO_{drift}$  = offset drift correction

$DNO_{cal}$  = dark signal derived from calibration sector data

$N_{orb}$  = orbit number

and all other parameters have been defined above.

Note that the drift correction is zero for the reference orbit in which the EV data are collected for the EV derived offset LUT update, as it should be to avoid biasing the offsets.

Finally, the dynamically corrected offsets applied in the ground processing are given by the sum of the ground offset LUT and the drift correction:

$$DNO(N_{orb}, f, d, g, m) = DNO_{drift}(N_{orb}, N_{seq}(f), d, g, m) + DNO_{ground}(f, d, g, m) \quad \text{Eq. 149}$$

where  $N_{seq}(f)$  is the sequence order associated with frame  $f$  and all other parameters have been defined above.

The dark signals,  $DNO_{cal}(N_{orb}, N_{seq}, d, m, g)$ , are determined by the following algorithm. For each calibration sector, sequence order, detector, mirror side and gain state, signals are collected over an entire orbit that satisfy the following three conditions at the time when the signals are acquired:

- (a) The satellite is in eclipse. (No solar illumination.)
- (b) The lunar illumination is below a prescribed level. (No significant lunar illumination.)
- (c) The entire swath is dark for the granule containing the signal. (No earthshine.)

Condition (a) is assured by requiring the Solar Zenith Angle (SZA) to be greater than a prescribed threshold in a LUT, so that the sun is below the horizon when the signal is acquired. Condition (b) is assured by requiring the lunar illumination for the time at which the signal is acquired to be less than a prescribed threshold. Both lunar illumination levels over time and this threshold are captured in LUTs. Condition (c) is assured by acquiring signals only from granules for which VIIRS is in Nighttime Operational mode. This operating mode information is available in VIIRS data product metadata.

Once the set of dark signals meeting the above conditions has been determined for each calibration sector, the dark signals from the different calibration sectors are pooled based on the value of a flag in a LUT. Any subset of the three calibration sectors can

be selected for use in dark signal determination. The dark signal values in the pooled set are ordered from least to greatest, and the value that is greater than a prescribed percentage of the values in the set is selected as the representative dark signal for the given orbit. This dark signal value is then ingested into a Robust Holt Winters smoothing algorithm, along with the smoothed dark signal value from the prior orbit, to generate the smoothed dark signal for the given orbit. Finally, a linear transformation is applied using an offset and scale factor from a LUT for fine tuning, if necessary, and it is this smoothed and tuned value that is captured in the array  $DNO_{cal}(N_{orb}, N_{seq}, d, m, g)$ .

## D6. DNB Gain Ratio Determination

Only the DNB LGS gain can be directly calculated from solar calibration data. The MGS and HGS are saturated when the sun illuminates the solar diffuser. The MGS and LGS gains are determined by on-orbit measurement of gain ratios between successive gain stages and application of these gain ratios to the measured LGS gain as multiplicative factors. The RSBAutoCal algorithm employs this same bootstrapping approach except that the gain ratios are derived from calibration sector data rather than from EV data.

DNB calibration data are acquired in all gain states in each calibration sector every scan, but for a single aggregation mode. The instrument cycles through the 32 EV aggregation modes and four test aggregation modes (36 total) in 72 scans, since the aggregation mode is held fixed over two successive scans to capture data from both mirror sides. When the satellite passes over the terminator region there is enough reflected earthshine in all three calibration sectors so that successive pairs of gain states are simultaneously unsaturated in some pixels. Such data are exploited to calculate gain ratios.

The algorithm for gain ratio determination is as follows. Pairs of unsaturated signals for successive gain states, e.g., MGS and LGS, MGS and HGA, or MGS and HGB, are identified and captured. Two filters are applied to these signals to allow further processing into gain ratios:

- (a) The raw signal must be less than a prescribed threshold acquired from a LUT.
- (b) The offset corrected signal must be greater than a prescribed threshold acquired from a LUT.

Condition (a) ensures that data used are sufficiently far from the high end digital saturation level to remain in the well behaved linear range of the gain state. Condition (b) ensures that the offset corrected signal is positive and sufficiently great to provide adequate SNR. The threshold values are chosen via offline testing and analysis. Note that the offset for calibration sector data is just the dark signal calculated from calibration sector data as described above.

For pairs of dark signals that pass through both filters, gain ratios are calculated as follows:

$$\frac{c_{MGS}}{c_{LGS}} = \frac{dn_{LGS}}{dn_{MGS}}$$

Eq. 150

$$\frac{c_{HGA}}{c_{MGS}} = \frac{1}{2} \frac{dn_{MGS}}{dn_{HGA}}$$

$$\frac{c_{HGB}}{c_{MGS}} = \frac{1}{2} \frac{dn_{MGS}}{dn_{HGB}}$$

where:

$c_{MGS}$  = MGS gain for 13 bit EV data

$c_{LGS}$  = LGS gain for 13 bit EV data

$c_{HGA}$  = HGA gain for 14 bit EV data

$c_{HGB}$  = HGB gain for 14 bit EV data

$dn_{LGS}$  = LGS offset corrected cal sector counts at 14 bits

$dn_{MGS}$  = MGS offset corrected cal sector counts at 14 bits

$dn_{HGA}$  = HGA offset corrected cal sector counts at 14 bits

$dn_{HGB}$  = HGB offset corrected cal sector counts at 14 bits

The above equations follow from the fact that both gain states view the same scene radiance. The factor of one half occurs in the equations involving HGA and HGB, because all the calibration data are acquired at 14 bits, whereas in the EV the MGS and LGS are at 13 bits. The HGS, which is the average of HGA and HGB, remains at 14 bits in the EV. All the desired gains are applied in EV and are consistent with the precision of the EV data.

The following equations describes the logic for determining the gain scale factor associated with changing precision from 14 bits to 13 bits:

$$L = c(14 \text{ bits}) dn(14 \text{ bits}) = c(14 \text{ bits}) 2 dn(13 \text{ bits}) = c(13 \text{ bits}) dn(13 \text{ bits})$$

where

L = scene radiance

$c(x \text{ bits})$  = gain for x bit data

$dn(x \text{ bits})$  = offset corrected signal at x bits

Once the gain ratios have been calculated for a given orbit for each calibration sector, detector, sequence order, and mirror side, the values for different calibration sectors are pooled together into a common set, depending upon the value of a flag in a LUT. Any subset of the three calibration sectors can be selected for use in dark signal

determination. The median of the pooled set is calculated as the representative value of the gain ratio for the given orbit. The gain ratio from the given orbit is combined with the smoothed value of the gain ratio from the prior orbit using Robust Holt Winters filtering to generate the smoothed value for the given orbit. Finally, a linear transformation is applied using an offset and scale factor from a LUT to perform tuning of the gain ratios, if deemed necessary.

## **D7. References**

[D1] Joint Polar Satellite System (JPSS) Operational Algorithm Description (OAD) Document for VIIRS Geolocation (GEO) Sensor Data Record (SDR) and Calibration (CAL) SDR Software, Joint Polar Satellite System (JPSS) Ground Project, Code 474, 474-00090, NASA Goddard Space Flight Center, Greenbelt, MD.

[D2] Gelper, S., Fried, R. & Croux, C. (2010). Robust forecasting with exponential and Holt-Winters smoothing, *Journal of Forecasting* , 29, 285-300.